



Universiteit
Leiden
The Netherlands

Molecular inheritance from cloud to disk: a story of complex organics and accretion shocks

Gelder, M.L. van

Citation

Gelder, M. L. van. (2022, November 24). *Molecular inheritance from cloud to disk: a story of complex organics and accretion shocks*. Retrieved from <https://hdl.handle.net/1887/3487189>

Version: Publisher's Version

License: [Licence agreement concerning inclusion of doctoral thesis in the Institutional Repository of the University of Leiden](#)

Downloaded from: <https://hdl.handle.net/1887/3487189>

Note: To cite this publication please use the final published version (if applicable).

Molecular inheritance from cloud to disk

- *A story of complex organics and accretion shocks* -

Proefschrift

ter verkrijging van
de graad van doctor aan de Universiteit Leiden,
op gezag van rector magnificus prof. dr. ir. H. Bijl,
volgens besluit van het college voor promoties
te verdedigen op donderdag 24 november 2022
klokke 12:30 uur
door

Martijn Lucas van Gelder

geboren te 's-Gravenhage, Nederland
in 1994

Promotores:

Prof. dr. E. F. van Dishoeck

Prof. dr. M. R. Hogerheijde Universiteit Leiden
Universiteit van Amsterdam

Co-promotor:

Dr. B. Tabone Université Paris-Saclay

Promotiecommissie:

Prof. dr. H. J. A. Röttgering

Prof. dr. S. Viti

Prof. dr. J. K. Jørgensen University of Copenhagen

Dr. B. Nisini INAF, Osservatorio Astronomico di Roma

Dr. B. A. McGuire MIT, Cambridge

ISBN: 978-94-6419-632-0

Cover design: Marta Paula Tychoniec

If the truth is worth telling,
it is worth making a fool of yourself to tell it.
- *Frederick Buechner*

Table of contents

1	Introduction	1
1.1	How do stars form?	2
1.1.1	Prestellar phases and start of collapse	2
1.1.2	Low-mass star formation	3
1.1.3	High-mass star formation	6
1.2	Chemistry during protostellar evolution	7
1.2.1	Prestellar cores	7
1.2.2	Hot cores	10
1.2.3	Shocks	10
1.3	Astronomical observatories	14
1.3.1	ALMA	14
1.3.2	JWST	15
1.4	Complex organic molecules in protostars	16
1.4.1	Ices	17
1.4.2	Gas phase	18
1.5	Inheritance versus reset: accretion shocks	23
1.6	This thesis	25
PART I	Chemical complexity in young protostars	29
2	Complex organic molecules in low-mass protostars on Solar System scales. I. Oxygen-bearing species	31
2.1	Introduction	33
2.2	Observations	35
2.3	Spectral modeling and results	37
2.3.1	Methodology	37
2.3.2	Column densities and excitation temperatures	39
2.3.3	Relative abundances	42
2.4	Discussion	43
2.4.1	Occurrence of COMs in young protostars	43
2.4.2	Dependence on source size	44
2.4.3	From cold (Band 3) to hot (Band 6) COMs	45
2.4.4	Comparison to other sources	48

2.4.5	Comparison with ices	50
2.4.6	Temperature dependence of deuterated methanol	50
2.5	Summary	51
	Appendices	53
2.A	Laboratory spectroscopic data	53
2.B	CASSIS modeling results	54
2.C	Full ALMA Band 6 spectra	61
2.D	B1-c Band 3 spectrum	67
2.E	Additional tables	71
3	Importance of source structure on complex organics emission.	
	I. Observations of CH₃OH from low-mass to high-mass protostars	95
3.1	Introduction	97
3.2	Methodology	98
3.2.1	Observations and archival data	98
3.2.2	Deriving the column density	100
3.2.3	Calculating the warm methanol mass	102
3.3	Results	103
3.3.1	Amount of warm methanol from low to high mass	103
3.3.2	Comparison to spherically symmetric infalling envelope	105
3.4	Discussion	107
3.4.1	Importance of source structure	107
3.4.2	Continuum optical depth	110
3.5	Conclusion	112
	Appendices	114
3.A	Observational details	114
3.B	Transitions of CH ₃ OH and isotopologues	126
3.C	Toy model of infalling envelope	128
3.D	Calculating the reference dust mass	129
4	Methanol deuteration in high-mass protostars	131
4.1	Introduction	133
4.2	Methodology	134
4.2.1	Observations	134
4.2.2	Deriving the column densities	136
4.3	Results	138
4.4	Discussion	140
4.4.1	Methanol deuteration from low to high mass	140
4.4.2	Singly vs doubly deuterated methanol	142
4.4.3	Linking the methanol D/H to the physical conditions during formation	143
4.5	Conclusion	146
	Appendices	149
4.A	Transitions of CH ₃ OH and isotopologues	149
4.B	Observational details	150
4.C	Methanol D/H ratios of sources in the literature	154

4.D	CHD ₂ OH in B1-c, Serpens S68N, and B1-bS	156
4.E	Additional figures	157
PART II Inheritance versus reset: accretion shocks		159
5	Modeling accretion shocks at the disk-envelope interface. Sul-	
	fur chemistry	161
5.1	Introduction	163
5.2	Accretion shock model	165
5.2.1	Shock model	165
5.2.2	Input parameters	168
5.3	Results	169
5.3.1	Temperature and density	169
5.3.2	Chemistry of SO and SO ₂	171
5.3.3	Effect of grain size and PAHs	176
5.3.4	Other molecular shock tracers: SiO, H ₂ O, H ₂ S, CH ₃ OH, and H ₂	176
5.4	Discussion	178
5.4.1	Comparison to SO and SO ₂ with ALMA	178
5.4.2	Predicting H ₂ , H ₂ O, and [S I] with JWST	179
5.5	Summary	180
	Appendices	182
5.A	Updated cooling of NH ₃	182
5.B	Input abundances	183
5.C	Changing the preshock conditions	183
5.D	Abundance grids	187
5.D.1	H ₂ S, H ₂ O, SiO, and CH ₃ OH for $G_0 = 1$	187
5.D.2	SO and SO ₂ for various G_0	188
5.E	Higher magnetized environments	190
5.E.1	C-type shocks	190
5.E.2	CJ-type shocks	191
6	Observing accretion shocks with ALMA. Searching for SO and	
	SO₂ in Class I disks	193
6.1	Introduction	195
6.2	Observations	197
6.3	Results	198
6.3.1	Dust continuum	198
6.3.2	SO and SO ₂	199
6.4	Discussion	202
6.4.1	Inheritance vs reset: constraining the shock strength	202
6.4.2	Relation between warm SO ₂ and source properties	203
6.5	Conclusions	205
	Appendices	207
6.A	Maps of c-C ₃ H ₂ and CH ₃ OH	207

6.B Spectra of SO and SO ₂ for IRS 4 and IRS 6	208
6.C Additional tables	209
Bibliography	210
Nederlandse samenvatting	233
Publications	241
Curriculum Vitae	243
Acknowledgements	245

Chapter 1

Introduction

Throughout the entire history of the human race, we have looked up at the sky at night and wondered what those blinking distant lights are. Even far before we knew their precise origin, we connected them into constellations and even used them to navigate ourselves. By looking at the night sky over long periods of time, the by then only known planets Venus, Mars, Jupiter, and Saturn could already be easily distinguished from the more "stationary" light sources.

Initially, the Earth was the center of the universe and everything else was thought to revolve around it, until Copernicus realized that it is the Sun that is the center of our Solar System and that all the planets revolve around the Sun (Copernicus 1543). Later, Galileo Galilei was the first to observe moons around another planet than our own Earth (around Jupiter; Galilei 1610). Over the following centuries, more and more became known about our own Solar System, but several questions remain unanswered. How did the Sun, our Earth, and all the other planets, moons, and comets in our Solar System form? How do all the other stars in our Galaxy form? Are there also planets around other stars? Are we alone?

Especially in the past century, with the level of technology increasing, telescopes have revealed a larger variety of astronomical objects. What were thought to be light dots in the sky, turned out to be distant stars, galaxies, planets, and much more. In addition, also various dark cloud-like areas were discovered (e.g., Barnard 1919; Bok & Reilly 1947). These dark areas, now better known to be molecular clouds, can be as large as hundreds of light-years across. Deep within these cold and dark molecular clouds are the stellar nurseries where new stars are born. So in order to answer the questions related to the formation of our own Solar System, we have to zoom in on the young stellar objects residing deeply within these molecular clouds.

This thesis focuses on how molecules are transported from cloud to disk in the youngest star-forming systems. Observations done with advanced telescopes such as the Atacama Large Millimeter/submillimeter Array (ALMA) are presented

which allow us to study the complex chemistry occurring in these young protostars and their surrounding dark and cold molecular clouds. Furthermore, shock modeling results are presented on whether the material that forms planets is inherited unchanged from the parent molecular cloud or whether it is modified en route.

1.1 How do stars form?

1.1.1 Prestellar phases and start of collapse

Stars are born in dense ($n \sim 10^4 - 10^6 \text{ cm}^{-3}$) and cold ($T \sim 10 - 20 \text{ K}$) molecular clouds (see e.g., review by Bergin & Tafalla 2007). These clouds consist mostly of molecular hydrogen (H_2) with carbon monoxide (CO), the next most abundant molecule, being 10000 times less abundant (Frerking et al. 1982; Lacy et al. 1994, 2017). About 1% of the total mass budget consists of small (sub)micron sized dust grains containing most of the abundant refractory heavy metals such as iron, silicon, and magnesium as well as a significant amount of carbon and oxygen (e.g., Draine & Lee 1984; Henning & Salama 1998; Whittet 2010). However, albeit making up only a small portion of the mass, these dust grains prove to be crucial as a catalyst for the chemistry taking place in these very cold environments (see Sect. 1.2.1).

Molecular clouds can be found throughout the entire Galaxy. Their sizes can vary from being much less than a parsec across (e.g., Bok globules; Bok & Reilly 1947) that will likely form single isolated stars to giant molecular clouds of up to 100 pc across that will likely form clusters of stars (Lada & Lada 2003; Ward-Thompson et al. 2007; Krumholz et al. 2014). Moreover, the total mass of a molecular cloud is also crucial in determining the mass of stars. Molecular clouds are often depicted in schematics as being large spherical clouds but observations in fact show that clouds are far from spherical and can show various possible shapes ranging from small irregular clouds to long filamentary structures (e.g., André et al. 2010; Hacar & Tafalla 2011; Hacar et al. 2013, 2017).

As molecular clouds evolve, the cores within them start to get denser and colder, making them unstable against collapse under their own gravity. At some point, whether it is due to an internal instability or an external trigger, dense cores within molecular clouds will start to collapse. For this, the Jeans criterion should be met (Jeans 1928), that is, that the internal pressure of the core can no longer resist gravity. As the core starts collapsing, the density in the center increases whilst the temperature remains constant. As the inner core becomes optically thick to radiation, it can no longer effectively radiate away the gravitational energy and the temperature of the core increases. The contraction of the core stops, leading to the formation of the First Hydrostatic Core (FHSC; Larson 1969). The temperature in the core keeps increasing until it reaches the threshold where H_2 dissociates ($\sim 2000 \text{ K}$) that cools down the core. Subsequently, the core contracts further to form a protostar.

In the following two sections, a distinction is made between the next stages of protostellar evolution based on the mass. Low-mass stars ($M < 8 M_\odot$) form

significantly slower (up to 10 Myr, see Sect. 1.1.2), whereas high-mass ($M > 8 M_{\odot}$) star formation is much quicker ($10^4 - 10^5$ years, see Sect. 1.1.3) leading to various crucial differences in the evolution of their protostellar phases.

1.1.2 Low-mass star formation

In the process of low-mass star formation, a clear distinction has to be made between evolutionary *Stages* (Shu et al. 1987; Robitaille et al. 2006) and observational *Classes* (Lada 1987; André et al. 1993). As a young protostar is formed, the subsequent evolution can be divided into four stages (see Fig. 1.1). In the first $\sim 100\,000$ years, the mass of the system is still dominated by the mass of the envelope (i.e., $M_{\text{env}} > M_{\star}$, Stage 0) and the accretion rate onto the protostar is high ($\dot{M} > 10^{-6} M_{\odot}/\text{yr}$). It is also in this stage that an accretion disk consisting of both gas and dust starts forming around the young protostar to conserve the angular momentum of the rotating core (Cassen & Moosman 1981; Shu et al. 1987). Simulations show that the collapse of a rotating core naturally leads to disks of $10 - 100$ au (e.g., Yorke et al. 1993), although the role of magnetic fields seems crucial in determining the size of the disk through magnetic breaking (e.g., Mellon & Li 2008; Li et al. 2014; Hennebelle et al. 2016). Any excess of angular momentum is removed from the system through bipolar jets and outflows. As the protostar accretes significant amounts of gas, its mass starts exceeding that remaining in the envelope (i.e., $M_{\star} > M_{\text{env}} > M_{\text{disk}}$, Stage 1). Over the next few hundred thousands of years, the protostar keeps accreting mass at a high rate ($\dot{M} > 10^{-6} M_{\odot}/\text{yr}$) from the disk whereas the envelope accretes onto the disk. Together, Stages 0 and 1 last about $\sim 500\,000$ years (Kristensen & Dunham 2018) and are commonly referred to as the *embedded phase of star formation*. The envelope dissipates due to accretion onto the disk and due to the outflow carving a cavity. What remains is a now-called pre-main sequence star which has accreted most of its final mass surrounded by a protoplanetary disk (i.e., $M_{\star} > M_{\text{disk}} > M_{\text{env}}$, Stage 2). The system now slowly evolves over the next $\sim 1 - 5$ million years, where the disk surrounding the pre-main sequence star dissipates through accretion onto the central star (at a much lower rate than in the embedded phase; $\dot{M} < 10^{-6} M_{\odot}/\text{yr}$), planet formation, and other processes such as photoevaporation. In the final phase (i.e., $M_{\star} \gg M_{\text{disk}} \gg M_{\text{env}}$, Stage 3), a pre-main sequence star remains that evolves toward the main sequence and which is surrounded by a gas-poor debris disk and (presumably) a young planetary system. Finally, the star reaches the main sequence and a young stellar system is born.

Observationally, these various stages are not always trivial to distinguish since the main parameters such as the age of the system, the mass, and accretion rates are not always directly observable. Therefore, these young protostellar systems are generally divided into various Classes based on their spectral energy distribution (SED) at infrared wavelengths (Lada 1987),

$$\alpha_{\text{IR}} = \frac{d \log \lambda \mathcal{F}_{\lambda}}{d \log \lambda}, \quad (1.1)$$

where α_{IR} is the so-called spectral index and \mathcal{F}_{λ} is the observed flux in a wavelength

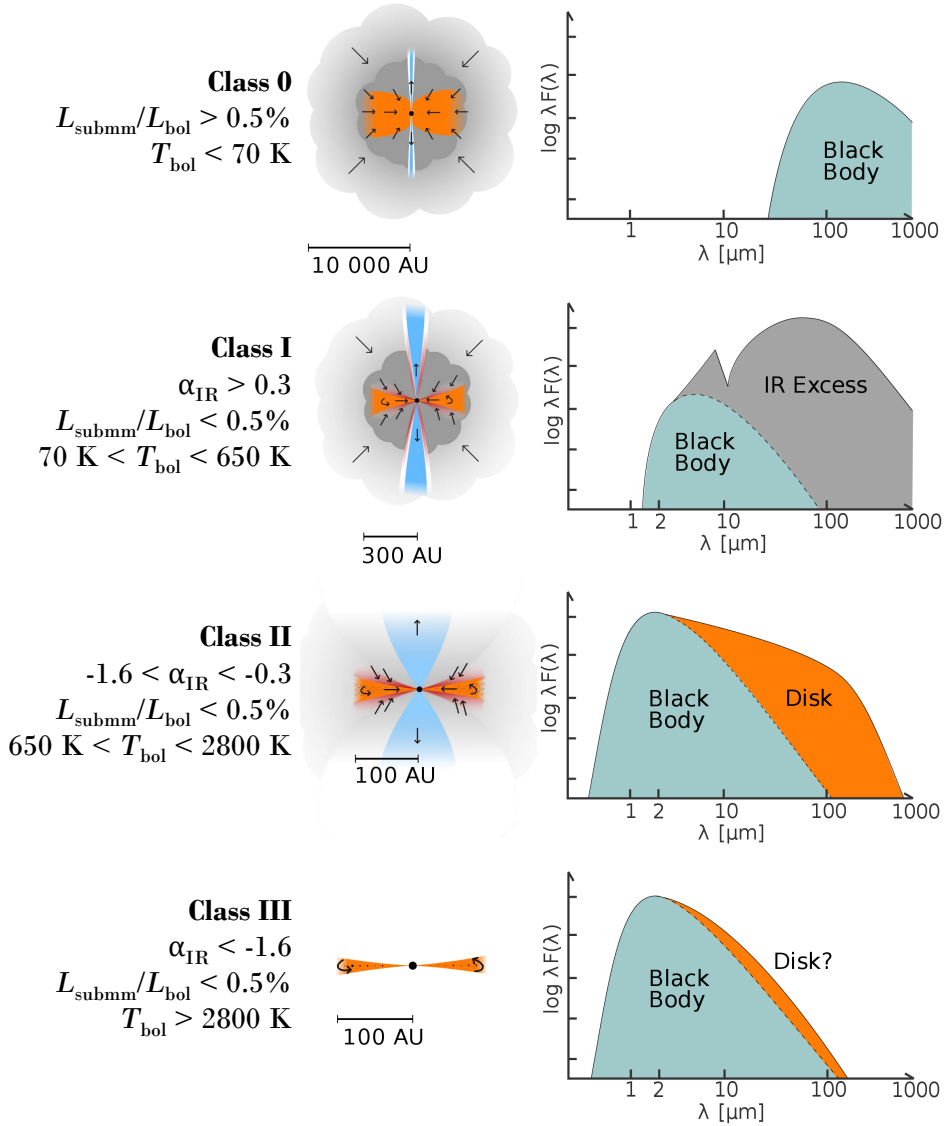


Figure 1.1: Schematic view of the various stages of low-mass star formation. For each observational classification (left), a corresponding schematic of the system (middle) and example SED (right) are presented. Adopted from figure by Magnus Persson.

range of $\lambda = 2 - 20 \mu\text{m}$. Initially, only three Classes were distinguished at infrared wavelengths (I, II, III; Lada 1987), but later different Classes were added such as Class 0 (sources which are too faint at IR wavelengths; André et al. 1993) and Flat-spectrum sources (Greene et al. 1994). Beside using α_{IR} for the classification of protostellar systems, also the bolometric temperature (T_{bol}) and the ratio between

the submillimeter luminosity and bolometric luminosity ($L_{\text{submm}}/L_{\text{bol}}$) can be used to classify protostellar systems (e.g., André et al. 1993; Chen et al. 1995). Generally, the evolutionary Stages and observational Classes match very well (i.e., a Class I protostar being in Stage I of its evolution). However, it is important to note that the observational parameters depend on the orientation of the source and therefore can mismatch theoretical stages (e.g., Crapsi et al. 2008).

Class 0 protostars are (nearly) invisible at near and mid-infrared wavelengths and are therefore not characterized by α_{IR} . Instead, Class 0 protostars are distinguished from more evolved Class I sources through a high $L_{\text{submm}}/L_{\text{bol}}$ ($> 0.5\%$) and low T_{bol} (< 70 K) (André et al. 1993). Despite strong observational contamination from the envelope, accretion disks are generally still relatively small in Class 0 systems (< 50 au; Tobin et al. 2016; Segura-Cox et al. 2018; Maury et al. 2019), but also large disks have been detected (up to ~ 200 au; Tobin et al. 2012; Murillo et al. 2013). Moreover, molecular jets and outflows that carry away excess angular momentum are most powerful in these young systems (see e.g., reviews by Frank et al. 2014; Bally 2016). Class 0 sources are also the warmest (van 't Hoff et al. 2020c) and most rich in molecular chemistry in their central hot cores (see e.g., review by Jørgensen et al. 2020).

More evolved Class I sources can be distinguished from Class 0 systems by having a high and detectable α_{IR} (> 0.3), lower $L_{\text{submm}}/L_{\text{bol}}$ ($< 0.5\%$), and higher T_{bol} (70-650 K). The disk mass reservoir in Class I sources is more significant relative to that in the envelope (Jørgensen et al. 2009), and more recently it was suggested that planet formation may start already in these embedded disks based on results on both mass and substructures in the disk (e.g., ALMA Partnership et al. 2015; Tychoniec et al. 2020; Segura-Cox et al. 2020). The bipolar outflows become weaker and more atomic in composition (Arce & Sargent 2006; Nisini et al. 2015). Furthermore, due to the presence of the disk and lower accretion rates, the overall temperature in the systems is lower than in Class 0 sources (van 't Hoff et al. 2018a, 2020b). An exception is in sources where a recent accretion burst has heated the system (van 't Hoff et al. 2018b; Lee et al. 2019b). Flat spectrum sources ($-0.3 < \alpha_{\text{IR}} < 0.3$) are suggested to be in an intermediate state between Class I and Class II sources (Greene et al. 1994).

Class II sources are generally also referred to as *T-Tauri stars*, named after the first identified example of a Class II source, and host a *protoplanetary disk* which often show detailed substructures (e.g., Andrews et al. 2018). Since the surrounding envelope has largely dissipated, the photosphere of the central pre-main sequence star can be detected at optical and near-infrared wavelengths as well as an infrared excess originating from the disk at longer wavelengths ($-1.6 < \alpha_{\text{IR}} < -0.3$) and a high bolometric temperature ($650 < T_{\text{bol}} < 2800$). At this stage, any jet is composed of mostly atomic and ionized material (e.g., Podio et al. 2011; Xie et al. 2021).

Class III sources have only a *debris disk* left containing residual dust that was not accreted onto planetesimals or planets and therefore have only minor infrared excess ($\alpha_{\text{IR}} < -1.6$) and high bolometric temperature ($T_{\text{bol}} > 2800$ K). These sources show mostly emission originating from the pre-main sequence star that is contracting until hydrogen fusion begins in the core.

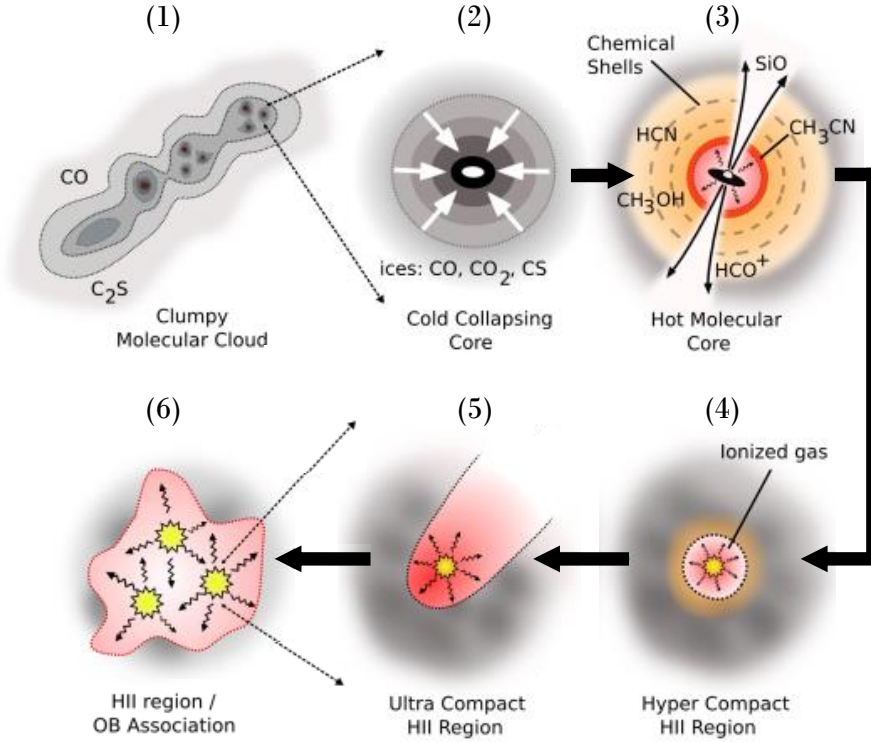


Figure 1.2: Schematic view of the various stages of high-mass star formation. Panels 2-5 are a zoomed in with respect to panel 1 and similarly panel 6 is a zoom-in of panels 2-5. Adopted from figure by Cormac Purcell.

1.1.3 High-mass star formation

In contrast to low-mass stars, high-mass stars are much more difficult to find. Because they are located on the upper end of the initial mass function (Salpeter 1955), they are much rarer than low-mass stars. However, despite being much rarer, high-mass stars are crucial for the evolution of molecular clouds due to their high ionizing radiation and their fate to end in supernova explosions, thereby also triggering sequential star formation. Moreover, high-mass stars form almost exclusively in multiple systems (e.g., Sana et al. 2012).

The formation of massive stars also occurs in a different way from their lower mass counterparts, see Fig. 1.2. High-mass stars form much faster (~ 0.1 Myr; Beuther et al. 2007) compared to lower mass stars ($\sim 1 - 5$ Myr), but overall high-mass star formation still remains poorly understood (see reviews by Beuther et al. 2007; Zinnecker & Yorke 2007; Tan et al. 2014; Motte et al. 2018). Starting from a giant molecular cloud, a protostar is formed through collapse in a similar manner as low-mass evolution (Sect 1.1.2). However, due to the large mass of the system, the *hot core* around the center reaches a temperature of ~ 100 K very early,

leading to very rich molecular chemistry (see also Sects 1.2.2 and 1.4.2). As the central protostar increases in mass and approaches the main sequence (whilst still being embedded in its natal envelope), it starts to produce significant amounts of ultraviolet (UV) radiation leading to the formation of an hyper compact HII region (Keto 2003). At this stage, a disk around the high-mass protostar is still likely present (see Beltrán & de Wit 2016, for a review). As the HII region grows into an ultra compact HII region (Churchwell 2002), accretion onto the central massive protostar likely only occurs through the massive disk (e.g., Keto 2007; Kuiper & Hosokawa 2018). Eventually, the radiation pressure disperses the disk completely and accretion halts, leaving a massive star surrounded by a classical HII region.

There are three main theories on how high-mass cores can acquire their mass from the large molecular clouds. In the *monolithic collapse* theory, high-mass star formation is basically a scaled-up version of low-mass star formation where a single cloud or core collapses into a single high-mass protostar (e.g., McKee & Tan 2002). In the *competitive accretion* scenario, high-mass protostars start off as low-mass cores but over time accrete significant amounts of mass from the surrounding molecular cloud (e.g., Bonnell et al. 2001; Bonnell & Bate 2006). Lastly, in the *stellar merger* theory, high-mass stars are suggested to form through mergers of multiple low-mass cores (Bonnell et al. 1998). In reality, all three cases may contribute to the formation of high-mass stars, although stellar mergers seem the least likely process due to the high density of protostellar cores required for stellar mergers to occur.

1.2 Chemistry during protostellar evolution

Atoms and molecules can be used as tracers of various aspects of protostellar evolution. In the local interstellar medium (ISM), the material is largely composed of hydrogen (90%) and helium (10%), with more heavier elements such as carbon (3×10^{-4}), oxygen (4×10^{-4}) and nitrogen (7.5×10^{-5}) occurring in far lower abundances (Wilson & Rood 1994). Furthermore, the metals of which dust grains are composed, such as silicon and iron, are present at even lower levels of $\lesssim 3 \times 10^{-5}$. Yet, despite these lower occurrences, these elements provide the crucial building blocks for the chemistry during the star-formation process, leading to the formation of simple molecules like water (H₂O), methane (CH₄), and ammonia (NH₃), as well as so-called *complex organic molecules* (COMs, molecules containing six or more atoms; Herbst & van Dishoeck 2009) such as methanol (CH₃OH), methyl formate (CH₃OCHO), and ethanol (C₂H₅OH). In total, 241 molecules have been detected in the ISM by mid 2021 (McGuire 2022). It is crucial to understand the relevant chemistry in order to understand why certain molecules trace certain regions in space (Tychoniec et al. 2021).

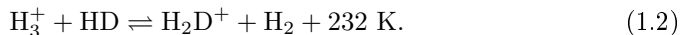
1.2.1 Prestellar cores

The chemistry in cold and dark prestellar cores is regulated by the low temperatures (< 15 K) and high densities (compared to the general ISM) of $10^4 - 10^6$ cm⁻³.

At these very low temperatures, the chemistry in the gas phase is dominated by exothermic barrierless reactions, mostly between ions and neutral species or between ions and electrons. The dominant ion in dark cores is H_3^+ , which originates from the impact of cosmic rays on H_2 . The H_3^+ ion can subsequently react with atoms such as C, O, and N, as well as molecules, leading to the attachment of hydrogen to these species. This eventually leads to the formation of simple molecules such as CO but also longer (and mostly unsaturated) carbon chains (e.g., Langer et al. 1997; Cernicharo et al. 2021, 2022).

Deuterium chemistry

A process that does benefit from the low temperatures in cold and dark clouds is deuterium (D) enhancement (see e.g., reviews by Tielens 2013; Ceccarelli et al. 2014). The canonical D/H fraction in the local ISM is observed to be $2.0 \pm 0.1 \times 10^{-5}$ (Linsky et al. 2006; Prodanović et al. 2010). However, the atomic D/H ratio in the gas phase can be increased through the exothermic reaction (Watson 1974),



Since the backward reaction is endothermic, it is less likely to occur at temperatures below $\lesssim 30 \text{ K}$. H_2D^+ can then subsequently recombine with a free electron to form H_2 and atomic D or transfer its deuterium to other species. It is important to note that Reaction (1.2) can also occur sequentially, leading to the formation D_2H^+ and D_3^+ . Moreover, the effectiveness of Reaction (1.2) is enhanced in the densest ($\gtrsim 10^5 \text{ cm}^{-3}$) regions of the core where CO is frozen out onto the dust grains since CO is the main destroyer of H_3^+ in the gas phase (Brown & Millar 1989; Roberts et al. 2003). Although Reaction 1.2 dominates the deuteration at low temperatures, at higher temperatures deuteration occurs mostly via CH_2D^+ which forms in a similar manner as H_2D^+ but with a higher activation energy barrier for the backward reaction (370 K; Roberts & Millar 2000)

Indeed high $\text{H}_2\text{D}^+/\text{H}_3^+$ ratios are observed toward the densest parts of prestellar cores (e.g., Caselli et al. 2003, 2008) and the outer parts of protostellar envelopes (Stark et al. 1999). The enhancement of H_2D^+ and CH_2D^+ directly translates into other species in the gas phase such as N_2D^+ , DCO^+ , DCN, and HDCO (e.g., Roberts et al. 2002; Crapsi et al. 2005). Moreover, species forming through hydrogenation on the surfaces of dust grains can inherit the high atomic D/H ratio leading to deuteration levels as high as a few % for molecules forming on the surfaces of grains (e.g., CH_3OH ; van Dishoeck et al. 1995; Bianchi et al. 2017a,b, see also Chapter 4). Due to the sensitivity of Reaction 1.2 to temperature (and density), the deuteration of molecules forming predominantly in the dense prestellar phases can thus be used as a measure of the physical conditions during their formation (e.g., Bøgelund et al. 2018; Taquet et al. 2019).

Grain-surface chemistry

Dust grains make up about 1% of the total mass of molecular clouds and consist mostly of silicates, iron-oxides and carbonaceous material. Yet, they are crucial

for the formation of a large variety of molecules (e.g., Charnley et al. 1992). Atoms such as carbon and nitrogen can stick to the dust grains and be hydrogenated by H-atoms diffusing over the surface (see reviews by van Dishoeck et al. 2013; Tielens 2013; Linnartz et al. 2015; Cuppen et al. 2017; Öberg & Bergin 2021). This leads to the formation of saturated molecules such as H_2O , NH_3 , and CH_4 which remain situated as ices on the surface.

In the cold (< 15 K) conditions of prestellar cores, even the most volatile species like CO can *freeze out* onto the dust grains, making them available for grain-surface chemistry through for example hydrogenation. Sequential hydrogenation of CO ice results in the formation of HCO, formaldehyde (H_2CO), and eventually CH_3OH (Watanabe & Kouchi 2002; Fuchs et al. 2009; Santos et al. 2022). Methanol is the simplest and most abundant *complex organic molecule* (Herbst & van Dishoeck 2009) and a poster child of grain-surface chemistry since gas-phase chemistry producing CH_3OH is highly ineffective at low-temperature conditions (e.g., Garrod et al. 2006; Geppert et al. 2006).

The chemistry on the surfaces does not stop at CH_3OH . Many more complex species have been observed toward hot cores (see Sect. 1.4.2) and many laboratory studies have been carried out to explain their formation on the surfaces of dust grains. Reactions between pre-products of CH_3OH , such as HCO and CH_2OH , can lead to even more complex species such as glycolaldehyde (CH_2OHCHO) and ethylene glycol ($(\text{CH}_2\text{OH})_2$; Fedoseev et al. 2015), and possibly even result in molecules as big as glycerol (Fedoseev et al. 2017). Furthermore, also the formation of several 3-carbon alcohols such as n-propanol ($\text{CH}_3\text{CH}_2\text{CH}_2\text{OH}$) was witnessed in the laboratory (Qasim et al. 2019a). Moreover, Fedoseev et al. (2022) find formation of ketene (H_2CCO), acetaldehyde (CH_3CHO), and ethanol ($\text{C}_2\text{H}_5\text{OH}$) in cold conditions by depositing CO together with atomic C and H. For some species such as methyl formate (CH_3OCHO), the chemistry seems to depend also on UV irradiation (Chuang et al. 2017). Alternatively, some COMs may also form through thermally induced chemistry (Theulé et al. 2013).

Interestingly, recent laboratory studies suggest that CO and its hydrogenation may not be required for the formation of all COMs. For multiple oxygen-bearing COMs such as CH_3CHO , H_2CCO , $\text{C}_2\text{H}_5\text{OH}$, and vinyl alcohol ($\text{C}_2\text{H}_3\text{OH}$), recent laboratory studies suggest that acetylene (C_2H_2) could be the initial molecule rather than (pre-products of) CH_3OH (Chuang et al. 2020, 2021). These molecules could thus already be made prior to CO freeze-out in the translucent cloud phase, and could even lead to the formation n-propenol, isopropenol, and glycine (Qasim et al. 2019b; Ioppolo et al. 2021).

The importance of grain-surface chemistry for nitrogen-bearing COMs remains far less well understood. The OCN^- anion and NH_3 remain the most complex nitrogen-bearing species that are securely detected in the ices (Grim & Greenberg 1987; Schutte & Greenberg 1997; Boogert et al. 2015). Although laboratory studies suggest that in the presence of UV irradiation nitrogen-bearing COMs such as ethyl cyanide ($\text{C}_2\text{H}_5\text{CN}$) can form from a methyl cyanide (CH_3CN) ice mixed with H_2O (Bulak et al. 2021), it remains unknown if and how CH_3CN forms in interstellar ices.

1.2.2 Hot cores

As the envelope material (both gas and dust) moves toward the accreting protostar, the physical conditions change due to the increase in density, temperature, and UV field (e.g., Aikawa et al. 1999; Visser et al. 2009; Drozdovskaya et al. 2014). As the dust grains heat up to 20–30 K, volatile ice species such as CO, N₂, and CH₄ start sublimating from the ices toward the gas phase. Despite the lower residence time of atomic H on the surfaces of dust grains, which hampers hydrogenation of molecules, modeling studies suggest that elevated dust temperatures (> 20 K) may actually be beneficial for forming complex molecules since species can diffuse more easily through the ices (Garrod & Herbst 2006; Garrod 2013; Garrod et al. 2022).

When the temperature reaches about 100–300 K in the central *hot core* (or *hot corino* for low-mass protostars), the most strongly bound species such as H₂O and COMs fully sublime into the gas phase. In theory, each molecule has its own binding energy and will therefore sublime at a different temperature (e.g., Collings et al. 2004; Penteado et al. 2017; Cuppen et al. 2017; Minissale et al. 2022), creating an onion shell-like structure of molecules. For example, species like H₂CCO, CH₃OH, CH₃CHO are relatively "cold" COMs sublimating at temperatures of 70–100 K, whereas (CH₂OH)₂ and formamide (NH₂CHO) likely sublime at much higher temperatures of > 200 K (e.g., Fedoseev et al. 2017). However the binding energies of molecules are also very dependent on the ice mixture (whether they are bound to a H₂O or CO dominated ice) and even on the type of grain surface (e.g., Tielens et al. 1991; Collings et al. 2004; Ferrero et al. 2020). Furthermore, several studies also suggest that the majority of the COMs sublime together with major ice species such as H₂O and CH₃OH at ~ 100 K.

The higher temperatures in hot cores also allow for endothermic reactions to occur more efficiently. Whilst several COMs such as CH₃OH do not have efficient gas-phase formation routes even at temperatures of > 100 K, some COMs such as NH₂CHO and CH₂OHCHO may have additional gas-phase formation routes (e.g., Skouteris et al. 2017, 2018). Moreover, other recent studies link the formation of primarily nitrogen-bearing COMs such as CH₃CN and C₂H₅CN to the $T > 300$ K region where these molecules are produced through top-down chemistry starting from sublimated carbon grains (van 't Hoff et al. 2020a). The most direct way to distinguish gas-phase chemistry from grain-surface chemistry is by comparing abundances in the ices (Sect. 1.4.1) with those observed in the gas (Sect. 1.4.2).

1.2.3 Shocks

Shocks are regions in space where the temperature and density increase significantly over a short distance and timescale through the collision of one "fluid" with another (see e.g., review by Draine & McKee 1993). They are common phenomena in the universe and can occur on large scales such as in supernova explosions as well as on smaller scales in for example late-type AGB stars. In young protostellar systems, shocks are often observed in the bipolar outflows and jets where the outflowing material impacts the surrounding envelope (e.g., McCaughrean et al. 1994) as well as internally within the jet (e.g., Lee et al. 2017a; Tychoniec et al. 2019).

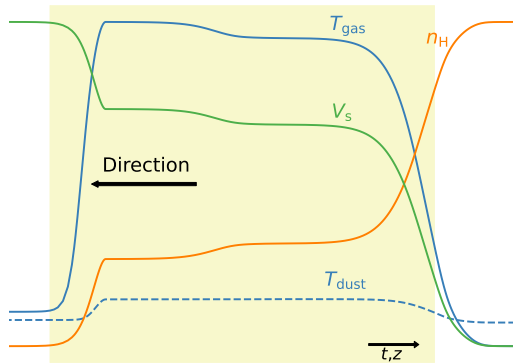


Figure 1.3: Schematic of the structure of a *J*-type shock. The hydrogen density and velocity are depicted in orange and green, respectively. The temperatures of the gas (solid) and dust (dashed) are shown in blue. The yellow shaded area indicates the shocked region. The black arrow denotes the direction in which the shock front propagates.

Another example of shocks in protostellar systems are those occurring where material is accreted onto the protostar itself (see e.g., review by Hartmann et al. 2016), which can be observed in less extincted sources in highly ionized species. On the disk scales of interest for this thesis, shocks are of significant importance in protostellar evolution at the disk-envelope interface (see Sect. 1.5). In this Section, first a short review of the physics of shocks is given before going into the shock chemistry.

Physics of interstellar shocks

Whenever a shock wave approaches at a velocity larger than the speed of sound, the material ahead has no warning about the approaching shock wave. As the shock wave hits, the material is compressed leading to a sudden, discrete, and irreversible increase in both temperature and density (see Fig. 1.3). In this compression, physical quantities such as mass, momentum, and energy are assumed to be conserved, allowing to write down a set of equations that govern the physics at the shock front (so-called Rankine-Hugoniot equations). These equations are commonly used to model the shock physics of interstellar shocks in a large variety of conditions (e.g., Flower & Pineau des Forêts 2003; Lesaffre et al. 2013; Godard et al. 2019).

The increase in temperature and density in the shock depends mainly on a few physical quantities: pre-shock density of hydrogen $n_{\text{H}} = n(\text{H}) + 2n(\text{H}_2)$, shock velocity V_{s} , and magnetic field strength B . In the absence of a magnetic field, the pre-shock material has no knowledge at all about the approaching shock wave and therefore both the temperature and density jump up discontinuously, creating a so-called *J*-type shock. For *J*-type shocks, all the material (ions and neutrals) are tied to one fluid and the maximum gas temperature (in K) reached in the shock can be calculated through (Lesaffre et al. 2013),

$$T_{\text{gas,max}} \approx 53V_{\text{s}}^2, \quad (1.3)$$

with V_{s} is the shock velocity in km s^{-1} . Similarly, the density can easily jump by more than 2 or 3 orders of magnitude in the post-shock region. The temperature of the dust (T_{dust}), however, only increases at high pre-shock densities ($\gtrsim 10^7 \text{ cm}^{-3}$)

due to gas-grain collisions and never reaches as high temperatures as the gas. J -type shocks can drastically change the composition of the material as it enables effective high-temperature gas-phase chemistry, and for the highest velocities can lead to complete dissociation of all the molecules ($V_s \gtrsim 25 \text{ km s}^{-1}$; Flower & Pineau des Forêts 2003) and even ionize them ($V_s \gtrsim 35 \text{ km s}^{-1}$; Lehmann et al. 2020).

In the presence of a magnetic field, the material has a way of knowing that a shock front is coming. The sudden jump at the shock front becomes smoother when the shock velocity V_s is smaller than the magnetosonic speed of the ions,

$$c_{\text{ims}} = \sqrt{c_i^2 + B^2/4\pi\rho_i^2}, \quad (1.4)$$

with c_i and ρ_i sound speed and density of the ions, respectively. When $V_s < c_{\text{ims}}$, a so-called magnetic precursor can develop: a region in front of the shock where the ions and electrons can decouple from the neutral species through the Lorentz force. Whilst slowing down, the ions exert a drag force on the neutral fluid, which therefore also smoothly decreases in velocity. The result is that ions, neutrals, and electrons decouple from each other, resulting in a continuous increase in both the temperature and the density (Draine 1980; Flower & Pineau des Forêts 2003). The resulting shock is referred to as a C -type shock. In intermediate magnetized environments, the drag force of the ions is insufficient to completely slow the neutrals before hitting the shock front and a discontinuous jump in density and temperature may still occur, creating a so-called CJ -type shock (Godard et al. 2019).

After the initial heating and compression, the shocked material starts to cool down. Depending on the heat released in the shock, cooling can be dominated by rotational and rovibrational transitions of simple molecules such as H_2 , CO , and NH_3 , or by optical and UV lines from atoms and ions (i.e., $[\text{OI}]$, $[\text{SiI}]$). Alternatively, gas-grain collisions in higher density shocks can contribute significantly to the cooling, where the gas transfers the heat to the dust which emits it away as thermal emission. Eventually, the shock cools down completely, leaving the now post-shock material irreversibly changed.

Chemistry of interstellar shocks

The gas-phase chemistry in shocks is dominated by endothermic reactions due to the high temperatures that are easily reached. A key reaction for shock chemistry is the formation of the highly reactive OH radical through,



which has an energy barrier and starts to become efficient as temperatures reach $> 100 \text{ K}$ (see also Fig. 1.4). The OH radical is a very reactive molecule and therefore easily reacts with other molecules. At higher temperatures of $> 300 \text{ K}$, the OH radical can react further with H_2 to form H_2O . Water is therefore a very important shock tracer in observations and is indeed commonly observed in high-velocity jets and outflows (e.g., with *Herschel*; Nisini et al. 2010; Herczeg et al. 2012; Kristensen et al. 2012; van Dishoeck et al. 2021).

the envelope and the disk (e.g., Sakai et al. 2014; Artur de la Villarmois et al. 2019, see Sect. 1.5).

Alternatively, there are also molecules in shocks which can solely form through interactions with dust grains. One key molecule tracing such interactions in shocks is SiO, which forms through the reaction of atomic Si with OH. In protostellar envelopes, almost all of the Si is locked up in refractory dust grains and is therefore not available for the chemistry. However, in *C*-type shocks, the Si can be sputtered off the dust grains through collisions between the gas and dust (Gusdorf et al. 2008a,b). Furthermore, in high-velocity *J*-type shocks, the dust grains may be thermally sputtered through collisions with heavy molecules or even completely sublimated (Guillet et al. 2009), therefore releasing Si back into the gas phase. Molecules like SiO are therefore powerful tracers of shocks such as those in high-velocity jets (e.g., Guilloteau et al. 1992; Tychoniec et al. 2019).

Also the ice mantle of dust grains can be sputtered. For ice sputtering to happen, it is crucial that the shock is of *C*-type since the drag between ions and neutrals allows for collisions of molecules with the dust grains. Through this process, dominant ice species like H₂O, CH₃OH, and other COMs can be released into the gas phase (e.g., Tielens et al. 1994; Arce et al. 2008; Suutarinen et al. 2014; Tychoniec et al. 2021).

1.3 Astronomical observatories

The largest advances in astronomical research are made when new observatories come online. These new observatories generally have significantly higher spatial and/or spectral resolution and sensitivity than their predecessors, resulting in exciting and often even unexpected results. In this Section, two observatories of particular importance for this thesis are discussed: ALMA and the *James Webb* Space Telescope (JWST).

1.3.1 ALMA

ALMA is an interferometer of in total 66 antennas that are situated at an altitude of 5000 m on the Chajnantor plateau of the Chilean Andes. The main array consists of 50 antennas with a diameter of 12 m that can be moved to different positions on the plateau. ALMA in its most compact configuration has maximum baselines of ~ 150 m, corresponding to an angular resolution of $1.47''$ at a frequency of 230 GHz (1.3 mm). In its most extended configuration, the maximum baselines reach up to ~ 16 km ($0.018''$ at 230 GHz). Besides the main array, also the Atacama Compact Array (ACA) consisting of 12 antennas with a diameter of 7 m and the Total Power array (four 12-m antennas) are situated on the Chajnantor plateau. The ACA is always fixed in the same configuration with a maximum baselines of 45 m ($5.45''$ at 230 GHz).

ALMA currently operates with 8 different receiver bands that can cover frequencies between 84 GHz (3.6 mm) and 950 GHz (0.32 mm) in between the strong atmospheric absorption bands. The total bandwidth that ALMA can observe

depends on the adopted spectral resolution (3.8 kHz – 15.6 MHz) but can not exceed 8 GHz. ALMA is therefore very suitable for observing rotational transitions of molecules. Furthermore, at millimeter wavelengths, the dust become (largely) optically thin, allowing for observing the dust continuum as well as molecular transitions deep within star-forming systems, for example in hot cores and protoplanetary disks.

The strong advantage of ALMA is the much higher angular resolution compared with single dish telescopes. Moreover, ALMA has unprecedented high sensitivity due to the high number of antennas, allowing for the detection of minor isotopologues (e.g., $^{13}\text{C}^{18}\text{O}$, $\text{CH}_3^{18}\text{OH}$). This is crucial for very abundant species for which spectral lines originating from the main isotopologue are optically thick; observing the optically thin isotopologues is then the only way to probe the total column of the main isotopologue. Furthermore, the high spectral resolution is important for molecular line studies of quiescent gas in, for example, protostellar envelopes since the spectral lines can be resolved down to $\sim 0.01 \text{ km s}^{-1}$. However, one of the disadvantages of using interferometric observations is that large-scale emission is filtered out, therefore not allowing to map both small scales (i.e., disks) and larger scales (envelopes) in a single configuration. Fortunately, the ACA has large maximum resolvable scales (up to) $29''$ at 230 GHz, and with the Total Power array even the largest scales can be probed. Another disadvantage is the relatively small bandwidth that can be covered with ALMA. Several other interferometers, such as the Submillimeter Array (SMA) and the Northern Extended Millimeter Array (NOEMA), have recently been updated with new receivers allowing higher frequency coverage within a single observation. Moreover, both the SMA and NOEMA are situated on the northern hemisphere and therefore more suitable to observe star-forming regions with higher declination such as Perseus.

1.3.2 JWST

With the first images of JWST released on July 12 2022, the infrared sky between $0.6 \mu\text{m}$ and $28 \mu\text{m}$ has been reopened, see Fig. 1.5. To observe this wavelength region, it is crucial to go into space since molecules in the Earth’s atmosphere such as O_2 , H_2O and CO_2 block most key wavelength bands (Smette et al. 2015, see Fig. 1.6). Moreover, the Earth’s atmosphere starts to thermally emit at wavelengths of $\gtrsim 2 \mu\text{m}$. This significantly hampers ground-based observations at infrared wavelengths and has therefore led to several earlier space missions such as the *Infrared Space Observatory* (ISO; Kessler et al. 1996) and the *Spitzer* Space Telescope (Werner et al. 2004).

The primary mirror of JWST has a diameter of 6.5 m, allowing for a spatial resolution between $\sim 0.07''$ at $0.6 \mu\text{m}$ to $\sim 2''$ at $28 \mu\text{m}$. The Near Infrared Spectrograph (NIRSpec) and Mid-Infrared Instrument (MIRI) instruments of JWST can achieve a medium spectral resolving power up to $R = \Delta\lambda/\lambda \sim 3500$ at smaller wavelengths ($\lesssim 10 \mu\text{m}$) which drops to $R \sim 1000$ at the highest wavelengths. This is higher than *Spitzer* but unfortunately not as high as for example *Herschel* achieved at longer wavelengths ($\sim 60 - 660 \mu\text{m}$) and will not allow for spectrally resolved lines in protostellar systems, but comparison with high-spectral resolution



Figure 1.5: A multi-color image of the Carina Nebula as observed with the NIRCAM instrument of JWST. The colors represent the various filters used: F090W (blue), F187N (cyan), F200W (green), F470N (yellow), F335M (orange), and F444W (red). The image shows various substructures within the cloud with exceptional detail and proves the high potential of the science which will be done with JWST over the coming years. Figure credit: NASA, ESA, CSA, and STScI.

data from ALMA can still provide information on the kinematics. Where JWST also exceeds its predecessors significantly is the sensitivity, which is up to two orders of magnitude higher than *Spitzer* achieved. This allows for deep observations at high spatial resolution in significantly lower integration times.

JWST will be very powerful in tracing the hot gas in protostellar systems, for example originating from the warm disk surface layers or from shocks, through observations of rovibrational lines of molecules as well as atomic lines. Furthermore, several bands of polycyclic aromatic hydrocarbons (PAHs) are within the NIR-Spec and MIRI wavelength ranges. Moreover, JWST will be able to observe ice absorption bands and more accurately constrain the ice composition in protostellar envelopes (see Sect. 1.4.1).

1.4 Complex organic molecules in protostellar systems

As discussed in Sect. 1.2.1 and argued in this thesis, the majority of the COMs likely form in the ices in the cold prestellar phases. As the ice coated dust grains move closer toward the protostar, the ices sublime into the gas phase in the hot core (Sect. 1.2.2). There are two direct ways to observe COMs in young protostellar

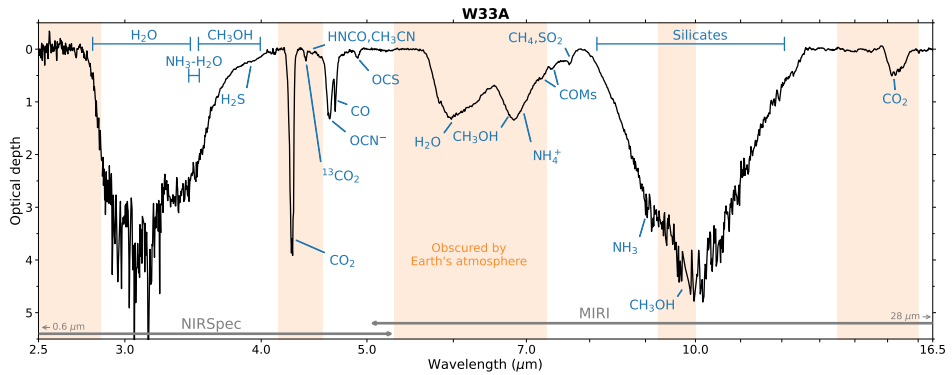


Figure 1.6: Infrared ice absorption spectrum taken with ISO toward the high-mass protostar W33A (Gibb et al. 2000). Various ice features are annotated together with their (presumed) molecular origin. In orange, the wavelength ranges that are completely obscured by the Earth’s atmosphere are highlighted. At the bottom, the wavelength ranges of the NIRSpect and MIRI instrument of the *James Webb Space Telescope* are shown.

systems: in the ices through infrared absorption bands (Sect. 1.4.1) and in the gas phase through rotational transitions at millimeter wavelengths (Sect. 1.4.2).

1.4.1 Ices

Molecules that are frozen out onto dust grains are unable to rotate since they are locked up in an ice matrix. Therefore, they cannot emit light through rotational emission lines, making them harder to observe than gaseous molecules. However, molecules in ices can still vibrate and therefore absorb light in their vibrational modes. For almost all molecules, these lie at infrared wavelengths between $\sim 3 - 60 \mu\text{m}$ (see review by e.g., Boogert et al. 2015).

Due to the limited sensitivities of spectrometers on early space telescopes such as ISO and *Spitzer*, only major ice species could be securely detected, mostly toward infrared-bright high-mass protostars, see Fig. 1.6. Water is one of the major ices and readily observed in high abundance (e.g., Boogert et al. 2008). Using observations of H_2O in various bands, even crystallized and amorphous water ice can be distinguished (e.g., Smith et al. 1989; Boogert et al. 2008; Terada & Tokunaga 2012). Similarly, strong ice absorption features are detected for other major ice species such as CO, CO_2 and NH_3 (e.g., Lacy et al. 1998; Gerakines et al. 1999; Pontoppidan et al. 2003b). However, more minor ice species remain difficult to detect. Definitive detections could still be made for molecules such as OCN^- , OCS, and CH_4 (Palumbo et al. 1997; van Broekhuizen et al. 2005; Öberg et al. 2008), but other molecules likely present in ices such as SO_2 and salts (NH_4^+) remain only tentatively identified (e.g., Knacke et al. 1982; Schutte & Khanna 2003; Boogert et al. 1997).

For similar reasons as mentioned above, the detection of COMs in ices remains

difficult. So far, CH_3OH is the only securely identified COM in the ices (e.g., Dartois et al. 1999; Pontoppidan et al. 2003a, 2004) and shows similar abundances with respect to H_2O across multiple low-mass sources (e.g., within about an order of magnitude; Boogert et al. 2008; Bottinelli et al. 2010). However, some other COMs do show tentative detections. The $7.2\ \mu\text{m}$ and $7.4\ \mu\text{m}$ bands were attributed to CH_3CHO and $\text{C}_2\text{H}_5\text{OH}$ (Schutte et al. 1999; Öberg et al. 2011), but these could not be securely confirmed due to the low spectral resolution and/or sensitivity of ISO-SWS and *Spitzer*. Moreover, they were only (tentatively) detected in one absorption band that could also be attributed to other molecules such formic acid (HCOOH).

JWST will allow for the determination of not only the major ice species but also more minor species due to its significantly higher spatial and spectral resolution and sensitivity than previous infrared space observatories. Clear detections of key molecules such as SO_2 and COMs like CH_3CHO and $\text{C}_2\text{H}_5\text{OH}$ are expected. This is also largely possible due to the many laboratory studies that have been carried out in the past decade to measure the infrared absorption bands of the majority of COMs such as CH_3CHO , $\text{C}_2\text{H}_5\text{OH}$, and CH_3OCH_3 (Terwisscha van Scheltinga et al. 2018), CH_3OCHO (Terwisscha van Scheltinga et al. 2021), acetone (CH_3COCH_3 ; Rachid et al. 2020), and methylamine (CH_3NH_2 ; Rachid et al. 2021).

1.4.2 Gas phase

Molecular emission can be directly observed through rotational lines at millimeter wavelengths as well as through rovibrational emission lines at infrared wavelengths. Since this thesis only uses pure rotational transitions, analyzing rovibrational lines will not be discussed further in detail.

Millimeter emission spectroscopy

Through collisions with mostly H_2 , molecules can be excited into higher rotational energy states. They can subsequently return to the ground state either through collisions or via radiative decay through the emission of photons. The latter is much more effective than the former in (outer) protostellar envelopes due to the low densities. Hence, once a molecule is excited through a collision, it will decay back to its ground state by emitting photons at frequencies that are specific for each transitions of each molecule. Linear molecules such as CO have only few linearly spaced rotational energy levels (indicated with quantum number J) whereas more asymmetric rotating molecules such as CH_3OH and other COMs have many more available energy levels (indicated with quantum numbers J , K_a , K_c).

When the physical conditions of the gas in which a molecule resides can be approximated to be in *local thermodynamic equilibrium* (LTE, i.e., when collisional excitation balances collisional and radiative de-excitation), the level populations of a molecule can be described by a single *excitation temperature* T_{ex} through the Boltzmann distribution,

$$\frac{n_{\text{u}}}{n_{\text{l}}} = \frac{g_{\text{u}}}{g_{\text{l}}} \exp^{-\Delta E/k_{\text{B}}T_{\text{ex}}}, \quad (1.8)$$

Observations of hot cores

The central hot cores of young protostars have been studied extensively over the past decades. Before large interferometers such as SMA, NOEMA, and ALMA existed, the chemical content of these hot cores were observed with single dish telescopes and smaller interferometers such as the IRAM-30m telescope, James Clerk Maxwell Telescope (JCMT), and Caltech Owens Valley Radio Observatory (OVRO) or with space observatories such as the *Herschel* Space Observatory (e.g., Blake et al. 1987; van Dishoeck et al. 1995; Belloche et al. 2013; Crockett et al. 2015). However, the sensitivity of these single-dish studies is limited and the observations suffered from severe beam dilution, which hampers the detectability of compact hot cores. This is of particular relevance for detecting optically thin isotopologues which allow for much more stringent constraints on the molecular abundances. In this section, the focus is primarily on the recent results obtained mostly with interferometric observatories such as ALMA and NOEMA.

Initially, the COMs were mostly studied in detail in individual sources. Among the low-mass sources, the IRAS 16293-2422 (hereafter IRAS 16293) binary system is one of the best known hot cores and has been observed extensively over the past decades (van Dishoeck et al. 1995; Cazaux et al. 2003). The ALMA Protostellar Interferometric Line Survey (PILS; Jørgensen et al. 2016) targeted IRAS 16293 using the full bandwidth of the ALMA Band 7 receiver (329 – 363 GHz). The resulting spectra are extremely rich in spectral lines with about one line every 3 km s⁻¹ (or 3.4 MHz, see Fig. 1.8). The PILS survey has led to several new molecular detections such deuterated formamide and acetic acid (NH₂CDO, NHDCHO, DNCO; Coutens et al. 2016), doubly deuterated methyl formate (CHD₂OCHO; Manigand et al. 2019), nitrous acid (HONO; Coutens et al. 2019), and chloromethane (CH₃Cl; Fayolle et al. 2017).

Among the high-mass sources, the Sagittarius B2 (hereafter Sgr B2) region and more nearby Orion KL regions are the best studied high-mass hot cores and are incredibly rich in their chemical content. Already in the pre-ALMA era, many first detections of COMs have been made toward these high-mass hot cores such as CH₃NH₂ (Kaifu et al. 1974), acetic acid (CH₃COOH; Mehringer et al. 1997), and CH₂OHCHO (Hollis et al. 2000). The chemical content of the Orion KL region was studied in depth with the OVRO spectral line survey, detecting 29 species in over 800 spectral lines (Blake et al. 1987). Similarly over 54 species in more than 4000 spectral lines were detected in a survey of Sgr B2(N) and Sgr B2(M) carried out with the IRAM 30m telescope (Belloche et al. 2013). More recently, with ALMA, the Sgr B2(N) region was resolved into several high-mass hot cores with narrower lines (Bonfand et al. 2017) and more stringent constraints on the chemical composition could be made (e.g., Belloche et al. 2014, 2016; Müller et al. 2016). Furthermore, with high-resolution ALMA data, the crowded region in Orion KL could be more easily disentangled allowing for more accurate studies of the hot core region (Pagani et al. 2017).

An interesting result from these single source studies is the physical differentiation between COMs within individual sources. With *Herschel*, significantly higher excitation temperatures were derived for nitrogen-bearing COMs (200 – 300 K)

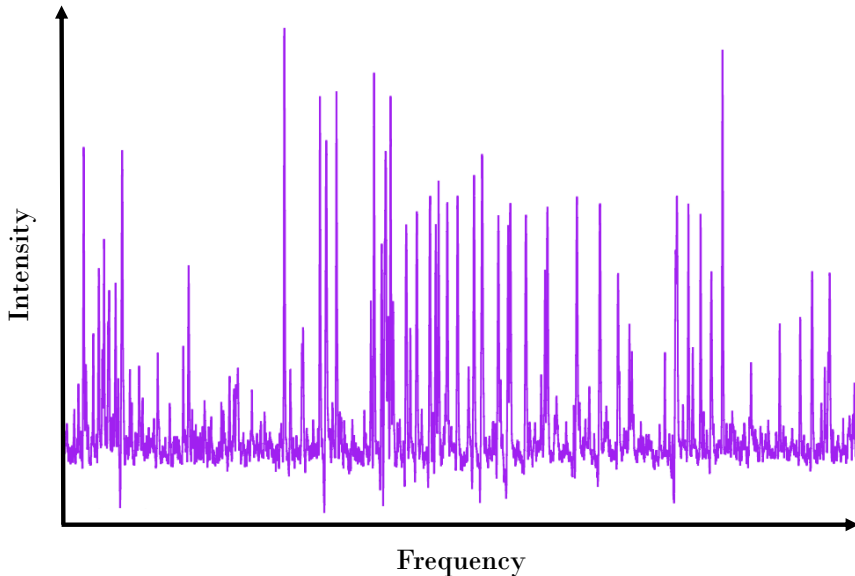


Figure 1.8: Part of the spectrum of the Class 0 protostar IRAS 16293-2422B as observed in the PILS survey at 338.5 GHz (Jørgensen et al. 2016). Only 1 GHz of bandwidth from the in total ~ 33 GHz is shown. The y-axis ranges up to 0.8 Jy beam^{-1} and the noise level is at about $0.01 \text{ Jy beam}^{-1}$. Each peak is a spectral line originating from a rotational transitions of a molecule. Figure adopted from Jørgensen et al. (2016).

than for oxygen-bearing COMs in Orion KL which was attributed to a difference in sublimation temperature (Crockett et al. 2015). Similarly, varying excitation temperatures between $\sim 100 - 300$ K as well as different levels of deuteration ($\text{D/H} \sim 2 - 8 \%$) were found for molecules in IRAS 16293B (Jørgensen et al. 2018). The former range was attributed to the COMs having different binding energies and thus sublimating at different temperatures. The latter range was suggested to originate from different formation times of the various COMs in the prestellar phases.

If indeed some COMs trace hotter regions closer to the protostar than others, the most straightforward way to verify this is to spatially resolve the hot core. Based on lower spatial resolution data with the SMA, Bisschop et al. (2008) suggested that there was spatial segregation between COMs toward IRAS 16293, but they could not yet spatially resolve individual hot cores. More recently, high-resolution ALMA data of a high-mass hot core show spatial segregation between nitrogen- and oxygen bearing COMs (Csengeri et al. 2019), but this difference likely originates from the oxygen-bearing COMs being released further out in either an accretion shock at the disk-envelope boundary or in the outflow rather than due passive heating by the protostar alone. Similarly, a physical differentiation between various COMs was observed in another high-mass hot core, but no clear link with the physical temperature structure in the source could be made (Law et al. 2021). For low-mass hot cores, only few high-resolution observations

are available, although these do show COMs emission originating, for example, from the surface of a disk (Lee et al. 2019a).

It is vital to compare various hot cores with each other in order to determine what physical or chemical properties set the chemical composition of young star-forming systems. Universal abundance ratios across various star-forming regions will point toward formation of COMs in similar physical conditions: on the surfaces of dust grains in cold prestellar cores. On the other hand, variations by orders of magnitude imply that local physical conditions such as temperature and UV field are crucial or that gas-phase chemistry in the hot cores can contribute. Some early single-dish observations suggested similar ratios of oxygen-bearing COMs with respect to CH_3OH but were affected by limited dynamical range (e.g., Jørgensen et al. 2005; Bergner et al. 2017). More recently, the $\text{CH}_3\text{OCHO}/\text{CH}_3\text{OCH}_3$ ratio was found to be remarkably constant (~ 1) across the full mass and evolutionary spectrum of protostellar evolution (Coletta et al. 2020), pointing toward very similar formation conditions between these two species. Also interferometric studies with ALMA and NOEMA show constant abundance ratios of several oxygen-bearing COMs with respect to CH_3OH (e.g., Jørgensen et al. 2018; Lee et al. 2019a; Jacobsen et al. 2019; Bergner et al. 2019; Bøgelund et al. 2019). However, differences between species become apparent as well, such as a bimodal abundance patterns between the isomers CH_3OCHO , CH_2OHCHO , and CH_3COOH in both low-mass and high-mass systems (El-Abd et al. 2019). Even protostars forming from the same cloud can show differences between their COMs abundances (e.g., IRAS 16293A and B; Manigand et al. 2020), although this could also be a physical effect (e.g., dust opacity; De Simone et al. 2020). Moreover, the deuteration of COMs such as CH_3OH seems to be significantly lower in high-mass protostars compared to their lower-mass counterparts (Bøgelund et al. 2018; Taquet et al. 2019), pointing toward higher temperatures in their prestellar phases. Nevertheless, these studies show that most COMs have comparable abundances across many star forming regions, suggesting similar formation conditions on the surfaces of dust grains in cold prestellar cores. Directly comparing the abundances in the gas phase with those to be derived in the ices with JWST for the same sources will further address this question.

Surprisingly, not all embedded protostars, high-mass or low-mass, show emission from COMs. Recent studies of larger samples of low-mass protostars have shown that only about $\sim 50 - 60\%$ show emission of CH_3OH originating from hot cores (Belloche et al. 2020; Yang et al. 2021), although the fraction of hot cores in some star forming regions can also be as low as $\sim 25\%$ (Bouvier et al. 2022). One reason for the absence of COMs emission from some sources could be low abundances of COMs in the ices, but this is not expected based on the large columns of CH_3OH ices that are observed toward protostellar envelopes (e.g., Pontoppidan et al. 2003a; Boogert et al. 2008; Bottinelli et al. 2010). A more likely explanation for the absence of COMs emission is the presence of a disk that affects the temperature structure in the system and casts a shadow on the envelope (Persson et al. 2016; Murillo et al. 2015, 2018, 2022). Alternatively, observations toward the protostellar binary system NGC 1333 IRAS 4A have shown that dust can become even optically thick at millimeter wavelengths and therefore hide the emission from

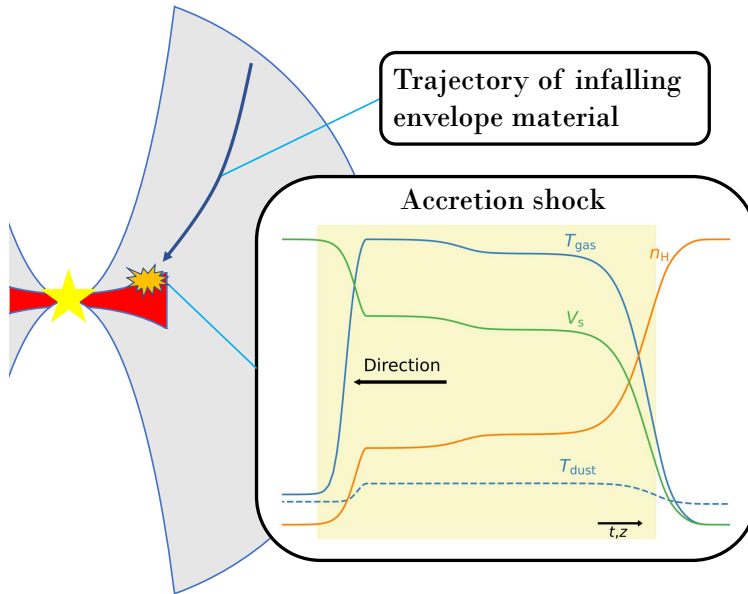


Figure 1.9: Simple schematic of a protostellar system highlighting the infall of envelope material onto the disk. At the disk-envelope boundary, an accretion shock may develop that can alter the chemistry.

the hot core (De Simone et al. 2020). Recent radiative transfer models have shown that both a disk and optically thick dust are needed to fully explain the absence of COMs emission in protostellar systems (Nazari et al. 2022b).

1.5 Inheritance versus reset: accretion shocks

Shocks are suggested to occur at the boundary between the infalling envelope and the surface of the disk, see Fig. 1.9. These shocks are commonly referred to as *accretion shocks*. The impact of such accretion shocks can be crucial for the evolution of the protostellar system. If the accretion shock is strong, it may (partially) *reset* the chemical composition (i.e., dissociate molecules into atoms) of the envelope material entering the disk. On the other hand, if the accretion shock is weak, it will not strongly affect the chemical composition and the hence the material entering the disk will be *inherited* from the parent envelope. Since planets are suggested to start forming in young embedded disks (Harsono et al. 2018; Tychoniec et al. 2020), the presence of an accretion shock is crucial for the composition of the material that is available for planet formation.

Numerical simulations of embedded protostellar systems frequently show accretion shocks (e.g., Cassen & Moosman 1981; Li et al. 2013). They can be very strong in the earliest phases when the disk is still small (< 1 au) and the velocities of infalling material high (> 10 km s $^{-1}$), leading to complete sublimation

or sputtering of the ices (Visser et al. 2009). This material, however, does not remain long in the disk and eventually ends up in the star, so it is not too relevant for the composition of a planet-forming disk. In later stages, when the disk is $\gtrsim 10$ au, the strength of the accretion shock likely decreases due to lower infall velocities ($\lesssim 10$ km s $^{-1}$) at larger radii, but the material entering the disk does not (directly) end up in the star. At these lower velocities, more strongly bound species such as H₂O likely remain in the ices (Visser et al. 2009; Miura et al. 2017). However, weaker bound species such as CO and SO can still be sublimated from the grain mantles. Moreover, the gas can reach temperatures of > 1000 K (Neufeld & Hollenbach 1994), enabling high-temperature gas-phase chemistry.

Despite the predictions by models, accretion shocks have not yet been unambiguously detected. The cleanest and most direct tracers of high-velocity shocks are optical forbidden lines of atoms or ions such as [OI] 6300 Å and [SII] 6371 Å (e.g., Banzatti et al. 2019), but these are not viable for accretion shocks due to the severe extinction by the natal envelope. Alternative tracers are spectral lines at mid-infrared wavelengths such as the [Si] 25 μ m, [OI] 63 μ m, and rovibrational H₂O lines. However, current mid-infrared observatories lack the spatial resolution and sensitivity to resolve these lines in order to separate them from the outflow (e.g., Kristensen et al. 2012; Nisini et al. 2015). Fortunately, the launch of JWST will solve this problem. At submillimeter wavelengths, observations with ALMA have suggested that SO and SO₂ may be good tracers of accretion shocks. An enhancement of SO emission was observed at the disk-envelope boundary of a few embedded protostars that could be kinematically distinguished from the inner envelope (Sakai et al. 2014, 2017; Oya et al. 2019). Similarly, warm SO₂ emission showing rotational profiles are observed toward embedded protostars (Artur de la Villarmois et al. 2019; Bjerkeli et al. 2019). More recently, warm SO and SO₂ related to accretion shocks were even observed in more evolved Class II systems at the boundary between disk and accretion streamers (Garufi et al. 2022). However, warm SO and SO₂ are not unambiguous tracers of accretion shocks in protostellar systems as these species can also be present in outflows and jets (e.g., Lee et al. 2017a; Taquet et al. 2020), disk winds (e.g., Tabone et al. 2017, 2020; Lee et al. 2018), or in inner envelopes where they are passively heated by the central protostar (Harsono et al. 2021). It therefore remains difficult to interpret emission of SO and SO₂ related to accretion shocks. Comparison between observations and models is crucial to solve this ambiguity. Moreover, observations of mid-infrared shock tracers will more directly reveal the hot spots where accretion shocks are taking place.

Sophisticated shock models have been developed to derive the physical conditions of shocks. All shock models in this thesis are computed using the Paris-Durham shock code, which has been developed over the past decades (Flower et al. 1985; Flower & Pineau des Forêts 2003, 2015; Lesaffre et al. 2013; Godard et al. 2019). The Paris-Durham shock code computes the dynamical, thermal, and chemical structure of stationary plane parallel shock waves (see Sect. 1.2.3), taking into account important physical effects such as magnetic fields that can lead to the emergence of *C*, *CJ*, and *J*-type shocks. In the case of *C* and *CJ*-type shocks, up to three fluids (neutrals, ions, and electrons) can be included to properly model

the physical evolution. The thermal balance of both the gas and dust is consistently calculated throughout shock. Over 140 different species are included that can interact through > 3000 chemical reactions. Moreover, an external UV field that irradiates the shock can be included that can be crucial for both the physical and chemical evolution of the shock by ionizing or dissociating molecules.

1.6 This thesis

This thesis aims to study how molecules are inherited from cloud to disk in young star-forming systems by studying both the physics and the chemistry. One of the main questions that is currently debated in the community is whether COMs form in the ices or in the gas phase. In order to answer this question two things are needed: 1) observations of gaseous COMs in much larger samples of hot cores than the handful of sources currently available and 2) direct detections of COMs in ices for the same sources. The focus of this thesis is on the gaseous content of oxygen-bearing COMs and on how universal gaseous COMs abundances are across multiple sources. This thesis also addresses whether the physical conditions in high-mass prestellar phases differ significantly from their lower-mass counterparts. Interestingly, some embedded sources do show emission originating from COMs while others do not. It remains uncertain whether this is a chemical effect (i.e., no COMs present at all) or a physical effect (i.e., COMs frozen out on dust grains or emission hidden by optically thick dust). Lastly, this thesis addresses the question of inheritance versus reset: is the chemical composition of planet-forming disks inherited from the cloud or is it (partially) reset in an accretion shock at the disk-envelope interface? The main results of this thesis are summarized below:

Chapter 2 presents observations with ALMA in Band 3 and Band 6 of several oxygen-bearing COMs in three low-mass protostars: B1-c, Serpens S68N, and B1-bS. The high spatial resolution and sensitivity of ALMA allowed for the detection of the optically thin $^{13}\text{CH}_3\text{OH}$ and $\text{CH}_3^{18}\text{OH}$ isotopologues which are crucial for the determination of abundance ratios with respect to CH_3OH . Using CASSIS, the column densities and excitation temperatures are derived. The abundance ratios of CH_3OCHO , CH_3OCH_3 , CH_3COCH_3 , and $(\text{CH}_2\text{OH})_2$ with respect to CH_3OH are remarkably similar for the three studied sources, as well as when compared to other low-mass protostars studied with interferometric observations. Moreover, the three studied sources show similar deuteration ratios of methanol as other low-mass sources. On the other hand, the abundance ratios of $\text{C}_2\text{H}_5\text{OH}$, CH_3CHO , CH_2OHCHO , H_2CCO , and t-HCOOH with respect to CH_3OH show variations of more than an order of magnitude. Using the combined Band 3 and Band 6 data, a cold ($T_{\text{ex}} < 70$ K) component of likely non-thermally desorbed COMs emission is found for B1-c with much lower column densities than the hot core.

Chapter 3 focuses on the emission of CH_3OH with the aim of determining why some embedded protostars do show emission of COMs and why others do not. A large sample of 148 low-mass and high-mass protostars is studied using ALMA data from Chapter 2, the Perseus ALMA Chemistry Survey (PEACHES), and the ALMA Evolutionary study of High Mass Protocluster Formation in the Galaxy

(ALMAGAL). Data for an additional 36 sources are added from the literature, giving a total of 184 different sources. Using the column density of CH_3OH derived from the optically thin ^{13}C and ^{18}O isotopologues, the warm ($T > 100$ K) gaseous methanol mass is derived for all sources and normalized by the dust mass derived from the dust continuum in order to take into account the mass of the inner envelope. A correlation between the normalized warm methanol mass and the bolometric luminosity L_{bol} was found, yet still a scatter of more than 4 orders of magnitude in the normalized warm methanol mass is present for both low-mass and high-mass sources. A simple toy model of a spherically symmetric infalling envelope provides a good fit to the sources with the highest normalized methanol mass. However, the large scatter can only be explained by the presence of (large) disks or by dust opacity effects, which is further investigated in Nazari et al. (2022b).

Chapter 4 studies the deuteration of methanol in high-mass protostars. Using the ALMAGAL data of Chapter 3, both singly (CH_2DOH) and doubly (CHD_2OH) deuterated methanol are used to derive the $(\text{D}/\text{H})_{\text{CH}_3\text{OH}}$ and $(\text{D}/\text{H})_{\text{CH}_2\text{DOH}}$ ratios for 98 high-mass protostellar systems. The observed $(\text{D}/\text{H})_{\text{CH}_3\text{OH}}$ ratios of high-mass sources lie in the range of $10^{-3} - 10^{-2}$. Including also high-mass sources from the literature, the mean $(\text{D}/\text{H})_{\text{CH}_3\text{OH}}$ is $1.3 \pm 0.8 \times 10^{-3}$, which is in good agreement with $(\text{D}/\text{H})_{\text{CH}_3\text{OH}}$ derived for high-mass starless cores but more than an order of magnitude lower than $(\text{D}/\text{H})_{\text{CH}_3\text{OH}}$ in low-mass protostars and low-mass prestellar cores. On the other hand, the average $(\text{D}/\text{H})_{\text{CH}_2\text{DOH}}$ of high-mass sources is $2.0 \pm 0.7 \times 10^{-1}$, which is in good agreement with low-mass protostars. Based on a comparison between the observed $(\text{D}/\text{H})_{\text{CH}_3\text{OH}}$ and GRAINOBLE models from the literature, we suggest that the high-mass prestellar phases are either warmer (20–25 K) than their lower mass counterpart (< 15 K) or, alternatively, high-mass prestellar phases have shorter timescales than low-mass prestellar phases.

Chapter 5 explores under which shock conditions the abundance of SO and SO_2 increases in accretion shocks at the disk-envelope interface. Detailed shock models of irradiated non-magnetized *J*-type shocks computed with the Paris-Durham shock code are presented for a large parameter space that is applicable for inner envelope conditions, that is, higher densities and lower shock velocities than for outflows. In low-velocity shocks ($\sim 3 \text{ km s}^{-1}$), the abundance of SO is increased through reactions of hydrocarbons (CH_4 , H_2CO) with the S^+ anion and atomic O. At higher shock velocities ($> 4 \text{ km s}^{-1}$), both SO and SO_2 are effectively formed as the shock cools down through subsequent reactions of atomic S with the OH radical. Here, the strength of the UV field is crucial through photodissociation of H_2O that formed earlier in the shock into OH. Thermal sublimation of SO and SO_2 ices only becomes relevant for higher densities ($\gtrsim 10^7 \text{ cm}^{-3}$) and shock velocities ($> 5 \text{ km s}^{-1}$).

Chapter 6 presents resolved ALMA observations with an angular resolution of $\sim 0.15''$ ($\sim 10 \text{ au}$ radius) of SO and SO_2 to search for the presence of accretion shocks in three Class I sources: TMC1A in Taurus and Ced 110 IRS 4 and IRS 6 in Chameleon. The dust disks in these three sources are clearly detected with radii of $\sim 30 \text{ au}$, $\sim 75 \text{ au}$, and $\sim 50 \text{ au}$ for TMC1A, IRS 4, and IRS 6, respec-

tively. Both SO and SO₂ are only detected toward TMC1A with narrow lines of $1.0 \pm 0.1 \text{ km s}^{-1}$. An excitation temperature of $50 \pm 20 \text{ K}$ is derived for SO₂ and a SO₂/SO column density ratio of 0.6 ± 0.1 . Based on the narrow lines, low excitation temperature, and comparison to sophisticated shock models, an accretion shock can be excluded as the origin of the SO and SO₂ emission. Similarly, the lack of SO and SO₂ toward the two Cederblad sources suggests the absence of a strong ($T_{\text{gas,max}} > 100 \text{ K}$) accretion shock. In turn, this implies that the chemical composition of these embedded disks could be directly inherited from their natal envelopes. Moreover, the presence of hot SO₂ originating from transitions with $E_{\text{up}} > 100 \text{ K}$ seems to be correlated to the bolometric luminosity L_{bol} , suggesting that energetic processes such as UV irradiation could be important for the chemistry of SO₂.

The main conclusions of this thesis are:

- Several oxygen-bearing COMs show remarkably similar abundance ratios with respect to CH₃OH between various low-mass protostars, indicating similar formation conditions, likely in the ices in the prestellar phases. On the other hand, the larger variation seen in some other COMs suggest that local physical conditions such as a UV field in an even earlier prestellar phase or gas-phase chemistry in the hot cores can contribute to their abundances.
- The absence of COMs emission in protostellar systems does not imply that they are not present. It rather shows that they are either still frozen out due to the presence of a disk or that their emission is hidden behind a layer of optically thick dust.
- High-mass prestellar phases are either warmer than their lower-mass counterpart or have shorter timescales.
- Warm SO and SO₂ emission can be used as a tracer of accretion shocks at the disk-envelope interface as long as a UV field is present.

The future of observations of both COMs in hot cores and accretion shocks is bright. ALMA has proven its worth with high resolution and sensitivity observations and will continue to provide us with new and exciting data. Where initially most ALMA studies focused on many COMs in single sources, the field is now shifting toward observing several COMs in a much larger sample of sources. This will give more insight on the chemical links between multiple COMs and their sensitivity to the physical conditions in the prestellar phases. Furthermore, more high-resolution ALMA observations of accretion shocks in SO, SO₂, but also other possible tracers such as H₂S and H₂CO will provide important information on the presence of such shocks and on their effect on the chemical composition.

With the launch of JWST, the mid-infrared sky will become available for astronomical observations at an unprecedented resolution and sensitivity. One of the key results that are expected are the detections of COMs larger than CH₃OH in the ices such as C₂H₅OH and CH₃CHO. Directly comparing the ice abundances to those derived in the gas phase for the same sources will be crucial for determining

the origin of COMs: ice chemistry of gas-phase chemistry. With JWST, also high-temperature infrared shock tracers such as [Si] $25\ \mu\text{m}$, rovibrational H_2O , and H_2 lines become available which can further constrain the presence and the strength of an accretion shock at the disk-envelope boundary and address the question of inheritance versus reset.

PART I

Chemical complexity in
young protostars

Chapter 2

Complex organic molecules in low-mass protostars on Solar System scales

I. Oxygen-bearing species

M. L. van Gelder, B. Tabone, Ł. Tychoniec, E. F. van Dishoeck, H.
Beuther, A. C. A. Boogert, A. Caratti o Garatti, P. D. Klaassen, H.
Linnartz, H. S. P. Müller, V. Taquet

A&A 639, A87 (2020)

Abstract

Context. Complex organic molecules (COMs) are thought to form on icy dust grains in the earliest phase of star formation. The evolution of these COMs from the youngest Class 0/I protostellar phases toward the more evolved Class II phase is still not fully understood. Since planet formation seems to start early, and mature disks are too cold for characteristic COM emission lines, studying the inventory of COMs on Solar-System scales in the Class 0/I stage is relevant. Our aim is to determine the abundance ratios of oxygen-bearing COMs in Class 0 protostellar systems on scales of ~ 100 AU radius.

Aims. We aim to compare these abundances with one another, and to the abundances of other low-mass protostars such as IRAS16293-2422B and HH 212. Additionally, using both cold and hot COM lines, the gas-phase abundances can be tracked from a cold to a hot component, and ultimately be compared with those in ices to be measured with the *James Webb* Space Telescope (JWST). The abundance of deuterated methanol allows us to probe the ambient temperature during the formation of this species.

Methods. Observations with the Atacama Large Millimeter/submillimeter Array (ALMA) in Band 3 (3 mm) and Band 6 (1 mm) are obtained for seven Class 0 protostars in the Perseus and Serpens star-forming regions. By modeling the inner protostellar region using local thermodynamic equilibrium (LTE) models, the excitation temperature and column densities are determined for several O-bearing COMs including methanol (CH_3OH), acetaldehyde (CH_3CHO), methyl formate (CH_3OCHO), and dimethyl ether (CH_3OCH_3). Abundance ratios are taken with respect to CH_3OH .

Results. Three out of the seven of the observed sources, B1-c, B1-bS (both Perseus), and Serpens S68N (Serpens), show COM emission. No clear correlation seems to exist between the occurrence of COMs and source luminosity. The abundances of several COMs such as CH_3OCHO , CH_3OCH_3 , acetone (CH_3COCH_3), and ethylene glycol ($(\text{CH}_2\text{OH})_2$) are remarkably similar for the three COM-rich sources; this similarity also extends to IRAS 16293-2422B and HH 212, even though collectively these sources originate from four different star-forming regions (i.e., Perseus, Serpens, Ophiuchus, and Orion). For other COMs like CH_3CHO , ethanol ($\text{CH}_3\text{CH}_2\text{OH}$), and glycolaldehyde (CH_2OHCHO), the abundances differ by up to an order of magnitude, indicating that local source conditions become important. B1-c hosts a cold ($T_{\text{ex}} \approx 60$ K), more extended component of COM emission with a column density of typically a few percent of the warm/hot ($T_{\text{ex}} \sim 200$ K) central component. A D/H ratio of 1–3 % is derived for B1-c, S68N, and B1-bS based on the $\text{CH}_2\text{DOH}/\text{CH}_3\text{OH}$ ratio (taking into account statistical weighting) suggesting a temperature of ~ 15 K during the formation of methanol. This ratio is consistent with other low-mass protostars, but is lower than for high-mass star-forming regions.

Conclusions. The abundance ratios of most O-bearing COMs are roughly fixed between different star-forming regions, and are presumably set at an earlier cold prestellar phase. For several COMs, local source properties become important. Future mid-infrared facilities such as JWST/MIRI will be essential for the direct observation of COM ices. Combining this with a larger sample of COM-rich sources with ALMA will allow ice and gas-phase abundances to be directly linked in order to constrain the routes that produce and maintain chemical complexity during the star formation process.

2.1 Introduction

Complex organic molecules (COMs) are molecules with six or more atoms of which at least one atom is carbon (see review by Herbst & van Dishoeck 2009). They have been observed toward high-mass and low-mass star-forming regions, both in young protostars (e.g., Caselli & Ceccarelli 2012; Jørgensen et al. 2016; McGuire 2018; Bøgelund et al. 2019) and in protostellar outflows (e.g., Arce et al. 2008; Öberg et al. 2010). As a protostellar system develops from the embedded Class 0/I phase toward the more evolved Class II phase, the COMs may eventually either be destroyed or become incorporated in the ice mantles of dust grains or planetesimals in disks (Visser et al. 2009, 2011; Drozdovskaya et al. 2016). Because planet formation can begin as soon as the embedded Class 0/I phase (e.g., Harsono et al. 2018; Manara et al. 2018), studying the inventory and abundances of COMs on Solar System scales in the earliest stages of star formation is essential to probing the initial conditions of planet formation. With the launch of the *James Webb* Space Telescope (JWST) in the near future, it will be possible to directly link the ice abundances of COMs to their gaseous counterpart.

In cold prestellar envelopes, the formation of COMs happens on the ice mantles of dust grains through hydrogenation of smaller molecules such as CO (Charnley et al. 1992; Watanabe & Kouchi 2002; Fuchs et al. 2009). This leads to the formation of methanol (CH_3OH), but these COMs may even get as complex as, for example, glycolaldehyde (CH_2OHCHO), ethylene glycol ($(\text{CH}_2\text{OH})_2$), and glycerol ($\text{HOCH}_2\text{CH}(\text{OH})\text{CH}_2\text{OH}$; Öberg et al. 2009; Chuang et al. 2016, 2017; Fedoseev et al. 2017). When the dust grains move inwards toward protostars, the ultraviolet (UV) radiation field increases (e.g., Visser et al. 2009; Drozdovskaya et al. 2016), leading to the dissociation of some COMs into smaller radicals (Gerakines et al. 1996; Öberg 2016). These radicals react with other COMs in the ice mantles to form larger species (Garrod & Herbst 2006; Garrod et al. 2008; Öberg et al. 2009), and at higher temperatures perhaps through thermal induced chemistry (Theulé et al. 2013). When the temperature of the dust grains reaches $T \approx 100 - 300$ K, all COMs desorb from the grains into the gas phase where they can be transformed by high temperature gas-phase chemistry and UV radiation (e.g., Charnley et al. 1992; Balucani et al. 2015; Skouteris et al. 2018). A fraction of the COMs may be incorporated into larger bodies in the cold midplane of an accretion disk.

Another reason for studying COMs in the earliest (Class 0) phase of star formation is that gaseous COM lines are hard to detect in the Class I phase (e.g., Artur de la Villarmois et al. 2019). An exception is when a (more evolved) source undergoes an accretion burst; the sudden increase in luminosity can release frozen COMs from the grains (van 't Hoff et al. 2018b; Lee et al. 2019b). In the ice phase, they are difficult to observe, with only well constrained abundances for CH_3OH and some limits or tentative detections for formic acid (HCOOH), acetaldehyde (CH_3CHO), and ethanol ($\text{CH}_3\text{CH}_2\text{OH}$; Boogert et al. 2015; Terwisscha van Scheltinga et al. 2018).

Most studies of gaseous COMs have been carried out on high-mass hot cores in massive star-forming regions such as Sagittarius B2 and Orion KL, where COMs are typically present in high abundances (e.g., Belloche et al. 2013; Neill et al.

2014; Crockett et al. 2014; Pagani et al. 2017). In low-mass young stellar objects, single-dish observations with beams of a few thousand astronomical units show that the abundances of oxygen-bearing COMs with respect to CH_3OH seem to be narrowly distributed (Bottinelli et al. 2004; Jørgensen et al. 2005; Bergner et al. 2017).

With the Atacama Large Millimeter/submillimeter Array (ALMA), it is now possible to spatially resolve individual protostellar systems on scales of ~ 50 AU. Additionally, the spectral coverage and sensitivity of ALMA allow a large variety of COMs and corresponding isotopologs to be observed in optically thin lines, resulting in more accurate abundance determinations. Gaseous COMs have been studied mostly in the Class 0 IRAS 16293-2422 binary system (hereafter IRAS 16293) as part of the ALMA PILS survey (Jørgensen et al. 2016). This has led to many detections of new species in the interstellar medium (ISM) such as HONO (Coutens et al. 2019), CH_3Cl (Fayolle et al. 2017), and CHD_2OCHO (Manigand et al. 2019). Furthermore, IRAS 16293 has been studied extensively for both oxygen and nitrogen-bearing COMs (Jørgensen et al. 2018; Calcutt et al. 2018; Ligterink et al. 2018a,b; Manigand et al. 2020). Other low-mass sources studied interferometrically on $\sim 50 - 150$ AU scales include HH 212 (Lee et al. 2019a), NGC 1333-IRAS 2A and IRAS 4A (hereafter IRAS 2A and IRAS 4A; Maury et al. 2014; Taquet et al. 2015, 2019), L483 (Jacobsen et al. 2019), three sources in the Serpens Main star-forming region (Bergner et al. 2019), and a larger sample in the CALYPSO survey (Belloche et al. 2020).

Single-dish observations show hints of a cold, more extended component of COM emission in Class 0 protostars where the excitation temperature may drop below 20–60 K. This component is present in addition to the ‘typical’ warm/hot, more compact COM emission with $T \gtrsim 100 - 300$ K (Bisschop et al. 2007; Isokoski et al. 2013; Marcelino et al. 2018). Currently, the chemical relationship between the cold COMs on large scales and warm/hot COMs on small scales is still unknown. The evolution of COMs from a cold extended component to a hot central component can be traced by observing COMs in multiple frequency bands.

The Perseus and Serpens star-forming regions are known to host many embedded protostars (e.g., Enoch et al. 2009; Tobin et al. 2016; Karska et al. 2018). In this paper, four protostellar regions with strong ice features in infrared observations (Boogert et al. 2008) are targeted with ALMA in Band 3 and Band 6. These targets are also part of the JWST/MIRI guaranteed time observations program (project ID 1290). The JWST/MIRI will, for instance, observe the $7.2 \mu\text{m}$ and $7.4 \mu\text{m}$ features for which $\text{CH}_3\text{CH}_2\text{OH}$ and CH_3CHO , respectively, are strong candidates based on laboratory spectroscopy (e.g., Schutte et al. 1999; Terwisscha van Scheltinga et al. 2018). Ultimately, this will allow gaseous and icy COMs to be directly compared. Some additional nearby sources falling within the ALMA field of view are also included here, leading to a total of seven sources: B1-b, B1-bS, B1-bN, and B1-c in the Perseus Barnard 1 cloud, and Serpens S68N (hereafter S68N), Ser-emb 8 (N), and Serpens SMM3 (hereafter SMM3) in the Serpens Main region.

B1-b (sometimes also referred to as B1-bW) is a bright infrared source with strong ice features in CH_3OH and (potentially) CH_3CHO (Öberg et al. 2011). B1-

bN is a suggested first hydrostatic core candidate (e.g., Pezzuto et al. 2012; Hirano & Liu 2014; Gerin et al. 2017), and B1-bS is proposed as a hot corino (Marcelino et al. 2018). B1-c is a young Class 0 object showing both strong CH_3OH ice and gas COM features in the hot corino (Boogert et al. 2008; Bergner et al. 2017), and a high velocity outflow (Jørgensen et al. 2006; Hatchell et al. 2007). Moreover, all Barnard 1 objects were extensively studied in the VLA Nascent Disk and Multiplicity (VANDAM) survey (Tobin et al. 2016; Tychoniec et al. 2018b), showing compact disk-like structures at scales of several tens of astronomical units. In Serpens, S68N and SMM3 are both Class 0 sources studied in detail by Kristensen et al. (2010). Hull et al. (2017) and Tychoniec et al. (2018a, 2019) observed several protostars in Serpens with ALMA, focusing on outflows. Interestingly, whereas Ser-emb 8 (N) hosts a high-velocity outflow, S68N only has a low-velocity outflow. The characteristics of our targets are shown in Table 2.1. We focus here on the O-bearing COMs in the data; the N-bearing species will be part of a future paper.

2.2 Observations

ALMA Cycle 5 observations (project 2017.1.01174.S; PI: E.F. van Dishoeck) were taken in Band 3 (3 mm) and Band 6 (1 mm). The key targeted COMs were CH_3OH , HCOOH , CH_3CHO , CH_3OCHO , $\text{CH}_3\text{CH}_2\text{OH}$, and NH_2CHO . We list the main technical properties of our ALMA images in Table 2.E.3. For B1-bN and SMM3, we lack Band 6 observations in our program. All data were taken using the 12m array, with a synthesized beam of $\sim 1.5\text{--}2.5''$ ($\sim 500\text{--}1000$ AU at the distances of our sources; C43-2 & C43-3 configuration) and $\sim 0.45''$ ($\sim 100\text{--}200$ AU; C43-4 configuration) for Band 3 and Band 6, respectively. The largest recoverable scales (LAS) were $\sim 20''$ ($\sim 6000\text{--}9000$ AU) and $\sim 6''$ ($\sim 2000\text{--}3000$ AU) for Band 3 and Band 6, respectively. The spectral resolution was ~ 0.2 km s^{-1} for most spectral windows, with a few windows in Band 3 having $\sim 0.3\text{--}0.4$ km s^{-1} . At this resolution, all lines are spectrally resolved. The line sensitivity is ~ 0.1 K. The absolute uncertainty on the flux calibration is $\leq 15\%$ for all observations. For SMM3, we use archival Band 6 data (project 2017.1.01350.S; PI: Ł. Tychoniec) at similar spatial resolution ($\sim 0.3''$) but lower spectral resolution (0.7 km s^{-1}).

The images were primary beam corrected, with factors of ~ 1 for sources in the center of the images (i.e., B1-b, B1-c, S68N, SMM3), and ~ 3 and ~ 4 for B1-bS and Ser-emb 8 (N) in Band 6, respectively. In Band 3 the primary beam correction for B1-bS, B1-bN, and Ser-emb 8 (N) was ~ 1.2 , ~ 2 , and ~ 1.3 , respectively.

Continuum images were made using line-free channels in all spectral windows. For the line-dense sources (e.g., B1-c) the line-free channels were carefully selected to exclude any line emission from the continuum images. Using the continuum solutions, all line data were continuum subtracted. From the pipeline product data, it was clear that all COM emission (except CH_3OH) was unresolved and centrally peaked on all sources. Therefore, line images were made using a mask size of a few times the size of the synthesized beam with the CASA 5.1.1 *tclean* task using a Briggs weighting of 0.5. Figure 2.1 shows the continuum overlaid on the spatial

Table 2.1: List of protostars discussed in this paper as well as their main astronomical properties.

Object	Cloud	R.A (J2000) (hh:mm:ss.ss)	Dec (J2000) (dd:mm:ss.ss)	d pc	L_{bol} L_{\odot}	T_{bol} K	M_{env} M_{\odot}	$\text{CH}_3\text{OH}/\text{H}_2\text{O}_{\text{ice}}$ (%)	COMs detected?	
									Band 3	Band 6
B1-b	Perseus	03:33:20.34	31:07:21.3	320 ¹	0.32 ²	151 ²	1.5 ²	11.2 ³	n	n
<i>B1-bN</i>	Perseus	03:33:21.21	31:07:43.6	320 ¹	0.28 ⁴	17 ⁴	0.4 ⁴	–	n	–
<i>B1-bS</i>	Perseus	03:33:21.36	31:07:26.3	320 ¹	0.57 ⁴	22 ⁴	0.4 ⁴	–	y	y
B1-c	Perseus	03:33:17.88	31:09:31.8	320 ¹	5.9 ⁵	46 ⁵	3.8 ²	<7.1 ³	y	y
S68N	Serpens	18:29:48.09	01:16:43.3	436 ⁶	5.4 ⁷	58 ⁶	9.4 ⁷	–	y	y
<i>Ser-emb 8 (N)</i>	Serpens	18:29:48.73	01:16:55.6	436 ⁶	–	–	–	–	n	y ⁸
SMM3	Serpens	18:29:57.75	01:14:06.7	436 ⁶	27.5 ⁵	37 ⁵	–	–	n	n ⁹

Notes. The objects in italics additionally fell within the field of view of the ALMA observations. In the last 2 columns, yes (y) indicates that COMs were detected in this work, no (n) indicates that the spectra lacked any COM detection, and – indicates that the Band was not observed for the corresponding target.

⁽¹⁾ Ortiz-León et al. (2018). ⁽²⁾ Enoch et al. (2009). ⁽³⁾ Boogert et al. (2008). ⁽⁴⁾ Hirano & Liu (2014). ⁽⁵⁾ Karska et al. (2018). ⁽⁶⁾ Ortiz-León et al. (2017). ⁽⁷⁾ Enoch et al. (2011). ⁽⁸⁾ Only CH₃OH emission related to the outflow detected. ⁽⁹⁾ Based on data from ALMA program 2017.1.01350.S

distribution of CH_3OH $2_{1,1}-1_{0,1}$ and CH_3OCHO $21_{7,14}-20_{7,13}$ emission in Band 6 from B1-c, S68N, and B1-bS. Figure 2.2 shows the emission of CH_3OCH_3 $7_{0,7}-6_{1,6}$ in Band 3. Spectra were extracted from the central beam of the sources.

2.3 Spectral modeling and results

In the Band 3 and Band 6 spectra of B1-b, B1-bN, Ser-emb 8 (N), and SMM3, COM emission features are absent at our detection sensitivity (see Table 2.E.3), except for spatially extended CH_3OH emission in Ser-emb 8 (N) which is related to the outflow (Tychoniec et al. 2018a, 2019). These sources are therefore excluded from further analysis and labeled as COM-poor sources. The other sources, B1-c, S68N, and B1-bS, are labeled as COM-rich sources, and analyzed further below.

2.3.1 Methodology

The spectral analysis tool CASSIS¹ was used to determine column densities and excitation temperatures of detected species. The line lists of each molecule were taken from the CDMS (Müller et al. 2001, 2005; Endres et al. 2016)² and JPL (Pickett et al. 1998)³ catalogs. The laboratory spectroscopy of molecules discussed in this paper is introduced in Appendix 2.A and a full list of lines can be found in Tables 2.E.1 and 2.E.2 for Band 3 and Band 6, respectively. On average, the transition upper energies of the spectral lines are lower in Band 3 compared to Band 6. The Band 3 and Band 6 data are modeled separately. For a fixed V_{LSR} , a grid of column densities, excitation temperatures, and full width half maximum (FWHM) of the line was set with steps of 0.05 on a logarithmic scale, and 10 K and 0.1 km s^{-1} on a linear scale, respectively. The total parameter space probed is $10^{13}-10^{17} \text{ cm}^{-2}$, 50–550 K, and 0.5–9.0 km s^{-1} , respectively; for CH_2DOH the explored parameter space of the column density is $10^{14}-5 \times 10^{17} \text{ cm}^{-2}$. For species with a small number of transitions in Band 6, the excitation temperature was fixed to $T_{\text{ex}} = 200 \text{ K}$, and only the column density and FWHM were varied. For most species in Band 3, we had to assume that T_{ex} is equal to the Band 6 temperature because the signal-to-noise ratio (S/N) is too low to detect multiple spectral lines. Since the FWHM of the lines in B1-bS was close to the spectral resolution limit, we fixed the FWHM to 1 km s^{-1} .

A source size of 0.45" (equal to the Band 6 beam) is used for all sources. Given the equation for beam dilution:

$$\text{Dilutionfactor}^{-1} = \frac{\theta_s^2}{\theta_b^2 + \theta_s^2}, \quad (2.1)$$

with θ_s being the (assumed) angular source size of 0.45" and θ_b the beam size, the beam dilution factor is ~ 20 and 2 for Band 3 and Band 6, respectively. In reality, the size of the emitting region is smaller than the assumed 0.45" and any derived

¹<http://cassis.irap.omp.eu/>

²<https://cdms.astro.uni-koeln.de/>

³<https://spec.jpl.nasa.gov/>

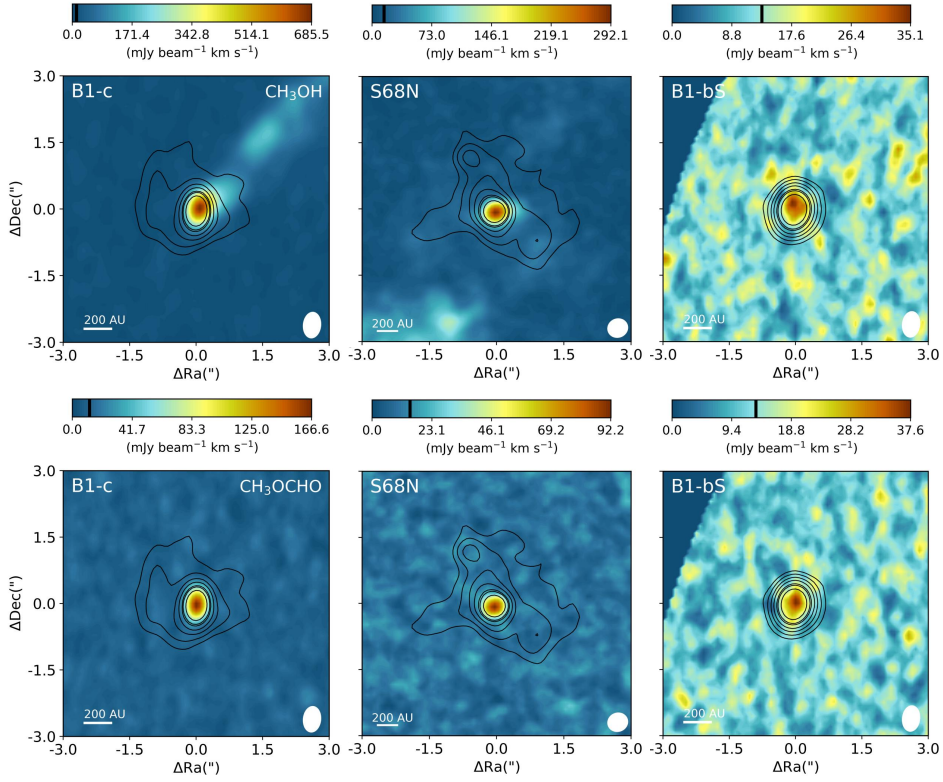


Figure 2.1: ALMA Band 6 moment-zero images of the COM-rich sources analyzed in this study: B1-c (left), S68N (middle), and B1-bS (right). In color the spatial distribution of CH_3OH $2_{1,1}-1_{0,1}$ (top row, $E_{\text{up}} = 28$ K) and CH_3OCHO $21_{7,14}-20_{7,13}$ emission (bottom row, $E_{\text{up}} = 170$ K) is shown, with the color scale shown on top of each image. The images are integrated over $[-10, 10]$ km s^{-1} with respect to the V_{lsr} . In the color bar, the $3\sigma_{\text{line}}$ level is indicated with the black bar, with $\sigma_{\text{line}} = 4.0, 4.9$, and 4.4 $\text{mJy beam}^{-1} \text{km s}^{-1}$ for B1-c, S68N, and B1-bS, respectively. The continuum is shown with the black contours with increasing $[3, 5, 8, 12, 18, 21, 30]$ σ_{cont} , where σ_{cont} is $1.5, 0.8$, and 1.0 $\text{mJy beam}^{-1} \text{km s}^{-1}$ for B1-c, S68N, and B1-bS, respectively. The size of the beam is shown in the lower right of each image, and in the lower left a scale bar is displayed. The image of B1-bS has a lower S/N since the source is located on the edge of the primary beam.

column densities are therefore lower limits. The effect of a smaller source size is discussed in Section 2.4.2

Each species is modeled separately, and optically thick lines and blended lines are excluded from the fitting procedure. Assuming that the populations of all levels can be described by a single excitation temperature T_{ex} , the χ^2 is computed for each grid point, after which the best fitting model is determined by the minimum reduced χ^2 . This method is often called ‘local thermodynamic equilibrium (LTE)’ since in the high-density limit of molecular excitation the excitation

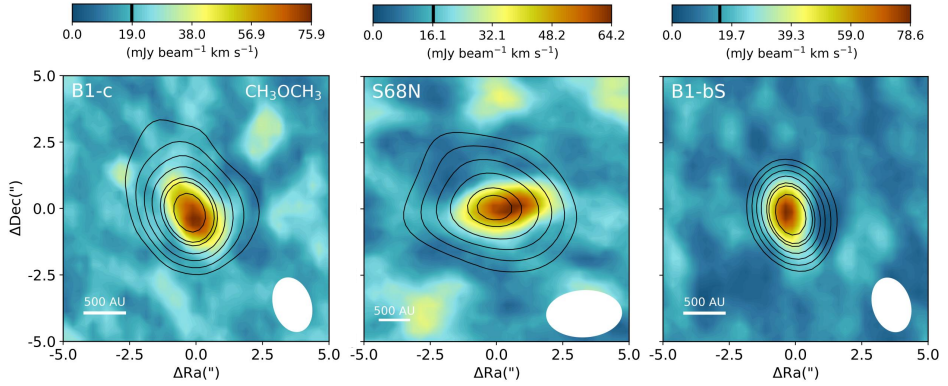


Figure 2.2: Same as Fig. 2.1, but now for CH_3OCH_3 $7_{0,7}-6_{1,6}$ ($E_{\text{up}} = 25$ K) in Band 3. Here, $\sigma_{\text{line}} = 6.3, 5.5,$ and 5.2 $\text{mJy beam}^{-1} \text{ km s}^{-1}$ for B1-c, S68N, and B1-bS, respectively. The continuum contours are $[3, 5, 8, 12, 18, 21, 30] \sigma_{\text{cont}}$, where σ_{cont} is $0.46, 0.54,$ and 0.71 $\text{mJy beam}^{-1} \text{ km s}^{-1}$ for B1-c, S68N, and B1-bS, respectively.

temperature approaches the kinetic temperature T_{kin} . Strictly speaking, thermodynamic equilibrium implies that not only the excitation but also the motions, ionization balance, and radiation field are in equilibrium at the same temperature. The word ‘local’ refers to a specific region in an atmosphere with varying temperature and density, the origin of which lies in stellar astrophysics. However, in radio astronomy of the interstellar medium, the term LTE often simply implies a single excitation temperature to characterize the level populations of a molecule, which is our intended meaning here.

The 2σ uncertainty on the column density, excitation temperature, and FWHM is computed from the grid. The main contributors to the uncertainty are the assumption of LTE, the flux calibration error of ALMA, and the assumption of Gaussian line profiles. For sources with a high line density, such as B1-c, many lines had to be excluded from the fit due to line blending, thereby increasing the uncertainty on the column densities and excitation temperatures.

2.3.2 Column densities and excitation temperatures

The column densities and excitation temperatures of all COM-rich sources are presented in Appendix 2.B. We consider a derived column density an upper limit if the error is more than 80% of the corresponding best fitting value. The number of lines used for fitting each species is listed in Tables 2.B.4-2.B.6. Upper limits (3σ) to the column density are provided if no unblended lines are detected. For B1-c in Band 6, unambiguous detections (i.e., > 5 unblended lines identified) are made for $^{13}\text{CH}_3\text{OH}$, $\text{CH}_3^{18}\text{OH}$, CH_2DOH , CH_3CHO , CH_3OCHO , CH_3OCH_3 , CH_3COCH_3 , and $\text{aGg}'(\text{CH}_2\text{OH})_2$. For S68N and B1-bS, line blending and sensitivity hampered unambiguous detections for several of these COMs, but tentative detections can still be made for most species. H_2CCO and t-HCOOH show less than three detected transitions, and their identifications are therefore considered tentative.

Table 2.2: Column densities of CH₃OH and abundance fractions (%) with respect to CH₃OH for all COM rich sources.

Species	Name	B1-c			S68N			B1-bs		
		Band 3	Band 6		Band 3	Band 6		Band 3	Band 6	
CH ₃ OH	Methanol	18 ± 4	19 ± 6		3.6 ± 0.8	14 ± 6		2.4 ± 0.7	5.0 ± 0.6	
¹³ CH ₃ OH		≡ 1.43	1.0 ± 0.3		≡ 1.43	0.7 ± 0.3		≡ 1.43	0.3 ± 0.1	
CH ₃ ¹⁸ OH		< 1.0	≡ 0.18		< 2.8	≡ 0.18		< 4.2	≡ 0.18	
CH ₂ DOH		5.7 ± 2.1	8.4 ± 2.8		< 13	4.3 ± 1.9		< 9.9	< 4.7	
CH ₃ CH ₂ OH	Ethanol	1.6 ± 0.9	0.8 ± 0.3		< 5.6	0.22 ± 0.09		< 8.3	< 0.6	
CH ₃ CHO	Acetaldehyde	1.3 ± 0.5	0.2 ± 0.1		< 1.4	0.07 ± 0.03		< 2.1	0.13 ± 0.02	
CH ₃ OCHO	Methyl formate	2.3 ± 1.0	1.0 ± 0.3		0.29 ± 0.07	1.1 ± 0.5		6.1 ± 1.8	0.75 ± 0.10	
CH ₃ OCH ₃	Dimethyl ether	1.0 ± 0.2	1.3 ± 0.4		1.8 ± 0.4	0.9 ± 0.4		4.3 ± 1.2	1.3 ± 0.2	
CH ₃ COCH ₃	Acetone	< 2.8	0.4 ± 0.1		< 14	0.4 ± 0.2		< 21	0.10 ± 0.03	
aGg'(CH ₂ OH) ₂	Ethylene glycol	< 2.4	0.3 ± 0.1		< 12	0.16 ± 0.07		< 18	< 0.43	
gGg'(CH ₂ OH) ₂		< 1.2	0.4 ± 0.1		< 6	< 0.81		< 8.9	< 0.43	
CH ₂ OHCHO	Glycolaldehyde	< 0.89	0.11 ± 0.04		< 2.2	< 0.06		< 3.3	< 0.064	
H ₂ CCO	Ketene	–	0.07 ± 0.02		–	0.07 ± 0.03		–	0.03 ± 0.01	
t-HCOOH	Formic acid	0.5 ± 0.1	0.04 ± 0.02		< 1.4	0.07 ± 0.03		< 4.2	< 0.1	

Notes. The CH₃OH entry is the column density in 10¹⁷ cm⁻² in a 0.45" beam derived from ¹³CH₃OH for Band 3 and CH₃¹⁸OH for Band 6 using ¹²C/¹³C = 70 and ¹⁶O/¹⁸O = 560, respectively. All other entries are abundances with respect to CH₃OH (in %). The errors are derived from the 2σ (95%) uncertainties on the column densities. Abundance ratios set to their respective isotope ratio are indicated with a ≡ symbol.

4.5 ± 0.5 , respectively. The average FWHM in Band 3 is therefore slightly lower than in Band 6 for B1-c and S68N, but within the uncertainties. This matches the expectation that the Band 3 observations trace the colder more extended regions and that Band 6 is more sensitive to warmer compact regions because the transition upper energies in Band 3 are on average lower than in Band 6 (see Tables 2.E.1 and 2.E.2) and because the beam size and LAS are larger. For all species for which T_{ex} was fixed in Band 3, no significant changes in the column densities or abundances arise from decreasing excitation temperature by 30 K. In Tables 2.B.7-2.B.9, the results of a fit with $T_{\text{ex}} = 100$ K to the Band 3 data are presented. The derived column densities are typically about a factor two lower than derived with T_{ex} as a free parameter or fixed to 200 K.

2.3.3 Relative abundances

Clear isotopolog detections are only made for methanol. The $^{13}\text{CH}_3\text{OH}/\text{CH}_3^{18}\text{OH}$ abundance ratio is less than 6 for all targets, which is lower than the elemental value of approximately 8. This hints at the possibility that even $^{13}\text{CH}_3\text{OH}$ is optically thick for these sources. The $\text{CH}_2\text{DOH}/\text{CH}_3\text{OH}$ ratio is on the order of $\sim 1 - 10\%$. Hints for features of isotopologs are seen for partially deuterated ethanol ($\text{CH}_2\text{DCH}_2\text{OH}$) and methyl formate ($\text{CH}_3\text{O}^{13}\text{CHO}$), but these lines are too weak to allow unambiguous confirmation or to derive physical properties.

In order to compare our derived column densities, we determine the abundance ratios of each species with respect to CH_3OH . Because CO, which is the usual tracer of H_2 , comes from more extended regions, CH_3OH is chosen as the reference species. In Table 2.2, the derived abundances are presented for the three COM-rich sources. The abundances vary between B1-c and S68N within a factor of two to three. This may simply be an effect of the source properties; the lines in S68N are, for example, a factor ~ 1.5 broader ($\sim 5.0 \text{ km s}^{-1}$ and $\sim 3.3 \text{ km s}^{-1}$ in Band 6, respectively) resulting in more blended lines. In S68N, our abundances of CH_3OCHO , CH_3OCH_3 , and H_2CCO are an order of magnitude lower than those derived by Bergner et al. (2019). The discrepancies are potentially due to different approaches to optical depth correction. Our observations of B1-bS have a low S/N. Nevertheless our derived abundance ratios coincide within a factor of a few with the hot (200 K) component modeled by Marcelino et al. (2018).

The abundances in Band 3 for B1-c deviate within a factor of approximately two from the abundances derived in Band 6. Only CH_3CHO and t-HCOOH are more abundant based on the Band 3 data. In S68N, CH_3OCHO is less abundant in Band 3 whereas CH_3OCH_3 is more abundant. In B1-bS, both CH_3OCHO and CH_3OCH_3 are significantly more abundant in Band 3, possibly because the column density of CH_3OH is underestimated.

2.4 Discussion

2.4.1 Occurrence of COMs in young protostars

The emission of COMs is assumed to originate from inside the $T_{\text{dust}} \sim 100 - 300$ K radius. Using the relation of Bisschop et al. (2007) for the 100 K radius in hot cores:

$$R_{T=100\text{K}} \approx 15.4 \sqrt{\frac{L}{L_{\odot}}} \text{AU}, \quad (2.2)$$

with L the source luminosity, implies an $R_{T=100\text{K}}$ of 37.4 AU, 35.8 AU, and 11.6 AU for B1-c, S68N, and B1-bS, respectively. Our Band 6 beam size of $\sim 0.45''$ (corresponding to a radius of ~ 72 AU and ~ 98 AU for Perseus and Serpens, respectively) is larger than this radius and thus agrees with all COM emission being unresolved, except for any CH_3OH emission related to an outflow.

Previous studies have found that a higher luminosity implies more emission of COMs (e.g., Jørgensen et al. 2002; Young & Evans 2005; Visser et al. 2009). Following Eq. 2.2 we would indeed expect the occurrence of COM emission to be correlated to the source luminosity. Here, three of the seven sources studied show emission of COMs. However, our most luminous source, SMM3, does not exhibit any COM emission. On the other end, the two sources with the lowest luminosity, B1-bN and B1-b, do not show any COM emission either. Interestingly, B1-bS also has a rather low luminosity but does exhibit COM emission. This suggests that, for the targets that we observed, no clear correlation exists between the occurrence of gaseous COMs and source luminosity.

Not finding such a correlation is surprising. However, the relation for $R_{T=100\text{K}}$ in Eq. (2.2) assumes a spherically symmetric infalling envelope (Bisschop et al. 2007). In reality, our Class 0 sources may be surrounded by an accretion disk (e.g., Tobin et al. 2012; Murillo et al. 2013). The presence of a disk or disk-like structure may shift the $R_{T=100\text{K}}$ inwards as the temperature in the midplane of a disk-like structure is lower than in the surface layers (e.g., Jørgensen et al. 2005; Visser et al. 2009). However, even for a fixed $R_{T=100\text{K}}$, the amount of material with $T_{\text{dust}} > 100$ K (e.g., high enough to release the COMs from the dust grains) can vary between different sources due to, for example, differences in the disk mass and radius (Persson et al. 2016).

The absence of COM emission can also originate from other source properties. B1-bN has been suggested as a first hydrostatic core candidate (e.g., Pezzuto et al. 2012; Hirano & Liu 2014; Gerin et al. 2017); the temperature in the inner regions may not have reached the threshold for ice COM sublimation. B1-b has a high bolometric temperature, and could therefore be more evolved than the other sources. Here, only a weak continuum is detected, indicating that B1-b may have a cleared inner region; all gaseous COMs have either already been destroyed or are incorporated as ices in the cold outer part. The strong ice absorption observed toward this source might originate in a region that is more extended than the inner B1-b envelope (Öberg et al. 2011). SMM3 shows strong continuum, which may imply that increased dust opacity hides any COM emission.

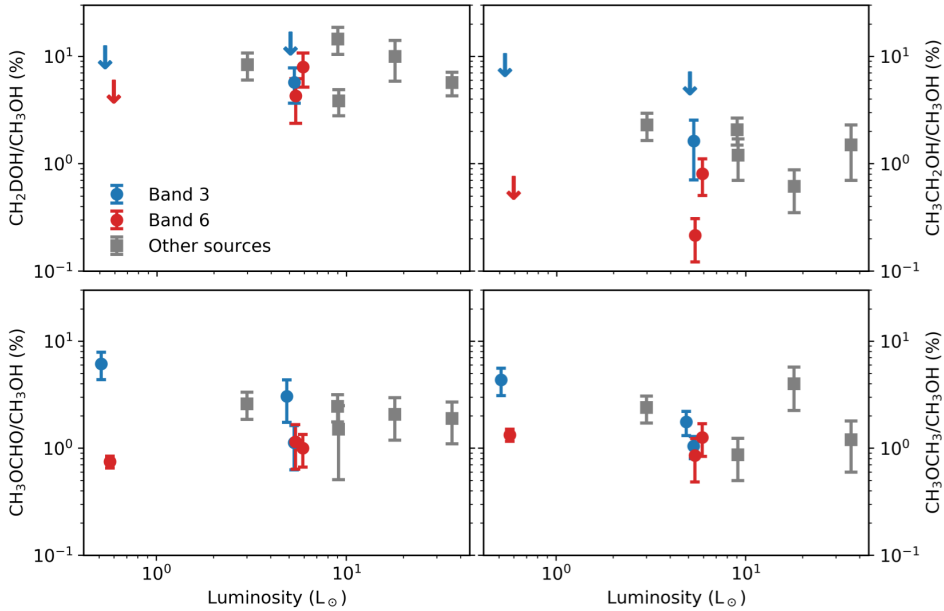


Figure 2.4: Abundance of CH_2DOH (top left), $\text{CH}_3\text{CH}_2\text{OH}$ (top right), CH_3OCHO (bottom left), and CH_3OCH_3 (bottom right) with respect to CH_3OH as a function of bolometric source luminosity. Both the abundances in Band 3 (blue) and Band 6 (red) are plotted; the Band 3 data points are slightly shifted in luminosity for clarity. Arrows denote upper limits. In gray, the abundances of IRAS 2A and IRAS 4A (Taquet et al. 2015, 2019), HH 112 (Lee et al. 2019a), IRAS 16293A (Manigand et al. 2020), and IRAS 16293B (Jørgensen et al. 2018) are presented.

Despite the absence of a clear correlation between the occurrence of COM emission and source luminosity, an increase in luminosity should result in higher temperatures and an increased UV radiation field (Visser et al. 2009; Drozdovskaya et al. 2016). The abundance of COMs with respect to CH_3OH may therefore be related to the source luminosity. However, Taquet et al. (2015) and Belloche et al. (2020) have shown that for most COM abundances, no clear correlation exists with luminosity, similar to what is found here; see Fig. 2.4. Our range of source luminosities is significantly smaller (up to $\sim 20 L_\odot$ compared to $10^6 L_\odot$; Taquet et al. 2015), and a similar scatter of abundances can be seen for their lower luminosities.

2.4.2 Dependence on source size

In modeling the COM emission, a source size equal to the beam size (0.45") was assumed for all sources. However, since the emission is spatially unresolved, the source size in reality will be smaller. A smaller emitting region will increase the derived column densities, and may result in spectral lines actually being optically thick. We can test this scenario by assuming the 100 K diameter as a source size.

This gives an emitting region of 0.23", 0.16", and 0.07" for B1-c, S68N, and B1-bS, respectively. Assuming the lines remain optically thin, the column densities derived for a 0.45" source size can be scaled to a smaller size by computing the difference in beam dilution (see Eq. (2.1)):

$$N_1 \frac{\theta_{s_1}^2}{\theta_b^2 + \theta_{s_1}^2} = N_2 \frac{\theta_{s_2}^2}{\theta_b^2 + \theta_{s_2}^2}, \quad (2.3)$$

where $N_{1,2}$ are the column densities for respective source sizes $\theta_{s_{1,2}}$, and θ_b is the beam size.

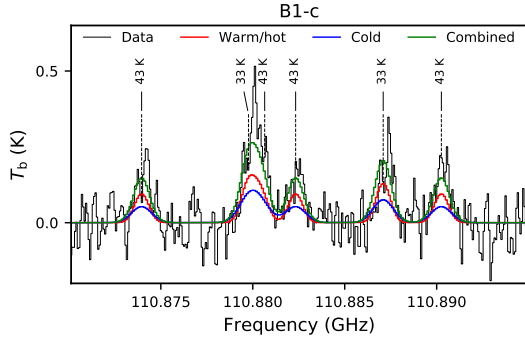
For B1-c and S68N, the resulting column densities still give optically thin ($\tau < 0.1$) lines for all species except CH_3OH . However, the lines of CH_3OH are already optically thick for a 0.45" source size and the column density is derived from the ^{13}C and ^{18}O isotopologs, whose lines remain optically thin. This means that the abundances derived above in Table 2.2 for these two sources remain the same. However, for B1-bS, most lines become optically thick (i.e., $\tau > 0.1$), indicating that the abundances derived in Table 2.2 for B1-bS should be used with care.

2.4.3 From cold (Band 3) to hot (Band 6) COMs

The temperature in the envelopes of Class 0 sources is expected to have an ‘onion’ layered shell structure, with increasing temperature when moving closer to the star (e.g., Jørgensen et al. 2002). In warmer layers, the COMs could be further processed to form more complex molecules (on the dust grains) and, more importantly, will all be released from the dust grains when the temperature reaches $T_{\text{dust}} \approx 100 - 300$ K. With our multi-band observations, we can check for hints of this onion-layered temperature structure by comparing the excitation temperature of COMs in Band 3, which is more sensitive to extended emission, to the COMs in Band 6, which is more sensitive to compact emission. Indeed, the average excitation temperature for the few species for which an excitation temperature could be derived in Band 3 (i.e., $\text{CH}_3\text{CH}_2\text{OH}$, CH_3OCHO , and CH_3OCH_3) is about 30 K lower than in Band 6. However, as mentioned in Section 2.3.2, no significant changes in the column densities and abundances arise if the Band 3 excitation temperature of all species for which T_{ex} was fixed is decreased by 30 K. The outcome of the Band 6 model does not change when all lines with a low $E_{\text{up}} < 100$ K are excluded.

Jørgensen et al. (2018) modeled the abundances of O-bearing COMs in IRAS 16293B and found that they can be divided in two classes with temperatures of ~ 125 K (warm) and ~ 300 K (hot). Most COMs in our sample have excitation temperatures of ~ 200 K, which falls in the middle between these two classes. Only CH_3OCH_3 consistently shows $T_{\text{ex}} \sim 100$ K, both in the Band 3 and Band 6 observations for all sources. This agrees with Jørgensen et al. (2018), who classified CH_3OCH_3 as a warm species. However, some ambiguity remains, since CH_3OCH_3 is also observed to have hot components in, for instance, higher mass cores (Belloche et al. 2013; Isokoski et al. 2013).

Figure 2.5: Part of the Band 3 spectrum of the warm/hot ($T_{\text{ex}} \sim 100 - 300$ K) compact (red), cold ($T_{\text{ex}} = 60$ K) extended (blue), and combined (green) model overlayed on the data (black). The spectral features are from CH_3OCHO , with the upper energy indicated on top.



The emission of COMs can be a superposition of a warm/hot inner component, and a second colder and more extended component. Earlier observational studies have shown that indeed a cold ($T < 100$ K, i.e., below the desorption temperature), more extended component may be present (e.g., Bisschop et al. 2007; Isokoski et al. 2013; Fayolle et al. 2015; Marcelino et al. 2018). Using our data, a possible cold component can be probed by fitting a multi-component model to the Band 3 data. This is only done for B1-c and S68N since the S/N of B1-bS in Band 3 is insufficient to carry out such an analysis. H_2CCO , CH_3COCH_3 , $(\text{CH}_2\text{OH})_2$, and CH_2OHCHO are excluded from this analysis due to the lack of clear detections in our Band 3 data.

For the warm/hot component, the best-fit model of Band 6 is adopted. This component is kept fixed. As a second component, a colder model is introduced. Here, an excitation temperature of 60 K was assumed and only the column density was fitted for. The FWHM was initially set as a free parameter, but fixed to that of the warm/hot component in the cases where fit results were unconstrained. A source size of $2.0''$ (equal to Band 3 beam) is assumed for the cold component, compared with the source size of the warm component of $0.45''$.

The results are presented in Table 2.3. Figure 2.5 shows part of the Band 3 spectrum of B1-c centered around several CH_3OCHO lines. The abundances of Table 2.3 are presented in a bar plot in Fig. 2.6. In B1-c, a cold ($T_{\text{ex}} = 60$ K) and more extended component is detected for most species. The column density of this cold component is typically a few percent but can rise up to 10% of the warm/hot inner component. The abundances of more complex species in the cold component are higher than those in the warm/hot component, which contradicts the idea that COMs are more effectively processed and released from icy grains in warmer layers. However, we highlight the fact that the column density of $^{13}\text{CH}_3\text{OH}$, and therefore CH_3OH , is likely underestimated.

Only for $\text{CH}_3\text{CH}_2\text{OH}$ and CH_3OCHO could a FWHM of 3.3 ± 0.8 be derived for the cold component which agrees with the average FWHM of the warm/hot component of 3.3 ± 0.2 . The line width of the cold component can be expected to be smaller since the emitting material is located further out in the envelope. However, Murillo et al. (2018) find that lower resolution data can also result in a larger line width, especially if the molecule is associated with the outflow or its cavity.

Table 2.3: Column densities resulting from the multi-component analysis.

Species	Component 1: warm/hot		Component 2: cold	
	N (cm^{-2})	$X/\text{CH}_3\text{OH}$ (%)	N (cm^{-2})	$X/\text{CH}_3\text{OH}$ (%)
B1-c				
CH_3OH	$(1.9 \pm 0.6) \times 10^{18}$	$\equiv 100$	$(1.2 \pm 0.7) \times 10^{16}$	$\equiv 100$
$^{13}\text{CH}_3\text{OH}$	$(1.8 \pm 0.2) \times 10^{16}$	1.0 ± 0.3	$(1.7 \pm 1.0) \times 10^{14}$	$\equiv 1.43$
$\text{CH}_3^{18}\text{OH}$	$(3.4 \pm 1.1) \times 10^{15}$	$\equiv 0.18$	$< 7.0 \times 10^{15}$	< 62
CH_2DOH	$(1.6 \pm 0.1) \times 10^{17}$	8.4 ± 2.8	$< 1.6 \times 10^{14}$	< 15
$\text{CH}_3\text{CH}_2\text{OH}$	$(1.5 \pm 0.3) \times 10^{16}$	0.8 ± 0.3	$(1.2 \pm 0.2) \times 10^{15}$	9.8 ± 6.1
CH_3CHO	$(4.6 \pm 1.0) \times 10^{15}$	0.24 ± 0.10	$(1.8 \pm 0.2) \times 10^{14}$	1.5 ± 0.9
CH_3OCHO	$(1.9 \pm 0.1) \times 10^{16}$	1.0 ± 0.3	$(4.7 \pm 0.3) \times 10^{14}$	3.8 ± 2.3
CH_3OCH_3	$(2.4 \pm 0.1) \times 10^{16}$	1.3 ± 0.4	$< 1.0 \times 10^{14}$	< 0.22
t-HCOOH	$(7.0 \pm 2.0) \times 10^{14}$	0.04 ± 0.02	$(2.2 \pm 0.2) \times 10^{14}$	1.8 ± 1.1
S68N				
CH_3OH	$(1.4 \pm 0.6) \times 10^{18}$	$\equiv 100$	$< 4.8 \times 10^{14}$	$\equiv 100$
$^{13}\text{CH}_3\text{OH}$	$(1.0 \pm 0.1) \times 10^{16}$	0.7 ± 0.3	$< 1.0 \times 10^{14}$	$\equiv 1.43$
$\text{CH}_3^{18}\text{OH}$	$(2.5 \pm 1.1) \times 10^{15}$	$\equiv 0.18$	$< 1.6 \times 10^{15}$	$-^1$
CH_2DOH	$(6.0 \pm 0.7) \times 10^{16}$	4.3 ± 1.9	$< 1.0 \times 10^{14}$	$-^1$
$\text{CH}_3\text{CH}_2\text{OH}$	$(3.0 \pm 0.2) \times 10^{15}$	0.22 ± 0.09	$< 1.0 \times 10^{14}$	$-^1$
CH_3CHO	$(1.0 \pm 0.1) \times 10^{15}$	0.07 ± 0.03	$< 1.0 \times 10^{14}$	$-^1$
CH_3OCHO	$(1.6 \pm 0.2) \times 10^{16}$	1.1 ± 0.5	$(1.0 \pm 0.5) \times 10^{14}$	$> 1^2$
CH_3OCH_3	$(1.2 \pm 0.1) \times 10^{16}$	0.9 ± 0.4	$< 1.0 \times 10^{14}$	$-^1$
t-HCOOH	$(9.1 \pm 2.1) \times 10^{14}$	0.07 ± 0.03	$< 1.0 \times 10^{14}$	$-^1$

Notes. The values of the warm/hot Component 1 are the same as derived for Band 6 in a 0.45" beam and are fixed during the fitting (typical $T_{\text{ex}} \sim 200$ K). Component 2 represents cold (typical $T_{\text{ex}} = 60$ K), more extended material in a 2.0" beam. The column density of CH_3OH is determined by scaling from $^{13}\text{CH}_3\text{OH}$ for Band 3 and $\text{CH}_3^{18}\text{OH}$ for Band 6 using $^{12}\text{C}/^{13}\text{C} = 70$ and $^{16}\text{O}/^{18}\text{O} = 560$. Abundance ratio's which are set to their respective isotope ratio are indicated with a \equiv symbol.

⁽¹⁾ No abundance is computed since the column densities of both this species and CH_3OH are upper limits. ⁽²⁾ Lower limit to the abundance due to an upper limit of the CH_3OH column density.

The presence of a cold component of COM emission indicates that some gas-phase formation routes are already efficient in the cold envelope as most COMs formed through grain-surface chemistry are still frozen out at these temperatures. Alternatively, this could indicate that other mechanisms are capable of transferring the COMs from the solid state to the gas phase. Possible mechanisms include photodesorption (Fayolle et al. 2011; Muñoz Caro et al. 2016), desorption of fragments following photo-dissociation (Bertin et al. 2016), low-temperature co-desorption (Fayolle et al. 2013; Ligterink et al. 2018c), or reactive desorption via a thermal hot-spot (Minissale et al. 2016; Chuang et al. 2018). Only for CH_3OCH_3 and the deuterated and ^{18}O isotopologs of CH_3OH does an extended component seem to be absent.

Formic acid is very abundant in the cold, extended component. This disagrees with the hot identification in IRAS 16293B (Jørgensen et al. 2018), but is more consistent with the cold identification in high-mass star-forming regions (Bisschop et al. 2007; Belloche et al. 2013) and that HCOOH is likely an abundant ice species (Öberg et al. 2011; Boogert et al. 2015). However, in both Band 3 and Band 6, only one to three lines could be fitted, and therefore the identification of *t*- HCOOH should be considered rather tentative.

In S68N, a cold component is less evident. Only for CH_3OCHO is a cold column density derived; for all other species only upper limits are found. These results suggest that a possible cold component would have a column density of $\lesssim 1\%$ of the warm component.

2.4.4 Comparison to other sources

Our Band 6 abundances are compared to the ALMA Band 7 abundances of IRAS 16293B (Jørgensen et al. 2018) and HH 212 (Lee et al. 2019a); see Fig. 2.7. The abundances of several COMs (i.e., CH_2DOH , CH_3OCHO , CH_3OCH_3 , and CH_3COCH_3) from this work are very similar to IRAS 16293B and HH 212; the distribution of abundances seems to span only a factor of a few. The abundances are also within a factor three of IRAS 2A and IRAS 4A (Taquet et al. 2015). This similarity in abundances is rather interesting given that the source properties (e.g., L_{bol} , T_{bol} , etc.) are different for all sources. For example, IRAS 2A has a luminosity of $36 L_{\odot}$, whereas the luminosity of B1-bS is two orders of magnitude lower ($0.57 L_{\odot}$). A similarly large range is seen for the bolometric temperature and envelope mass. Moreover, these sources originate from four different star-forming regions: Perseus (B1-bS, B1-c, IRAS 2A, IRAS 4A), Serpens (S68N), Ophiuchus (IRAS 16293B), and Orion (HH 212). It appears that, despite the differences in source properties and local environment, the internal distribution of these COM abundances is roughly similar. This indicates that their formation schemes must follow a similar recipe, for instance following the atom addition and abstraction reaction networks proposed to govern the surface chemistry in cold interstellar clouds (e.g., Chuang et al. 2016). This implies that solid-state processes are already enriching the complex organic inventory of the interstellar medium in the prestellar phase.

Interestingly, our sources are under-abundant up to more than one order of

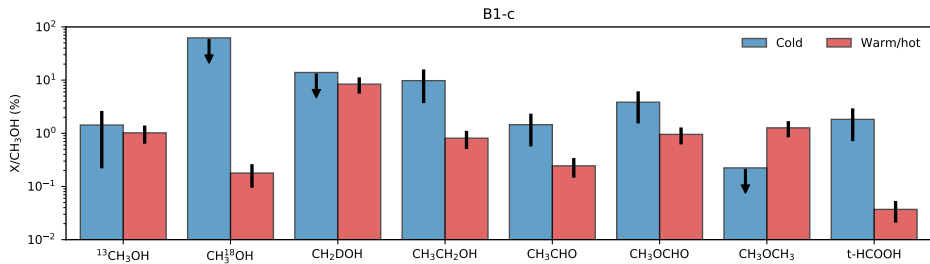


Figure 2.6: Abundance of several species with respect to CH₃OH for our multi-component analysis. The warm ($T_{\text{ex}} \sim 200$ K) component is fixed to the Band 6 model with a 0.45" source size, whereas the cold ($T_{\text{ex}} = 60$ K) component is fitted with a more extended 2.0" source size. The 2σ (95%) errors are shown in black, with arrows denoting upper limits. The CH₃OH column density is determined by scaling from ¹³CH₃OH using ¹²C/¹³C = 70 and ¹⁶O/¹⁸O = 560, respectively. The higher abundances in the cold component are likely due to an underestimate of the column density of ¹³CH₃OH.

magnitude in CH₃CH₂OH, CH₃CHO, and CH₂OHCHO compared with IRAS 16293B, HH 212, IRAS 2A, and IRAS 4A. Our abundances of these COMs indeed fall within a factor of a few with IRAS 16293A (Manigand et al. 2020). This suggests that for some COMs, local source conditions do become important for the formation or the destruction. The column density ratio of CH₃OCHO to CH₂OHCHO of B1-c is consistent with the lower part of the bimodal distribution found by El-Abd et al. (2019). For H₂CCO and t-HCOOH, our sources also have lower abundances. The abundance of t-HCOOH in the cold component of the multi-component analysis (see Section 2.4.3) is consistent with IRAS 16293B and HH 212. However, the detections of these species are rather tentative since only less than three clear unblended lines (not taking into account (hyper)fine structured lines) are detected.

In more massive star-forming regions, a larger scatter in COM abundances seems to be present. AFGL 4176 has abundances very similar to ours for most COMs (Bøgelund et al. 2019), whereas those in Orion KL show deviations: the abundance of CH₃CH₂OH is similar (Tercero et al. 2018), but CH₃OCHO and CH₃OCH₃ have lower abundances in our sources and CH₃COCH₃ has higher abundances (see Table 6 in Bøgelund et al. 2019). Even larger deviations are found toward Sagittarius B2, where the abundances of all COMs are higher by up to an order of magnitude (Belloche et al. 2016).

The abundances derived here are higher than those in chemical models of a collapsing cloud for most COMs (e.g., Garrod 2013). Especially for CH₃COCH₃ and (CH₂OH)₂, these models underestimate the abundances by up to an order of magnitude. This may be a direct result of a still not fully characterized solid-state and gas-phase chemistry and underlying gas-grain interactions (see discussion by Bøgelund et al. 2019).

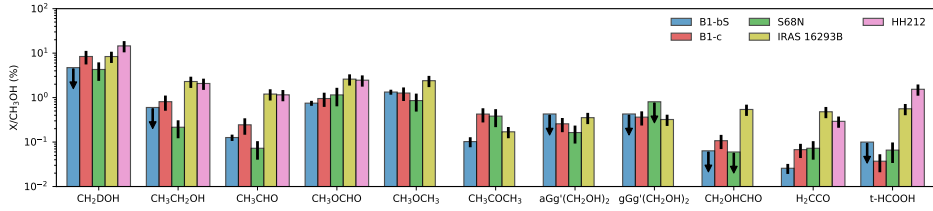


Figure 2.7: Bar plot comparing our derived Band 6 abundances to those of other sources. The IRAS 16293B abundances for all species except $(\text{CH}_2\text{OH})_2$, CH_2OHCHO , and CH_3COCH_3 are from Jørgensen et al. (2018); the $(\text{CH}_2\text{OH})_2$ and CH_2OHCHO abundances are from Jørgensen et al. (2016), and the CH_3COCH_3 abundances from Lykke et al. (2017). The HH 212 abundances are from Lee et al. (2019a). The 2σ (95%) errors are shown in black, with arrows denoting upper limits. We note that the abundances of our targets are remarkably similar and show comparable values to those derived for IRAS 16293B and HH 212.

2.4.5 Comparison with ices

No clear COM ice features have yet been observed toward any of our COM-rich sources. However, hints for CH_3CHO , $\text{CH}_3\text{CH}_2\text{OH}$, and t-HCOOH ice have been detected toward B1-b (from the same cloud as B1-c) with an abundance of $\sim 10\%$ with respect to CH_3OH (Öberg et al. 2011; Boogert et al. 2015). These are higher than those derived for the gaseous warm/hot component in this work ($\sim 0.1\text{--}1\%$). A possible explanation for this is that, besides typical grain-surface chemistry, additional gas-phase chemistry following thermal desorption in the warm inner envelope can contribute to further processing the COMs into more complex species.

To better compare the abundances of COMs in the ice and gas phase, it is essential to directly observe the ices. However, the above mentioned detections are still very uncertain, with only CH_3OH being securely identified in interstellar ices. Measuring the column densities of interstellar COM ices remains difficult because current infrared telescopes lack the sensitivity or wavelength coverage, and because the spectral features originating from ices are broad and depend on the ice composition. Moreover, the number of COMs for which extensive high-resolution infrared laboratory spectra have become available is limited (Hudson et al. 2018; Terwisscha van Scheltinga et al. 2018). Future mid-infrared facilities such as JWST/MIRI will allow COMs to be directly observed in the ice, which will be essential for studying their formation and evolution from the cold envelope toward the warm inner regions.

2.4.6 Temperature dependence of deuterated methanol

The deuteration fraction of methanol is an indication of the temperature during the solid-state formation of this species. At low temperatures, deuterium is more efficient than regular hydrogen in the hydrogenation process on interstellar dust grains (e.g., Nagaoka et al. 2005). This leads to a higher deuteration fraction than the elemental ratio ($\text{D}/\text{H} \sim 10^{-5}$; Caselli & Ceccarelli 2012). Bøgelund et al.

(2018) investigated the effect of temperature during the formation of methanol with the astrochemical GRAINOBLE model (Taquet et al. 2012). In order to compare our methanol D/H ratios to their model results, our gas-phase CH_2DOH abundances have to be corrected for statistical weights; a D atom has a three-times-higher probability of sticking into the CH_3 group than into the OH group. In Band 3, this gives a D/H ratio of $1.9 \pm 0.7\%$, $< 4.3\%$, and $< 3.3\%$ for B1-c, S68N, and B1-bS respectively. In Band 6, this is $2.7 \pm 0.9\%$, $1.4 \pm 0.6\%$, and $< 1.6\%$. These deuteration fractions correspond to a temperature during the formation of methanol of ~ 15 K, where a density of $n_{\text{H}} = 10^{5-6} \text{ cm}^{-3}$ was assumed (cf. Fig. 8 of Bøgelund et al. 2018).

Our derived methanol D/H fractions agree well with other well-studied low-mass protostars such as IRAS16293B ($\sim 2\%$; Jørgensen et al. 2018), IRAS 2A and IRAS 4A ($\sim 2\%$ and $\sim 1\%$, respectively; Taquet et al. 2019), and HH 212 ($\sim 1\%$ after taking into account statistical weights; Bianchi et al. 2017b; Taquet et al. 2019). Our fractions are up to an order of magnitude higher than for high-mass star-forming regions such as NGC 6334I ($\sim 0.1\%$ on average; Bøgelund et al. 2018), and Sagittarius B2 (0.04% after statistical correction; Belloche et al. 2016). The lower D/H ratios in more massive star-forming regions hint at a higher temperature (i.e., > 20 K) already during the earliest phase of high-mass star formation.

2.5 Summary

In this paper, the content of oxygen bearing COMs is studied in seven young protostellar systems. High-resolution ALMA observations in both Band 3 and Band 6 were used to determine the column densities and excitation temperatures. The main conclusions are as follows:

- Three out of the seven sources exhibit warm COM emission features with typical $T_{\text{ex}} \sim 200$ K. There seems to be no correlation between the bolometric luminosity (and temperature) and occurrence of COMs of these Class 0 sources. Other effects, such as disk formation and clearing of an inner region, may play a role as well.
- A multi-component model was introduced to check whether a cold ($T_{\text{ex}} = 60$ K), more extended component of COM emission is present. Only B1-c shows clear signs of such a cold component, with typically a few percent of the column density of the warm component. This indicates that in the cold envelope already gas-phase formation may take place and that this could be a direct consequence of the grain-gas transitions of COMs or (radical) COM fragments. t-HCOOH is significantly more abundant in the cold component, hinting at the cold origin of this species.
- The abundance of several COMs (i.e., CH_3OCHO , CH_3OCH_3 , CH_3COCH_3 , and $(\text{CH}_2\text{OH})_2$) are remarkably similar in comparison to other young Class 0 protostars in different star-forming regions such as IRAS 16293B and HH 212. This similarity suggests that the distribution of these COM abundances is

roughly fixed at an early, cold, i.e., prestellar, stage. However, the abundances of some COMs (i.e., $\text{CH}_3\text{CH}_2\text{OH}$, CH_3CHO , and CH_2OHCHO) in our sources differ significantly from those found for IRAS 16293B and HH 212, possibly because local source conditions become important and affect formation and destruction pathways in different ways. Astrochemical modeling will be needed to further investigate these findings.

- The D/H ratio of deuterated CH_3OH is around a few percent for all COM-rich sources, suggesting a dust temperature of ~ 15 K during its solid-state formation. The derived formation temperature is similar to that found for other low-mass protostars, but is lower than that found in high-mass star-forming regions (> 20 K).

Our sample of COM-rich protostars studied on Solar System scales remains small. How much of the prestellar cloud material is reprocessed during evolution toward protostellar systems and more evolved sources remains unknown. The abundance of most COMs in the ice phase is still highly uncertain. Future mid-infrared facilities, most notably JWST, will provide vital information on COM ices. A larger sample of COM-rich sources with ALMA, both in the Class 0 phase and in the more evolved Class I phase where most COM emission has already disappeared, would provide better constraints on the chemical complexity during these earliest phases of star formation. The present work already shows that such studies will be valuable, given the rich distribution in COMs discussed here.

Acknowledgments

We would like to thank the anonymous referee for his/her constructive comments on the manuscript. This paper makes use of the following ALMA data: ADS/JAO.ALMA#2017.1.01174.S and ADS/JAO.ALMA#2017.1.01350.S. ALMA is a partnership of ESO (representing its member states), NSF (USA) and NINS (Japan), together with NRC (Canada), MOST and ASIAA (Taiwan), and KASI (Republic of Korea), in cooperation with the Republic of Chile. The Joint ALMA Observatory is operated by ESO, AUI/NRAO and NAOJ. Astrochemistry in Leiden is supported by the Netherlands Research School for Astronomy (NOVA). BT acknowledges support from the Dutch Astrochemistry Network II with project number 614.001.751, financed by the Netherlands Organisation for Scientific Research (NWO). H.B. acknowledges support from the European Research Council under the Horizon 2020 Framework Program via the ERC Consolidator Grant CSF-648505. H.B. also acknowledges support from the Deutsche Forschungsgemeinschaft (DFG) via Sonderforschungsbereich (SFB) 881 “The Milky Way System” (sub-project B1).

Appendix

2.A Laboratory spectroscopic data

All laboratory spectroscopic data were acquired using the CDMS (Müller et al. 2001, 2005; Endres et al. 2016) and JPL (Pickett et al. 1998) catalogs. In some of the entries, vibrational or torsional states are not taken into account in the calculation of the partition function. At low temperatures, the contribution of these states are negligible. However, at higher temperatures (i.e., $T > 100$ K), a so-called vibrational correction factor must be applied if the torsional and vibrational states are not accounted for in the partition functions. Below, we detail the laboratory spectroscopy of each individual species discussed in this paper and indicate if a vibrational correction factor was applied.

The data of CH_3OH are taken from the CDMS database and are based on the work of Xu et al. (2008). The ground state and first three torsional states are taken into account in the partition function. The entry of the ^{13}C isotopolog takes the first two torsional states into account (Xu & Lovas 1997). These latter authors assumed that the dipole moment is the same as the main isotopolog and calculated the partition function taking only the permanent dipole moment into account. The $\text{CH}_3^{18}\text{OH}$ entry is based mostly on the data of Fisher et al. (2007). The spectroscopic data of CH_2DOH are taken from the JPL catalog, where the entry is based on the work of Pearson et al. (2012). The vibrational correction factor at 200 K is calculated to be 1.181 by summing up over torsional substates extrapolated from Lauvergnat et al. (2009).

$\text{CH}_3\text{CH}_2\text{OH}$ exists as two conformers: *trans* and *gauche*, which originates from the torsion in the OH group. The spectroscopic data are taken from the CDMS catalog, where the entry is based on Pearson et al. (2008) and updated by Müller et al. (2016), who noticed that the old catalog entry did not predict the line intensities correctly around 3 mm in Sagittarius B2. This applies also to other frequency regions, but not to all transitions. Both conformers are included in the entry.

The data of CH_3CHO are taken from the JPL catalog. It is based on laboratory spectroscopy of Kleiner et al. (1996) and includes the first and second torsional state in its partition function.

The spectroscopic data of CH_3OCHO are taken from the JPL database. The entry is based on the work of Ilyushin et al. (2009) and Brown et al. (1975). The partition function includes states up to the first torsional state.

CH_3OCH_3 data are taken from the CDMS entry, which includes mostly the work of Endres et al. (2009). The partition function includes the ground vibrational state and excited states up to 500 cm^{-1} . However, for the excitation temperatures derived in this work (~ 100 K), the contribution of higher order vibrational states to the partition function is negligible.

The CH_3COCH_3 data are taken from the JPL catalog. The rotational transitions were calculated by Groner et al. (2002) and include only the ground state. Here, we use an updated version of the entry. It is based on the study of Ordu

et al. (2019) with the majority of the lines from Groner et al. (2002).

The $(\text{CH}_2\text{OH})_2$ structure consists of three coupled rotors, which give rise to ten different stable configurations (Christen et al. 2001). Here, only the two lowest energy conformers of $(\text{CH}_2\text{OH})_2$ are studied. The aGg' state is the lowest energy state whereas the gGg' state lies about 290 K above that (Müller & Christen 2004). The spectroscopic data are taken from the CDMS entries, which are based on the work of Christen et al. (1995) and Christen & Müller (2003) for the aGg' conformer and Christen et al. (2001) and Müller & Christen (2004) for the gGg' conformer. For gGg' $(\text{CH}_2\text{OH})_2$, the partition function and line intensities were calculated assuming as if it is the lowest energy state conformer. For these calculations, only the ground state is considered, and therefore we approximate the effect of vibrational states using a vibrational correction factor of 2.143 for both conformers at 200 K.

The CH_2OHCHO data are taken from the CDMS catalog. The entry is based on the work of Butler et al. (2001) and only includes data on the ground vibrational state. A vibrational correction factor of 1.5901 is calculated at 200 K in the harmonic approximation.

The spectroscopic data of H_2CCO are acquired from the CDMS catalog. The entry is calculated mostly by Johnson & Strandberg (1952), Fabricant et al. (1977), and Brown et al. (1990). The contribution of vibrational states is assumed to be negligible.

Formic acid, HCOOH , exists both in a *trans* and *cis* state, where the lowest energy state of c- HCOOH is about 2000 K higher than for t- HCOOH . In this study we only detect t- HCOOH , for which we use the entry of the JPL catalog. This is based on the work of Bellet et al. (1971). The vibrational correction is < 1.1 at 200 K and is therefore neglected.

2.B CASSIS modeling results

Table 2.B.1: Computed Band 3 and Band 6 column densities and excitation temperatures of B1-c.

B1-c							
Species	Catalog	Band 3			Band 6		
		T_{ex} (K)	N^I (cm $^{-2}$)	X/CH $_3$ OH (%)	T_{ex} (K)	N^I (cm $^{-2}$)	X/CH $_3$ OH (%)
CH $_3$ OH	CDMS	–	$(1.8 \pm 0.4) \times 10^{18}$	$\equiv 100$	–	$(1.9 \pm 0.6) \times 10^{18}$	$\equiv 100$
13 CH $_3$ OH	CDMS	[190]	$(2.6 \pm 0.6) \times 10^{16}$	$\equiv 1.43$	190 ± 30	$(1.8 \pm 0.2) \times 10^{16}$	1.0 ± 0.3
CH $_3^{18}$ OH	CDMS	[140]	$< 1.8 \times 10^{16}$	< 1.0	140 ± 60	$(3.4 \pm 1.1) \times 10^{15}$	$\equiv 0.18$
CH $_2$ DOH	JPL	210 ± 60	$(1.0 \pm 0.3) \times 10^{17}$	5.7 ± 2.1	180 ± 20	$(1.6 \pm 0.1) \times 10^{17}$	8.4 ± 2.8
CH $_3$ CH $_2$ OH	CDMS	160 ± 60	$(2.9 \pm 1.5) \times 10^{16}$	1.6 ± 0.9	250 ± 60	$(1.5 \pm 0.3) \times 10^{16}$	0.8 ± 0.3
CH $_3$ CHO	JPL	260 ± 50	$(2.4 \pm 0.8) \times 10^{16}$	1.3 ± 0.5	260 ± 60	$(4.6 \pm 1.0) \times 10^{15}$	0.24 ± 0.10
CH $_3$ OCHO	JPL	120 ± 40	$(2.0 \pm 0.8) \times 10^{16}$	1.1 ± 0.5	180 ± 20	$(1.9 \pm 0.1) \times 10^{16}$	1.0 ± 0.3
CH $_3$ OCH $_3$	CDMS	100 ± 10	$(1.9 \pm 0.1) \times 10^{16}$	1.0 ± 0.2	120 ± 10	$(2.4 \pm 0.1) \times 10^{16}$	1.3 ± 0.4
CH $_3$ COCH $_3$	JPL	[200]	$< 5.0 \times 10^{16}$	< 2.8	[200]	$(8.0 \pm 0.9) \times 10^{15}$	0.4 ± 0.1
aGg' (CH $_2$ OH) $_2$	CDMS	[180]	$< 4.2 \times 10^{16}$	< 2.4	180 ± 100	$(4.8 \pm 0.6) \times 10^{15}$	0.3 ± 0.1
gGg' (CH $_2$ OH) $_2$	CDMS	[200]	$< 2.2 \times 10^{16}$	< 1.2	[200]	$(6.8 \pm 0.8) \times 10^{15}$	0.4 ± 0.1
CH $_2$ OHCHO	CDMS	[200]	$< 1.6 \times 10^{16}$	< 0.89	[200]	$(2.0 \pm 0.2) \times 10^{15}$	0.11 ± 0.04
H $_2$ CCO	CDMS	–	–	–	[200]	$(1.3 \pm 0.1) \times 10^{15}$	0.07 ± 0.02
t-HCOOH	JPL	[200]	$(9.0 \pm 1.0) \times 10^{15}$	0.5 ± 0.1	[200]	$(7.0 \pm 2.0) \times 10^{14}$	0.04 ± 0.02

Notes. The column density of CH₃OH is determined by scaling ¹³CH₃OH for Band 3 and CH₃¹⁸OH for Band 6 using ¹²C/¹³C = 70 and ¹⁶O/¹⁸O = 560, respectively. A value between squared brackets means the parameter was fixed to that value during the computation. Abundance ratios which are set to their respective isotope ratio are indicated with a \equiv symbol.

(¹) The presented column densities are derived for a 0.45" source size. However, in reality the source sizes will be smaller, and the presented column densities therefore represent lower limits.

Table 2.B.2: Computed Band 3 and Band 6 column densities and excitation temperatures of S68N.

S68N

Species	Catalog	Band 3			Band 6		
		T_{ex} (K)	N^I (cm $^{-2}$)	X/CH $_3$ OH (%)	T_{ex} (K)	N^I (cm $^{-2}$)	X/CH $_3$ OH (%)
CH $_3$ OH	CDMS	–	$(3.6 \pm 0.8) \times 10^{17}$	$\equiv 100$	–	$(1.4 \pm 0.6) \times 10^{18}$	$\equiv 100$
$^{13}\text{CH}_3\text{OH}$	CDMS	[160]	$(5.1 \pm 1.2) \times 10^{15}$	$\equiv 1.43$	160 ± 20	$(1.0 \pm 0.1) \times 10^{16}$	0.7 ± 0.3
CH $_3^{18}\text{OH}$	CDMS	[200]	$< 1.0 \times 10^{16}$	< 2.8	200 ± 80	$(2.5 \pm 1.1) \times 10^{15}$	$\equiv 0.18$
CH $_2\text{DOH}$	JPL	[200]	$< 4.7 \times 10^{16}$	< 13	[200]	$(6.0 \pm 0.7) \times 10^{16}$	4.3 ± 1.9
CH $_3\text{CH}_2\text{OH}$	CDMS	[200]	$< 2.0 \times 10^{16}$	< 5.6	[200]	$(3.0 \pm 0.2) \times 10^{15}$	0.22 ± 0.09
CH $_3\text{CHO}$	JPL	[200]	$< 5.0 \times 10^{15}$	< 1.4	[200]	$(1.0 \pm 0.1) \times 10^{15}$	0.07 ± 0.03
CH $_3\text{OCHO}$	JPL	220 ± 80	$(1.6 \pm 0.9) \times 10^{16}$	3.9 ± 2.5	290 ± 30	$(1.6 \pm 0.2) \times 10^{16}$	1.1 ± 0.5
CH $_3\text{OCH}_3$	CDMS	110 ± 10	$(6.4 \pm 0.7) \times 10^{15}$	1.8 ± 0.4	90 ± 10	$(1.2 \pm 0.1) \times 10^{16}$	0.9 ± 0.4
CH $_3\text{COCH}_3$	JPL	[200]	$< 5.0 \times 10^{16}$	< 14	[200]	$(5.3 \pm 0.3) \times 10^{15}$	0.4 ± 0.2
aGg'(CH $_2\text{OH})_2$	CDMS	[200]	$< 4.2 \times 10^{16}$	< 12	[200]	$(2.3 \pm 0.1) \times 10^{15}$	0.16 ± 0.07
gGg'(CH $_2\text{OH})_2$	CDMS	[200]	$< 2.2 \times 10^{16}$	< 6	[200]	$< 1.1 \times 10^{16}$	< 0.81
CH $_2\text{OHCHO}$	CDMS	[200]	$< 8.0 \times 10^{15}$	< 2.2	[200]	$< 8.0 \times 10^{14}$	< 0.06
H $_2\text{CCO}$	CDMS	–	–	–	[200]	$(1.0 \pm 0.1) \times 10^{15}$	0.07 ± 0.03
t-HCOOH	JPL	[200]	$< 5.0 \times 10^{15}$	< 1.4	[200]	$(9.1 \pm 2.1) \times 10^{14}$	0.07 ± 0.03

Notes. The column density of CH $_3$ OH is determined by scaling $^{13}\text{CH}_3\text{OH}$ for Band 3 and CH $_3^{18}\text{OH}$ for Band 6 using $^{12}\text{C}/^{13}\text{C} = 70$ and $^{16}\text{O}/^{18}\text{O} = 560$, respectively. A value between squared brackets means the parameter was fixed to that value during the computation. Abundance ratios which are set to their respective isotope ratio are indicated with a \equiv symbol.

(I) The presented column densities are derived for a 0.45" source size. However, in reality the source sizes will be smaller, and the presented column densities therefore represent lower limits.

Table 2.B.3: Computed Band 3 and Band 6 column densities and excitation temperatures of B1-bS.

Species	Catalog	Band 3			Band 6		
		T_{ex} (K)	N^I (cm $^{-2}$)	X/CH $_3$ OH (%)	T_{ex} (K)	N^I (cm $^{-2}$)	X/CH $_3$ OH (%)
CH $_3$ OH	CDMS	–	$(2.4 \pm 0.7) \times 10^{17}$	$\equiv 100$	–	$(5.0 \pm 0.6) \times 10^{17}$	$\equiv 100$
$^{13}\text{CH}_3\text{OH}$	CDMS	[160]	$(3.5 \pm 1.0) \times 10^{15}$	$\equiv 1.43$	160 ± 40	$(1.5 \pm 0.5) \times 10^{15}$	0.3 ± 0.1
CH $_3^{18}\text{OH}$	CDMS	[200]	$< 1.0 \times 10^{16}$	< 4.2	[200]	$(9.0 \pm 1.0) \times 10^{14}$	$\equiv 0.18$
CH $_2\text{DOH}$	JPL	[200]	$< 2.4 \times 10^{16}$	< 9.9	[200]	$< 2.4 \times 10^{16}$	< 4.7
CH $_3\text{CH}_2\text{OH}$	CDMS	[200]	$< 2.0 \times 10^{16}$	< 8.3	[200]	$< 3.0 \times 10^{15}$	< 0.6
CH $_3\text{CHO}$	JPL	[200]	$< 5.0 \times 10^{15}$	< 2.1	[200]	$(6.4 \pm 0.7) \times 10^{14}$	0.13 ± 0.02
CH $_3\text{OCHO}$	JPL	[200]	$(1.5 \pm 0.1) \times 10^{16}$	6.1 ± 1.8	[200]	$(3.8 \pm 0.2) \times 10^{15}$	0.75 ± 0.10
CH $_3\text{OCH}_3$	CDMS	90 ± 10	$(1.1 \pm 0.1) \times 10^{16}$	4.3 ± 1.2	110 ± 10	$(6.7 \pm 0.4) \times 10^{15}$	1.3 ± 0.2
CH $_3\text{COCH}_3$	JPL	[200]	$< 5.0 \times 10^{16}$	< 21	[200]	$(5.1 \pm 1.2) \times 10^{14}$	0.10 ± 0.03
aGg' (CH $_2\text{OH})_2$	CDMS	[200]	$< 4.2 \times 10^{16}$	< 18	[200]	$< 2.2 \times 10^{15}$	< 0.43
gGg' (CH $_2\text{OH})_2$	CDMS	[200]	$< 2.2 \times 10^{16}$	< 8.9	[200]	$< 2.2 \times 10^{15}$	< 0.43
CH $_2\text{OHCHO}$	CDMS	[200]	$< 8.0 \times 10^{15}$	< 3.3	[200]	$< 3.2 \times 10^{14}$	< 0.064
H $_2\text{CCO}$	CDMS	–	–	–	[200]	$(1.3 \pm 0.3) \times 10^{14}$	0.03 ± 0.01
t-HCOOH	JPL	[200]	$< 1.0 \times 10^{16}$	< 4.2	[200]	$< 5.0 \times 10^{14}$	< 0.1

Notes. The column density of CH $_3$ OH is determined by scaling $^{13}\text{CH}_3\text{OH}$ for Band 3 and CH $_3^{18}\text{OH}$ for Band 6 using $^{12}\text{C}/^{13}\text{C} = 70$ and $^{16}\text{O}/^{18}\text{O} = 560$, respectively. A value between squared brackets means the parameter was fixed to that value during the computation. Abundance ratios which are set to their respective isotope ratio are indicated with a \equiv symbol.

⁽¹⁾ The presented column densities are derived for a 0.45" source size. However, in reality the source sizes will be smaller, and the presented column densities therefore represent lower limits.

Table 2.B.4: Number of transitions and lines fitted for B1-c.

B1-c						
Species	Band 3			Band 6		
	T	L	F	T	L	F
CH ₃ OH	1	1	0	3	3	0
¹³ CH ₃ OH	2	1	1	8	7	4
CH ₃ ¹⁸ OH	4	0	0	20	16	8
CH ₂ DOH	5	2	2	16	9	6
CH ₃ CH ₂ OH	12	3	3	30	14	8
CH ₃ CHO	17	2	2	27	6	5
CH ₃ OCHO	34	16	13	111	12	7
CH ₃ OCH ₃	16	8	8	112	27	20
CH ₃ COCH ₃	59	0	0	128	6	5
aGg'(CH ₂ OH) ₂	25	0	0	105	18	8
gGg'(CH ₂ OH) ₂	43	0	0	115	4	2
CH ₂ OHCHO	15	0	0	27	5	3
H ₂ CCO	0	0	0	6	2	2
t-HCOOH	6	3	3	3	1	1

Notes. T is the number of transitions, L is the number of lines in the model with a 3σ detection, and F is the number of unblended lines (i.e., no other line within one FWHM) that are included in the fit.

Table 2.B.5: Number of transitions and lines fitted for S68N.

S68N						
Species	Band 3			Band 6		
	T	L	F	T	L	F
CH ₃ OH	1	1	0	3	3	0
¹³ CH ₃ OH	2	1	1	8	5	5
CH ₃ ¹⁸ OH	4	0	0	20	2	2
CH ₂ DOH	5	0	0	16	2	2
CH ₃ CH ₂ OH	12	0	0	30	3	2
CH ₃ CHO	17	0	0	27	2	2
CH ₃ OCHO	34	7	7	111	10	7
CH ₃ OCH ₃	16	8	8	112	27	20
CH ₃ COCH ₃	59	0	0	128	2	1
aGg'(CH ₂ OH) ₂	25	0	0	105	1	1
gGg'(CH ₂ OH) ₂	43	0	0	115	0	0
CH ₂ OHCHO	15	0	0	27	0	0
H ₂ CCO	0	0	0	6	2	1
t-HCOOH	6	0	0	3	1	1

Notes. T is the number of transitions, L is the number of lines in the model with a 3σ detection, and F is the number of unblended lines (i.e., no other line within one FWHM) that are included in the fit.

Table 2.B.6: Number of transitions and lines fitted for B1-bS.

B1-bS						
Species	Band 3			Band 6		
	T	L	F	T	L	F
CH ₃ OH	1	1	0	3	3	0
¹³ CH ₃ OH	2	1	1	8	4	3
CH ₃ ¹⁸ OH	4	0	0	20	13	5
CH ₂ DOH	3	0	0	16	0	0
CH ₃ CH ₂ OH	12	0	0	30	0	0
CH ₃ CHO	17	2	2	27	3	2
CH ₃ OCHO	34	8	8	111	10	7
CH ₃ OCH ₃	16	6	6	112	63	60
CH ₃ COCH ₃	59	0	0	128	1	1
aGg'(CH ₂ OH) ₂	25	0	0	0	0	0
gGg'(CH ₂ OH) ₂	43	0	0	0	0	0
CH ₂ OHCHO	15	0	0	0	0	0
H ₂ CCO	0	0	0	6	1	1
t-HCOOH	6	0	0	3	0	0

Notes. T is the number of transitions, L is the number of lines in the model with a 3σ detection, and F is the number of unblended lines (i.e., no other line within one FWHM) that are included in the fit.

Table 2.B.7: Computed column densities and abundance ratios for B1-c in Band 3, assuming $T_{\text{ex}} = 100$ K.

B1-c			
Species	Band 3		
	T_{ex} (K)	N (cm ⁻²)	X/CH ₃ OH (%)
CH ₃ OH	–	$(6.7 \pm 1.1) \times 10^{17}$	$\equiv 100$
¹³ CH ₃ OH	[100]	$(9.6 \pm 1.6) \times 10^{15}$	$\equiv 1.43$
CH ₃ ¹⁸ OH	[100]	$< 2.2 \times 10^{16}$	< 3.4
CH ₂ DOH	[100]	$(5.7 \pm 0.7) \times 10^{16}$	8.4 ± 1.7
CH ₃ CH ₂ OH	[100]	$(1.8 \pm 0.2) \times 10^{16}$	2.7 ± 0.5
CH ₃ CHO	[100]	$(4.7 \pm 1.6) \times 10^{15}$	0.7 ± 0.3
CH ₃ OCHO	[100]	$(1.6 \pm 0.2) \times 10^{16}$	2.4 ± 0.5
CH ₃ OCH ₃	[100]	$(1.9 \pm 0.1) \times 10^{16}$	2.8 ± 0.5
CH ₃ COCH ₃	[100]	$< 5.0 \times 10^{16}$	< 7.5
aGg'(CH ₂ OH) ₂	[100]	$< 2.1 \times 10^{16}$	< 3.2
gGg'(CH ₂ OH) ₂	[100]	$< 2.1 \times 10^{16}$	< 3.2
CH ₂ OHCHO	[100]	$< 8.0 \times 10^{15}$	< 1.2
t-HCOOH	[100]	$(4.3 \pm 0.7) \times 10^{15}$	0.6 ± 0.2

Notes. The column density of CH₃OH is determined by scaling ¹³CH₃OH using ¹²C/¹³C = 70. A value between squared brackets means the parameter was fixed to that value during the computation. Abundance ratios which are set to their respective isotope ratio are indicated with a \equiv symbol.

Table 2.B.8: Computed column densities and abundance ratios for S68N in Band 3, assuming $T_{\text{ex}} = 100$ K.

S68N			
Species	Band 3		
	T_{ex} (K)	N (cm^{-2})	X/ CH_3OH (%)
CH_3OH	–	$(2.1 \pm 0.7) \times 10^{17}$	$\equiv 100$
$^{13}\text{CH}_3\text{OH}$	[100]	$(3.0 \pm 1.0) \times 10^{15}$	$\equiv 1.43$
$\text{CH}_3^{18}\text{OH}$	[100]	$< 2.0 \times 10^{16}$	< 9.8
CH_2DOH	[100]	$< 1.0 \times 10^{17}$	< 49
$\text{CH}_3\text{CH}_2\text{OH}$	[100]	$< 2.0 \times 10^{16}$	< 9.8
CH_3CHO	[100]	$< 2.9 \times 10^{14}$	< 0.14
CH_3OCHO	[100]	$(4.7 \pm 0.3) \times 10^{15}$	2.3 ± 0.8
CH_3OCH_3	[100]	$(6.0 \pm 0.3) \times 10^{15}$	2.9 ± 1.0
CH_3COCH_3	[100]	$< 5.0 \times 10^{16}$	< 25
$\text{aGg}'(\text{CH}_2\text{OH})_2$	[100]	$< 4.3 \times 10^{16}$	< 21
$\text{gGg}'(\text{CH}_2\text{OH})_2$	[100]	$< 4.3 \times 10^{16}$	< 21
CH_2OHCHO	[100]	$< 1.6 \times 10^{16}$	< 7.8
t-HCOOH	[100]	$< 5.0 \times 10^{15}$	< 2.5

Notes. The column density of CH_3OH is determined by scaling $^{13}\text{CH}_3\text{OH}$ using $^{12}\text{C}/^{13}\text{C} = 70$. A value between squared brackets means the parameter was fixed to that value during the computation. Abundance ratios which are set to their respective isotope ratio are indicated with a \equiv symbol.

Table 2.B.9: Computed column densities and abundance ratios for B1-bS in Band 3, assuming $T_{\text{ex}} = 100$ K.

B1-bS			
Species	Band 3		
	T_{ex} (K)	N (cm^{-2})	X/ CH_3OH (%)
CH_3OH	–	$(1.1 \pm 0.3) \times 10^{17}$	$\equiv 100$
$^{13}\text{CH}_3\text{OH}$	[100]	$(1.6 \pm 0.4) \times 10^{15}$	$\equiv 1.43$
$\text{CH}_3^{18}\text{OH}$	[100]	$< 1.0 \times 10^{16}$	< 8.9
CH_2DOH	[100]	$< 2.0 \times 10^{16}$	< 18
$\text{CH}_3\text{CH}_2\text{OH}$	[100]	$< 2.0 \times 10^{16}$	< 18
CH_3CHO	[100]	$(1.4 \pm 0.2) \times 10^{15}$	1.2 ± 0.3
CH_3OCHO	[100]	$(5.7 \pm 0.7) \times 10^{15}$	5.0 ± 1.3
CH_3OCH_3	[100]	$(1.2 \pm 0.1) \times 10^{16}$	11 ± 3
CH_3COCH_3	[100]	$< 1.0 \times 10^{16}$	< 8.9
$\text{aGg}'(\text{CH}_2\text{OH})_2$	[100]	$< 1.1 \times 10^{16}$	< 9.6
$\text{gGg}'(\text{CH}_2\text{OH})_2$	[100]	$< 2.1 \times 10^{16}$	< 19
CH_2OHCHO	[100]	$< 8.0 \times 10^{15}$	< 7.2
t-HCOOH	[100]	$< 1.0 \times 10^{16}$	< 8.9

Notes. The column density of CH_3OH is determined by scaling $^{13}\text{CH}_3\text{OH}$ using $^{12}\text{C}/^{13}\text{C} = 70$. A value between squared brackets means the parameter was fixed to that value during the computation. Abundance ratios which are set to their respective isotope ratio are indicated with a \equiv symbol.

2.C Full ALMA Band 6 spectra

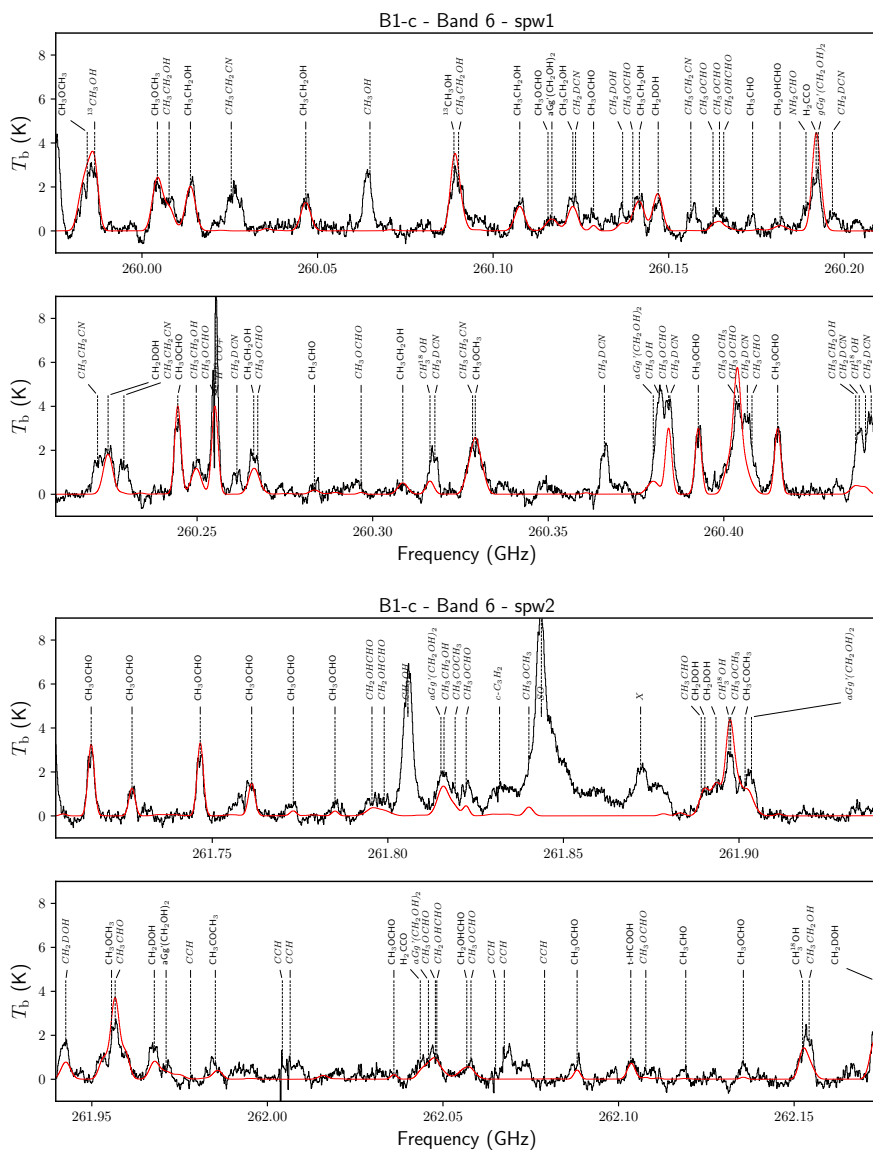
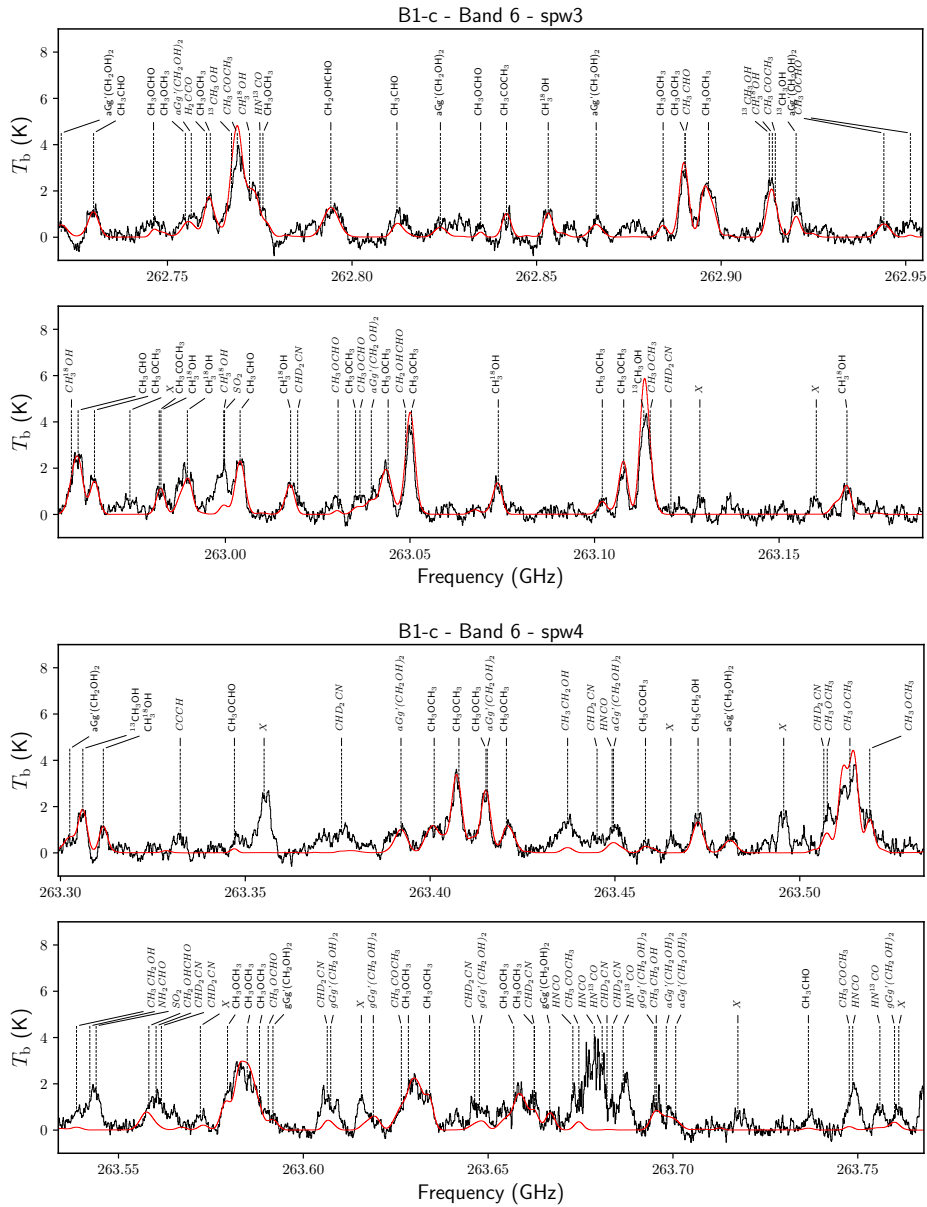


Figure 2.C.1: Full Band 6 spectrum of B1-c (black) with best fitting CASSIS model overplotted (red). We indicate the positions of species, where lines in italic are excluded in the fitting. Lines annotated with an ‘X’ are unidentified.



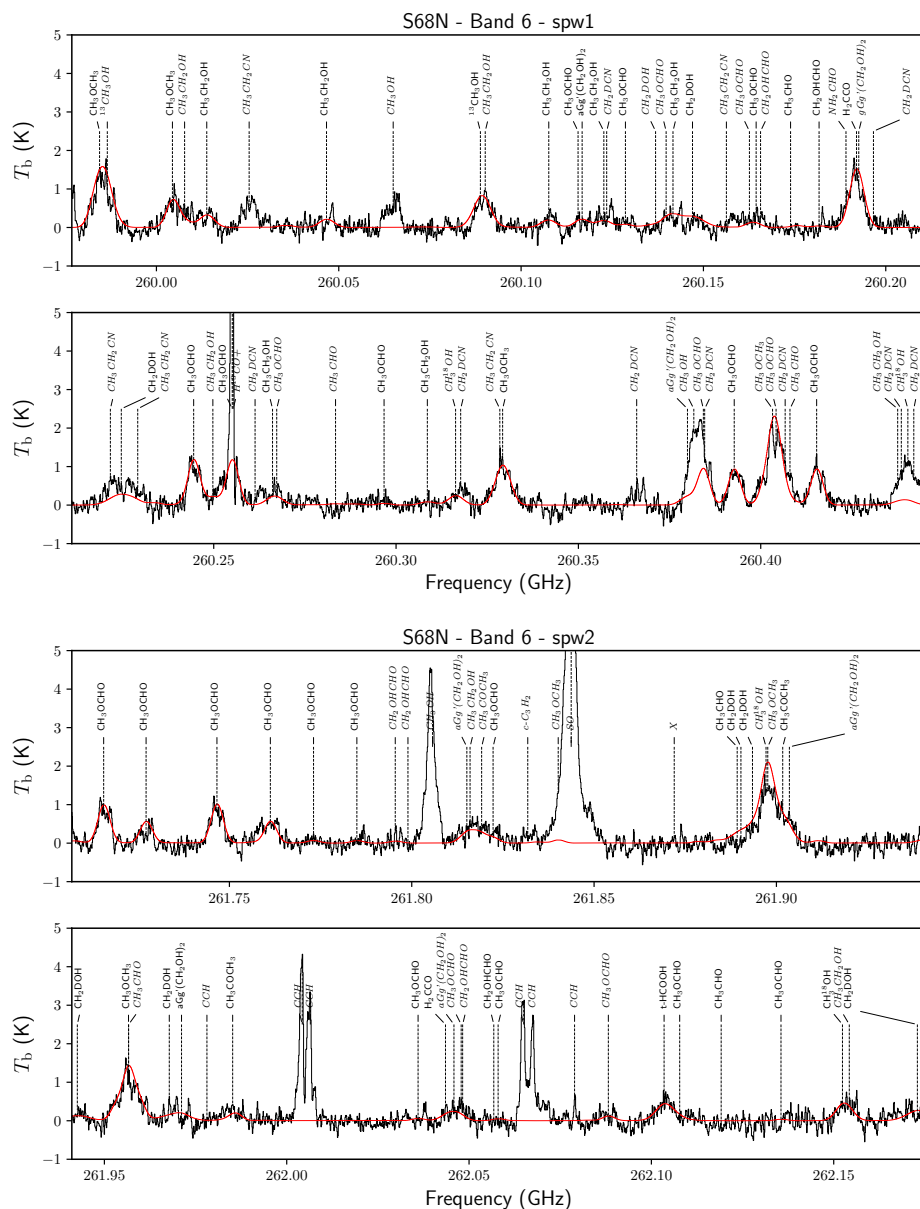


Figure 2.C.2: Same as Fig. 2.C.1 but now for S68N.

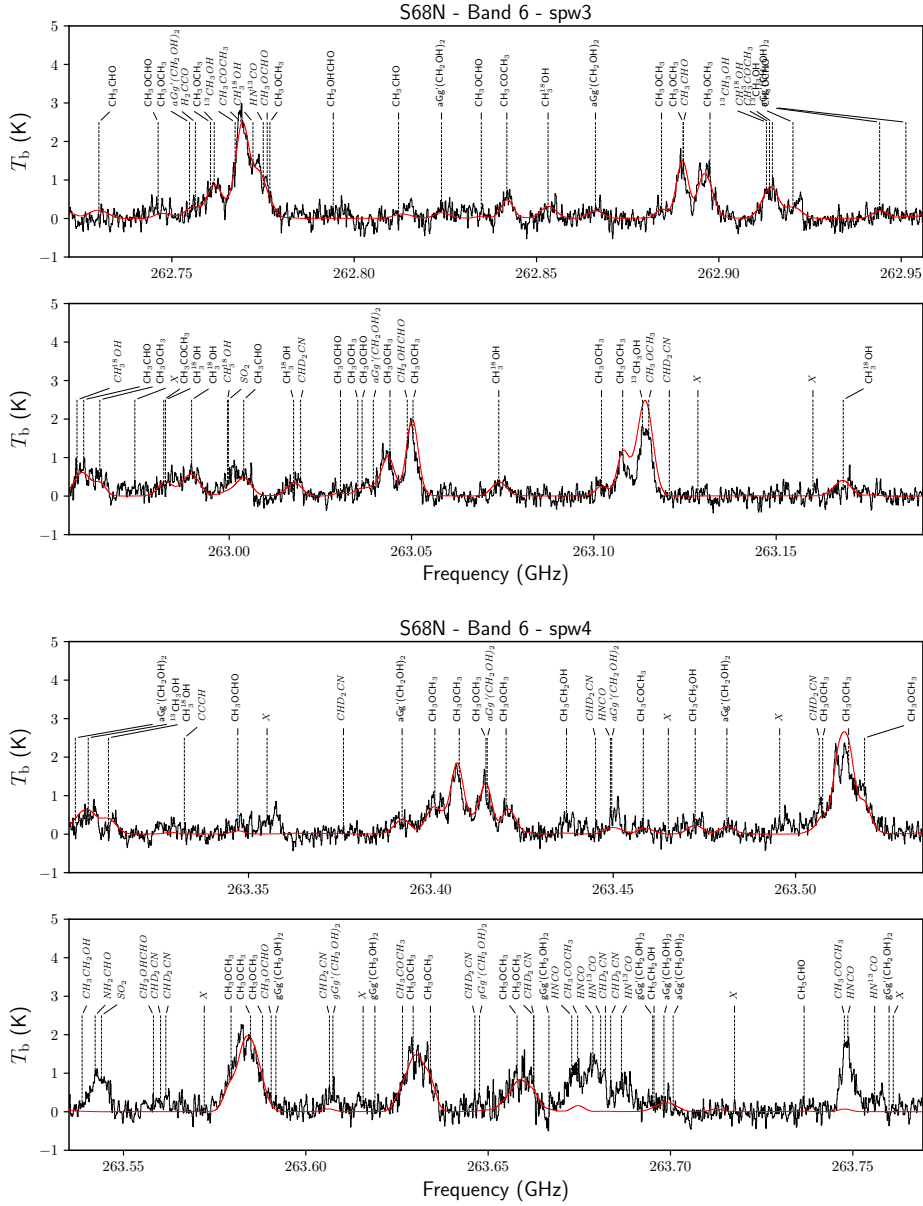
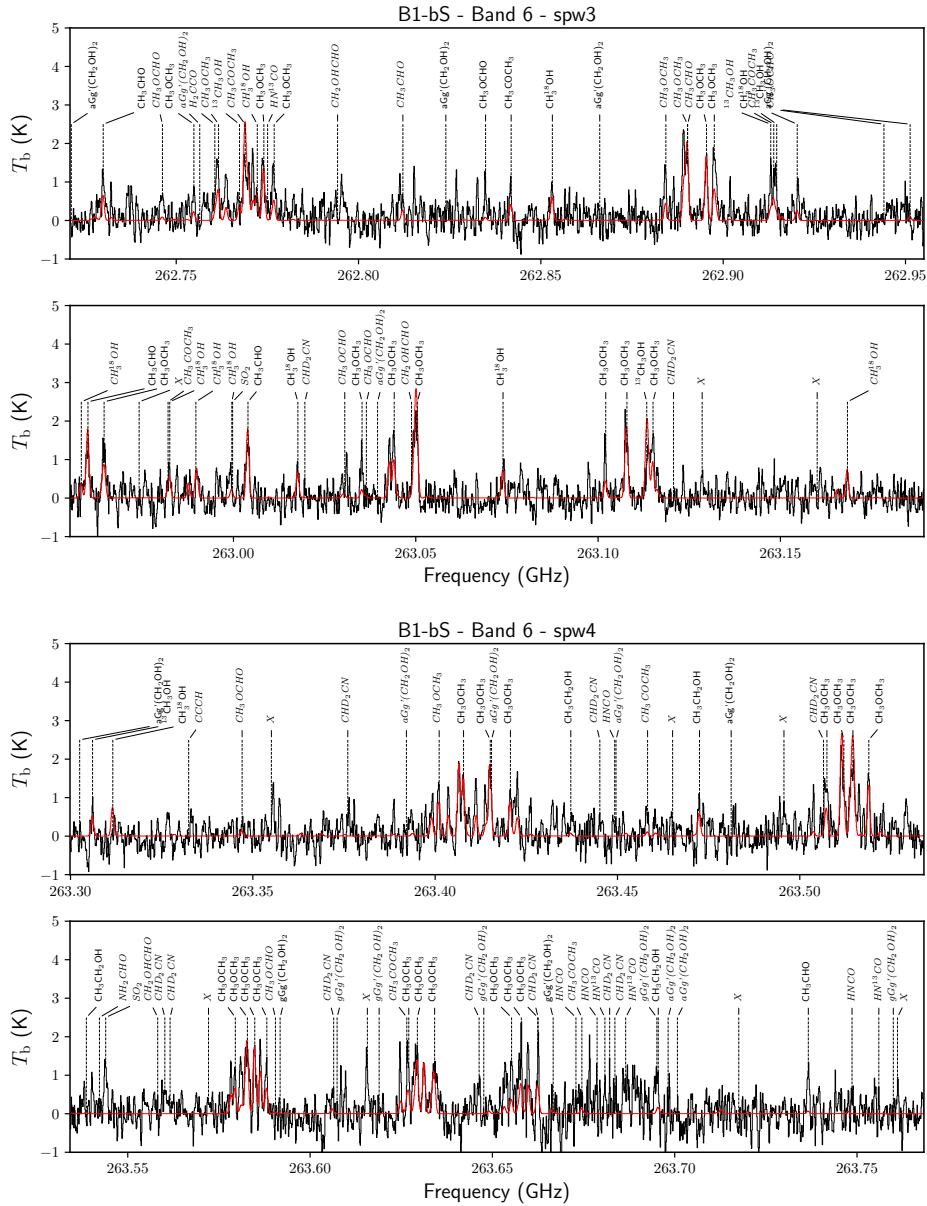


Figure 2.C.2: (Continued)



2.D B1-c Band 3 spectrum

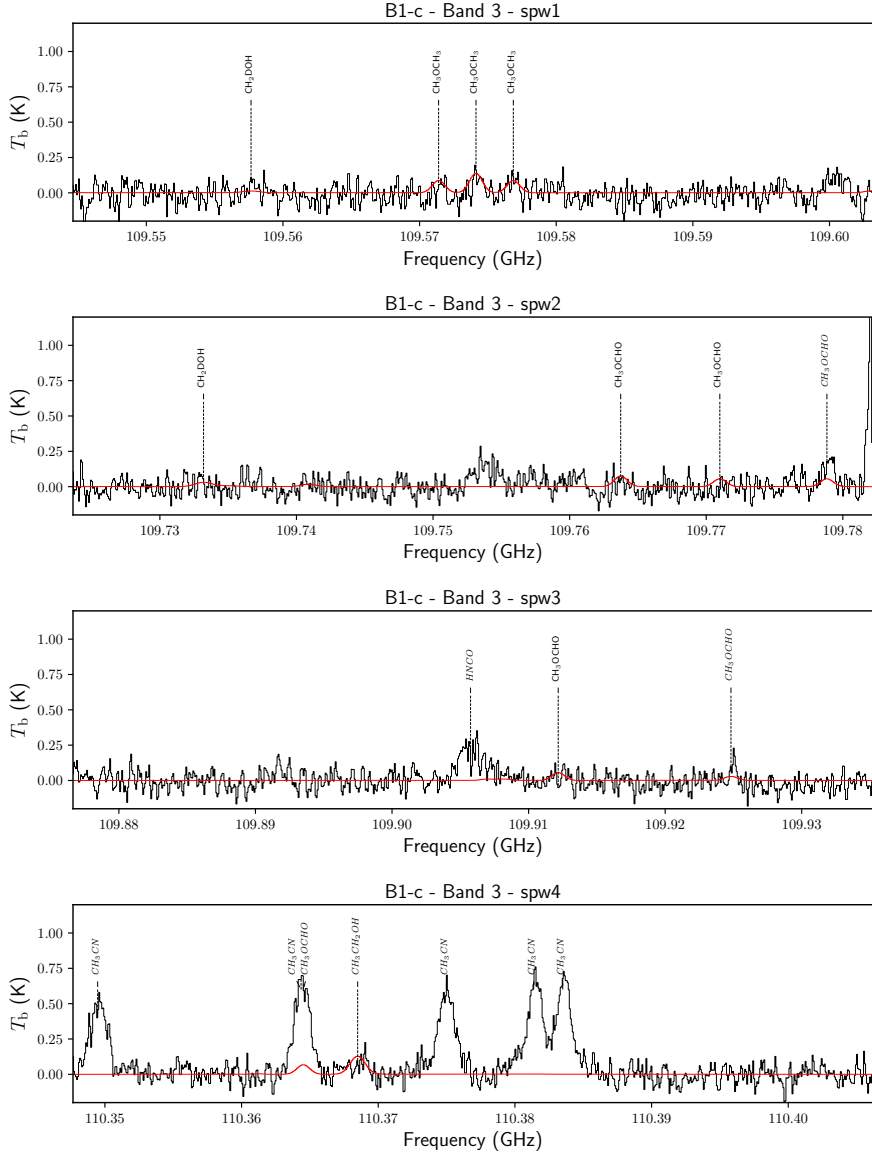


Figure 2.D.1: Full Band 3 spectrum of B1-c (black) with best fitting CASSIS model overplotted (red). We indicate the positions of species, where lines in *italic* are excluded in the fitting.

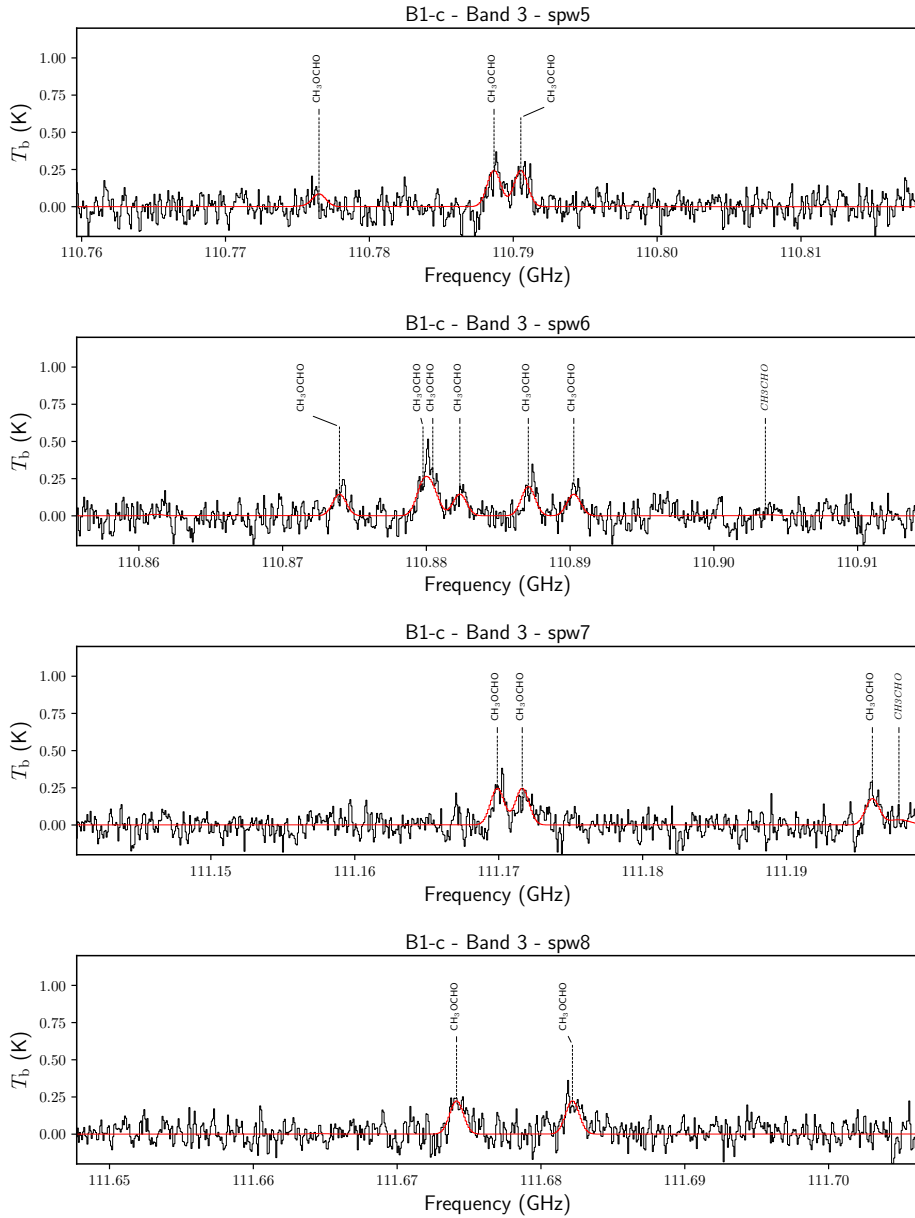


Figure 2.D.1: (Continued)

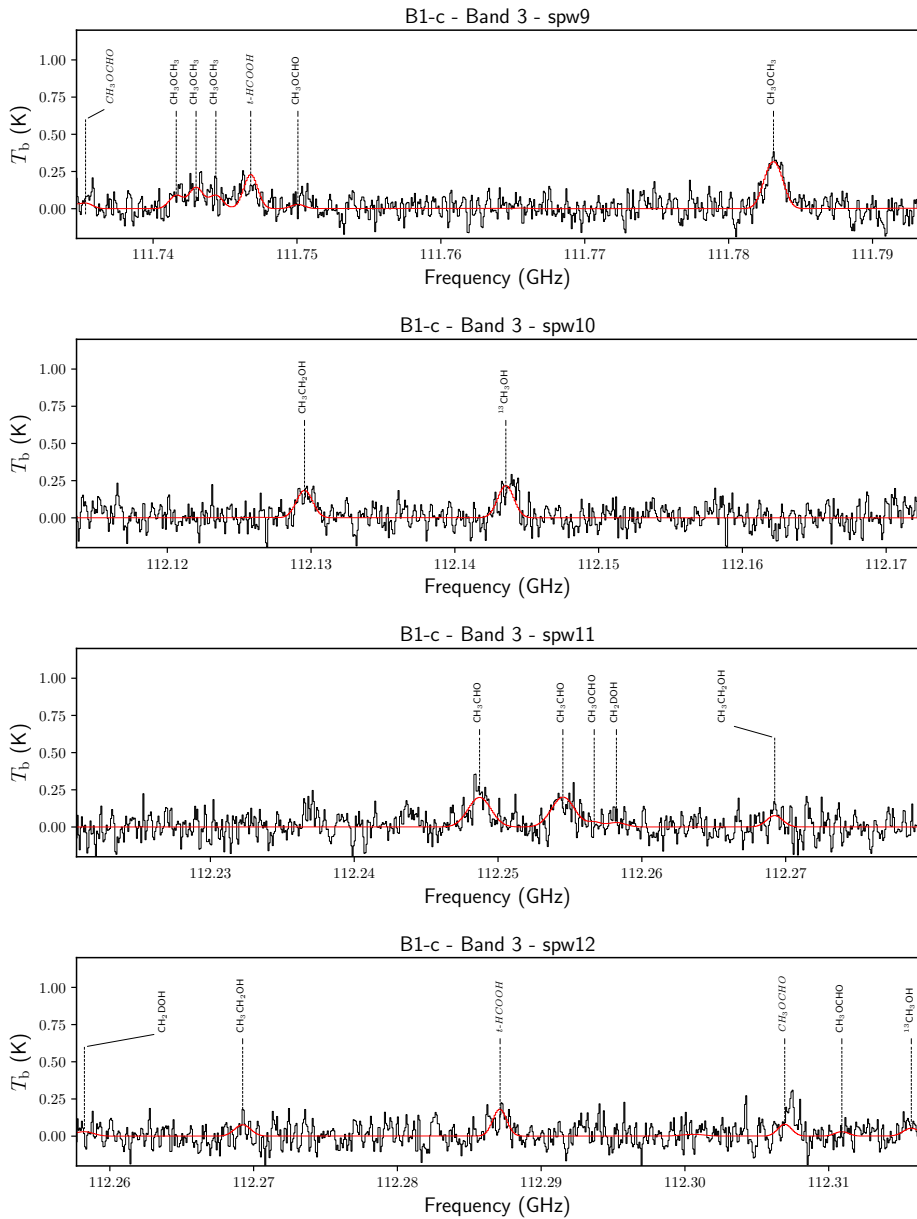


Figure 2.D.1: (Continued)

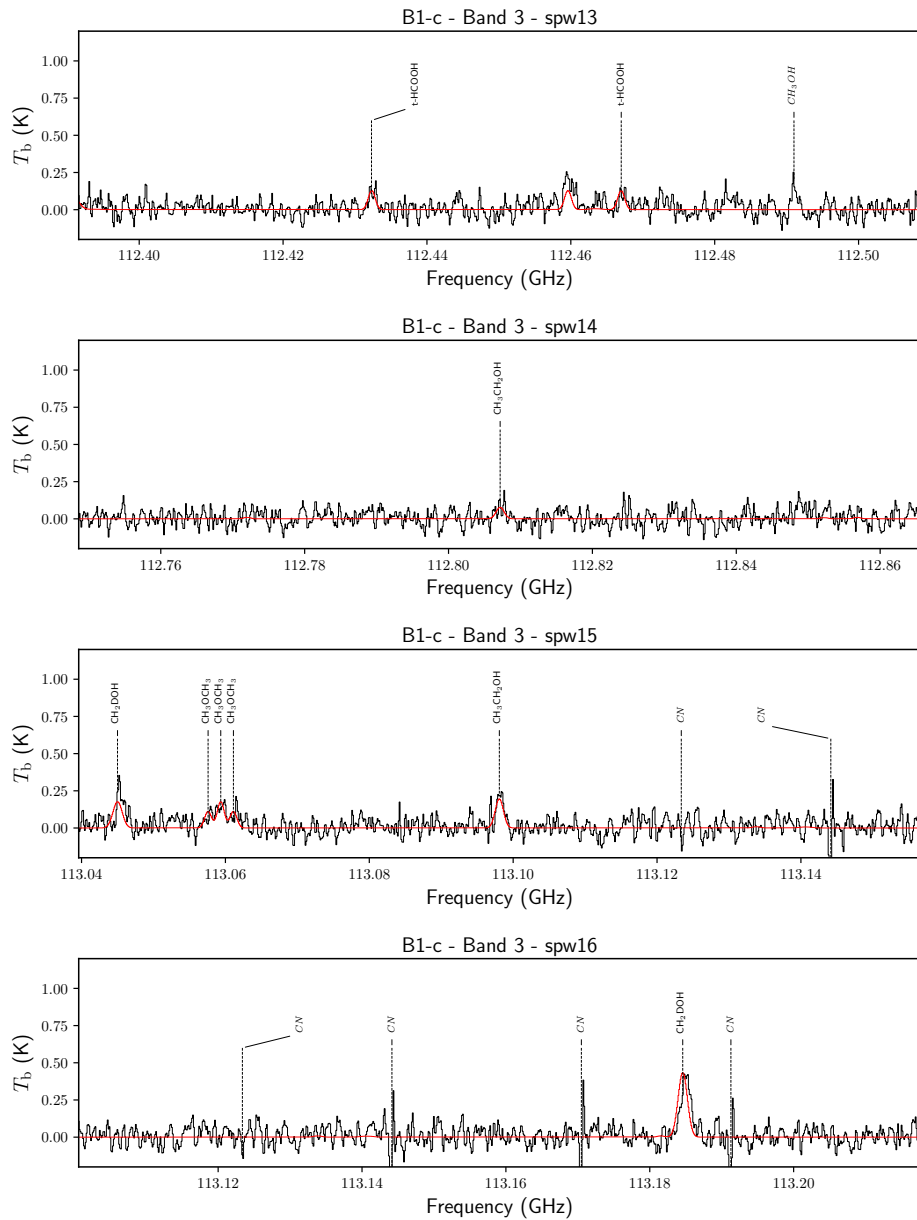


Figure 2.D.1: (Continued)

2.E Additional tables

Table 2.E.1: Lines per species used for fitting the Band 3 data.

Species	Transition		Frequency (GHz)	A_{ij} (s^{-1})	E_{up} (K)
	(J K L M)	- J K L M)			
$^{13}\text{CH}_3\text{OH}$	3 1 3 +0	- 4 0 4 +0	112.1435	7.1×10^{-6}	28.0
	17 -2 16 0	- 17 1 16 0	112.3157	2.1×10^{-6}	373.0
$\text{CH}_3^{18}\text{OH}$	21 3 18 4	- 20 2 18 4	110.9133	5.0×10^{-6}	834.9
	18 1 17 4	- 19 2 17 4	111.6514	1.1×10^{-6}	790.6
	13 3 11 1	- 14 2 13 1	112.3039	2.6×10^{-6}	265.0
	25 0 25 1	- 25 1 25 1	113.0484	1.2×10^{-6}	730.9
CH_2DOH	28 0 28 2	- 28 1 28 1	109.7332	5.3×10^{-6}	878.3
	12 1 11 1	- 12 0 12 1	113.0450	2.5×10^{-6}	185.1
	10 1 9 2	- 10 0 10 2	113.1846	6.2×10^{-6}	141.6
$\text{CH}_3\text{CH}_2\text{OH}$	20 3 17 0	- 19 4 15 1	109.7409	1.5×10^{-6}	245.0
	8 1 8 1	- 8 0 8 0	110.3685	9.5×10^{-6}	91.7
	28 9 19 1	- 27 10 17 0	110.7978	1.0×10^{-6}	498.5
	28 9 20 1	- 27 10 18 0	110.7978	1.0×10^{-6}	498.5
	12 3 9 2	- 12 2 10 2	112.1295	8.4×10^{-6}	77.1
	9 1 8 0	- 8 0 8 1	112.2692	5.2×10^{-6}	96.5
	11 3 9 1	- 10 4 7 0	112.7463	1.1×10^{-6}	127.5
	2 2 1 2	- 1 1 0 2	112.8072	1.1×10^{-5}	7.5
	45 5 41 1	- 45 4 41 0	112.8196	5.0×10^{-6}	954.0
	28 5 24 0	- 27 6 22 1	113.0453	1.6×10^{-6}	426.0
	10 2 9 2	- 10 1 10 2	113.0981	8.8×10^{-6}	51.0
	31 1 31 0	- 30 2 29 1	113.1338	2.3×10^{-6}	449.9
CH_3CHO	17 4 13 6	- 18 3 16 6	109.5448	1.5×10^{-6}	570.8
	20 6 14 2	- 21 5 16 2	109.7350	1.2×10^{-6}	275.5
	34 9 25 3	- 35 8 28 3	109.7646	1.2×10^{-6}	937.4
	34 9 26 3	- 35 8 27 3	109.7657	1.2×10^{-6}	937.4
	23 3 21 1	- 22 4 18 2	110.9036	1.3×10^{-6}	275.9
	13 1 12 0	- 13 0 13 0	111.1978	5.0×10^{-6}	88.4
	15 1 15 7	- 14 1 13 8	111.7924	2.2×10^{-6}	489.6
	18 2 16 8	- 18 2 17 7	112.1263	2.4×10^{-6}	555.7
	6 1 6 0	- 5 1 5 0	112.2487	4.5×10^{-5}	21.1
	6 1 6 1	- 5 1 5 1	112.2545	4.5×10^{-5}	21.2
	6 1 5 6	- 6 0 6 6	112.3004	9.9×10^{-6}	392.2
	6 1 6 3	- 5 1 5 3	112.3908	4.6×10^{-5}	227.6
	14 5 10 4	- 15 4 11 5	112.3939	1.1×10^{-6}	358.6
	15 5 11 0	- 16 4 12 0	112.4634	1.2×10^{-6}	167.5
	27 3 24 8	- 27 3 25 7	112.8593	1.7×10^{-6}	755.2
	6 1 6 6	- 5 1 5 6	113.0365	4.4×10^{-5}	391.0
	15 5 10 2	- 16 4 13 1	113.1407	1.2×10^{-6}	167.4

Table 2.E.1: continued.

Species	Transition						Frequency (GHz)	A_{ij} (s ⁻¹)	E_{up} (K)
	(J K L M	-	J K L M)						
CH ₃ OCHO	10 0 10 5	-	9 1 9 4			109.6030	2.7×10^{-6}	217.2	
	9 6 3 3	-	8 6 2 3			109.6085	1.1×10^{-5}	238.2	
	9 6 4 3	-	8 6 3 3			109.6085	1.1×10^{-5}	238.2	
	9 3 7 3	-	8 3 6 3			109.7637	1.7×10^{-5}	220.2	
	9 5 5 3	-	8 5 4 3			109.7710	1.3×10^{-5}	230.8	
	9 5 4 3	-	8 5 3 3			109.7788	1.3×10^{-5}	230.8	
	15 4 12 3	-	15 3 13 3			109.9070	1.9×10^{-6}	269.0	
	28 6 22 5	-	28 5 23 5			109.9082	2.7×10^{-6}	455.2	
	9 5 4 5	-	8 5 3 5			109.9122	1.3×10^{-5}	230.6	
	9 7 3 4	-	8 7 2 4			109.9248	7.7×10^{-6}	246.1	
	9 4 5 5	-	8 4 4 5			110.3645	1.6×10^{-5}	224.6	
	9 1 8 3	-	8 1 7 3			110.7765	1.9×10^{-5}	215.7	
	10 1 10 1	-	9 1 9 1			110.7887	2.0×10^{-5}	30.3	
	10 1 10 0	-	9 1 9 0			110.7905	2.0×10^{-5}	30.3	
	15 4 12 4	-	15 3 13 4			110.8612	1.8×10^{-6}	268.6	
	9 5 4 2	-	8 5 3 2			110.8740	1.4×10^{-5}	43.2	
	9 3 7 1	-	8 3 6 1			110.8798	1.8×10^{-5}	32.6	
	9 5 5 0	-	8 5 4 0			110.8804	1.4×10^{-5}	43.2	
	9 5 5 1	-	8 5 4 1			110.8823	1.4×10^{-5}	43.2	
	9 3 7 0	-	8 3 6 0			110.8871	1.8×10^{-5}	32.6	
	9 5 4 0	-	8 5 3 0			110.8903	1.4×10^{-5}	43.2	
	10 0 10 2	-	9 0 9 2			111.1699	2.0×10^{-5}	30.2	
	10 0 10 0	-	9 0 9 0			111.1716	2.0×10^{-5}	30.2	
	9 4 6 0	-	8 4 5 0			111.1960	1.6×10^{-5}	37.2	
	9 1 8 2	-	8 1 7 2			111.6741	2.0×10^{-5}	28.1	
	9 1 8 0	-	8 1 7 0			111.6822	2.0×10^{-5}	28.1	
	23 6 17 3	-	23 5 18 3			111.7071	2.6×10^{-6}	375.2	
	10 1 10 1	-	9 0 9 2			111.7340	3.0×10^{-6}	30.3	
	10 1 10 0	-	9 0 9 0			111.7353	3.0×10^{-6}	30.3	
	28 6 22 0	-	28 5 23 0			111.7501	2.8×10^{-6}	269.8	
	25 5 20 2	-	25 4 21 2			112.2567	2.5×10^{-6}	214.4	
	9 3 6 3	-	8 3 5 3			112.3069	1.8×10^{-5}	220.5	
	25 5 20 0	-	25 4 21 0			112.3109	2.5×10^{-6}	214.4	
	16 2 14 3	-	16 1 15 3			113.1815	1.5×10^{-6}	272.4	
CH ₃ OCH ₃	8 2 7 3	-	8 1 8 3			109.5714	5.4×10^{-6}	38.3	
	8 2 7 5	-	8 1 8 5			109.5714	5.4×10^{-6}	38.3	
	8 2 7 1	-	8 1 8 1			109.5741	5.4×10^{-6}	38.3	
	8 2 7 0	-	8 1 8 0			109.5769	5.4×10^{-6}	38.3	
	19 3 16 3	-	19 2 17 3			111.7416	1.1×10^{-5}	187.5	
	19 3 16 5	-	19 2 17 5			111.7416	1.1×10^{-5}	187.5	
	19 3 16 1	-	19 2 17 1			111.7430	1.1×10^{-5}	187.5	
	19 3 16 0	-	19 2 17 0			111.7444	1.1×10^{-5}	187.5	

Table 2.E.1: continued.

Species	Transition						Frequency (GHz)	A_{ij} (s ⁻¹)	E_{up} (K)
	(J K L M	-	J K L M)						
	7 0 7 0	-	6 1 6 0			111.7826	7.4×10^{-6}	25.2	
	7 0 7 1	-	6 1 6 1			111.7831	7.4×10^{-6}	25.2	
	7 0 7 5	-	6 1 6 5			111.7836	7.4×10^{-6}	25.3	
	7 0 7 3	-	6 1 6 3			111.7836	7.4×10^{-6}	25.3	
	17 3 14 5	-	17 2 15 5			113.0576	1.1×10^{-5}	153.1	
	17 3 14 3	-	17 2 15 3			113.0576	1.1×10^{-5}	153.1	
	17 3 14 1	-	17 2 15 1			113.0594	1.1×10^{-5}	153.1	
	17 3 14 0	-	17 2 15 0			113.0611	1.1×10^{-5}	153.1	
CH ₃ COCH ₃	32 23 10 1	-	32 22 11 1			109.6011	3.5×10^{-5}	444.0	
	32 23 10 1	-	32 22 11 2			109.6030	3.4×10^{-5}	444.0	
	9 6 3 1	-	8 7 2 2			109.9047	1.4×10^{-6}	37.3	
	26 21 6 0	-	26 20 7 1			110.3754	2.6×10^{-5}	306.6	
	29 22 7 0	-	29 21 8 1			110.3788	2.8×10^{-5}	371.8	
	29 22 7 0	-	29 21 8 0			110.3828	3.1×10^{-5}	371.8	
	26 21 5 0	-	26 20 6 1			110.3933	2.6×10^{-5}	306.6	
	6 5 2 0	-	5 4 1 0			110.4013	3.4×10^{-5}	18.2	
	8 4 5 0	-	7 3 4 1			110.4094	3.1×10^{-5}	26.8	
	22 20 3 0	-	22 19 4 1			110.7627	1.6×10^{-5}	232.1	
	42 25 17 0	-	42 24 18 1			110.7636	5.9×10^{-5}	732.4	
	47 31 16 1	-	47 30 17 1			110.7727	4.4×10^{-5}	928.6	
	38 25 14 0	-	38 24 15 1			110.8606	5.2×10^{-5}	609.5	
	8 4 4 0	-	7 5 3 0			110.9171	1.6×10^{-5}	28.4	
	8 4 4 1	-	7 5 3 2			111.1413	1.6×10^{-5}	28.6	
	37 25 13 0	-	37 24 14 1			111.6404	4.9×10^{-5}	581.8	
	37 25 13 1	-	37 24 14 2			111.6834	4.1×10^{-5}	581.7	
	14 10 4 0	-	14 7 7 1			111.6931	1.8×10^{-6}	88.0	
	24 11 13 1	-	24 10 14 1			111.7369	3.2×10^{-5}	230.4	
	24 11 13 1	-	24 10 14 2			111.7372	3.2×10^{-5}	230.4	
	14 10 4 0	-	14 7 7 0			111.7505	1.9×10^{-6}	87.9	
	24 12 13 1	-	24 11 14 1			111.7591	3.2×10^{-5}	230.4	
	24 12 13 1	-	24 11 14 2			111.7593	3.2×10^{-5}	230.4	
	24 11 13 0	-	24 10 14 1			111.7973	3.2×10^{-5}	230.4	
	37 25 13 1	-	37 24 14 1			111.7996	4.2×10^{-5}	581.7	
	34 24 11 0	-	34 23 12 1			112.1478	4.1×10^{-5}	497.9	
	31 18 14 0	-	31 17 15 0			112.1507	3.9×10^{-5}	396.7	
	34 24 11 0	-	34 23 12 0			112.1546	3.9×10^{-5}	497.9	
	31 18 14 0	-	31 17 15 1			112.1592	4.0×10^{-5}	396.6	
	31 18 14 1	-	31 17 15 2			112.1677	3.9×10^{-5}	396.6	
	31 18 14 1	-	31 17 15 1			112.1684	3.9×10^{-5}	396.6	
	45 27 18 1	-	45 26 19 1			112.1796	4.6×10^{-5}	840.2	
	21 20 1 0	-	21 19 2 1			112.2312	1.1×10^{-5}	216.8	
	21 20 2 0	-	21 19 3 1			112.3046	1.2×10^{-5}	216.7	

Table 2.E.1: continued.

Species	Transition						Frequency (GHz)	A_{ij} (s ⁻¹)	E_{up} (K)
	(J K L M	-	J K L M)						
	45 30 15 0	-	45 29 16 0			112.4518	4.5×10^{-5}	854.0	
	6 5 1 1	-	5 4 1 2			112.4951	1.4×10^{-5}	18.5	
	38 24 15 0	-	38 23 16 0			112.5018	4.4×10^{-5}	604.2	
	23 10 13 1	-	23 9 14 1			112.7549	3.1×10^{-5}	209.3	
	23 10 13 1	-	23 9 14 2			112.7551	3.1×10^{-5}	209.3	
	23 11 13 1	-	23 10 14 1			112.7621	3.1×10^{-5}	209.3	
	23 11 13 1	-	23 10 14 2			112.7622	3.1×10^{-5}	209.3	
	25 21 4 0	-	25 20 5 1			112.8283	2.4×10^{-5}	288.2	
	23 10 13 0	-	23 9 14 1			112.8310	3.2×10^{-5}	209.3	
	31 23 8 1	-	31 22 9 2			112.8320	2.7×10^{-5}	421.0	
	23 11 13 0	-	23 10 14 1			112.8382	3.2×10^{-5}	209.3	
	25 21 5 0	-	25 20 6 1			112.8397	2.4×10^{-5}	288.2	
	31 23 8 0	-	31 22 9 1			112.8422	2.7×10^{-5}	421.0	
	45 27 18 0	-	45 26 19 0			112.8627	4.7×10^{-5}	840.3	
	31 23 8 0	-	31 22 9 0			112.8694	3.5×10^{-5}	421.1	
	37 23 15 0	-	37 22 16 1			113.0468	5.3×10^{-5}	571.2	
	25 21 4 0	-	25 20 5 0			113.0648	2.4×10^{-5}	288.3	
	25 21 5 0	-	25 20 6 0			113.0707	2.4×10^{-5}	288.3	
	39 25 15 0	-	39 24 16 0			113.0911	4.5×10^{-5}	638.0	
	37 23 15 1	-	37 22 16 2			113.1143	4.4×10^{-5}	571.2	
	37 23 15 1	-	37 22 16 1			113.1226	4.4×10^{-5}	571.2	
	20 20 0 1	-	20 19 1 2			113.1584	6.2×10^{-6}	202.2	
	45 30 15 0	-	45 29 16 1			113.2046	6.6×10^{-5}	854.0	
	10 7 3 0	-	9 8 1 1			113.2057	1.2×10^{-6}	45.9	
	31 23 9 1	-	31 22 10 2			113.2179	2.7×10^{-5}	421.0	
aGg ⁺ (CH ₂ OH) ₂	18 6 13 0	-	18 5 14 0			109.5468	3.6×10^{-6}	102.0	
	45 9 36 1	-	45 8 37 1			109.7212	5.9×10^{-6}	555.5	
	25 7 19 1	-	24 8 16 1			109.7295	1.0×10^{-6}	184.8	
	27 7 20 1	-	27 6 21 1			109.7364	4.3×10^{-6}	211.3	
	23 6 18 1	-	22 7 15 1			109.7545	1.2×10^{-6}	154.4	
	10 1 9 1	-	9 1 8 0			109.7605	2.4×10^{-5}	28.5	
	16 6 11 0	-	16 5 12 0			110.4055	3.5×10^{-6}	84.7	
	15 6 10 1	-	15 5 11 1			110.8540	3.8×10^{-6}	77.1	
	23 4 20 1	-	23 3 21 1			111.6959	2.7×10^{-6}	144.1	
	11 6 5 1	-	11 5 6 1			112.1232	3.4×10^{-6}	50.5	
	11 6 6 0	-	11 5 7 0			112.1340	3.1×10^{-6}	50.1	
	11 6 6 1	-	11 5 7 1			112.1506	3.4×10^{-6}	50.5	
	46 9 37 0	-	46 8 38 0			112.2790	6.0×10^{-6}	578.7	
	10 6 4 0	-	10 5 5 0			112.3116	2.9×10^{-6}	44.7	
	9 6 3 0	-	9 5 4 0			112.4602	2.7×10^{-6}	39.8	
	9 6 4 0	-	9 5 5 0			112.4637	2.7×10^{-6}	39.8	
	9 6 3 1	-	9 5 4 1			112.4783	2.9×10^{-6}	40.1	

Table 2.E.1: continued.

Species	Transition						Frequency (GHz)	A_{ij} (s ⁻¹)	E_{up} (K)
	(J K L M	-	J K L M)						
	9 6 4 1	-	9 5 5 1			112.4818	2.9×10^{-6}	40.1	
	25 6 20 0	-	25 5 21 0			112.8157	4.5×10^{-6}	178.4	
	10 2 9 1	-	9 1 8 1			112.8355	1.2×10^{-6}	29.0	
	10 2 9 0	-	9 1 8 0			113.0314	1.1×10^{-5}	28.7	
	27 7 21 1	-	27 6 21 0			113.0501	2.6×10^{-6}	211.2	
	19 1 18 1	-	19 0 19 1			113.1029	1.3×10^{-6}	92.8	
	42 9 33 1	-	42 8 34 1			113.1433	6.0×10^{-6}	488.4	
	19 1 18 0	-	19 0 19 0			113.1609	1.3×10^{-6}	92.4	
gGg'(CH ₂ OH) ₂	46 9 37 0	-	46 8 38 0			109.5531	1.1×10^{-5}	574.1	
	39 7 32 1	-	39 6 33 1			109.5776	9.8×10^{-6}	412.0	
	46 9 37 1	-	46 8 38 1			109.6094	1.1×10^{-5}	574.1	
	35 8 27 0	-	35 7 28 0			109.7473	9.8×10^{-6}	341.1	
	24 6 19 0	-	24 5 20 0			109.7560	8.3×10^{-6}	164.8	
	24 6 19 1	-	24 5 20 1			109.7601	8.0×10^{-6}	164.8	
	27 8 20 1	-	26 9 18 0			109.8720	1.9×10^{-6}	216.3	
	27 7 20 0	-	27 6 21 0			109.8996	8.2×10^{-6}	209.4	
	15 6 10 1	-	15 5 10 0			110.3408	7.0×10^{-6}	76.2	
	13 6 8 1	-	13 5 9 1			110.3980	6.9×10^{-6}	62.0	
	25 7 18 1	-	24 8 17 1			110.4062	2.0×10^{-6}	183.2	
	19 2 18 1	-	19 1 19 1			110.7957	2.4×10^{-6}	92.0	
	19 2 18 0	-	19 1 19 0			110.7993	2.6×10^{-6}	91.9	
	11 6 5 1	-	11 5 6 1			110.8835	6.5×10^{-6}	49.8	
	11 6 5 0	-	11 5 6 0			110.8971	6.4×10^{-6}	49.7	
	11 5 7 0	-	10 5 6 1			110.9012	9.7×10^{-6}	44.4	
	11 6 6 1	-	11 5 7 1			110.9086	6.5×10^{-6}	49.8	
	15 6 9 1	-	15 5 11 0			110.9138	5.7×10^{-6}	76.2	
	11 5 6 0	-	10 5 5 1			110.9170	9.7×10^{-6}	44.4	
	6 3 3 1	-	5 2 3 0			111.7594	6.9×10^{-6}	14.7	
	11 6 6 1	-	11 5 6 0			112.1434	5.8×10^{-6}	49.8	
	12 0 12 0	-	11 0 11 1			112.1530	9.4×10^{-6}	36.1	
	40 9 32 0	-	40 8 32 1			112.1613	5.8×10^{-6}	442.2	
	11 6 5 1	-	11 5 7 0			112.1696	5.8×10^{-6}	49.8	
	20 4 17 1	-	19 5 15 0			112.2534	2.4×10^{-6}	110.7	
	7 2 6 1	-	6 1 6 0			112.4572	5.4×10^{-6}	15.6	
	9 6 4 1	-	9 5 4 0			112.5023	5.2×10^{-6}	39.5	
	9 6 3 1	-	9 5 5 0			112.5055	5.2×10^{-6}	39.5	
	6 6 1 1	-	6 5 1 0			112.7433	2.3×10^{-6}	27.8	
	6 6 0 1	-	6 5 2 0			112.7434	2.3×10^{-6}	27.8	
	18 4 14 1	-	17 5 13 1			112.7800	1.5×10^{-6}	92.6	
	8 1 7 1	-	7 0 7 0			112.8301	5.7×10^{-6}	18.7	
	11 8 3 1	-	10 8 2 0			113.0460	6.1×10^{-6}	63.4	
	11 8 4 1	-	10 8 3 0			113.0460	6.1×10^{-6}	63.4	

Table 2.E.1: continued.

Species	Transition		Frequency (GHz)	A_{ij} (s ⁻¹)	E_{up} (K)
	(J K L M - J K L M)				
	23 6 17 0 - 22 7 16 0		113.0973	2.4×10^{-6}	153.1
	12 0 12 1 - 11 1 11 1		113.1070	9.2×10^{-6}	36.2
	23 6 17 1 - 22 7 16 1		113.1093	2.4×10^{-6}	153.1
	12 0 12 0 - 11 1 11 0		113.1156	1.6×10^{-5}	36.1
	11 7 4 1 - 10 7 3 0		113.1237	7.7×10^{-6}	56.1
	11 7 5 1 - 10 7 4 0		113.1237	7.7×10^{-6}	56.1
	26 6 21 0 - 26 5 22 0		113.1609	9.0×10^{-6}	189.9
	26 6 21 1 - 26 5 22 1		113.1851	8.9×10^{-6}	190.0
	47 9 38 0 - 47 8 39 0		113.2009	1.2×10^{-5}	597.8
CH ₂ OHCHO	4 3 1 - 3 2 2		109.8771	2.3×10^{-5}	11.0
	15 3 13 - 15 2 14		110.4025	1.6×10^{-5}	71.8
	45 26 19 - 46 25 22		110.4059	2.2×10^{-6}	984.4
	45 26 20 - 46 25 21		110.4059	2.2×10^{-6}	984.4
	49 18 32 - 48 19 29		111.6495	4.3×10^{-6}	878.4
	49 18 31 - 48 19 30		111.6495	4.3×10^{-6}	878.4
	10 5 5 - 10 4 6		111.7349	2.0×10^{-5}	45.8
	34 21 13 - 35 20 16		112.1106	2.0×10^{-6}	597.9
	34 21 14 - 35 20 15		112.1106	2.0×10^{-6}	597.9
	13 5 9 - 13 4 10		112.1777	2.3×10^{-5}	65.9
	20 6 14 - 20 5 15		112.2480	2.8×10^{-5}	139.6
	11 5 7 - 11 4 8		112.4443	2.2×10^{-5}	51.9
	14 5 10 - 14 4 11		112.4728	2.4×10^{-5}	73.8
	10 5 6 - 10 4 7		112.7734	2.1×10^{-5}	45.8
	9 5 5 - 9 4 6		113.1188	2.0×10^{-5}	40.2
t-HCOOH	5 0 5 - 4 0 4		111.7468	1.4×10^{-5}	16.1
	5 2 4 - 4 2 3		112.2871	1.2×10^{-5}	28.9
	5 4 2 - 4 4 1		112.4323	5.3×10^{-6}	67.1
	5 4 1 - 4 4 0		112.4323	5.3×10^{-6}	67.1
	5 3 3 - 4 3 2		112.4596	9.4×10^{-6}	44.8
	5 3 2 - 4 3 1		112.4670	9.4×10^{-6}	44.8

Table 2.E.2: Lines per species used for fitting the Band 6 data.

Species	Transition		Frequency (GHz)	A_{ij} (s ⁻¹)	E_{up} (K)
	(J K L M - J K L M)				
CH ₃ OH	20 8 13 2 - 21 7 14 2		260.0643	2.1×10^{-5}	808.2
	20 3 18 0 - 20 2 19 0		260.3815	9.1×10^{-5}	536.9
	2 1 1 1 - 1 0 1 1		261.8057	5.6×10^{-5}	28.0
¹³ CH ₃ OH	2 1 1 0 - 1 0 1 0		259.9865	5.5×10^{-5}	27.9
	18 3 16 +0 - 18 2 17 -0		260.0888	9.2×10^{-5}	437.2
	20 3 18 +0 - 20 2 19 -0		262.7673	9.4×10^{-5}	525.4

Table 2.E.2: continued.

Species	Transition		Frequency	A_{ij}	E_{up}
	(J K L M - J K L M)		(GHz)	(s^{-1})	(K)
	7 4 4 -0 - 8 3 5 -0		262.9130	1.7×10^{-5}	144.2
	7 4 3 +0 - 8 3 6 +0		262.9203	1.7×10^{-5}	144.2
	5 2 3 0 - 4 1 3 0		263.1133	7.4×10^{-5}	56.3
	11 2 10 -0 - 10 3 7 -0		263.3060	2.9×10^{-5}	187.3
	25 -7 18 0 - 26 -6 20 0		263.5779	2.8×10^{-5}	996.5
$\text{CH}_3^{18}\text{OH}$	12 2 10 4 - 13 3 10 4		260.0355	7.1×10^{-5}	537.2
	16 3 13 0 - 16 2 14 0		260.3163	9.3×10^{-5}	352.6
	15 1 15 1 - 14 2 13 1		260.4403	2.8×10^{-5}	272.2
	12 3 9 0 - 12 2 10 0		261.8972	9.2×10^{-5}	223.6
	11 3 8 0 - 11 2 9 0		262.1524	9.2×10^{-5}	196.9
	7 3 4 0 - 7 2 5 0		262.7722	8.6×10^{-5}	112.4
	6 3 3 0 - 6 2 4 0		262.8532	8.3×10^{-5}	96.8
	5 3 2 0 - 5 2 3 0		262.9139	7.7×10^{-5}	83.5
	4 3 1 0 - 4 2 2 0		262.9583	6.8×10^{-5}	72.3
	5 3 3 0 - 5 2 4 0		262.9825	7.7×10^{-5}	83.5
	4 3 2 0 - 4 2 3 0		262.9878	6.8×10^{-5}	72.3
	3 3 0 0 - 3 2 1 0		262.9897	4.8×10^{-5}	63.4
	6 3 4 0 - 6 2 5 0		262.9900	8.3×10^{-5}	96.8
	3 3 1 0 - 3 2 2 0		262.9995	4.8×10^{-5}	63.4
	7 3 5 0 - 7 2 6 0		263.0177	8.6×10^{-5}	112.4
	8 3 6 0 - 8 2 7 0		263.0739	8.9×10^{-5}	130.2
	9 3 7 0 - 9 2 8 0		263.1684	9.0×10^{-5}	150.2
	10 3 8 0 - 10 2 9 0		263.3116	9.2×10^{-5}	172.5
	16 5 12 4 - 17 6 12 4		263.4603	5.8×10^{-5}	846.9
	11 3 9 0 - 11 2 10 0		263.5151	9.2×10^{-5}	196.9
CH_2DOH	25 5 20 2 - 24 6 19 2		260.0710	3.7×10^{-6}	811.2
	25 5 21 2 - 24 6 18 2		260.0956	3.7×10^{-6}	811.2
	28 2 26 1 - 28 1 27 1		260.1369	3.5×10^{-5}	902.1
	16 6 10 2 - 17 5 12 1		260.1467	1.1×10^{-5}	448.1
	16 6 11 2 - 17 5 13 1		260.1470	1.1×10^{-5}	448.1
	10 6 5 1 - 11 5 7 2		260.2246	7.1×10^{-6}	269.6
	10 6 4 1 - 11 5 6 2		260.2247	7.1×10^{-6}	269.6
	24 6 19 1 - 23 7 16 0		260.4056	1.2×10^{-5}	793.9
	24 6 18 1 - 23 7 17 0		260.4067	1.2×10^{-5}	793.9
	22 2 20 1 - 22 0 22 2		261.7345	1.0×10^{-6}	571.6
	21 5 17 1 - 20 6 14 0		261.8903	2.7×10^{-5}	602.5
	21 5 16 1 - 20 6 15 0		261.8934	2.7×10^{-5}	602.5
	18 4 14 2 - 17 5 12 1		261.9426	9.3×10^{-6}	448.2
	18 4 15 2 - 17 5 13 1		261.9678	9.4×10^{-6}	448.2
	10 1 9 1 - 9 2 8 1		262.1729	6.5×10^{-6}	135.5
	30 0 30 0 - 29 2 28 2		262.7597	1.3×10^{-6}	978.8
$\text{CH}_3\text{CH}_2\text{OH}$	36 7 29 2 - 35 8 28 2		259.9564	3.4×10^{-5}	623.2

Table 2.E.2: continued.

Species	Transition						Frequency (GHz)	A_{ij} (s ⁻¹)	E_{up} (K)
	(J K L M	-	J K L M)						
	25 2 24 2	-	25 1 25 2			260.0077	1.1×10^{-4}	272.8	
	15 6 10 0	-	14 6 9 0			260.0138	1.3×10^{-4}	200.5	
	15 6 9 0	-	14 6 8 0			260.0138	1.3×10^{-4}	200.5	
	15 3 13 1	-	14 3 12 1			260.0466	1.5×10^{-4}	172.5	
	15 1 14 0	-	14 1 13 0			260.0902	1.6×10^{-4}	159.6	
	15 5 11 1	-	14 5 10 1			260.1076	1.4×10^{-4}	192.1	
	15 5 10 1	-	14 5 9 1			260.1227	1.4×10^{-4}	192.1	
	15 3 13 0	-	14 3 12 0			260.1416	1.5×10^{-4}	167.7	
	15 5 11 0	-	14 5 10 0			260.2498	1.4×10^{-4}	187.2	
	15 5 10 0	-	14 5 9 0			260.2661	1.4×10^{-4}	187.2	
	13 2 11 1	-	13 1 13 0			260.3086	6.2×10^{-5}	143.3	
	7 1 6 1	-	6 0 6 0			260.4376	6.7×10^{-5}	86.7	
	28 3 26 2	-	28 2 27 2			261.8160	1.1×10^{-4}	351.0	
	34 4 31 2	-	33 5 28 2			261.9750	4.1×10^{-5}	520.7	
	23 16 7 0	-	24 15 9 1			262.0787	4.1×10^{-6}	599.0	
	23 16 8 0	-	24 15 10 1			262.0787	4.1×10^{-6}	599.0	
	13 2 12 2	-	12 1 11 2			262.1543	6.7×10^{-5}	81.0	
	43 5 38 2	-	43 4 39 2			262.8568	1.1×10^{-4}	840.5	
	35 3 32 1	-	35 3 33 1			263.0739	2.4×10^{-6}	604.2	
	22 2 20 0	-	22 1 22 1			263.1656	6.4×10^{-5}	276.2	
	43 11 33 1	-	42 12 31 0			263.4075	1.7×10^{-5}	996.0	
	43 11 32 1	-	42 12 30 0			263.4080	1.7×10^{-5}	996.0	
	32 4 29 2	-	31 5 26 2			263.4372	4.1×10^{-5}	464.7	
	15 3 12 1	-	14 3 11 1			263.4725	1.6×10^{-4}	173.0	
	38 8 31 0	-	38 7 31 1			263.5386	6.2×10^{-5}	752.0	
	30 16 14 2	-	31 15 17 2			263.6169	1.5×10^{-5}	711.0	
	30 16 15 2	-	31 15 16 2			263.6169	1.5×10^{-5}	711.0	
	13 3 11 0	-	12 2 11 1			263.6955	4.4×10^{-5}	143.6	
	39 6 34 0	-	38 7 32 1			263.7078	2.2×10^{-5}	751.8	
	CH ₃ CHO	31 10 22 4	-	32 9 24 4			259.9788	1.4×10^{-5}	886.7
44 6 39 0		-	43 7 36 0			260.0225	1.9×10^{-5}	998.9	
32 2 30 6		-	33 1 33 6			260.1158	1.8×10^{-6}	887.2	
6 1 5 8		-	5 1 5 7			260.1739	4.1×10^{-5}	406.7	
19 3 17 0		-	19 2 18 0			260.2834	5.7×10^{-5}	196.4	
13 1 13 1		-	12 0 12 2			260.4080	7.7×10^{-5}	83.9	
13 1 13 4		-	12 0 12 5			261.8892	7.6×10^{-5}	288.3	
14 5 10 6		-	13 5 9 6			261.9566	5.7×10^{-4}	545.7	
14 5 9 6		-	13 5 8 6			261.9567	5.7×10^{-4}	545.7	
17 0 17 8		-	16 1 16 7			261.9591	7.2×10^{-5}	516.5	
10 1 10 7		-	9 0 9 8			262.1191	5.3×10^{-5}	431.0	
9 2 7 6		-	9 1 8 6			262.7285	7.8×10^{-5}	427.8	
14 0 14 3	-	13 0 13 3			262.7300	6.3×10^{-4}	302.3		

Table 2.E.2: continued.

Species	Transition						Frequency (GHz)	A_{ij} (s^{-1})	E_{up} (K)
	(J K L M	-	J K L M)						
	14 1 14 6	-	13 1 13 6			262.8122	5.9×10^{-4}	466.8	
	17 7 10 2	-	18 6 12 2			262.8291	1.2×10^{-5}	252.0	
	14 9 5 8	-	13 9 4 8			262.8903	3.8×10^{-4}	664.5	
	14 0 14 2	-	13 0 13 2			262.9601	6.2×10^{-4}	95.8	
	7 5 3 3	-	8 4 4 3			262.9883	5.7×10^{-6}	285.4	
	7 5 2 3	-	8 4 5 3			262.9893	5.7×10^{-6}	285.4	
	14 0 14 0	-	13 0 13 0			263.0040	6.2×10^{-4}	95.7	
	29 4 25 5	-	29 3 26 5			263.0099	7.5×10^{-5}	645.8	
	10 1 10 6	-	9 0 9 6			263.1973	7.9×10^{-5}	421.7	
	23 1 22 5	-	23 0 23 5			263.3144	3.5×10^{-5}	466.0	
	6 2 5 1	-	5 1 5 1			263.4217	1.1×10^{-5}	28.5	
	10 2 9 7	-	10 0 10 8			263.5180	2.4×10^{-6}	440.1	
	15 2 13 5	-	15 1 15 4			263.7146	3.1×10^{-6}	327.0	
	7 2 6 1	-	6 1 5 2			263.7366	3.4×10^{-5}	34.9	
CH ₃ OCHO	35 8 27 3	-	34 9 26 3			260.0750	5.8×10^{-6}	605.4	
	44 11 34 4	-	44 10 35 4			260.1058	2.5×10^{-5}	853.7	
	46 8 38 3	-	46 7 39 3			260.1156	2.5×10^{-5}	881.6	
	21 10 12 1	-	21 9 13 1			260.1286	2.1×10^{-5}	202.8	
	21 10 11 2	-	21 9 12 2			260.1398	2.1×10^{-5}	202.8	
	21 10 11 0	-	21 9 12 0			260.1626	2.1×10^{-5}	202.8	
	21 10 12 0	-	21 9 13 0			260.1645	2.1×10^{-5}	202.8	
	43 11 33 0	-	43 10 34 0			260.1757	2.8×10^{-5}	644.0	
	44 11 34 0	-	44 10 35 0			260.1818	2.8×10^{-5}	670.6	
	43 11 33 1	-	43 10 34 1			260.2286	2.8×10^{-5}	644.0	
	44 9 36 4	-	44 8 37 4			260.2328	2.6×10^{-5}	829.2	
	44 11 34 1	-	44 10 35 1			260.2341	2.8×10^{-5}	670.5	
	13 4 10 4	-	12 3 10 4			260.2388	3.8×10^{-6}	251.4	
	43 11 33 4	-	43 10 34 4			260.2415	2.4×10^{-5}	827.3	
	21 3 18 2	-	20 3 17 2			260.2445	2.6×10^{-4}	146.8	
	21 3 18 0	-	20 3 17 0			260.2551	2.6×10^{-4}	146.8	
	25 10 15 3	-	25 9 16 3			260.2673	2.3×10^{-5}	445.1	
	12 3 9 2	-	11 2 10 1			260.2897	4.5×10^{-6}	53.2	
	25 10 16 3	-	25 9 17 3			260.2967	2.3×10^{-5}	445.1	
	12 3 9 0	-	11 2 10 0			260.3608	4.5×10^{-6}	53.2	
	21 8 13 2	-	20 8 12 2			260.3843	2.3×10^{-4}	179.2	
	21 8 14 0	-	20 8 13 0			260.3927	2.3×10^{-4}	179.2	
	21 8 14 1	-	20 8 13 1			260.4040	2.3×10^{-4}	179.2	
	21 8 13 0	-	20 8 12 0			260.4153	2.3×10^{-4}	179.2	
	38 11 28 4	-	38 10 28 5			260.4369	1.6×10^{-6}	705.0	
	38 11 27 2	-	38 10 28 2			261.7075	2.7×10^{-5}	520.6	
	21 7 14 2	-	20 7 13 2			261.7155	2.4×10^{-4}	169.6	
	43 9 35 0	-	42 10 32 0			261.7196	3.6×10^{-6}	619.6	

Table 2.E.2: continued.

Species	Transition						Frequency (GHz)	A_{ij} (s ⁻¹)	E_{up} (K)
	(J K L M	-	J K L M)						
	21 6 15 5	-	20 6 14 5			261.7271	2.4×10^{-4}	348.0	
	43 9 35 1	-	42 10 32 2			261.7273	3.6×10^{-6}	619.6	
	21 7 14 0	-	20 7 13 0			261.7466	2.4×10^{-4}	169.5	
	44 9 36 4	-	43 10 33 5			261.7591	3.4×10^{-6}	829.2	
	21 6 15 3	-	20 6 14 3			261.7612	2.5×10^{-4}	348.1	
	17 10 8 1	-	17 9 9 1			261.7731	1.8×10^{-5}	156.6	
	17 10 7 2	-	17 9 8 2			261.7850	1.8×10^{-5}	156.6	
	17 10 7 0	-	17 9 8 0			261.8223	1.8×10^{-5}	156.6	
	17 10 8 0	-	17 9 9 0			261.8223	1.8×10^{-5}	156.6	
	39 9 31 4	-	39 7 32 5			261.8334	6.1×10^{-6}	703.9	
	42 10 33 4	-	41 11 31 4			261.8559	3.2×10^{-6}	789.0	
	42 9 34 3	-	41 10 31 3			261.8562	4.4×10^{-6}	777.0	
	24 10 14 5	-	24 9 15 5			261.9112	2.3×10^{-5}	430.6	
	46 10 37 3	-	46 9 38 3			261.9118	2.8×10^{-5}	895.3	
	38 9 30 0	-	38 7 31 0			261.9944	6.0×10^{-6}	496.2	
	16 10 7 1	-	16 9 8 1			262.0360	1.7×10^{-5}	146.6	
	16 10 6 2	-	16 9 7 2			262.0478	1.7×10^{-5}	146.6	
	41 11 31 0	-	41 10 32 0			262.0580	2.8×10^{-5}	592.7	
	38 9 30 1	-	38 7 31 2			262.0825	6.0×10^{-6}	496.2	
	16 10 6 0	-	16 9 7 0			262.0882	1.7×10^{-5}	146.6	
	16 10 7 0	-	16 9 8 0			262.0882	1.7×10^{-5}	146.6	
	37 5 32 5	-	37 5 33 4			262.1035	8.9×10^{-6}	625.0	
	41 11 31 1	-	41 10 32 1			262.1078	2.8×10^{-5}	592.7	
	21 7 14 2	-	20 7 14 1			262.1113	4.6×10^{-6}	169.6	
	19 4 16 4	-	18 3 15 5			262.1355	1.7×10^{-5}	309.7	
	41 11 31 4	-	41 10 32 4			262.7105	2.4×10^{-5}	776.5	
	43 9 35 0	-	43 7 36 0			262.7268	9.2×10^{-6}	619.6	
	46 11 36 0	-	46 10 37 0			262.7278	2.9×10^{-5}	725.6	
	23 10 13 5	-	23 9 14 5			262.7323	2.3×10^{-5}	416.5	
	12 10 2 0	-	12 9 3 0			262.7462	1.1×10^{-5}	112.4	
	12 10 3 0	-	12 9 4 0			262.7462	1.1×10^{-5}	112.4	
	43 9 35 1	-	43 7 36 2			262.7498	9.2×10^{-6}	619.6	
	11 10 2 1	-	11 9 3 1			262.7698	8.3×10^{-6}	105.3	
	46 11 36 1	-	46 10 37 1			262.7761	2.9×10^{-5}	725.5	
	11 10 1 2	-	11 9 2 2			262.7821	8.3×10^{-6}	105.3	
	12 3 9 3	-	11 1 10 3			262.8302	2.4×10^{-6}	240.5	
	10 10 1 1	-	10 9 2 1			262.8348	4.7×10^{-6}	98.8	
	11 10 1 0	-	11 9 2 0			262.8348	8.3×10^{-6}	105.3	
	11 10 2 0	-	11 9 3 0			262.8348	8.3×10^{-6}	105.3	
	10 10 0 2	-	10 9 1 2			262.8472	4.7×10^{-6}	98.8	
	32 7 25 3	-	31 8 24 3			262.8826	6.5×10^{-6}	535.9	
	10 10 0 0	-	10 9 1 0			262.9019	4.7×10^{-6}	98.8	

Table 2.E.2: continued.

Species	Transition		Frequency	A_{ij}	E_{up}
	(J K L M - J K L M)		(GHz)	(s^{-1})	(K)
	10 10 1 0 - 10 9 2 0		262.9019	4.7×10^{-6}	98.8
	39 7 33 1 - 39 6 34 1		262.9162	2.2×10^{-5}	497.3
	39 7 33 0 - 39 6 34 0		262.9513	2.2×10^{-5}	497.3
	43 7 36 3 - 43 7 37 3		262.9776	9.4×10^{-6}	790.0
	51 14 38 1 - 50 15 35 2		262.9834	2.0×10^{-6}	918.0
	44 9 36 3 - 43 10 33 3		263.0190	3.6×10^{-6}	828.7
	42 10 33 1 - 41 11 30 2		263.0193	5.5×10^{-6}	605.5
	20 10 10 3 - 20 9 11 3		263.0300	2.1×10^{-5}	377.5
	20 10 11 3 - 20 9 12 3		263.0305	2.1×10^{-5}	377.5
	22 10 13 4 - 22 9 14 4		263.0364	2.2×10^{-5}	402.5
	29 1 28 3 - 29 1 29 3		263.0528	2.8×10^{-6}	427.4
	29 1 28 3 - 29 0 29 3		263.0529	5.2×10^{-6}	427.4
	29 2 28 3 - 29 1 29 3		263.0536	5.2×10^{-6}	427.4
	29 2 28 3 - 29 0 29 3		263.0536	2.8×10^{-6}	427.4
	42 10 33 0 - 41 11 30 0		263.0820	5.5×10^{-6}	605.5
	44 11 34 1 - 43 12 31 2		263.1054	5.5×10^{-6}	670.5
	44 11 34 0 - 43 12 31 0		263.1933	5.6×10^{-6}	670.6
	51 14 38 1 - 50 15 36 1		263.3156	3.5×10^{-6}	918.0
	43 9 35 4 - 42 10 32 5		263.3286	3.9×10^{-6}	803.0
	40 6 34 3 - 40 6 35 3		263.3459	9.2×10^{-6}	704.3
	19 10 10 3 - 19 9 11 3		263.3471	2.1×10^{-5}	365.7
	19 10 9 3 - 19 9 10 3		263.3471	2.1×10^{-5}	365.7
	49 9 40 2 - 49 8 41 2		263.3632	2.7×10^{-5}	798.0
	42 8 35 3 - 42 7 36 3		263.3690	2.5×10^{-5}	765.2
	39 7 33 1 - 39 5 34 2		263.3753	9.7×10^{-6}	497.3
	49 9 40 0 - 49 8 41 0		263.3938	2.7×10^{-5}	798.0
	39 7 33 0 - 39 5 34 0		263.4086	9.7×10^{-6}	497.3
	22 10 12 5 - 22 9 13 5		263.4524	2.2×10^{-5}	403.0
	9 6 4 4 - 8 5 4 4		263.4606	2.9×10^{-5}	237.4
	29 6 23 3 - 28 7 22 3		263.4713	7.7×10^{-6}	472.9
	47 12 35 5 - 47 11 36 5		263.5168	2.5×10^{-5}	950.7
	31 8 24 4 - 31 6 25 5		263.5309	3.7×10^{-6}	523.5
	51 10 42 0 - 50 11 39 0		263.5493	2.1×10^{-6}	859.8
	37 6 32 4 - 37 5 33 4		263.5905	2.0×10^{-5}	625.0
	51 10 42 1 - 50 11 39 2		263.5969	2.1×10^{-6}	859.8
	18 10 8 3 - 18 9 9 3		263.6061	2.0×10^{-5}	354.6
	18 10 9 3 - 18 9 10 3		263.6061	2.0×10^{-5}	354.6
	21 10 12 4 - 21 9 13 4		263.6491	2.2×10^{-5}	389.6
	40 11 30 0 - 40 10 31 0		263.6666	2.9×10^{-5}	568.0
	37 6 32 4 - 37 4 33 5		263.7116	9.1×10^{-6}	625.0
	40 11 30 1 - 40 10 31 1		263.7127	2.9×10^{-5}	568.0
CH ₃ OCH ₃	20 5 16 3 - 20 4 17 3		259.9825	9.2×10^{-5}	226.6

Table 2.E.2: continued.

Species	Transition						Frequency (GHz)	A_{ij} (s ⁻¹)	E_{up} (K)
	(J K L M	-	J K L M)						
	20 5 16 5	-	20 4 17 5			259.9826	9.2×10^{-5}	226.6	
	20 5 16 1	-	20 4 17 1			259.9844	9.2×10^{-5}	226.6	
	20 5 16 0	-	20 4 17 0			259.9863	9.2×10^{-5}	226.6	
	24 5 20 3	-	24 4 21 3			260.0034	9.6×10^{-5}	308.9	
	24 5 20 5	-	24 4 21 5			260.0034	9.6×10^{-5}	308.9	
	24 5 20 1	-	24 4 21 1			260.0044	9.6×10^{-5}	308.9	
	24 5 20 0	-	24 4 21 0			260.0054	9.6×10^{-5}	308.9	
	19 5 15 3	-	19 4 16 3			260.3271	9.1×10^{-5}	208.3	
	19 5 15 5	-	19 4 16 5			260.3272	9.1×10^{-5}	208.3	
	19 5 15 1	-	19 4 16 1			260.3292	9.1×10^{-5}	208.3	
	19 5 15 0	-	19 4 16 0			260.3313	9.1×10^{-5}	208.3	
	16 5 11 5	-	16 4 12 5			260.4005	8.7×10^{-5}	159.0	
	16 5 11 3	-	16 4 12 3			260.4011	8.6×10^{-5}	159.0	
	16 5 11 1	-	16 4 12 1			260.4032	8.7×10^{-5}	159.0	
	16 5 11 0	-	16 4 12 0			260.4056	8.7×10^{-5}	159.0	
	28 4 25 0	-	27 5 22 0			261.8399	2.3×10^{-5}	393.2	
	28 4 25 1	-	27 5 22 1			261.8402	2.3×10^{-5}	393.2	
	28 4 25 3	-	27 5 22 3			261.8404	2.3×10^{-5}	393.2	
	28 4 25 5	-	27 5 22 5			261.8404	2.3×10^{-5}	393.2	
	14 5 10 3	-	14 4 10 3			261.8785	1.1×10^{-5}	130.8	
	14 5 10 1	-	14 4 10 1			261.8832	3.9×10^{-6}	130.8	
	14 5 9 5	-	14 4 10 5			261.8941	8.6×10^{-5}	130.8	
	14 5 9 3	-	14 4 10 3			261.8965	7.5×10^{-5}	130.8	
	14 5 9 1	-	14 4 10 1			261.8976	8.2×10^{-5}	130.8	
	14 5 9 0	-	14 4 10 0			261.8998	8.6×10^{-5}	130.8	
	15 5 11 3	-	15 4 12 3			261.9530	8.4×10^{-5}	144.4	
	15 5 11 5	-	15 4 12 5			261.9543	8.7×10^{-5}	144.4	
	15 5 11 1	-	15 4 12 1			261.9566	8.6×10^{-5}	144.4	
	15 5 11 0	-	15 4 12 0			261.9596	8.7×10^{-5}	144.4	
	15 5 10 3	-	15 4 12 3			261.9814	3.7×10^{-6}	144.4	
	15 5 10 1	-	15 4 12 1			261.9830	1.0×10^{-6}	144.4	
	12 5 7 3	-	12 4 8 3			262.7548	2.8×10^{-5}	106.2	
	12 5 8 1	-	12 4 8 1			262.7616	2.3×10^{-5}	106.2	
	12 5 7 5	-	12 4 8 5			262.7637	8.2×10^{-5}	106.2	
	12 5 8 3	-	12 4 8 3			262.7688	5.4×10^{-5}	106.2	
	12 5 7 1	-	12 4 8 1			262.7690	5.9×10^{-5}	106.2	
	12 5 7 0	-	12 4 8 0			262.7699	8.2×10^{-5}	106.2	
	8 2 6 5	-	7 1 7 5			262.7712	3.3×10^{-5}	38.6	
	8 2 6 3	-	7 1 7 3			262.7712	3.3×10^{-5}	38.6	
	8 2 6 1	-	7 1 7 1			262.7740	3.3×10^{-5}	38.6	
	8 2 6 0	-	7 1 7 0			262.7769	3.3×10^{-5}	38.6	
	12 5 7 3	-	12 4 9 3			262.8843	5.5×10^{-5}	106.2	

Table 2.E.2: continued.

Species	Transition						Frequency (GHz)	A_{ij} (s ⁻¹)	E_{up} (K)
	(J K L M	-	J K L M)						
	12 5 8 5	-	12 4 9 5			262.8893	8.2×10^{-5}	106.2	
	12 5 8 1	-	12 4 9 1			262.8902	5.9×10^{-5}	106.2	
	12 5 8 0	-	12 4 9 0			262.8954	8.2×10^{-5}	106.2	
	12 5 7 1	-	12 4 9 1			262.8976	2.3×10^{-5}	106.2	
	12 5 8 3	-	12 4 9 3			262.8982	2.8×10^{-5}	106.2	
	27 5 23 3	-	27 4 24 3			262.9642	1.0×10^{-4}	380.2	
	27 5 23 5	-	27 4 24 5			262.9642	1.0×10^{-4}	380.2	
	27 5 23 1	-	27 4 24 1			262.9645	1.0×10^{-4}	380.2	
	27 5 23 0	-	27 4 24 0			262.9649	1.0×10^{-4}	380.2	
	11 5 6 3	-	11 4 7 3			263.0353	2.6×10^{-5}	95.2	
	11 5 7 1	-	11 4 7 1			263.0428	2.8×10^{-5}	95.2	
	11 5 6 5	-	11 4 7 5			263.0441	8.0×10^{-5}	95.2	
	11 5 7 3	-	11 4 7 3			263.0494	5.3×10^{-5}	95.2	
	11 5 6 1	-	11 4 7 1			263.0500	5.1×10^{-5}	95.2	
	11 5 6 0	-	11 4 7 0			263.0504	8.0×10^{-5}	95.2	
	11 5 6 3	-	11 4 8 3			263.1021	5.3×10^{-5}	95.2	
	11 5 7 5	-	11 4 8 5			263.1075	8.0×10^{-5}	95.2	
	11 5 7 1	-	11 4 8 1			263.1079	5.1×10^{-5}	95.2	
	11 5 7 0	-	11 4 8 0			263.1138	8.0×10^{-5}	95.2	
	11 5 6 1	-	11 4 8 1			263.1151	2.8×10^{-5}	95.2	
	11 5 7 3	-	11 4 8 3			263.1163	2.6×10^{-5}	95.2	
	9 5 4 3	-	9 4 6 3			263.3887	6.4×10^{-6}	76.1	
	9 5 5 1	-	9 4 5 1			263.3991	1.5×10^{-5}	76.1	
	9 5 4 5	-	9 4 5 5			263.4011	7.3×10^{-5}	76.1	
	9 5 5 3	-	9 4 6 3			263.4037	6.6×10^{-5}	76.1	
	9 5 4 1	-	9 4 5 1			263.4066	5.8×10^{-5}	76.1	
	9 5 4 0	-	9 4 5 0			263.4078	7.3×10^{-5}	76.1	
	9 5 4 3	-	9 4 5 3			263.4114	6.6×10^{-5}	76.1	
	9 5 5 5	-	9 4 6 5			263.4140	7.3×10^{-5}	76.1	
	9 5 5 1	-	9 4 6 1			263.4151	5.8×10^{-5}	76.1	
	9 5 5 0	-	9 4 6 0			263.4206	7.3×10^{-5}	76.1	
	9 5 4 1	-	9 4 6 1			263.4226	1.5×10^{-5}	76.1	
	9 5 5 3	-	9 4 5 3			263.4263	6.4×10^{-6}	76.1	
	8 5 3 3	-	8 4 5 3			263.4921	1.1×10^{-6}	67.9	
	8 5 4 1	-	8 4 4 1			263.5038	3.8×10^{-6}	67.9	
	8 5 3 5	-	8 4 4 5			263.5071	6.7×10^{-5}	67.9	
	8 5 4 3	-	8 4 5 3			263.5074	6.6×10^{-5}	67.9	
	8 5 3 1	-	8 4 4 1			263.5115	6.3×10^{-5}	67.9	
	8 5 3 3	-	8 4 4 3			263.5118	6.6×10^{-5}	67.9	
	8 5 4 5	-	8 4 5 5			263.5121	6.7×10^{-5}	67.9	
	8 5 3 0	-	8 4 4 0			263.5140	6.7×10^{-5}	67.9	
	8 5 4 1	-	8 4 5 1			263.5146	6.3×10^{-5}	67.9	

Table 2.E.2: continued.

Species	Transition		Frequency	A_{ij}	E_{up}
	(J K L M - J K L M)		(GHz)	(s^{-1})	(K)
	8 5 4 0 - 8 4 5 0		263.5189	6.7×10^{-5}	67.9
	8 5 3 1 - 8 4 5 1		263.5222	3.8×10^{-6}	67.9
	8 5 4 3 - 8 4 4 3		263.5271	1.1×10^{-6}	67.9
	7 5 3 3 - 7 4 4 3		263.5784	6.0×10^{-5}	60.6
	7 5 2 5 - 7 4 3 5		263.5795	6.0×10^{-5}	60.6
	7 5 3 5 - 7 4 4 5		263.5812	6.0×10^{-5}	60.6
	7 5 2 3 - 7 4 3 3		263.5822	6.0×10^{-5}	60.6
	7 5 2 1 - 7 4 3 1		263.5828	5.9×10^{-5}	60.6
	7 5 3 1 - 7 4 4 1		263.5848	5.9×10^{-5}	60.6
	7 5 2 0 - 7 4 3 0		263.5865	6.0×10^{-5}	60.6
	7 5 3 0 - 7 4 4 0		263.5881	6.0×10^{-5}	60.6
	6 5 2 3 - 6 4 3 3		263.6249	4.9×10^{-5}	54.3
	6 5 1 5 - 6 4 2 5		263.6266	4.9×10^{-5}	54.3
	6 5 2 5 - 6 4 3 5		263.6271	4.9×10^{-5}	54.3
	6 5 1 3 - 6 4 2 3		263.6288	4.9×10^{-5}	54.3
	6 5 1 1 - 6 4 2 1		263.6294	4.8×10^{-5}	54.3
	6 5 2 1 - 6 4 3 1		263.6313	4.8×10^{-5}	54.3
	6 5 1 0 - 6 4 2 0		263.6337	4.9×10^{-5}	54.3
	6 5 2 0 - 6 4 3 0		263.6342	4.9×10^{-5}	54.3
	5 5 1 3 - 5 4 2 3		263.6534	3.1×10^{-5}	48.8
	5 5 0 5 - 5 4 1 5		263.6553	3.1×10^{-5}	48.8
	5 5 1 5 - 5 4 2 5		263.6553	3.1×10^{-5}	48.8
	5 5 0 3 - 5 4 1 3		263.6573	3.1×10^{-5}	48.8
	5 5 0 1 - 5 4 1 1		263.6579	3.1×10^{-5}	48.8
	5 5 1 1 - 5 4 2 1		263.6599	3.1×10^{-5}	48.8
	5 5 0 0 - 5 4 1 0		263.6625	3.1×10^{-5}	48.8
	5 5 1 0 - 5 4 2 0		263.6625	3.1×10^{-5}	48.8
CH ₃ COCH ₃	38 26 12 0 - 38 23 15 0		260.0197	2.3×10^{-5}	615.2
	10 9 2 1 - 9 6 3 1		260.0832	4.7×10^{-6}	49.8
	25 19 7 0 - 25 16 10 1		260.0881	2.4×10^{-6}	277.8
	29 27 2 0 - 28 28 1 0		260.1037	1.0×10^{-6}	404.6
	29 27 3 0 - 28 28 0 0		260.1037	1.0×10^{-6}	404.6
	23 16 8 1 - 22 17 5 1		260.1095	3.5×10^{-5}	229.8
	28 25 4 0 - 27 26 2 1		260.1376	3.3×10^{-6}	370.0
	27 23 5 0 - 26 24 2 0		260.1771	7.1×10^{-6}	337.4
	27 23 4 0 - 26 24 3 0		260.1771	7.1×10^{-6}	337.4
	25 19 7 1 - 25 16 10 1		260.1828	4.4×10^{-6}	277.8
	28 17 11 0 - 28 14 14 0		260.1892	7.0×10^{-6}	330.6
	34 24 11 1 - 34 21 13 2		260.1953	1.7×10^{-6}	497.8
	9 9 0 0 - 8 6 3 0		260.2293	1.2×10^{-6}	42.7
	44 14 30 0 - 44 13 31 0		260.2497	3.0×10^{-4}	690.3
	44 15 30 0 - 44 14 31 0		260.2497	3.0×10^{-4}	690.3

Table 2.E.2: continued.

Species	Transition						Frequency (GHz)	A_{ij} (s ⁻¹)	E_{up} (K)
	(J K L M	-	J K L M)						
	44 14 30 0	-	44 13 31 1			260.2689	3.4×10^{-5}	690.3	
	44 14 30 0	-	44 14 31 1			260.2689	3.4×10^{-5}	690.3	
	44 15 30 0	-	44 13 31 1			260.2689	3.9×10^{-4}	690.3	
	44 15 30 0	-	44 14 31 1			260.2689	3.9×10^{-4}	690.3	
	29 27 3 0	-	28 28 0 1			260.2727	1.0×10^{-6}	404.5	
	28 17 11 0	-	28 14 14 1			260.2796	7.0×10^{-6}	330.6	
	44 14 30 1	-	44 14 31 2			260.2881	3.0×10^{-4}	690.2	
	44 15 30 1	-	44 13 31 2			260.2881	3.0×10^{-4}	690.2	
	44 14 30 1	-	44 14 31 1			260.2881	3.0×10^{-4}	690.2	
	44 15 30 1	-	44 13 31 1			260.2881	3.0×10^{-4}	690.2	
	27 19 9 1	-	27 16 12 2			260.3305	6.5×10^{-6}	315.8	
	28 25 3 0	-	27 26 1 1			260.3326	3.3×10^{-6}	370.0	
	36 25 11 0	-	36 22 14 1			260.3392	2.0×10^{-5}	555.0	
	28 17 11 1	-	28 14 14 1			260.3691	6.9×10^{-6}	330.5	
	28 17 11 1	-	28 14 14 2			260.3772	6.9×10^{-6}	330.5	
	28 25 4 1	-	27 26 2 2			260.4195	3.3×10^{-6}	369.9	
	29 27 3 1	-	28 28 0 2			260.4414	1.0×10^{-6}	404.4	
	38 26 12 1	-	38 23 15 2			261.7077	2.0×10^{-5}	615.2	
	18 9 9 0	-	18 6 12 0			261.7099	1.0×10^{-6}	134.3	
	26 21 6 0	-	25 22 4 1			261.7369	1.3×10^{-5}	306.6	
	30 22 8 1	-	30 19 11 2			261.7414	4.8×10^{-6}	393.3	
	41 11 30 1	-	41 11 31 2			261.7560	2.6×10^{-4}	576.3	
	41 12 30 1	-	41 10 31 2			261.7560	2.6×10^{-4}	576.3	
	41 11 30 1	-	41 10 31 1			261.7561	2.6×10^{-4}	576.3	
	41 12 30 1	-	41 11 31 1			261.7561	2.6×10^{-4}	576.3	
	30 22 8 0	-	30 19 11 1			261.7703	5.6×10^{-6}	393.3	
	41 11 30 0	-	41 10 31 1			261.7955	1.5×10^{-4}	576.4	
	41 11 30 0	-	41 11 31 1			261.7955	1.5×10^{-4}	576.4	
	41 12 30 0	-	41 10 31 1			261.7955	2.0×10^{-4}	576.4	
	41 12 30 0	-	41 11 31 1			261.7955	2.0×10^{-4}	576.4	
	10 9 1 0	-	9 6 3 1			261.7975	2.4×10^{-6}	49.8	
	20 7 13 1	-	19 8 12 2			261.8181	4.9×10^{-4}	151.2	
	20 7 13 1	-	19 8 12 1			261.8182	4.9×10^{-4}	151.2	
	20 8 13 1	-	19 7 12 2			261.8191	4.9×10^{-4}	151.2	
	20 8 13 1	-	19 7 12 1			261.8192	4.9×10^{-4}	151.2	
	41 11 30 0	-	41 10 31 0			261.8347	2.6×10^{-4}	576.4	
	41 12 30 0	-	41 11 31 0			261.8347	2.6×10^{-4}	576.4	
	30 22 8 0	-	30 19 11 0			261.8621	7.7×10^{-6}	393.3	
	20 7 13 0	-	19 8 12 1			261.9017	4.9×10^{-4}	151.1	
	20 8 13 0	-	19 7 12 1			261.9027	4.9×10^{-4}	151.1	
	40 27 13 0	-	40 24 16 0			261.9051	2.9×10^{-5}	678.6	
	21 18 3 1	-	21 15 6 1			261.9131	1.1×10^{-6}	206.3	

Table 2.E.2: continued.

Species	Transition						Frequency (GHz)	A_{ij} (s ⁻¹)	E_{up} (K)
	(J K L M	-	J K L M)						
	20 7 13 0	-	19 8 12 0			261.9852	4.9×10^{-4}	151.1	
	20 8 13 0	-	19 7 12 0			261.9862	4.9×10^{-4}	151.1	
	26 21 5 1	-	25 22 3 2			261.9892	1.3×10^{-5}	306.6	
	26 21 6 1	-	25 22 3 1			262.0656	1.3×10^{-5}	306.5	
	26 21 5 1	-	25 22 4 1			262.0681	1.3×10^{-5}	306.5	
	26 21 6 1	-	25 22 4 2			262.1439	1.3×10^{-5}	306.5	
	10 9 1 1	-	9 6 3 2			262.1591	2.6×10^{-6}	49.9	
	40 10 30 1	-	40 10 31 2			262.1740	2.4×10^{-4}	540.1	
	40 11 30 1	-	40 9 31 2			262.1740	2.4×10^{-4}	540.1	
	40 10 30 1	-	40 10 31 1			262.1741	2.4×10^{-4}	540.1	
	40 11 30 1	-	40 9 31 1			262.1741	2.4×10^{-4}	540.1	
	50 23 28 1	-	49 24 25 1			262.7522	2.6×10^{-6}	964.3	
	39 10 30 0	-	39 9 31 0			262.7529	2.3×10^{-4}	504.8	
	39 9 30 0	-	39 8 31 0			262.7529	2.3×10^{-4}	504.8	
	50 22 28 0	-	49 25 25 1			262.7640	4.1×10^{-6}	964.3	
	50 23 28 0	-	49 24 25 1			262.7644	4.1×10^{-6}	964.3	
	21 6 15 1	-	20 7 14 2			262.7689	5.7×10^{-4}	158.3	
	21 7 15 1	-	20 6 14 2			262.7689	5.7×10^{-4}	158.3	
	21 6 15 1	-	20 7 14 1			262.7689	5.7×10^{-4}	158.3	
	21 7 15 1	-	20 6 14 1			262.7689	5.7×10^{-4}	158.3	
	50 22 28 0	-	49 25 25 0			262.7764	2.5×10^{-6}	964.4	
	50 23 28 0	-	49 24 25 0			262.7767	2.6×10^{-6}	964.4	
	40 27 13 0	-	40 24 16 1			262.8043	3.7×10^{-5}	678.6	
	21 6 15 0	-	20 7 14 1			262.8419	5.7×10^{-4}	158.2	
	21 7 15 0	-	20 6 14 1			262.8419	5.7×10^{-4}	158.2	
	30 17 13 1	-	29 20 10 1			262.8726	6.8×10^{-6}	374.2	
	30 17 13 0	-	29 20 10 1			262.9092	6.8×10^{-6}	374.3	
	38 8 30 1	-	38 8 31 2			262.9134	2.1×10^{-4}	470.2	
	38 9 30 1	-	38 7 31 2			262.9134	2.1×10^{-4}	470.2	
	38 8 30 1	-	38 8 31 1			262.9135	2.1×10^{-4}	470.2	
	38 9 30 1	-	38 7 31 1			262.9135	2.1×10^{-4}	470.2	
	21 6 15 0	-	20 7 14 0			262.9147	5.7×10^{-4}	158.2	
	21 7 15 0	-	20 6 14 0			262.9147	5.7×10^{-4}	158.2	
	30 17 13 0	-	29 20 10 0			262.9170	6.8×10^{-6}	374.3	
	30 17 13 1	-	29 20 10 2			262.9385	6.7×10^{-6}	374.2	
	23 16 7 1	-	22 17 5 2			262.9661	2.7×10^{-5}	230.0	
	14 11 4 0	-	13 10 3 0			262.9821	4.6×10^{-4}	90.4	
	21 18 3 1	-	21 15 6 2			262.9920	1.0×10^{-6}	206.4	
	38 8 30 0	-	38 7 31 1			263.0452	2.3×10^{-5}	470.3	
	38 8 30 0	-	38 8 31 1			263.0452	3.9×10^{-5}	470.3	
	38 9 30 0	-	38 7 31 1			263.0452	2.2×10^{-4}	470.3	
	38 9 30 0	-	38 8 31 1			263.0452	2.4×10^{-4}	470.3	

Table 2.E.2: continued.

Species	Transition						Frequency (GHz)	A_{ij} (s^{-1})	E_{up} (K)
	(J K L M	-	J K L M)						
	21 18 4 1	-	21 15 7 2			263.1102	1.0×10^{-6}	206.2	
	38 8 30 0	-	38 7 31 0			263.1764	2.1×10^{-4}	470.3	
	38 9 30 0	-	38 8 31 0			263.1764	2.1×10^{-4}	470.3	
	14 11 4 1	-	13 10 4 2			263.3286	4.4×10^{-4}	90.4	
	14 11 3 1	-	13 10 3 2			263.3983	4.4×10^{-4}	90.6	
	37 7 30 0	-	37 6 31 1			263.4085	5.1×10^{-6}	436.6	
	37 7 30 0	-	37 7 31 1			263.4085	5.1×10^{-6}	436.6	
	37 8 30 0	-	37 6 31 1			263.4085	2.2×10^{-4}	436.6	
	37 8 30 0	-	37 7 31 1			263.4085	2.2×10^{-4}	436.6	
	18 10 9 0	-	17 9 8 1			263.4583	3.2×10^{-4}	134.4	
	21 18 3 0	-	21 15 6 0			263.5077	1.1×10^{-6}	206.4	
	14 11 3 0	-	13 10 3 1			263.5148	4.0×10^{-4}	90.5	
	40 27 13 1	-	40 24 16 1			263.5282	2.9×10^{-5}	678.6	
	36 6 30 1	-	36 5 31 2			263.5343	1.7×10^{-4}	403.8	
	36 7 30 1	-	36 6 31 2			263.5343	1.7×10^{-4}	403.8	
	36 6 30 1	-	36 6 31 1			263.5344	1.7×10^{-4}	403.8	
	36 7 30 1	-	36 5 31 1			263.5344	1.7×10^{-4}	403.8	
	37 7 30 0	-	37 7 31 0			263.5783	1.9×10^{-4}	436.6	
	37 8 30 0	-	37 6 31 0			263.5783	1.9×10^{-4}	436.6	
	18 10 9 0	-	17 9 8 0			263.6265	3.2×10^{-4}	134.4	
	23 16 7 0	-	22 17 6 0			263.6422	3.6×10^{-5}	230.0	
	14 11 4 0	-	13 10 4 1			263.6745	3.9×10^{-4}	90.4	
	14 10 4 1	-	13 9 5 1			263.6827	3.0×10^{-4}	88.0	
	10 8 3 1	-	9 5 5 2			263.7026	2.1×10^{-6}	47.5	
	25 19 7 0	-	24 20 4 0			263.7264	2.2×10^{-5}	277.8	
	36 6 30 0	-	36 5 31 1			263.7477	4.5×10^{-5}	403.8	
	36 6 30 0	-	36 6 31 1			263.7477	4.5×10^{-5}	403.8	
	36 7 30 0	-	36 5 31 1			263.7477	1.5×10^{-4}	403.8	
	36 7 30 0	-	36 6 31 1			263.7477	1.5×10^{-4}	403.8	
aGg ⁺ (CH ₂ OH) ₂	46 11 35 1	-	45 12 34 1			259.9713	1.3×10^{-5}	593.8	
	47 3 44 0	-	47 3 45 1			259.9736	8.1×10^{-6}	546.3	
	47 4 44 0	-	47 2 45 1			259.9737	8.1×10^{-6}	546.3	
	55 14 41 1	-	55 13 43 0			260.0722	1.2×10^{-5}	855.4	
	26 12 14 0	-	25 12 13 1			260.1167	3.4×10^{-4}	243.3	
	26 12 15 0	-	25 12 14 1			260.1167	3.4×10^{-4}	243.3	
	17 5 13 0	-	16 4 13 1			260.1561	2.1×10^{-5}	87.8	
	30 13 18 1	-	30 12 18 0			260.2226	8.7×10^{-6}	311.9	
	30 13 17 1	-	30 12 19 0			260.2226	8.7×10^{-6}	311.9	
	47 14 34 0	-	47 13 34 1			260.2259	9.0×10^{-6}	651.5	
	47 14 33 0	-	47 13 35 1			260.2706	8.8×10^{-6}	651.5	
	29 5 24 1	-	28 6 23 1			260.2757	3.6×10^{-5}	231.5	
	26 11 16 0	-	25 11 15 1			260.3799	3.5×10^{-4}	232.1	

Table 2.E.2: continued.

Species	Transition						Frequency (GHz)	A_{ij} (s ⁻¹)	E_{up} (K)
	(J K L M	-	J K L M)						
	26 11 15 0	-	25 11 14 1			260.3799	3.5×10^{-4}	232.1	
	46 6 41 1	-	45 7 39 0			260.4379	2.3×10^{-6}	547.7	
	23 5 18 0	-	22 5 18 0			261.7385	2.2×10^{-6}	149.9	
	24 13 11 1	-	24 12 13 0			261.7715	8.0×10^{-6}	230.7	
	24 13 12 1	-	24 12 12 0			261.7715	8.0×10^{-6}	230.7	
	24 5 19 1	-	23 5 18 0			261.8151	4.2×10^{-4}	162.5	
	53 14 40 0	-	52 15 37 0			261.8547	1.0×10^{-5}	801.3	
	53 14 40 1	-	52 15 37 1			261.8655	1.4×10^{-5}	801.5	
	59 9 51 1	-	59 8 52 1			261.8778	4.0×10^{-5}	914.0	
	18 4 15 0	-	17 3 15 1			261.8919	9.2×10^{-6}	92.3	
	26 8 19 0	-	25 8 18 1			261.9036	4.0×10^{-4}	204.5	
	53 14 39 0	-	52 15 38 0			261.9265	1.0×10^{-5}	801.3	
	59 9 51 0	-	59 8 52 0			261.9386	4.6×10^{-5}	913.6	
	53 14 39 1	-	52 15 38 1			261.9416	1.4×10^{-5}	801.5	
	23 13 10 1	-	23 12 12 0			261.9447	7.8×10^{-6}	218.9	
	23 13 11 1	-	23 12 11 0			261.9447	7.8×10^{-6}	218.9	
	60 8 52 0	-	60 8 53 1			261.9497	1.7×10^{-5}	942.7	
	26 8 18 0	-	25 8 17 1			261.9712	4.0×10^{-4}	204.5	
	34 9 26 0	-	34 7 27 1			262.0007	2.2×10^{-6}	333.6	
	50 14 36 1	-	50 13 37 1			262.0294	5.5×10^{-5}	724.4	
	23 5 18 1	-	22 5 18 1			262.0416	3.6×10^{-6}	150.3	
	25 3 22 1	-	24 3 21 0			262.0459	4.7×10^{-4}	167.7	
	45 14 32 0	-	45 13 32 1			262.0479	9.2×10^{-6}	605.6	
	45 14 31 0	-	45 13 33 1			262.0631	9.1×10^{-6}	605.6	
	50 14 36 0	-	50 13 37 0			262.0948	5.4×10^{-5}	724.1	
	22 13 10 1	-	22 12 10 0			262.0986	7.5×10^{-6}	207.6	
	22 13 9 1	-	22 12 11 0			262.0986	7.5×10^{-6}	207.6	
	14 6 8 1	-	13 5 8 0			262.1074	1.2×10^{-5}	69.7	
	34 5 29 1	-	33 6 27 0			262.1490	2.4×10^{-6}	311.8	
	58 12 47 1	-	58 10 48 0			262.1613	8.3×10^{-6}	917.2	
	12 7 5 1	-	11 6 5 0			262.7122	1.4×10^{-5}	62.7	
	12 7 6 1	-	11 6 6 0			262.7128	1.4×10^{-5}	62.7	
	26 7 20 0	-	25 7 19 1			262.7212	4.0×10^{-4}	197.4	
	18 5 14 0	-	17 4 13 0			262.7275	2.6×10^{-5}	96.7	
	25 18 7 1	-	24 18 6 0			262.7483	2.1×10^{-4}	319.0	
	25 18 8 1	-	24 18 7 0			262.7483	2.1×10^{-4}	319.0	
	15 13 2 1	-	15 12 4 0			262.7550	3.9×10^{-6}	142.3	
	15 13 3 1	-	15 12 3 0			262.7550	3.9×10^{-6}	142.3	
	25 13 12 1	-	24 13 11 0			262.7564	3.2×10^{-4}	243.0	
	25 13 13 1	-	24 13 12 0			262.7564	3.2×10^{-4}	243.0	
	51 5 46 1	-	51 4 47 1			262.7644	3.1×10^{-5}	664.3	
	51 6 46 1	-	51 5 47 1			262.7705	3.1×10^{-5}	664.3	

Table 2.E.2: continued.

Species	Transition						Frequency (GHz)	A_{ij} (s ⁻¹)	E_{up} (K)
	(J K L M	-	J K L M)						
	14 13 1 1	-	14 12 3 0			262.8042	2.9×10^{-6}	134.9	
	14 13 2 1	-	14 12 2 0			262.8042	2.9×10^{-6}	134.9	
	25 19 6 1	-	24 19 5 0			262.8144	1.9×10^{-4}	337.2	
	25 19 7 1	-	24 19 6 0			262.8144	1.9×10^{-4}	337.2	
	26 3 24 1	-	25 3 23 0			262.8239	4.3×10^{-4}	174.2	
	44 14 31 0	-	44 13 31 1			262.8422	9.2×10^{-6}	583.4	
	13 13 1 1	-	13 12 1 0			262.8455	1.6×10^{-6}	128.1	
	44 14 30 0	-	44 13 32 1			262.8508	9.2×10^{-6}	583.4	
	18 5 14 1	-	17 4 13 1			262.8516	1.6×10^{-5}	97.0	
	25 12 13 1	-	24 12 12 0			262.8661	3.4×10^{-4}	230.8	
	25 12 14 1	-	24 12 13 0			262.8661	3.4×10^{-4}	230.8	
	10 8 2 1	-	9 7 2 0			262.8770	1.7×10^{-5}	58.8	
	10 8 3 1	-	9 7 3 0			262.8770	1.7×10^{-5}	58.8	
	51 5 46 0	-	51 4 47 0			262.8941	3.2×10^{-5}	664.0	
	25 20 5 1	-	24 20 4 0			262.8963	1.6×10^{-4}	356.3	
	25 20 6 1	-	24 20 5 0			262.8963	1.6×10^{-4}	356.3	
	51 6 46 0	-	51 5 47 0			262.9008	3.2×10^{-5}	664.0	
	26 2 24 1	-	25 2 23 0			262.9441	4.4×10^{-4}	174.2	
	24 8 17 0	-	24 6 18 1			262.9878	1.3×10^{-6}	179.2	
	25 21 4 1	-	24 21 3 0			262.9924	1.3×10^{-4}	376.4	
	25 21 5 1	-	24 21 4 0			262.9924	1.3×10^{-4}	376.4	
	25 11 15 1	-	24 11 14 0			263.0395	3.6×10^{-4}	219.6	
	25 11 14 1	-	24 11 13 0			263.0395	3.6×10^{-4}	219.6	
	50 5 45 1	-	50 5 46 0			263.0857	1.2×10^{-5}	640.1	
	50 6 45 1	-	50 4 46 0			263.0967	1.2×10^{-5}	640.1	
	25 22 3 1	-	24 22 2 0			263.1018	1.0×10^{-4}	397.4	
	25 22 4 1	-	24 22 3 0			263.1018	1.0×10^{-4}	397.4	
	25 10 16 1	-	24 10 15 0			263.3025	3.7×10^{-4}	209.3	
	25 10 15 1	-	24 10 14 0			263.3026	3.7×10^{-4}	209.3	
	49 14 35 1	-	49 13 36 1			263.3298	5.6×10^{-5}	699.7	
	25 24 1 1	-	24 24 0 0			263.3565	3.5×10^{-5}	442.4	
	25 24 2 1	-	24 24 1 0			263.3565	3.5×10^{-5}	442.4	
	49 14 35 0	-	49 13 36 0			263.3831	5.4×10^{-5}	699.5	
	29 1 29 0	-	28 1 28 1			263.3921	4.5×10^{-4}	196.9	
	29 0 29 0	-	28 0 28 1			263.3921	4.5×10^{-4}	196.9	
	27 7 20 0	-	27 4 23 0			263.3926	1.4×10^{-6}	211.0	
	26 7 19 0	-	25 7 18 1			263.4155	4.1×10^{-4}	197.5	
	49 14 36 1	-	49 13 37 1			263.4359	5.6×10^{-5}	699.7	
	26 6 21 0	-	25 6 20 1			263.4496	3.8×10^{-4}	191.4	
	27 6 21 0	-	27 3 24 0			263.4667	1.7×10^{-6}	205.7	
	25 5 21 1	-	24 5 20 0			263.4812	4.4×10^{-4}	173.3	
	49 14 36 0	-	49 13 37 0			263.4838	5.3×10^{-5}	699.4	

Table 2.E.2: continued.

Species	Transition						Frequency (GHz)	A_{ij} (s ⁻¹)	E_{up} (K)
	(J K L M	-	J K L M)						
	42 9 34 1	-	41 10 32 0			263.4896	5.6×10^{-6}	487.2	
	43 14 30 0	-	43 13 30 1			263.5672	9.3×10^{-6}	561.7	
	43 14 29 0	-	43 13 31 1			263.5721	9.3×10^{-6}	561.7	
	44 10 35 1	-	43 11 33 0			263.6747	9.7×10^{-6}	539.0	
	47 11 37 0	-	46 12 35 1			263.6974	6.4×10^{-6}	616.8	
	25 9 17 1	-	24 9 16 0			263.6982	3.9×10^{-4}	200.1	
	25 9 16 1	-	24 9 15 0			263.7007	3.9×10^{-4}	200.1	
	36 5 31 1	-	35 6 29 0			263.7327	1.8×10^{-6}	347.0	
gGg'(CH ₂ OH) ₂	60 8 52 0	-	60 8 53 1			259.9804	2.7×10^{-5}	936.2	
	50 14 37 1	-	50 13 38 1			260.0226	1.2×10^{-4}	718.7	
	50 14 37 0	-	50 13 38 0			260.0388	9.8×10^{-5}	718.6	
	47 6 42 0	-	46 6 40 0			260.0511	5.8×10^{-6}	566.1	
	57 4 53 0	-	56 5 51 1			260.0513	1.7×10^{-5}	799.2	
	57 5 53 0	-	56 6 51 1			260.0516	1.7×10^{-5}	799.2	
	30 7 24 0	-	30 4 26 1			260.0601	8.1×10^{-6}	252.2	
	28 0 28 1	-	27 1 27 1			260.1916	1.7×10^{-4}	183.2	
	28 1 28 1	-	27 0 27 1			260.1917	1.7×10^{-4}	183.2	
	28 0 28 0	-	27 1 27 0			260.1931	1.7×10^{-4}	183.1	
	28 1 28 0	-	27 0 27 0			260.1932	1.7×10^{-4}	183.1	
	48 6 43 0	-	47 7 41 1			260.2289	2.0×10^{-5}	588.9	
	54 6 48 1	-	54 6 49 0			260.2348	5.6×10^{-6}	747.1	
	54 7 48 1	-	54 5 49 0			260.2368	8.1×10^{-6}	747.1	
	53 14 40 0	-	52 15 37 0			260.2665	2.2×10^{-5}	795.2	
	53 14 40 1	-	52 15 37 1			260.2737	2.5×10^{-5}	795.2	
	49 5 45 1	-	49 3 46 0			260.2761	5.1×10^{-6}	600.5	
	49 4 45 1	-	49 4 46 0			260.2762	5.0×10^{-6}	600.5	
	53 14 39 0	-	52 15 38 0			260.3312	2.5×10^{-5}	795.2	
	53 14 39 1	-	52 15 38 1			260.3391	2.3×10^{-5}	795.2	
	18 2 16 1	-	17 2 16 1			260.4196	4.2×10^{-6}	87.3	
	35 7 28 1	-	34 8 27 1			261.7538	2.8×10^{-5}	335.9	
	48 5 43 0	-	47 7 41 0			261.7594	3.6×10^{-6}	588.9	
	15 6 9 0	-	14 5 9 1			261.7612	1.0×10^{-4}	76.2	
	49 14 35 1	-	49 13 37 0			261.7776	8.8×10^{-5}	694.2	
	45 3 43 1	-	45 2 44 1			261.7792	2.8×10^{-5}	488.4	
	45 2 43 1	-	45 1 44 1			261.7792	2.8×10^{-5}	488.4	
	51 13 39 0	-	50 14 37 1			261.7989	3.4×10^{-5}	731.2	
	45 3 43 0	-	45 2 44 0			261.8089	2.8×10^{-5}	488.3	
	45 2 43 0	-	45 1 44 0			261.8089	2.8×10^{-5}	488.3	
	30 7 24 1	-	30 4 26 0			261.8350	8.3×10^{-6}	252.3	
	57 8 50 1	-	57 6 51 0			261.9016	1.4×10^{-5}	839.2	
	26 7 19 1	-	26 4 22 1			261.9779	4.5×10^{-6}	196.1	
	41 8 34 1	-	40 9 32 0			261.9959	3.7×10^{-5}	454.8	

Table 2.E.2: continued.

Species	Transition								Frequency (GHz)	A_{ij} (s ⁻¹)	E_{up} (K)
	(J K L M	-	J K L M)		(J K L M)		(J K L M)				
	15 6 10 0	-	14 5 10 1		262.0159		1.1×10^{-4}	76.1			
	43 2 42 1	-	43 1 43 1		262.0203		1.5×10^{-5}	435.8			
	43 1 42 1	-	43 0 43 1		262.0203		1.5×10^{-5}	435.8			
	48 6 43 0	-	47 6 41 0		262.0213		4.4×10^{-6}	588.9			
	51 13 38 0	-	50 14 36 1		262.0401		2.2×10^{-5}	731.2			
	43 1 42 0	-	43 0 43 0		262.0499		1.5×10^{-5}	435.7			
	43 2 42 0	-	43 1 43 0		262.0499		1.5×10^{-5}	435.7			
	26 7 19 0	-	26 4 22 0		262.0555		3.2×10^{-6}	196.0			
	47 4 44 1	-	47 2 45 0		262.0701		4.1×10^{-6}	543.3			
	47 3 44 1	-	47 3 45 0		262.0702		4.1×10^{-6}	543.3			
	12 4 9 0	-	11 1 10 0		262.1539		2.6×10^{-6}	45.9			
	52 6 47 1	-	52 5 48 1		262.7561		6.2×10^{-5}	684.3			
	52 5 47 1	-	52 4 48 1		262.7563		6.2×10^{-5}	684.3			
	48 14 35 1	-	48 13 35 0		262.7790		8.2×10^{-5}	670.1			
	58 4 54 0	-	57 5 52 1		262.7833		1.7×10^{-5}	826.0			
	58 5 54 0	-	57 6 52 1		262.7835		1.8×10^{-5}	826.0			
	52 6 47 0	-	52 5 48 0		262.7850		6.2×10^{-5}	684.3			
	52 5 47 0	-	52 4 48 0		262.7851		6.2×10^{-5}	684.3			
	49 5 44 0	-	48 6 42 1		262.7944		2.3×10^{-5}	612.1			
	56 11 45 1	-	56 10 47 0		262.8056		3.1×10^{-5}	846.1			
	54 10 44 1	-	53 10 43 0		262.8323		7.1×10^{-6}	769.2			
	48 14 34 1	-	48 13 36 0		262.8480		8.7×10^{-5}	670.1			
	15 6 10 1	-	14 5 9 1		262.9243		8.5×10^{-5}	76.2			
	48 6 43 1	-	47 7 41 0		262.9262		2.2×10^{-5}	588.9			
	15 6 10 0	-	14 5 9 0		262.9573		7.7×10^{-5}	76.1			
	51 13 39 1	-	50 14 37 0		262.9728		2.3×10^{-5}	731.3			
	25 4 21 1	-	24 4 20 0		263.0163		1.6×10^{-4}	170.5			
	45 3 43 1	-	45 1 44 0		263.0586		2.9×10^{-6}	488.4			
	45 2 43 1	-	45 2 44 0		263.0586		2.9×10^{-6}	488.4			
	26 3 23 1	-	25 3 22 0		263.0676		9.8×10^{-5}	178.9			
	25 5 20 0	-	24 5 19 1		263.0725		1.6×10^{-4}	173.6			
	25 7 19 0	-	25 4 21 1		263.0877		3.3×10^{-6}	183.1			
	17 5 13 0	-	16 4 13 1		263.1057		9.6×10^{-5}	87.1			
	30 6 25 0	-	30 3 27 1		263.1423		3.9×10^{-6}	246.1			
	48 5 43 1	-	47 6 41 0		263.1708		2.1×10^{-5}	588.9			
	32 5 27 0	-	32 4 29 1		263.1942		6.3×10^{-6}	276.0			
	43 2 42 1	-	43 0 43 0		263.3325		1.6×10^{-6}	435.8			
	44 10 34 0	-	43 11 32 1		263.4029		3.7×10^{-5}	535.1			
	46 14 33 0	-	46 13 33 1		263.5562		8.7×10^{-5}	623.6			
	26 18 8 0	-	25 18 7 1		263.5570		8.8×10^{-5}	328.6			
	26 18 9 0	-	25 18 8 1		263.5570		8.8×10^{-5}	328.6			
	26 17 10 0	-	25 17 9 1		263.5577		9.7×10^{-5}	311.6			

Table 2.E.2: continued.

Species	Transition		Frequency	A_{ij}	E_{up}
	(J K L M - J K L M)		(GHz)	(s ⁻¹)	(K)
	26 17 9 0 - 25 17 8 1		263.5577	9.7×10^{-5}	311.6
	26 19 7 0 - 25 19 6 1		263.5670	7.8×10^{-5}	346.5
	26 19 8 0 - 25 19 7 1		263.5670	7.8×10^{-5}	346.5
	26 16 10 0 - 25 16 9 1		263.5730	1.1×10^{-4}	295.6
	26 16 11 0 - 25 16 10 1		263.5730	1.1×10^{-4}	295.6
	46 14 32 0 - 46 13 34 1		263.5813	8.6×10^{-5}	623.6
	26 20 6 0 - 25 20 5 1		263.5846	6.9×10^{-5}	365.4
	26 20 7 0 - 25 20 6 1		263.5846	6.9×10^{-5}	365.4
	9 9 0 1 - 8 8 1 1		263.5918	1.9×10^{-4}	61.4
	9 9 1 1 - 8 8 0 1		263.5918	1.9×10^{-4}	61.4
	26 21 5 0 - 25 21 4 1		263.6069	5.8×10^{-5}	385.3
	26 21 6 0 - 25 21 5 1		263.6069	5.8×10^{-5}	385.3
	26 15 11 0 - 25 15 10 1		263.6074	1.1×10^{-4}	280.6
	26 15 12 0 - 25 15 11 1		263.6074	1.1×10^{-4}	280.6
	13 7 7 1 - 12 6 6 1		263.6167	1.1×10^{-4}	68.3
	13 7 6 1 - 12 6 7 1		263.6186	1.1×10^{-4}	68.3
	9 9 0 0 - 8 8 1 0		263.6196	1.9×10^{-4}	61.3
	9 9 1 0 - 8 8 0 0		263.6196	1.9×10^{-4}	61.3
	26 22 4 0 - 25 22 3 1		263.6311	4.8×10^{-5}	406.1
	26 22 5 0 - 25 22 4 1		263.6311	4.8×10^{-5}	406.1
	13 7 7 0 - 12 6 6 0		263.6457	1.1×10^{-4}	68.2
	13 7 6 0 - 12 6 7 0		263.6476	1.1×10^{-4}	68.2
	27 2 25 1 - 26 3 24 1		263.6485	8.9×10^{-5}	185.6
	26 23 3 0 - 25 23 2 1		263.6545	3.6×10^{-5}	427.8
	26 23 4 0 - 25 23 3 1		263.6545	3.6×10^{-5}	427.8
	27 2 25 0 - 26 3 24 0		263.6585	1.6×10^{-4}	185.5
	11 8 4 1 - 10 7 3 1		263.6667	1.4×10^{-4}	63.4
	11 8 3 1 - 10 7 4 1		263.6667	1.4×10^{-4}	63.4
	26 14 12 0 - 25 14 11 1		263.6670	1.2×10^{-4}	266.5
	26 14 13 0 - 25 14 12 1		263.6670	1.2×10^{-4}	266.5
	26 24 2 0 - 25 24 1 1		263.6744	2.5×10^{-5}	450.6
	26 24 3 0 - 25 24 2 1		263.6744	2.5×10^{-5}	450.6
	26 25 1 0 - 25 25 0 1		263.6877	1.3×10^{-5}	474.3
	26 25 2 0 - 25 25 1 1		263.6877	1.3×10^{-5}	474.3
	11 8 4 0 - 10 7 3 0		263.6951	1.4×10^{-4}	63.3
	11 8 3 0 - 10 7 4 0		263.6951	1.4×10^{-4}	63.3
	26 13 13 0 - 25 13 12 1		263.7599	1.3×10^{-4}	253.4
	26 13 14 0 - 25 13 13 1		263.7599	1.3×10^{-4}	253.4
	43 9 35 1 - 42 10 32 1		263.7620	2.4×10^{-5}	504.6
CH ₂ OHCHO	27 11 16 - 27 10 17		260.1657	2.8×10^{-4}	283.9
	27 11 17 - 27 10 18		260.1817	2.8×10^{-4}	283.9
	45 9 37 - 45 8 38		261.7386	3.0×10^{-4}	632.0

Table 2.E.2: continued.

Species	Transition						Frequency (GHz)	A_{ij} (s ⁻¹)	E_{up} (K)
	(J K L M	-	J K L M)						
	25 11 14	-	25 10 15			261.7955	2.7×10^{-4}	254.2	
	25 11 15	-	25 10 16			261.7990	2.7×10^{-4}	254.2	
	41 12 29	-	41 11 30			261.8305	3.3×10^{-4}	569.0	
	25 1 24	-	24 2 23			262.0482	4.6×10^{-4}	170.8	
	25 2 24	-	24 2 23			262.0513	6.9×10^{-6}	170.8	
	25 1 24	-	24 1 23			262.0537	6.9×10^{-6}	170.8	
	25 2 24	-	24 1 23			262.0568	4.6×10^{-4}	170.8	
	43 7 36	-	43 6 37			262.7212	2.7×10^{-4}	570.1	
	26 0 26	-	25 1 25			262.7943	5.3×10^{-4}	173.0	
	26 1 26	-	25 1 25			262.7943	7.1×10^{-6}	173.0	
	26 0 26	-	25 0 25			262.7943	7.1×10^{-6}	173.0	
	26 1 26	-	25 0 25			262.7943	5.3×10^{-4}	173.0	
	43 10 34	-	42 11 31			262.7994	6.2×10^{-5}	593.1	
	51 14 37	-	50 15 36			262.9430	6.9×10^{-5}	861.3	
	23 11 12	-	23 10 13			263.0488	2.6×10^{-4}	226.9	
	23 11 13	-	23 10 14			263.0495	2.6×10^{-4}	226.9	
	38 5 33	-	38 4 34			263.3786	2.2×10^{-4}	433.8	
	30 1 29	-	30 0 30			263.4168	5.6×10^{-5}	240.8	
	30 2 29	-	30 1 30			263.4168	5.6×10^{-5}	240.8	
	22 11 11	-	22 10 12			263.5580	2.5×10^{-4}	214.1	
	22 11 12	-	22 10 13			263.5582	2.5×10^{-4}	214.1	
	46 8 38	-	46 7 39			263.5591	3.0×10^{-4}	657.2	
	22 6 16	-	21 6 15			263.7526	6.6×10^{-6}	164.3	
	38 6 33	-	38 5 34			263.7558	2.2×10^{-4}	433.8	
	H ₂ CCO	13 1 13	-	12 1 12			260.1920	2.0×10^{-4}	100.5
		13 8 5	-	12 8 4			261.8202	1.3×10^{-4}	918.9
		13 8 6	-	12 8 5			261.8202	1.3×10^{-4}	918.9
		13 7 6	-	12 7 5			262.0435	1.5×10^{-4}	725.0
13 7 7		-	12 7 6			262.0435	1.5×10^{-4}	725.0	
13 2 11		-	12 2 10			262.7609	2.0×10^{-4}	140.5	
t-HCOOH	12 0 12	-	11 0 11			262.1036	1.9×10^{-4}	82.8	
	20 3 17	-	20 2 18			263.0581	5.1×10^{-6}	257.2	
	3 2 2	-	2 1 1			263.7624	3.4×10^{-6}	19.2	

Table 2.E.3: List of ALMA image properties from program 2017.1.01774.S.

	B1-b ¹			B1-c			S68N ²			SMM3					
	Band 3	Band 6	C43-3	Band 3	Band 6	C43-4	Band 3	Band 6	C43-2	Band 3	Band 6	C43-4	Band 3	Band 6	C43-2
Configuration	C43-3	C43-4	C43-3	C43-3	C43-4	C43-4	C43-2	C43-4	C43-2	C43-2	C43-4	C43-4	C43-2	C43-2	C43-2
Beam (")	2.1×1.4	0.58×0.39	2.1×1.4	2.1×1.4	0.58×0.39	0.58×0.39	2.8×1.8	2.8×1.8	0.46×0.42	0.46×0.42	2.8×1.8	2.8×1.8	0.46×0.42	0.46×0.42	2.8×1.8
LAS (")	16	6	16	16	6	6	22	22	6	6	22	22	6	6	22
ΔV (km s ⁻¹)	0.2 / 0.4	0.14	0.2 / 0.4	0.2 / 0.4	0.14	0.14	0.17 / 0.32	0.17 / 0.32	0.14	0.14	0.17 / 0.32	0.17 / 0.32	0.14	0.14	0.17 / 0.32
Continuum rms (mJy)	8.5	5.4	14.4	14.4	24.4	24.4	14.6	14.6	9.2	9.2	14.6	14.6	9.2	9.2	5.1
Line rms (K)	0.05	0.16	0.06	0.06	0.14	0.14	0.04	0.04	0.15	0.15	0.06	0.06	0.15	0.15	0.06
Flux uncertainty (%)	3	12	3	3	12	12	5	5	9	9	5	5	9	9	5

Notes. ⁽¹⁾ Including B1-bN and B1-bS. ⁽²⁾ Including Ser-emb 8 (N).

Chapter 3

Importance of source structure on complex organics emission

I. Observations of CH₃OH from low-mass to high-mass protostars

M. L. van Gelder, P. Nazari, B. Tabone, A. Ahmadi, E. F. van Dishoeck, M. T. Beltrán, G. A. Fuller, N. Sakai, Á. Sánchez-Monge, P. Schilke, Y.-L. Yang, Y. Zhang

A&A 662, A67 (2022)

Abstract

Context. Complex organic molecules (COMs) are often observed toward embedded Class 0 and I protostars. However, not all Class 0 and I protostars exhibit COM emission.

Aims. The aim is to study variations in methanol (CH_3OH) emission and use this as an observational tracer of hot cores to test if the absence of CH_3OH emission can be linked to source properties.

Methods. A sample of 148 low-mass and high-mass protostars is investigated using new and archival observations with the Atacama Large Millimeter/submillimeter Array (ALMA) that contain lines of CH_3OH and its isotopologues. Data for an additional 36 sources are added from the literature, giving a total of 184 different sources. The warm ($T \gtrsim 100$ K) gaseous CH_3OH mass, $M_{\text{CH}_3\text{OH}}$, is determined for each source using primarily optically thin isotopologues and is compared to a simple toy model of a spherically symmetric infalling envelope that is passively heated by the central protostar.

Results. A scatter of more than four orders of magnitude is found for $M_{\text{CH}_3\text{OH}}$ among the low-mass protostars, with values ranging between $10^{-7} M_\odot$ and $\lesssim 10^{-11} M_\odot$. On average, Class I protostellar systems seem to have less warm $M_{\text{CH}_3\text{OH}}$ ($\lesssim 10^{-10} M_\odot$) than younger Class 0 sources ($\sim 10^{-7} M_\odot$). High-mass sources in our sample show more warm $M_{\text{CH}_3\text{OH}}$, up to $\sim 10^{-7} - 10^{-3} M_\odot$. To take into account the effect of the source's overall mass on $M_{\text{CH}_3\text{OH}}$, a normalized CH_3OH mass is defined as $M_{\text{CH}_3\text{OH}}/M_{\text{dust},0}$, where $M_{\text{dust},0}$ is the cold plus warm dust mass in the disk and inner envelope within a fixed radius measured from the ALMA dust continuum. A correlation between $M_{\text{CH}_3\text{OH}}/M_{\text{dust},0}$ and L_{bol} is found. Excluding upper limits, a simple power-law fit to the normalized warm CH_3OH masses results in $M_{\text{CH}_3\text{OH}}/M_{\text{dust},0} \propto L_{\text{bol}}^{0.70 \pm 0.05}$ over an L_{bol} range of $10^{-1} - 10^6 L_\odot$. This is in good agreement with the toy model, which predicts that the normalized $M_{\text{CH}_3\text{OH}}$ increases with $L_{\text{bol}}^{0.75}$ due to the snow line moving outward. Sources for which the size of the disk is equivalent to or smaller than the estimated 100 K radius fall within the 3σ range of the best-fit power-law model, whereas sources with significantly larger disks show normalized warm CH_3OH masses that are up to two orders of magnitude lower.

Conclusions. The agreement between sources that are rich in CH_3OH with the toy model of a spherically symmetric infalling envelope implies that the thermal structure of the envelopes in these sources is likely not strongly affected by a disk. However, based on the disagreement between the toy model and sources that show less warm CH_3OH mass, we suggest that source structure such as a disk can result in colder gas and thus fewer COMs in the gas phase. Additionally, optically thick dust can hide the emission of COMs. Advanced modeling is necessary to quantify the effects of a disk and/or continuum optical depth on the presence of gaseous COMs in young protostellar systems.

3.1 Introduction

Complex organic molecules (COMs), molecules with six or more atoms (see Herbst & van Dishoeck 2009; Jørgensen et al. 2020, for reviews), are commonly observed toward both low-mass and high-mass young embedded protostellar systems (e.g., Belloche et al. 2013; Ceccarelli et al. 2014; Jørgensen et al. 2016; Bøgelund et al. 2019; van Gelder et al. 2020; Nazari et al. 2021; Yang et al. 2021). They are also detected in protostellar outflows (e.g., Arce et al. 2008; Codella et al. 2017; Tychoniec et al. 2021) and in low abundances in cold clouds (Bacmann et al. 2012; Scibelli et al. 2021; Jiménez-Serra et al. 2021). The simplest COMs, such as methanol (CH_3OH) and methyl cyanide (CH_3CN), have also been detected toward more evolved low-mass Class II systems (Walsh et al. 2014; Öberg et al. 2015), in some cases hinting at an inheritance between pre-stellar cores and protoplanetary disks (Booth et al. 2021; van der Marel et al. 2021). It is particularly important to assess the chemical complexity during the embedded Class 0/I phases of star formation since planet formation is thought to start early (e.g., Harsono et al. 2018; Manara et al. 2018; Alves et al. 2020; Tychoniec et al. 2020).

The earliest Class 0 and I phases are also most suitable for studying COMs in the gas phase since the temperatures in the inner hot cores are high enough to sublimate COMs from ices (e.g., van 't Hoff et al. 2020c). However, not all Class 0 and I sources show emission from COMs, even when observed at high sensitivity with interferometers such as the Atacama Large Millimeter/submillimeter Array (ALMA) and the Northern Extended Millimeter Array (NOEMA). Yang et al. (2021) find that CH_3OH , the most abundant COM, is present in only 56 % of the 50 surveyed embedded sources in Perseus. Similarly, Belloche et al. (2020) detect emission from CH_3OH toward 50 % of the 26 low-mass protostars in their sample. A main question remains as to why some embedded sources show emission of COMs while others do not.

One possible explanation for the absence of gaseous COM emission could be the presence of a disk that casts a shadow on the inner envelope and therefore decreases the temperature throughout the system (Persson et al. 2016; Murillo et al. 2015, 2018). Most COMs will then likely be frozen out in the inner envelopes and cold midplanes of these disks. For low-mass sources in the Class 0 phase, these disks are usually small ($< 10 - 50$ au; Segura-Cox et al. 2018; Maury et al. 2019), but larger disks of up to ~ 100 au have also been observed (e.g., Tobin et al. 2012; Murillo et al. 2013; Sakai et al. 2019). Around more evolved Class I systems, larger disks are more common (e.g., Harsono et al. 2014; Yen et al. 2017; Artur de la Villarmois et al. 2019), although some Class I sources still also show small disks of < 10 au (Segura-Cox et al. 2018). Furthermore, disk-like structures seem to be present around some high-mass protostars (e.g., Sánchez-Monge et al. 2013; Johnston et al. 2015; Ilee et al. 2016; Maud et al. 2019; Zhang et al. 2019; Moscadelli et al. 2021), but not all (Beltrán & de Wit 2016). The effect of a disk on the presence of COM emission, however, remains largely unknown.

Alternatively, optically thick dust at (sub)millimeter wavelengths can hide the emission of COMs in protostellar systems. This was recently shown to be the case in NGC 1333 IRAS4A1, where De Simone et al. (2020) used the Very Large Array

(VLA) to show that this source, which was thought to be poor in COMs based on observations with ALMA (López-Sepulcre et al. 2017), has emission of CH_3OH at centimeter wavelengths. Similarly, Rivilla et al. (2017) found high dust opacities affecting the molecular lines of COMs toward the high-mass source G31.41+0.31.

Some sources may also be intrinsically deficient in COMs, although this is not expected based on the large columns of CH_3OH ice observed toward pre-stellar and starless cores (e.g., Chu et al. 2020; Goto et al. 2021) and many protostellar systems (Pontoppidan et al. 2003a; Boogert et al. 2008; Öberg et al. 2011; Bottinelli et al. 2010; Perotti et al. 2020, 2021). Furthermore, recent chemical models of the collapse from pre-stellar core to protostellar system do not show a significant destruction of COMs, including CH_3OH (Drozdovskaya et al. 2014; Aikawa et al. 2020).

In this work, the amount of warm CH_3OH is determined for a large sample of 148 sources, covering both low-mass and high-mass protostellar systems. Furthermore, literature values of an additional 36 sources are collected, giving a total sample of 184 sources. The goal is to determine, from an observational point of view, how source structures, such as a disk or optically thick dust, affect gaseous COM emission. Optically thin isotopologues of CH_3OH are used to mitigate line optical depth effects. The reduction of the ALMA data sets used in this work and the determination of the amount of warm CH_3OH from the ALMA observations are described in Sect. 3.2. The results are presented in Sect. 3.3 and discussed in Sect. 3.4. Our main conclusions are summarized in Sect. 3.5. In this paper, the amount of warm CH_3OH is only compared to a simple analytic toy model of a spherically symmetric infalling envelope passively heated by the luminosity of the protostar; a full comparison to sophisticated disk plus envelope models that include dust optical depth effects is presented in a companion paper (Nazari et al. 2022b).

3.2 Methodology

3.2.1 Observations and archival data

The data analyzed in this work consist of a combination of multiple ALMA data sets that encompass 148 different sources. These data sets are all taken in Band 6 (~ 1.2 mm) but in different setups, covering different transitions of CH_3OH and its ^{13}C and ^{18}O isotopologues. Moreover, the observations are taken with different beam sizes and sensitivities, and the observed sources are located at various distances, which need to be taken into account in the analysis (see Sect. 3.2.3). The full list of sources and their observational properties are presented in Table 3.A.1.

The reduction of the 2017.1.01174.S (PI: E.F. van Dishoeck) data set, which contains four protostars in Perseus and three in Serpens, is described by van Gelder et al. (2020). Only the Band 6 data with a $0.45''$ beam, which contain transitions of both the ^{13}C and ^{18}O isotopologues of CH_3OH , are used in this work. Three out of seven sources in this program show emission from COMs. For Serpens SMM3, archival pipeline imaged product data are used from the 2017.1.01350.S (PI: Ł. Tychoniec) program (Tychoniec et al. 2021).

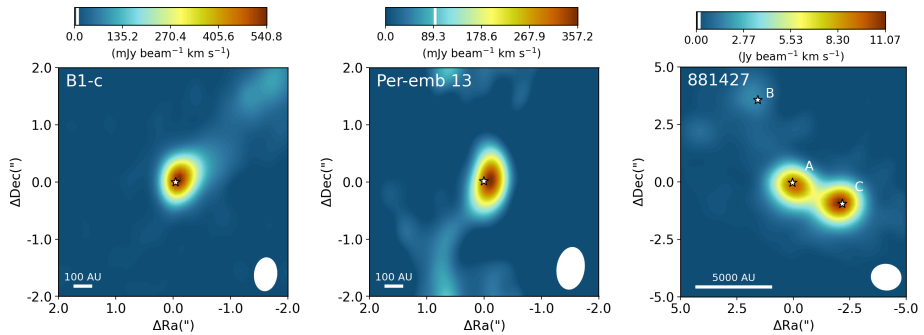


Figure 3.1: Integrated intensity maps of the $\text{CH}_3\text{OH } 2_{1,1} - 1_{0,1}$ line for the low-mass protostar B1-c (left), the $\text{CH}_3\text{OH } 5_{1,4} - 4_{1,3}$ line for the low-mass protostar Per-emb 13 from PEACHES (middle), and the $\text{CH}_3\text{OH } 8_{0,8} - 7_{1,6}$ line for the high-mass 881427 cluster (right). The color scale is shown on top of each image. The images are integrated over $[-5, 5] \text{ km s}^{-1}$ with respect to the V_{lsr} . The white vertical line in the colorbar indicates the 3σ threshold. The peaks in the continuum are indicated with the white stars. The white ellipse in the lower right of each image depicts the beam size, and in the lower left a physical scale bar is displayed.

In total, 50 protostars in Perseus were observed in the Perseus ALMA Chemistry Survey (PEACHES) in programs 2016.1.01501.S and 2017.1.01462.S (PI: N. Sakai). The goal of this program is to probe the complex chemistry toward embedded protostars in Perseus at $\sim 0.4''$ (i.e., 150 au) scales. The full list of PEACHES sources is presented in Table 3.A.1. The reduction and imaging of the PEACHES data are described in detail by Yang et al. (2021). Only two transitions of $\text{CH}_3^{18}\text{OH}$ are covered at low spectral resolution ($\sim 1.2 \text{ km s}^{-1}$). Furthermore, the PEACHES data contain three transitions of $^{13}\text{CH}_3\text{OH}$, of which the 259.03649 GHz line is blended with HDCO for most COM-rich sources. Several strong transitions of the main CH_3OH isotopologue, which likely produce optically thick lines, are covered. All PEACHES sources were also observed in the VLA Nascent Disk and Multiplicity Survey (VANDAM), which showed that $\sim 50\%$ of the Class 0 and $\sim 20\%$ of the Class I sources are part of multiple systems (Tobin et al. 2016). Moreover, the presence of disks at $> 10 \text{ au}$ scales around several Perseus sources was presented by Segura-Cox et al. (2018).

The ALMA Evolutionary study of High Mass Protocluster Formation in the Galaxy (ALMAGAL) survey (2019.1.00195.L; PI: S. Molinari) is a large program that targeted over 1000 dense clumps with $M > 500 M_\odot$ and $d < 7.5 \text{ kpc}$ in Band 6. The ALMAGAL sources were targeted based on compact sources within the *Herschel* Hi-GAL survey (Molinari et al. 2010; Elia et al. 2017, 2021). In this paper, a subsample of 40 high-mass protostellar cores has been selected based on a combination of high bolometric luminosity ($\gtrsim 1000 L_\odot$) and richness in spectral lines. Moreover, only archival data with a beam size smaller than $2''$ ($\sim 1000\text{--}5000 \text{ au}$) that were public in February 2021 are included. As discussed below, this selection introduces a bias. The data are pipeline-calibrated and imaged with

Common Astronomy Software Applications¹ (CASA; McMullin et al. 2007) version 5.6.1. The ALMAGAL data cover multiple transitions of (likely) optically thick CH_3OH , four transitions of $^{13}\text{CH}_3\text{OH}$, and nine transitions of $\text{CH}_3^{18}\text{OH}$. Especially for the line-rich sources with broad lines, many of these lines are unfortunately affected by line blending.

The integrated intensity maps of CH_3OH are presented in Fig. 3.1 for a few representative sources: B1-c from the 2017.1.01174.S program, Per-emb 13 (NGC 1333 IRAS 4B) from PEACHES, and 881427 from ALMAGAL. For B1-c and Per-emb 13, some outflow emission is evident, but this does not influence the analysis below. The position of the continuum emission peak for all sources is listed in Table 3.A.1, and the peak continuum flux within the central beam for each source is listed in Table 3.A.2. All spectra are extracted from the central pixel on the continuum peak positions.

Several of the sources used in this work (e.g., 881427 in Fig. 3.1) are resolved into small clusters in the higher-resolution ALMA images (see Table 3.A.1). However, their luminosity is often estimated from *Herschel* observations within a $\sim 15''$ beam (Murillo et al. 2016; Elia et al. 2017, 2021), and therefore luminosity estimates of the individual cores are unknown. In such cases, as a zeroth-order approximation, the luminosity of each individual core was estimated by dividing the luminosity over the multiple sources. The fraction attributed to each source was computed as the peak continuum flux of the corresponding core divided by the sum of peak continuum fluxes from all cores.

3.2.2 Deriving the column density

The column density of CH_3OH , $N_{\text{CH}_3\text{OH}}$, was calculated from the spectrum through local thermodynamic equilibrium models using the spectral analysis tool CASSIS² (Vastel et al. 2015). Since spectral lines originating from the main isotopologue of CH_3OH are likely optically thick, lines from optically thin isotopologues such as $^{13}\text{CH}_3\text{OH}$ and $\text{CH}_3^{18}\text{OH}$ need to be invoked to get an accurate estimate of the column density. The $^{12}\text{C}/^{13}\text{C}$ and $^{16}\text{O}/^{18}\text{O}$ ratios are dependent on the galactocentric distance and are determined using the relations of Milam et al. (2005) and Wilson & Rood (1994), respectively. For the local interstellar medium, this results in ratios of $^{12}\text{C}/^{13}\text{C} \sim 70$ and $^{16}\text{O}/^{18}\text{O} \sim 560$. The full line lists were acquired from the CDMS catalog³ (Müller et al. 2001, 2005; Endres et al. 2016) and are presented for each data set in Appendix 3.B.

For the PEACHES and ALMAGAL data sets, generally only a few lines of each isotopologue are detected. Therefore, for simplicity, an excitation temperature of $T_{\text{ex}} = 150$ K was assumed, which is roughly the average of what is observed toward both low-mass and high-mass protostellar systems (typical values lie in the range of 100 – 300 K; e.g., Bøgelund et al. 2018, 2019; van Gelder et al. 2020; Yang et al. 2021). Changing the excitation temperature within the 100 – 300 K range leads to only a factor of ~ 2 variation in the derived column densities since lines

¹<https://casa.nrao.edu/>

²<http://cassis.irap.omp.eu/>

³<https://cdms.astro.uni-koeln.de/>

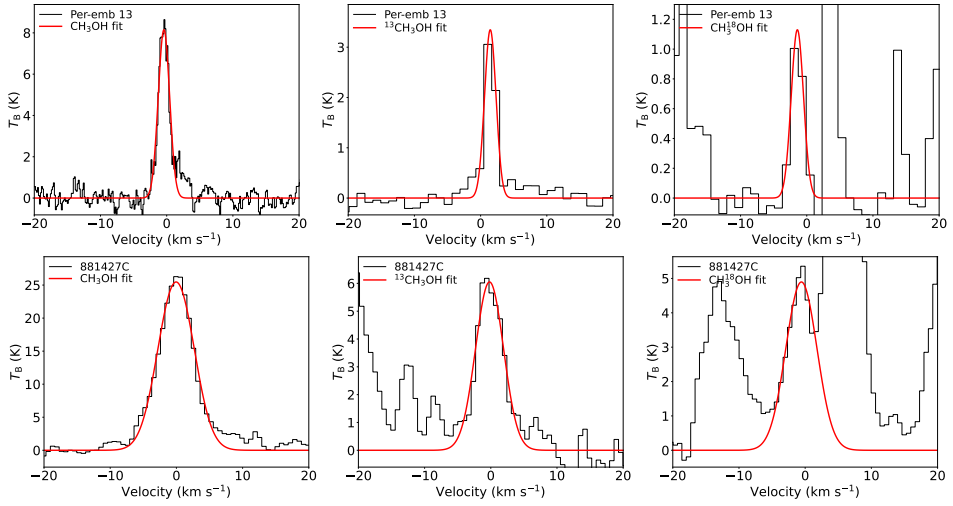


Figure 3.2: Spectral line fits of CH_3OH (left), $^{13}\text{CH}_3\text{OH}$ (middle), and $\text{CH}_3^{18}\text{OH}$ (right) for Per-emb 13 from the PEACHES sample (top row) and 881427C from the ALMAGAL sample (bottom row). The data corrected for the V_{LSR} are shown in black, and the fit for $T_{\text{ex}} = 150$ K is shown in red. All lines are $> 3\sigma$ detections. The top row shows the CH_3OH $5_{1,4} - 4_{1,3}$ ($E_{\text{up}} = 50$ K), $^{13}\text{CH}_3\text{OH}$ $23_{3,20} - 23_{2,21}$ ($E_{\text{up}} = 675$ K), and $\text{CH}_3^{18}\text{OH}$ $11_{2,10} - 10_{3,7}$ ($E_{\text{up}} = 184$ K) lines, and the bottom row shows the CH_3OH $8_{0,8} - 7_{1,6}$ ($E_{\text{up}} = 97$ K), $^{13}\text{CH}_3\text{OH}$ $14_{1,13} - 13_{2,12}$ ($E_{\text{up}} = 254$ K), and $\text{CH}_3^{18}\text{OH}$ $8_{1,8} - 7_{0,7}$ ($E_{\text{up}} = 86$ K) lines.

with a range of E_{up} from ~ 50 K to ~ 800 K are available for the analysis. The column density, N , of each isotopologue is derived separately using a grid fitting method similar to that presented in van Gelder et al. (2020), with N and the full width at half maximum (FWHM) of the line as free parameters. The size of the emitting region was set equal to the beam size and is presented for each source in Table 3.A.2. To exclude emission associated with outflows, only narrow lines ($\text{FWHM} \lesssim \text{few km s}^{-1}$) with $E_{\text{up}} \gtrsim 50$ K were used in the analysis. Moreover, blended lines were excluded from the fit. The 2σ uncertainty on N was derived from the grid. Careful inspection by eye was conducted to test the validity of the fits and derived column densities.

In Fig. 3.2, fits to lines of CH_3OH and its isotopologues are presented for Per-emb 13 from the PEACHES sample and 881427C from the ALMAGAL sample. All lines in Fig. 3.2 are $> 3\sigma$ detections. The $\text{CH}_3^{18}\text{OH}$ lines suffer from line blending in 881427C as well as in many other PEACHES and ALMAGAL sources. Since all other lines originating from $^{13}\text{CH}_3\text{OH}$ in the PEACHES data suffer from line blending (e.g., with HDCO), the $^{13}\text{CH}_3\text{OH}$ $23_{3,20} - 23_{2,21}$ ($E_{\text{up}} = 675$ K) line in Fig. 3.2 often provides the only constraint on the column density.

The derived CH_3OH column densities are presented in Table 3.A.2. The column densities of the sources in the 2017.1.01174.S and 2017.1.01350.S data sets were derived by van Gelder et al. (2020). Only the Band 6 results are used in this

work. When no lines originating from $\text{CH}_3^{18}\text{OH}$ were detected, the column density of CH_3OH was derived from $^{13}\text{CH}_3\text{OH}$ lines. In cases where only upper limits on the column densities of both $^{13}\text{CH}_3\text{OH}$ and $\text{CH}_3^{18}\text{OH}$ could be derived, $N_{\text{CH}_3\text{OH}}$ was calculated by setting the 3σ upper limit based on scaling the 3σ upper limit of $^{13}\text{CH}_3\text{OH}$ and the lower limit based on the main isotopologue. This situation results in rather large error bars on $N_{\text{CH}_3\text{OH}}$ for 9 low-mass and 25 high-mass sources. When the main isotopologue of CH_3OH is also not detected, the 3σ upper limit is reported. The upper limits on $N_{\text{CH}_3\text{OH}}$ are not homogeneous across the full sample since they are derived from various ALMA programs with a range of sensitivities covering different transitions of CH_3OH with different upper energy levels and Einstein A_{ij} coefficients. For sources with detections, this inhomogeneity is not present, except for the uncertainty based on the assumed T_{ex} .

Besides the sources presented in Table 3.A.1, other sources with or without warm ($T \gtrsim 100$ K) CH_3OH detections are also included from the literature. These sources include well-known low-mass hot cores, such as IRAS 16293-2422 (Jørgensen et al. 2016, 2018; Manigand et al. 2020), NGC 1333 IRAS4A (De Simone et al. 2020), BHR 71 (Yang et al. 2020), and L438 (Jacobsen et al. 2019), but also sources with disks that show emission of COMs, such as HH 212 (Lee et al. 2017c, 2019a), and outbursting sources, such as SVS 13A (Bianchi et al. 2017a; Hsieh et al. 2019) and V883 Ori (van 't Hoff et al. 2018b; Lee et al. 2019b). Non-detections of CH_3OH , such as found for several Class I sources in Ophiuchus, are also included (Artur de la Villarmois et al. 2019). Moreover, classical high-mass hot cores, such as AFGL 4176 (Bøgelund et al. 2019), NGC 6334I (Bøgelund et al. 2018), and Sgr B2 (Belloche et al. 2013; Müller et al. 2016; Bonfand et al. 2017), are taken into account. A 20% uncertainty on $N_{\text{CH}_3\text{OH}}$ was assumed for literature sources where no uncertainty on the column density was reported. The full list of literature sources is also presented in Table 3.A.2. Including the 36 literature sources, the total sample studied in this work contains 184 unique sources (some sources, such as B1-bS and Per-emb 44 (SVS 13A), are covered in both our data and literature studies).

3.2.3 Calculating the warm methanol mass

In order to get a measurement of the amount of warm ($T \gtrsim 100$ K) CH_3OH gas, observational dependences should be taken into account. Column densities provide a measure of the amount of CH_3OH , but they depend on the assumed size of the emitting region. From the 184 sources studied in this work, ~ 30 (mostly high-mass) sources show spatially resolved CH_3OH emission; nevertheless, in these cases most of the CH_3OH emission is still located within the central beam. Furthermore, emission from $^{13}\text{CH}_3\text{OH}$ and $\text{CH}_3^{18}\text{OH}$, which gives more stringent constraints on $N_{\text{CH}_3\text{OH}}$, is only spatially resolved in a few high-mass sources. Therefore, in this work the size of the emitting region is assumed to be equal to the size of the beam. Because our sample consists of many different types of sources at a range of distances taken with different ALMA programs, all derived column densities were multiplied by the physical area of the beam to derive the total number of

CH_3OH molecules, $\mathcal{N}_{\text{CH}_3\text{OH}}$, within the beam,

$$\mathcal{N}_{\text{CH}_3\text{OH}} = N_{\text{CH}_3\text{OH}} \pi R_{\text{beam}}^2. \quad (3.1)$$

Here, $N_{\text{CH}_3\text{OH}}$ is the observed column density in the beam and R_{beam} is the physical radius of the beam,

$$R_{\text{beam}} = d \tan \left(\frac{\theta_{\text{beam}}}{2} \right), \quad (3.2)$$

with d the distance to the source and θ_{beam} the angular size of the beam. For some of the literature sources, the adopted emitting region is different from the beam size (e.g., Bianchi et al. 2017a; Jacobsen et al. 2019). In these cases, the assumed size of the emitting region was adopted in the computation of $\mathcal{N}_{\text{CH}_3\text{OH}}$ (see the θ_{source} column in Table 3.A.2). However, it is important to note that the assumed size of the emitting region does not alter the resulting value of $\mathcal{N}_{\text{CH}_3\text{OH}}$ as long as the beam-averaged column density is derived from optically thin lines (i.e., from the ^{13}C or ^{18}O isotopologues). If the lines are optically thick, this approach provides a lower limit on $\mathcal{N}_{\text{CH}_3\text{OH}}$. Finally, the warm gaseous CH_3OH mass, $M_{\text{CH}_3\text{OH}}$, was computed through

$$M_{\text{CH}_3\text{OH}} = \mathcal{N}_{\text{CH}_3\text{OH}} m_{\text{CH}_3\text{OH}}, \quad (3.3)$$

where $m_{\text{CH}_3\text{OH}}$ is the molar mass of a methanol molecule of 5.32×10^{-23} gr or $2.67 \times 10^{-56} M_{\odot}$.

3.3 Results

3.3.1 Amount of warm methanol from low to high mass

The derived values of $M_{\text{CH}_3\text{OH}}$ are presented in Table 3.A.2 for all sources. In Fig. 3.3, $M_{\text{CH}_3\text{OH}}$ is plotted as a function of the bolometric luminosity, L_{bol} . A clear trend in $M_{\text{CH}_3\text{OH}}$ as a function of L_{bol} is evident: more luminous sources have more CH_3OH in the gas phase. Excluding upper limits, a simple power-law fit to the results gives a $M_{\text{CH}_3\text{OH}} \propto L_{\text{bol}}^{0.78 \pm 0.04}$ relation, which is presented in Fig. 3.3 along with the 3σ uncertainty on the fit. The positive correlation found here agrees well with that found for low-mass Class 0 protostars in Orion (Hsu et al. 2022). The positive correlation is in line with the expectation that $M_{\text{CH}_3\text{OH}}$ increases with L_{bol} since sources with a higher luminosity are expected to have their CH_3OH snow line at larger radii, which results in more CH_3OH in the gas phase. Furthermore, the envelopes of sources with higher L_{bol} are more massive and thus contain more CH_3OH mass in the first place. However, the result of the fit strongly depends on the difference in warm $M_{\text{CH}_3\text{OH}}$ between the low-mass ($L_{\text{bol}} \lesssim 100 L_{\odot}$) and high-mass ($L_{\text{bol}} \gtrsim 1000 L_{\odot}$) protostars. Fitting these two subsamples individually gives a weaker correlation between $M_{\text{CH}_3\text{OH}}$ and L_{bol} ($M_{\text{CH}_3\text{OH}} \propto L_{\text{bol}}^{0.42 \pm 0.12}$ and $M_{\text{CH}_3\text{OH}} \propto L_{\text{bol}}^{0.34 \pm 0.13}$ for low-mass and high-mass protostars, respectively). Due to the large uncertainties on the fits of both subsamples, no significant conclusions can be made.

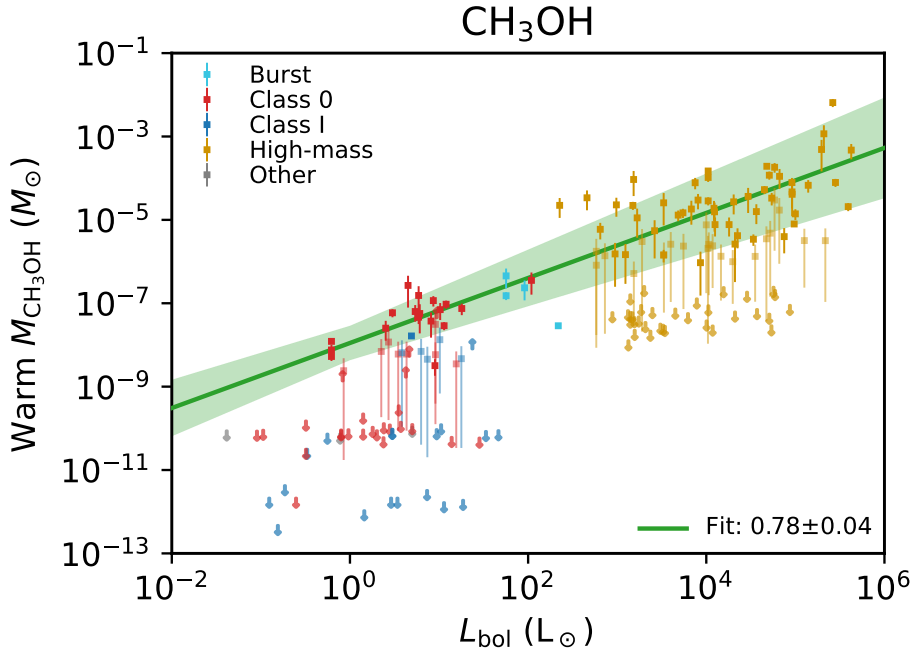


Figure 3.3: Warm CH_3OH mass as a function of the bolometric luminosity. Different colors denote different observational classes, and all sources with $L_{\text{bol}} > 1000 L_{\odot}$ are classified as high-mass sources. Additionally, sources that are suggested to currently be in a burst phase (e.g., V883 Ori and IRAS 2A; van 't Hoff et al. 2018b; Lee et al. 2019b; Hsieh et al. 2019) are highlighted. Sources in the "other" category include Class II and flat spectrum sources. The green line indicates the best-fit power-law model to the data points (excluding the upper limits) and the green shaded area the 3σ uncertainty on the fit.

For the lower-mass sources ($L_{\text{bol}} \lesssim 100 L_{\odot}$), a scatter of more than four orders of magnitude is present. On average, Class 0 sources seem to show more CH_3OH mass ($\sim 10^{-7} M_{\odot}$) compared to more evolved Class I sources ($\lesssim 10^{-10} M_{\odot}$). In fact, for the majority of the Class I sources, only upper limits can be derived on $M_{\text{CH}_3\text{OH}}$ (e.g., the Class I sources in Ophiuchus; Artur de la Villarmois et al. 2019), but some Class I sources do show emission of COMs, including CH_3OH (e.g., L1551 IRS5; Bianchi et al. 2020). Moreover, known bursting sources, such as IRAS 2A (or Per-emb 27; Hsieh et al. 2019; Yang et al. 2021) and V883 Ori (van 't Hoff et al. 2018b; Lee et al. 2019b), show a large amount of CH_3OH mass despite the presence of disk-like structures (Segura-Cox et al. 2018; Maury et al. 2019).

The high-mass ($L_{\text{bol}} \gtrsim 1000 L_{\odot}$) sources show higher gaseous CH_3OH masses (i.e., $10^{-7} - 10^{-3} M_{\odot}$) compared to the lower-mass sources. A similar scatter of about four orders of magnitude is present, but fewer sources seem to show lower CH_3OH masses. This is likely a sample bias effect since mostly very line-

rich sources from the ALMAGAL data set are analyzed, whereas many ALMAGAL sources show upper limits. Hence, in reality, more sources with $M_{\text{CH}_3\text{OH}} \lesssim 10^{-7} M_\odot$ will be present among the high-mass sources as well. Alternatively, the emitting region in high-mass sources could be larger than the typical disk sizes reached, resulting in fewer sources for which the disk has a significant effect on the thermal structure.

3.3.2 Comparison to spherically symmetric infalling envelope

To quantify the effect of the luminosity on the amount of warm methanol, a simple toy model of a spherically symmetric infalling envelope was constructed (see Appendix 3.C). In this simple toy model, the warm methanol mass is linked to L_{bol} ,

$$M_{\text{CH}_3\text{OH}} \propto M_0 L_{\text{bol}}^{3/4}, \quad (3.4)$$

where M_0 is the total warm plus cold mass contained within a reference radius, R_0 . As qualitatively discussed in Sect. 3.3.1, the warm methanol mass is thus dependent on both the envelope mass within a reference radius (or, alternatively, the density at a reference radius) and the luminosity of the source. The former is straightforward since a higher mass will result in a higher initial methanol mass. The latter is the result of the snow line of CH_3OH moving to larger radii for larger luminosities.

Hence, to probe the effect of the luminosity on the snow line radius in our observations, the values of $M_{\text{CH}_3\text{OH}}$ presented in Sect. 3.3.1 should be divided by a reference mass, M_0 , defined within a reference radius, R_0 . The protostellar envelope mass, M_{env} , is not as good an option as M_0 since it is not consistently constrained for many sources and depends on the adopted outer radius (e.g., Kristensen et al. 2012). Therefore, in this work the dust mass within a common arbitrary radius of 200 au, denoted as $M_{\text{dust},0}$, is used as the reference mass. The computation of $M_{\text{dust},0}$ from the continuum flux is detailed in Appendix 3.D, and the derived values are reported in Table 3.A.2. The choice for $R_0 = 200$ au is based on it being larger than the typical disk size of low-mass protostars. Despite 200 au being smaller than the typical size of a high-mass hot core, we do not expect this to influence our analysis since the scale on which the continuum flux is measured (> 1000 au) is dominated by the envelope. Furthermore, the continuum flux on 200 au scales is not filtered out in either the PEACHES or ALMAGAL observations.

In Fig. 3.4, the normalized warm gaseous CH_3OH mass, $M_{\text{CH}_3\text{OH}}/M_{\text{dust},0}$, is presented as a function of L_{bol} . It is important to note that the $M_{\text{CH}_3\text{OH}}/M_{\text{dust},0}$ ratio is a dimensionless quantity and does not represent an abundance of CH_3OH in the system. The warm gaseous CH_3OH mass was derived from a region taken to have a size similar to that of the beam. The dust mass, $M_{\text{dust},0}$, includes both cold and warm material in the disk and envelope and is defined as the mass within the fixed radius, $R_0 = 200$ au. For most low-mass sources, the snow line is expected to be well within 200 au, whereas for high-mass sources the snow line is at radii

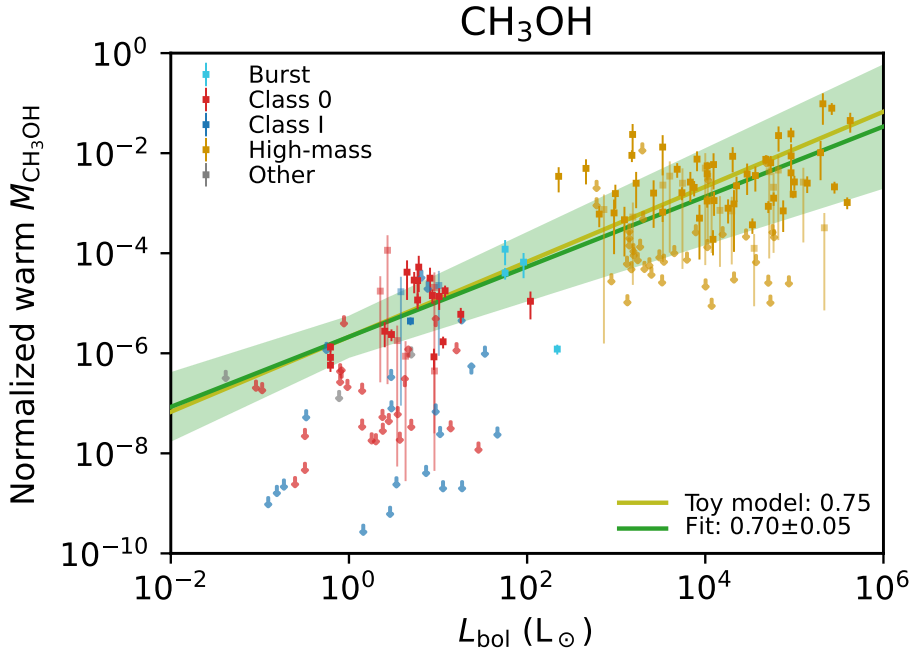


Figure 3.4: Normalized warm gaseous CH_3OH mass, $M_{\text{CH}_3\text{OH}}/M_{\text{dust},0}$, as a function of the bolometric luminosity. Different colors denote different observational classes, and all sources with $L_{\text{bol}} > 1000 L_{\odot}$ are classified as high-mass sources. Additionally, sources that are suggested to currently be in a burst phase (e.g., V883 Ori and IRAS2A; van 't Hoff et al. 2018b; Lee et al. 2019b; Hsieh et al. 2019) are highlighted. Sources in the "other" category include Class II and flat spectrum sources. The green line indicates the best-fit power-law model to the data points (excluding the upper limits) and the green shaded area the 3σ uncertainty on the fit. The yellow line indicates the relation for the toy model of Eq. (3.4) scaled to match the best-fit power-law model.

larger than 200 au. However, changing the normalization to larger or smaller R_0 does not affect the results discussed below.

Despite $M_{\text{CH}_3\text{OH}}/M_{\text{dust},0}$ not representing an abundance of CH_3OH , it can be seen as a lower limit on the abundance of CH_3OH in the hot cores of sources where the expected snow line radius lies inward of 200 au (i.e., when $L_{\text{bol}} \lesssim 100 L_{\odot}$). For typical values of $M_{\text{CH}_3\text{OH}}/M_{\text{dust},0} \sim 10^{-5}$, this implies abundances of $\gtrsim 10^{-7}$ with respect to H_2 (assuming a gas-to-dust mass ratio of 100), which is in agreement with the CH_3OH ice abundances in protostellar envelopes ($\sim 10^{-6}$ with respect to H_2 ; Boogert et al. 2008; Bottinelli et al. 2010; Öberg et al. 2011).

A positive correlation of $M_{\text{CH}_3\text{OH}}/M_{\text{dust},0}$ with L_{bol} is evident (again excluding upper limits), $M_{\text{CH}_3\text{OH}}/M_{\text{dust},0} \propto L_{\text{bol}}^{0.70 \pm 0.05}$. The slope of the power law is in good agreement with the slope derived in Eq. (3.4) for the simple toy model (yellow line in Fig. 3.4 scaled to match the best-fit power-law mode). This indicates that for sources with high $M_{\text{CH}_3\text{OH}}/M_{\text{dust},0}$ the thermal structure of the envelope is likely

not affected by the disk. Since the sources are corrected for the source's mass, the increase in the $M_{\text{CH}_3\text{OH}}/M_{\text{dust},0}$ ratio originates from the snow line moving farther out in systems with higher luminosity. In turn, this leads to a higher mass of gaseous warm CH_3OH . Therefore, the agreement with the toy model can be considered as an observational confirmation of the scaling between the sublimation radius (i.e., the snow line radius) and the source luminosity of $R_{\text{sub}} \propto L_{\text{bol}}^{1/2}$ found in radiative transfer calculations (i.e., Eq. (3.8); Bisschop et al. 2007; van 't Hoff et al. 2022).

The correlation between $M_{\text{CH}_3\text{OH}}/M_{\text{dust},0}$ and L_{bol} is most evident when the low-mass and high-mass samples are combined. A positive correlation is less evident when the two subsamples are examined individually: $M_{\text{CH}_3\text{OH}}/M_{\text{dust},0} \propto L_{\text{bol}}^{0.38 \pm 0.17}$ and $M_{\text{CH}_3\text{OH}}/M_{\text{dust},0} \propto L_{\text{bol}}^{0.15 \pm 0.10}$ for the low-mass and high-mass protostars, respectively. However, the uncertainties on the fits are large due to the large scatter within each subsample. Moreover, the fits are more sensitive to individual data points (e.g., B1-bS at low L_{bol}). Therefore, no significant conclusions can be made.

Similarly to Fig. 3.3, a scatter of more than four orders of magnitude is evident in Fig. 3.4 among both the low-mass and high-mass sources. Likewise, on average, the Class I sources show lower values ($M_{\text{CH}_3\text{OH}}/M_{\text{dust},0} \lesssim 10^{-6}$) than the (younger) Class 0 sources ($M_{\text{CH}_3\text{OH}}/M_{\text{dust},0} \sim 10^{-5}$). The large scatter indicates that the normalized gaseous CH_3OH mass cannot be solely explained by the toy model of a spherically symmetric infalling envelope.

3.4 Discussion

3.4.1 Importance of source structure

If all embedded protostellar systems behaved solely as spherically symmetric infalling envelopes, a larger luminosity for a given mass of the source would result in the CH_3OH snow line moving farther out and, thus, more CH_3OH in the gas phase. However, the large scatter in Fig. 3.4 indicates that other mechanisms affect the gaseous CH_3OH mass. One possible explanation could be the presence of a disk that alters the temperature structure of the system and thus lowers the amount of warm CH_3OH . Alternatively, the continuum optical depth can hide the emission of COMs. These cases could explain the deviation from the toy model relation of Eq. (3.4).

In Fig. 3.5, the normalized warm gaseous CH_3OH mass is presented as a function of L_{bol} , similarly to Fig. 3.4 but now with colors indicating whether the source has a confirmed disk on > 10 au scales (blue) or whether the absence of a > 50 au disk is confirmed. All sources where no information on the presence of a disk is available (e.g., high-mass sources) are assigned to the "other" category. Besides the sources with well-known disks, such as HH 212 (e.g., Lee et al. 2017c, 2019a), the presence of a disk is indicated by Keplerian rotation (e.g., L1527 and V883 Ori; Tobin et al. 2012; Lee et al. 2019b) or based on the elongated dust continuum (e.g., Segura-Cox et al. 2018; Maury et al. 2019).

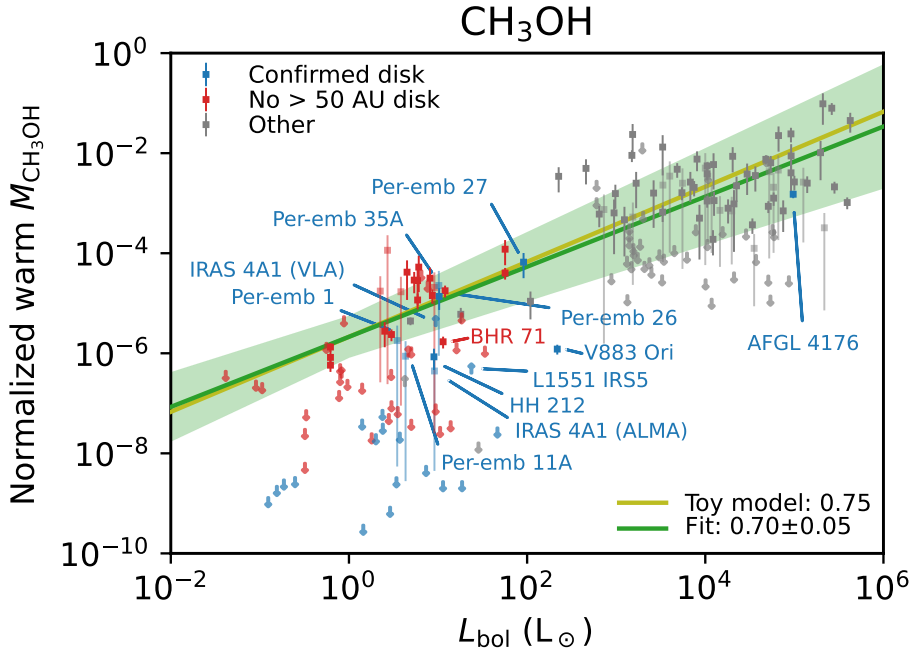


Figure 3.5: Normalized warm gaseous CH_3OH mass with respect to M_{dust} within a 200 au radius as a function of the bolometric luminosity. Sources around which a disk has been detected on > 10 au scales are indicated in blue, and sources where no disk is confirmed on > 50 au scales are indicated in red. All other sources (i.e., with no information about a disk) are shown in gray. The green line indicates the best-fit power-law model to the data points (excluding the upper limits) and the green shaded area the 3σ uncertainty on the fit. The yellow line indicates the relation for the toy model of Eq. (3.4) scaled to match the best-fit power-law model.

Among the low-mass sources, the presence of a disk does not directly imply that no significant COM emission can be present, given that the emission of COMs can be in the part of the envelope not shadowed by the disk or in the warm upper atmosphere of the disk (e.g., HH 212; Lee et al. 2017c, 2019a). Excluding the lower limits for IRAS 4A1 (Per-emb 12A; De Simone et al. 2020) and L1551 IRS5 (Bianchi et al. 2020), there are only seven sources in our sample with both a confirmed disk and a CH_3OH detection: HH 212, Per-emb 27 (IRAS 2A), V883 Ori, Per-emb 35A (IRAS 1A), Per-emb 26 (L1448-mm), Per-emb 1 (HH211), and Per-emb 11A (IC 348 MMS). Their normalized warm CH_3OH masses as well as their estimated dust disk radii are listed in Table 3.1.

The normalized warm $M_{\text{CH}_3\text{OH}}$ of Per-emb 27, Per-emb 35A, and Per-emb 26 lie well within the 3σ range of the best-fit power-law model in Fig. 3.5 (green shaded area). Similarly, the lower limit of IRAS 4A1 (VLA) also falls within this area. This suggests that for these sources the thermal structure of the envelope is not significantly affected by the disk. This suggestion is further supported by the

Table 3.1: Disk and estimated 100 K radii for sources with both a disk and CH₃OH detection.

Source	R_{disk} au	$R_{100\text{K}}$ au	Normalized $M_{\text{CH}_3\text{OH}}$
Per-emb 27	20 ⁽¹⁾	147	6.6±3.5(-5)
Per-emb 35A	20 ⁽¹⁾	49	2.3±2.2(-5)
IRAS 4A1 (VLA)	35 ⁽¹⁾	46	>4.4(-6)
Per-emb 26	37 ⁽²⁾	49	1.4±0.6(-5)
Per-emb 1	30 ⁽³⁾	30	1.8±1.7(-6)
Per-emb 11A	40 ⁽²⁾	30	8.8±8.7(-7)
HH 212	60 ⁽⁴⁾	46	8.5±3.9(-7)
L1551 IRS5	140 ⁽⁵⁾	91	>5.0(-7)
V883 Ori	320 ⁽⁶⁾	227	1.2±0.3(-6)

Notes. $a(b)$ represents $a \times 10^b$. The 100 K radius was determined using the relation derived by Bisschop et al. (2007) for high-mass hot cores, $R_{100\text{K}} \approx 15.4\sqrt{L_{\text{bol}}/L_{\odot}}$ au, which also seems to hold for low-mass protostars (van 't Hoff et al. 2022).

⁽¹⁾ Segura-Cox et al. (2018). ⁽²⁾ Maury et al. (2019). ⁽³⁾ Lee et al. (2018). ⁽⁴⁾ Lee et al. (2017b). ⁽⁵⁾ Cruz-Sáenz de Miera et al. (2019). ⁽⁶⁾ Cieza et al. (2016).

derived radii compared to the estimated 100 K radius based on their luminosities, assuming that the thermal structure of the envelope is not dominated by the disk (see Table 3.1). Especially for Per-emb 27 (IRAS 2A), the disk is much smaller than the estimated 100 K radius ($R_{\text{disk}} = 20$ au and $R_{100\text{K}} = 147$ au), suggesting that indeed the disk does not significantly affect the thermal structure.

On the other hand, V883 Ori shows normalized warm $M_{\text{CH}_3\text{OH}}$ that is more than two orders of magnitude lower than the 3σ range of the best-fit power-law model in Fig. 3.5. Likewise, HH 212, the ranges of Per-emb 1 and Per-emb 11A, and the lower limit of L1551 IRS5 lie about an order of magnitude below the 3σ . One possible explanation for this discrepancy is the size of the disk for these sources. The large disks around V883 Ori and L1551 IRS5 compared to their estimated 100 K radii suggest that these disks have a stronger impact on the thermal structure of these sources compared to the sources discussed above, therefore lowering the amount warm gas in the inner envelope. Since both Per-emb 27 and V883 Ori are currently in an outbursting phase (e.g., Lee et al. 2019b; Hsieh et al. 2019), this cannot explain the more than one order of magnitude difference in normalized $M_{\text{CH}_3\text{OH}}$. For HH 212, the edge-on disk is slightly larger than the 100 K radius, but the COMs in this source are detected through very high-angular-resolution observations (~ 12 au) in the part of the envelope not shadowed by the disk or the disk atmosphere (Lee et al. 2017c, 2019a). The disks around Per-emb 1 and Per-emb 11A are similar in size to the estimated 100 K radius, but since the error bars on their normalized warm CH₃OH masses are rather large, no further conclusions can be made.

Of the 46 sources where no disk is confirmed on > 50 au scales, 26 sources fall within 3σ of the best-fit power-law model, indicating that the thermal structure in

these sources is indeed not dominated by a (large) disk. However, 20 sources where no disk is confirmed on > 50 au scales lie up to two orders of magnitude below the 3σ of the best-fit power-law model. One example is BHR 71, which shows a warm normalized CH_3OH mass that is about an order of magnitude lower than the 3σ range of the best-fit power-law model shown in Fig. 3.5. Hints of a ~ 50 au Keplerian disk are visible in the $^{13}\text{CH}_3\text{OH}$ lines (Yang et al. 2020), which is roughly similar in size to the estimated 100 K radius of ~ 57 au (Bisschop et al. 2007). Most of the other upper limits in Fig. 3.5 have constraints on their disk size down to ~ 10 au scales due to high-angular-resolution continuum observations in, for example, the VANDAM survey (Tobin et al. 2016; Segura-Cox et al. 2018). Therefore, it is unlikely that large disks are the explanation for the low normalized warm $M_{\text{CH}_3\text{OH}}$ in these sources, but small disks that can affect the thermal structure may still be present. An alternative reason could be the dust opacity (see Sect. 3.4.2).

Among the high-mass sources, only AFGL 4176 is known to host a large, ~ 2000 au, disk (Johnston et al. 2015); additionally, it also shows a large amount of COMs in the disk, including CH_3OH (Bøgelund et al. 2019). Several other high-mass sources are likely to also host large warm disks as this seems to be common at least for A- and B-type stars (Beltrán & de Wit 2016). However, since no information on the presence or absence of disks is available for the high-mass sources, all other high-mass sources have been assigned to the "other" category.

3.4.2 Continuum optical depth

Another way to hide large amounts of COMs is through the continuum optical depth at (sub)millimeter wavelengths. If a layer of optically thick dust is present and coincides with or is in front of the hot core, all emission from the hot core will be extincted. Alternatively, continuum over-subtraction due to the presence of bright (optically thick) continuum emission behind the methanol emission can hide CH_3OH emission (e.g., Boehler et al. 2017; Rosotti et al. 2021). A recent example of a low-mass source where optically thick dust hides emission from COMs at submillimeter wavelengths is NGC 1333 IRAS4A1 (López-Sepulcre et al. 2017; De Simone et al. 2020). For high-mass sources, the effect dust opacity on the molecular line intensities of COMs toward G31.41+0.31 was shown by Rivilla et al. (2017). Optically thick dust thus does not reduce the amount of COMs present in the gas phase, but it hides the emission from the hot core at millimeter wavelengths.

As a zeroth-order approximation, the continuum optical depth toward the sources studied in this work can be quantified using the continuum flux and assuming the dust temperature, T_{dust} (see Eq. (2) of Rivilla et al. 2017),

$$\tau_\nu = -\ln\left(1 - \frac{F_\nu}{\Omega_{\text{beam}} B_\nu(T_{\text{dust}})}\right), \quad (3.5)$$

where Ω_{beam} is the beam solid angle and F_ν is the flux density within the beam at frequency ν . Here, we assume that $T_{\text{dust}} = 30$ K and $T_{\text{dust}} = 50$ K for the low-mass and high-mass sources, respectively (see Sect. 3.3.2).

For the PEACHES sample, the highest optical depth value at 243 GHz (i.e., 1.23 mm) is for IRAS 4A1 (i.e., Per-emb 12A, $\tau_\nu = 3.9$), which is consistent with

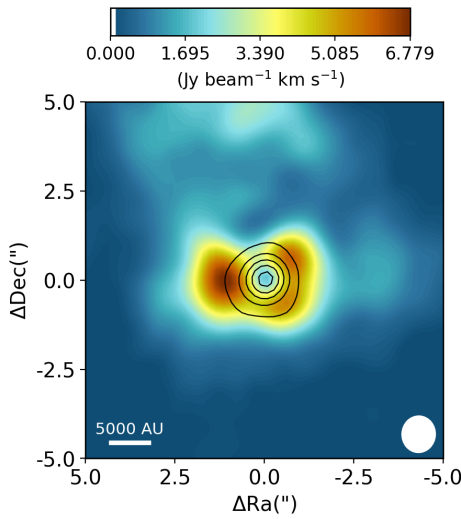


Figure 3.6: Integrated intensity maps of the CH_3OH $8_{0,8} - 7_{1,6}$ line for 693050. The color scale is shown on top of the image. The image is integrated over $[-5, 5] \text{ km s}^{-1}$ with respect to the V_{lsr} . The white vertical line in the colorbar indicates the 3σ threshold. The continuum flux is indicated with the black contours at $[0.1, 0.3, 0.5, 0.7, 0.9]$ times the peak continuum flux, $F_{\text{cont}} = 1.92 \text{ Jy beam}^{-1}$. The white ellipse in the lower right of each image depicts the beam size, and in the lower left a physical scale bar is displayed.

a non-detection of emission by CH_3OH (it is in fact in absorption at millimeter wavelengths; Sahu et al. 2019) since any COM emission is extinguished with a factor of ≈ 50 . The effect of dust opacity on the normalized warm $M_{\text{CH}_3\text{OH}}$ of IRAS 4A1 is also shown in Fig. 3.5, where the lower limit derived at centimeter wavelengths (IRAS 4A1 (VLA); De Simone et al. 2020) is more than two orders of magnitude higher than the normalized warm $M_{\text{CH}_3\text{OH}}$ derived from absorption lines at millimeter wavelengths (IRAS 4A1 (ALMA)). In contrast to source A, Per-emb 12B has significantly lower extinction by the dust ($\tau_\nu = 0.56$), explaining why source B appears rich in COMs at millimeter wavelengths. Moreover, both these optical depth estimates are consistent with those derived by De Simone et al. (2020) at 143 GHz when assuming that $\tau_\nu \propto \nu^{\alpha-2}$ for $\alpha = 2.5$ (Tychoniec et al. 2020).

In the ALMAGAL sample, the effect of dust opacity is evidently visible in the source 693050, where the CH_3OH emission is ring-shaped around the continuum peak (see Fig. 3.6). Using Eq. (3.5) for a dust temperature of 50 K, the continuum optical depth is estimated to be $\tau_\nu = 0.68$ at 219 GHz. This could explain the decrease in emission in the center, but since the optical depth is not as high as in Per-emb 12A, CH_3OH is still detected outside the central beam. Similarly, the CH_3OH emission peaks slightly off-source for 707948 ($\tau_\nu = 0.24$), but significant emission is still present within the central beam. The reason why these optical depth values are lower than for some of the PEACHES sample could be that the solid angle of the optically thick emitting region is in reality much smaller than the beam size. However, the fact that 693050 shows ring-shaped CH_3OH emission and also has the highest optical depth of the high-mass sources is a clear case of the dust attenuation reducing the emission of CH_3OH .

3.5 Conclusion

In this work, the warm ($T > 100$ K) gaseous methanol mass, $M_{\text{CH}_3\text{OH}}$, is derived for a large sample of both low-mass and high-mass embedded protostellar systems. The sample includes new and archival observations of 148 sources with ALMA as well as 36 sources added from the literature, leading to a combined sample size of 184 sources. Using a simple analytic toy model of a spherically symmetric infalling envelope that is passively heated by the central protostar, the effect of source structure (e.g., a disk) and dust opacity on the amount of warm gaseous methanol is investigated. The main conclusions are as follows:

- Among the low-mass protostars, a scatter of more than four orders of magnitude in $M_{\text{CH}_3\text{OH}}$ is observed, with values ranging between $10^{-7} M_\odot$ and $\lesssim 10^{-11} M_\odot$. On average, Class 0 sources have more CH_3OH mass ($\sim 10^{-7} M_\odot$) than the more evolved Class I sources ($\lesssim 10^{-10} M_\odot$). High-mass sources in our biased sample show higher warm gaseous CH_3OH masses, between $\sim 10^{-7}$ and $10^{-3} M_\odot$. This scatter can be due to either source structure (e.g., the presence of a disk) or dust optical depth.
- To take into account the effect of the source's overall mass and to test the effect of the bolometric luminosity on the snow line radius, the normalized warm $M_{\text{CH}_3\text{OH}}$ is defined as $M_{\text{CH}_3\text{OH}}/M_{\text{dust},0}$. Here, $M_{\text{dust},0}$ is the cold plus warm dust mass in the disk and inner envelope within a fixed radius measured from the ALMA dust continuum. A simple power-law fit to the normalized warm $M_{\text{CH}_3\text{OH}}$ of the line-rich sources gives a positive correlation with the bolometric luminosity: $M_{\text{CH}_3\text{OH}}/M_{\text{dust},0} \propto L_{\text{bol}}^{0.70 \pm 0.05}$ over an L_{bol} range of $10^{-1} - 10^6 L_\odot$. This is in good agreement with the toy hot core model, which predicts that $M_{\text{CH}_3\text{OH}}/M_0 \propto L_{\text{bol}}^{0.75}$ and can be considered as an observational confirmation of the scaling between the sublimation radius (i.e., snow line radius) and the source luminosity of $R_{\text{sub}} \propto L_{\text{bol}}^{1/2}$ found in radiative transfer calculations.
- Most sources where the disk radius is equivalent to or smaller than the estimated 100 K envelope radius agree well with the power-law fit to normalized warm $M_{\text{CH}_3\text{OH}}$, indicating that the thermal structure of the envelope in these sources is likely not affected by the disk. On the other hand, sources for which the disk radius is significantly larger have up to two orders of magnitude lower normalized warm CH_3OH masses, suggesting that these disks significantly affect the thermal structure of these sources.
- High dust opacity can hide emission from COMs, leading to low observed CH_3OH masses. Clear cases of this effect in our sample are the low-mass source Per-emb 12A (IRAS 4A1) and the high-mass source 693050.

This work shows that the absence of COM emission in embedded protostellar systems does not mean that the abundance of COMs in such sources is low but instead that it may be a physical effect due to the structure of the source, most

notably the presence of a disk. It is therefore very important to understand the physical structure of embedded protostellar systems in order to understand the chemistry. The modeling work done by Nazari et al. (2022b) quantifies the effect that a disk has on the temperature structure of an embedded protostellar system and thus on the amount of warm methanol. Additionally, observations at longer wavelengths can solve the problem of dust optical depth.

Acknowledgments

The authors would like to thank the anonymous referee for their constructive comments on the manuscript. This paper makes use of the following ALMA data: ADS/JAO.ALMA#2017.1.01174.S, ADS/JAO.ALMA#2017.1.01350.S, ADS/JAO.ALMA#2016.1.01501.S, ADS/JAO.ALMA#2017.1.01462.S, and ADS/JAO.ALMA#2019.1.00195.L. ALMA is a partnership of ESO (representing its member states), NSF (USA) and NINS (Japan), together with NRC (Canada), MOST and ASIAA (Taiwan), and KASI (Republic of Korea), in co-operation with the Republic of Chile. The Joint ALMA Observatory is operated by ESO, AUI/NRAO and NAOJ. Astrochemistry in Leiden is supported by the Netherlands Research School for Astronomy (NOVA), by funding from the European Research Council (ERC) under the European Union’s Horizon 2020 research and innovation programme (grant agreement No. 101019751 MOLDISK), and by the Dutch Research Council (NWO) grants TOP-1 614.001.751, 648.000.022, and 618.000.001. Support by the Danish National Research Foundation through the Center of Excellence “InterCat” (Grant agreement no.: DNRF150) is also acknowledged. G.A.F acknowledges support from the Collaborative Research Centre 956, funded by the Deutsche Forschungsgemeinschaft (DFG) project ID 184018867. Y.-L. Yang acknowledges the support from the Virginia Initiative of Cosmic Origins (VICO) Postdoctoral Fellowship.

Appendix

3.A Observational details

Table 3.A.1: ALMA Band 6 Observations of protostars.

ID ⁽¹⁾	Source	RA (J2000)	Dec (J2000)	V_{lsr} km s ⁻¹	Detected species		
					CH ₃ OH	¹³ CH ₃ OH	CH ₃ ¹⁸ OH
1	B1-c	03:33:17.88	31:09:31.8	6.0	Y	Y	Y
	B1-b	03:33:20.34	31:07:21.3	6.0	N	N	N
	B1-bN	03:33:21.21	31:07:43.6	6.0	N	N	N
	B1-bS	03:33:21.36	31:07:26.3	6.0	Y	Y	Y
	Serpens S68N	18:29:48.09	01:16:43.3	8.5	Y	Y	Y
	Ser-emb 8 (N)	18:29:48.73	01:16:55.6	8.5	N	N	N
2	Serpens SMM3	18:29:57.75	01:14:06.7	8.5	N	N	N
3	Per-emb 22B	03:25:22.35	30:45:13.11	4.3	Y	N	N
	Per-emb 22A	03:25:22.41	30:45:13.26	4.3	Y	Y	Y
	L1448 NW	03:25:35.67	30:45:34.16	4.2	N	N	N
	Per-emb 33BC	03:25:36.32	30:45:15.19	5.3	N	N	N
	Per-emb 33A	03:25:36.38	30:45:14.72	4.3	Y	N	N
	L1448 IRS 3A	03:25:36.50	30:45:21.90	4.6	Y	N	N
	Per-emb 26	03:25:38.88	30:44:05.28	5.4	Y	Y	N
	Per-emb 42	03:25:39.14	30:43:57.90	5.8	Y	N	N
	Per-emb 25	03:26:37.51	30:15:27.81	5.5	N	N	N
	Per-emb 17	03:27:39.11	30:13:02.96	6.0	Y	Y	Y
	Per-emb 20	03:27:43.28	30:12:28.88	5.3	Y	N	N
	L1455 IRS 2	03:27:47.69	30:12:04.33	5.1	N	N	N
	Per-emb 35A	03:28:37.10	31:13:30.77	7.4	Y	N	N
	Per-emb 35B	03:28:37.22	31:13:31.74	7.3	Y	N	N
	Per-emb 27	03:28:55.57	31:14:36.97	6.5	Y	Y	Y
	EDJ2009 172	03:28:56.65	31:18:35.43	—	N	N	N
Per-emb 36		03:28:57.37	31:14:15.77	6.9	N	N	N
	Per-emb 54	03:29:01.55	31:20:20.49	7.9	N	N	N

Table 3.A.1: continued.

ID ⁽¹⁾	Source	RA (J2000)	Dec (J2000)	V_{lsr} km s ⁻¹	Detected species		
					CH ₃ OH	¹³ CH ₃ OH	CH ₃ ¹⁸ OH
	SVS 13B	03:29:03.08	31:15:51.73	8.5	N	N	N
	SVS 13A2	03:29:03.39	31:16:01.58	8.4	Y	N	N
	Per-emb 44	03:29:03.76	31:16:03.70	8.7	Y	Y	Y
	Per-emb 15	03:29:04.06	31:14:46.23	6.8	N	N	N
	Per-emb 50	03:29:07.77	31:21:57.11	9.3	N	N	N
	Per-emb 12B	03:29:10.44	31:13:32.08	6.9	Y	Y	Y
	Per-emb 12A	03:29:10.54	31:13:30.93	6.9	A ⁽²⁾	N	N
	Per-emb 21	03:29:10.67	31:18:20.16	8.6	N	N	N
	Per-emb 18	03:29:11.27	31:18:31.09	8.1	Y	N	N
	Per-emb 13	03:29:12.02	31:13:07.99	7.1	Y	Y	Y
	IRAS 4B2	03:29:12.85	31:13:06.87	7.1	N	N	N
	Per-emb 14	03:29:13.55	31:13:58.12	7.9	N	N	N
	EDJ2009 235	03:29:18.26	31:23:19.73	7.7	N	N	N
	EDJ2009 237	03:29:18.74	31:23:25.24	–	N	N	N
	Per-emb 37	03:29:18.97	31:23:14.28	7.5	N	N	N
	Per-emb 60	03:29:20.05	31:24:07.35	–	N	N	N
4	Per-emb 5	03:31:20.94	30:45:30.24	7.3	Y	Y	N
	Per-emb 2	03:32:17.92	30:49:47.81	7.0	N	N	N
	Per-emb 10	03:33:16.43	31:06:52.01	6.4	Y	N	N
	Per-emb 40	03:33:16.67	31:07:54.87	7.4	N	N	N
	Per-emb 29	03:33:17.88	31:09:31.74	6.1	Y	Y	Y
	B1-bN	03:33:21.21	31:07:43.63	6.6	N	N	N
	B1-bS	03:33:21.36	31:07:26.34	6.6	Y	Y	N
	Per-emb 16	03:43:50.97	32:03:24.12	8.8	N	N	N
	Per-emb 28	03:43:51.01	32:03:08.02	8.6	N	N	N

Table 3.A.1: continued.

ID(<i>I</i>)	Source	RA (J2000)	Dec (J2000)	V_{lsr} km s ⁻¹	Detected species		
					CH ₃ OH	¹³ CH ₃ OH	CH ₃ ¹⁸ OH
	Per-emb 1	03:43:56.81	32:00:50.16	9.4	Y	N	N
	Per-emb 11B	03:43:56.88	32:03:03.08	9.0	N	N	N
	Per-emb 11A	03:43:57.07	32:03:04.76	9.0	Y	N	N
	Per-emb 11C	03:43:57.70	32:03:09.82	9.0	N	N	N
	Per-emb 55	03:44:43.30	32:01:31.22	12.0	N	N	N
	Per-emb 8	03:44:43.98	32:01:35.19	11.0	N	N	N
	Per-emb 53	03:47:41.59	32:51:43.62	10.2	N	N	N
5	81635A	18:25:00.82	-13:15:34.46	—	N	N	N
	81635B	18:25:01.01	-13:15:38.57	—	N	N	N
	81635C	18:25:01.65	-13:15:28.99	—	N	N	N
	83968A	18:25:10.57	-12:42:22.43	—	N	N	N
	83968B	18:25:10.69	-12:42:26.14	—	N	N	N
	83968C	18:25:10.80	-12:42:24.68	46.2	Y	N	N
	83968D	18:25:10.57	-12:42:19.91	—	N	N	N
	83968E	18:25:10.64	-12:42:24.53	—	N	N	N
	86213A	18:26:48.89	-12:26:23.75	—	N	N	N
	86213B	18:26:47.94	-12:26:20.77	66.0	Y	N	N
	86213C	18:26:48.73	-12:26:26.24	63.9	Y	N	N
	101899	18:34:40.28	-09:00:38.33	77.3	Y	Y	N
	103421	18:33:23.96	-08:33:31.64	78.5	Y	N	N
	106756A	18:34:23.99	-07:54:48.28	80.0	Y	N	N
	106756B	18:34:25.55	-07:54:46.39	—	N	N	N
	106756C	18:34:25.59	-07:54:43.11	—	N	N	N
	126120A	18:42:37.58	-04:02:05.58	80.2	Y	N	N
	126120B	18:42:37.64	-04:02:07.32	81.2	Y	N	N

Table 3.A.1: continued.

ID ⁽¹⁾	Source	RA (J2000)	Dec (J2000)	V_{lsr} km s ⁻¹	Detected species		
					CH ₃ OH	¹³ CH ₃ OH	CH ₃ ¹⁸ OH
126120C		18:42:36.85	-04:02:17.66	—	N	N	N
126120D		18:42:37.14	-04:02:02.37	—	N	N	N
126348		18:42:51.99	-03:59:54.06	76.9	Y	Y	Y
565926A		08:02:42.97	-34:31:48.77	—	N	N	N
565926B		08:02:42.94	-34:31:49.96	—	N	N	N
565926C		08:02:42.72	-34:31:49.61	—	N	N	N
586092A		08:32:08.65	-43:13:45.58	9.7	Y	Y	N
586092B		08:32:08.47	-43:13:49.06	15.5	Y	N	N
586092C		08:32:09.06	-43:13:43.28	—	N	N	N
615590		09:24:41.96	-52:02:07.98	40.4	Y	Y	Y
640076		10:20:15.74	-58:03:55.86	10.9	Y	N	N
644284A		10:31:29.73	-58:02:19.54	0.5	Y	Y	Y
644284B		10:31:29.60	-58:02:18.57	2.7	Y	Y	Y
693050		12:35:35.09	-63:02:31.97	-41.0	Y	Y	Y
695243		12:43:31.51	-62:36:13.25	—	N	N	N
704792		13:11:14.14	-62:45:06.80	—	N	N	N
705768		13:12:36.18	-62:33:34.75	-34.5	Y	Y	Y
706733A		13:14:22.77	-62:45:59.07	—	N	N	N
706733B		13:14:22.99	-62:45:54.35	—	N	N	N
706733C		13:14:23.07	-62:45:47.54	—	N	N	N
706785A		13:14:26.86	-62:44:29.95	-39.8	Y	N	N
706785B		13:14:26.52	-62:44:31.40	-40.8	Y	N	N
706785C		13:14:26.38	-62:44:30.24	—	N	N	N
706785D		13:14:25.68	-62:44:29.97	-40.2	Y	N	N
707948		13:16:43.21	-62:58:32.86	-35.4	Y	Y	Y

Table 3.A.1: continued.

ID ⁽¹⁾	Source	RA (J2000)	Dec (J2000)	V_{lsr} km s ⁻¹	Detected species		
					CH ₃ OH	¹³ CH ₃ OH	CH ₃ ¹⁸ OH
717461A		13:43:01.66	-62:08:51.37	-53.5	Y	Y	Y
717461B		13:43:01.74	-62:08:55.34	—	N	N	N
721992		13:51:58.32	-61:15:41.19	-57.5	Y	N	N
724566		13:59:30.93	-61:48:38.20	-57.3	Y	Y	N
732038		14:13:15.05	-61:16:52.92	-63.4	Y	N	N
744757A		14:45:26.37	-59:49:15.29	-41.1	Y	Y	Y
744757B		14:45:26.13	-59:49:19.56	-41.0	Y	N	N
759150A		15:10:43.04	-57:44:49.11	—	N	N	N
759150B		15:10:43.52	-57:44:44.82	—	N	N	N
759150C		15:10:44.48	-57:44:47.33	—	N	N	N
759150D		15:10:42.71	-57:44:52.85	—	N	N	N
759150E		15:10:44.10	-57:44:52.03	—	N	N	N
767784		15:29:19.37	-56:31:22.25	-68.4	Y	Y	Y
800287		16:11:26.56	-51:41:56.99	-83.5	Y	Y	N
854214A		16:52:32.73	-43:23:49.20	-71.0	Y	N	N
854214B		16:52:33.14	-43:23:49.42	-72.2	Y	N	N
863312A		17:02:08.36	-41:46:56.89	—	N	N	N
863312B		17:02:09.14	-41:46:45.04	—	N	N	N
865468A		17:05:10.90	-41:29:06.93	-26.8	Y	Y	N
865468B		17:05:11.20	-41:29:07.21	-27.5	Y	Y	Y
865468C		17:05:11.10	-41:29:03.22	-25.7	Y	Y	Y
876288		17:11:51.03	-39:09:29.12	-96.0	Y	Y	Y
881427A		17:20:06.29	-38:57:14.88	-12.0	Y	Y	Y
881427B		17:20:06.42	-38:57:11.24	-10.6	Y	Y	Y
881427C		17:20:06.10	-38:57:15.81	-10.4	Y	Y	Y

Table 3.A.1: continued.

ID ⁽¹⁾	Source	RA (J2000)	Dec (J2000)	V_{lsr} km s ⁻¹	Detected species		
					CH ₃ OH	¹³ CH ₃ OH	CH ₃ ¹⁸ OH
G023.3891+00.1851		18:33:14.32	-08:23:57.61	75.5	Y	Y	N
G023.6566-00.1273		18:34:51.55	-08:18:21.57	81.2	Y	Y	N
G025.6498+01.0491		18:34:20.92	-05:59:42.02	41.2	Y	Y	Y
G030.1981-00.1691		18:47:03.06	-02:30:36.39	105.3	Y	Y	N
G233.8306-00.1803		07:30:16.73	-18:35:49.06	—	N	N	N
G305.2017+00.2072A1		13:11:10.47	-62:34:38.58	-41.2	Y	Y	Y
G305.2017+00.2072A2		13:11:13.12	-62:34:42.74	-40.9	Y	N	N
G310.0135+00.3892		13:51:37.84	-61:39:07.53	-43.0	Y	N	N
G314.3197+00.1125		14:26:26.26	-60:38:31.34	-50.0	Y	N	Y
G316.6412-00.0867		14:44:18.33	-59:55:11.52	-20.0	Y	Y	Y
G318.0489+00.0854B		14:53:42.68	-59:08:53.01	-50.4	Y	Y	Y
G318.9480-00.1969A1		15:00:55.30	-58:58:52.42	-35.0	Y	Y	Y
G318.9480-00.1969A2		15:00:55.23	-58:58:55.88	-35.0	Y	N	N
G323.7399-00.2617B1		15:31:45.64	-56:30:50.16	-51.5	Y	Y	Y
G323.7399-00.2617B2		15:31:45.45	-56:30:50.06	-51.3	Y	Y	Y
G323.7399-00.2617B3		15:31:45.73	-56:30:51.93	-51.3	Y	N	N
G323.7399-00.2617B4		15:31:45.94	-56:30:51.34	-50.5	Y	N	N
G323.7399-00.2617B5		15:31:45.62	-56:30:45.62	-52.0	Y	N	N
G323.7399-00.2617B6		15:31:45.84	-56:30:47.68	-49.7	Y	N	N
G323.7399-00.2617B7		15:31:45.91	-56:30:46.10	-49.3	Y	N	N
G327.1192+00.5103		15:47:32.72	-53:52:38.55	-84.7	Y	Y	Y
G343.1261-00.0623		16:58:17.23	-42:52:07.67	-35.0	Y	Y	N
G345.5043+00.3480		17:04:22.88	-40:44:22.92	-19.7	Y ⁽³⁾	Y ⁽³⁾	Y ⁽³⁾

Table 3.A.1: continued.

ID ⁽¹⁾	Source	RA (J2000)	Dec (J2000)	V_{lsr} km s ⁻¹	Detected species		
					CH ₃ OH	¹³ CH ₃ OH	CH ₃ ¹⁸ OH
	G348.7342-01.0359B1	17:20:07.12	-38:57:11.69	-10.7	Y	N	N
	G348.7342-01.0359B2	17:20:07.26	-38:57:09.82	-13.1	Y	N	N
	G348.7342-01.0359B3	17:20:07.38	-38:57:10.15	–	N	N	N

Notes. The coordinates mark the peak of the continuum emission. The last three columns indicate if unblended transitions of CH₃OH and its isotopologues are detected at the 3 σ limit (Y) or if the all the lines of a particular isotopologue were either too blended for a fit or not detected at the 3 σ detection (N).

⁽¹⁾ ALMA program IDs. 1: 2017.1.01174.S. 2: 2017.1.01350.S. 3: 2016.1.01501.S. 4: 2017.1.01462.S. 5: 2019.1.00195.L. ⁽²⁾ Lines in absorption. ⁽³⁾ Lines consist of two components. Fits are done to the strongest peak.

Table 3.A.2: Protostellar properties and derived physical quantities.

Source	Class	Disk	d pc	L_{bol} L_{\odot}	F_{cont} mJy/beam	$\theta_{\text{b,c}}$ ''	λ_{cont} mm	$M_{\text{dust},0}$ M_{\odot}	θ_{b} ''	θ_{a} ''	$N\text{CH}_3\text{OH}$ cm^{-2}	$M\text{CH}_3\text{OH}$ M_{\odot}	Ref.
B1-c	0	N	320	5.9	93	0.45	1.14	$4.0\pm0.6(-3)$	0.45	0.45	$1.9\pm0.6(18)$	$4.6\pm1.5(-8)$	TW.1.2,3
Serpens S68N	0	N	436	5.4	44	0.45	1.14	$2.2\pm0.3(-8)$	0.45	0.45	$1.4\pm0.6(18)$	$6.3\pm2.7(-8)$	TW.3.4,5
B1-HS	0	N	320	0.6	1.5(2)	0.39	1.22	$9.2\pm1.4(-3)$	0.45	0.45	$5.0\pm0.6(17)$	$1.2\pm0.2(-8)$	TW.1.3,6
B1-b	I	N	320	0.3	9.9	0.45	1.14	$4.2\pm0.6(-4)$	0.45	0.45	$<1.0(15)$	$<2.4(-11)$	TW.1.3,7
B1-bN	0	N	320	0.3	76	0.39	1.22	$4.8\pm0.7(-3)$	0.45	0.45	$<1.0(15)$	$<2.4(-11)$	TW.1.3,6
Serpens SMM3	0	-	436	28	48	0.45	1.33	$3.5\pm0.5(-3)$	0.45	0.45	$<1.0(15)$	$<4.5(-11)$	TW.2.3,4
B1-bN	0	N	320	0.3	76	0.39	1.22	$4.8\pm0.7(-3)$	0.39	0.39	$<6.3(15)$	$<1.2(-10)$	TW.1.6
B1-HS	0	N	320	0.6	1.5(2)	0.39	1.22	$9.2\pm1.4(-3)$	0.39	0.39	$4.1\pm1.4(17)$	$7.6\pm2.5(-9)$	TW.1.6
EDJ2009 172	II	N	320	0.8	12	0.58	1.22	$4.1\pm0.6(-4)$	0.58	0.58	$<1.4(15)$	$<6.7(-11)$	TW.1.8
EDJ2009 235	II	N	320	4.0(-2)	5.5	0.58	1.22	$1.9\pm0.3(-4)$	0.58	0.58	$<1.7(15)$	$<6.7(-11)$	TW.1.6
IRAS 4B2	0	N	320	-	2.3	0.58	1.22	$8.1\pm1.2(-5)$	0.58	0.58	$<1.9(15)$	$<7.7(-11)$	TW.1
IRAS 4B2	0	N	320	3.4	1.2(2)	0.58	1.22	$4.0\pm0.6(-3)$	0.58	0.58	$<6.6(15)$	$<2.7(-10)$	TW.1.6
L1448 IRS 3A	I	N	320	18	48	0.53	1.22	$1.9\pm0.3(-3)$	0.53	0.53	$1.4\pm1.3(17)$	$4.7\pm4.6(-9)$	TW.1.8
L1448 NW	0	N	320	2.7	50	0.54	1.22	$1.9\pm0.3(-3)$	0.54	0.54	$<2.6(15)$	$<9.3(-11)$	TW.1.8
L1455 IRS 2	Flat	N	320	4.8	2	0.53	1.22	$8.0\pm1.2(-5)$	0.53	0.53	$<2.4(15)$	$<8.2(-11)$	TW.1.8
Per-emb 1	0	Y	320	3.5	52	0.38	1.22	$3.4\pm0.5(-3)$	0.38	0.38	$3.5\pm3.4(17)$	$6.0\pm5.9(-9)$	TW.1.8,9
Per-emb 2	0	N	320	1.7	66	0.39	1.22	$4.1\pm0.6(-3)$	0.39	0.39	$<4.5(15)$	$<8.2(-11)$	TW.1.8
Per-emb 5	0	N	320	2.5	1.5(2)	0.39	1.22	$9.2\pm1.4(-3)$	0.39	0.39	$1.4\pm0.7(18)$	$2.5\pm1.3(-8)$	TW.1.8
Per-emb 8	0	Y	320	3.6	81	0.38	1.22	$5.3\pm0.8(-3)$	0.38	0.38	$<6.2(15)$	$<1.1(-10)$	TW.1.6,9
Per-emb 10	0	N	320	0.8	17	0.38	1.22	$1.1\pm0.2(-3)$	0.38	0.38	$1.4\pm1.3(17)$	$2.4\pm2.3(-9)$	TW.1.6
Per-emb 11A	0	Y	320	4.3	1.1(2)	0.38	1.22	$6.9\pm1.0(-3)$	0.38	0.38	$3.5\pm3.4(17)$	$6.0\pm5.9(-9)$	TW.1.8,9
Per-emb 11B	0	N	320	8.7(-2)	4.5	0.38	1.22	$3.0\pm0.4(-4)$	0.38	0.38	$<3.8(15)$	$<6.6(-11)$	TW.1.8
Per-emb 11C	0	N	320	0.1	5.3	0.38	1.22	$3.5\pm0.5(-4)$	0.38	0.38	$<4.0(15)$	$<7.0(-11)$	TW.1.8
Per-emb 12A	0	Y	320	9.1	3.9(2)	0.59	1.22	$1.3\pm0.2(-2)$	0.59	0.59	$1.4\pm1.3(17)$	$5.8\pm5.7(-9)$	TW.1.8,9
Per-emb 12B	0	N	320	4.5	1.9(2)	0.59	1.22	$6.4\pm1.0(-3)$	0.59	0.59	$6.4\pm4.5(18)$	$2.7\pm1.9(-7)$	TW.1.8
Per-emb 13	0	N	320	8.6	2.3(2)	0.58	1.22	$8.1\pm1.2(-3)$	0.58	0.58	$2.9\pm0.8(18)$	$1.2\pm0.3(-7)$	TW.1.6
Per-emb 14	0	Y	320	1.4	55	0.58	1.22	$1.9\pm0.3(-3)$	0.58	0.58	$<1.7(15)$	$<7.0(-11)$	TW.1.8,9
Per-emb 15	0	N	320	0.8	4.1	0.58	1.22	$1.4\pm0.2(-4)$	0.58	0.58	$<1.7(15)$	$<6.8(-11)$	TW.1.8
Per-emb 16	0	N	320	0.8	3.9	0.39	1.22	$2.4\pm0.4(-4)$	0.39	0.39	$<3.9(15)$	$<7.1(-11)$	TW.1.8
Per-emb 17	0	N	320	8.1	30	0.53	1.22	$1.2\pm0.2(-3)$	0.53	0.53	$1.1\pm0.7(18)$	$3.7\pm2.2(-8)$	TW.1.8
Per-emb 18	0	N	320	9.1	44	0.58	1.22	$1.5\pm0.2(-3)$	0.58	0.58	$7.7\pm7.6(17)$	$3.1\pm3.0(-8)$	TW.1.6
Per-emb 20	0	N	320	2.7	2.6	0.53	1.22	$1.0\pm0.2(-4)$	0.53	0.53	$3.5\pm3.4(17)$	$1.2\pm1.1(-8)$	TW.1.8
Per-emb 21	0	N	320	13	39	0.58	1.22	$1.4\pm0.2(-3)$	0.58	0.58	$<1.2(15)$	$<4.7(-11)$	TW.1.8
Per-emb 22A	0	N	320	6.1	27	0.53	1.22	$1.1\pm0.2(-3)$	0.53	0.53	$1.7\pm1.1(18)$	$5.7\pm3.8(-8)$	TW.1.6
Per-emb 22B	0	N	320	2.2	10	0.53	1.22	$4.0\pm0.6(-4)$	0.53	0.53	$2.1\pm2.0(17)$	$7.0\pm6.8(-9)$	TW.1.6
Per-emb 25	0	Y	320	2.3	82	0.53	1.22	$3.2\pm0.5(-3)$	0.53	0.53	$<3.0(15)$	$<1.0(-10)$	TW.1.8,9
Per-emb 26	0	Y	320	10	1.3(2)	0.53	1.22	$5.1\pm0.8(-3)$	0.53	0.53	$2.1\pm0.9(18)$	$7.0\pm3.1(-8)$	TW.1.6,10
Per-emb 27	Burst	Y	320	91	1.0(2)	0.59	1.22	$3.5\pm0.5(-3)$	0.59	0.59	$5.6\pm2.8(18)$	$2.3\pm1.2(-7)$	TW.1.6,9
Per-emb 28	0	N	320	1.4	14	0.39	1.22	$8.8\pm1.3(-4)$	0.39	0.39	$<9.3(15)$	$<1.7(-10)$	TW.1.8
Per-emb 29	0	N	320	5.9	86	0.39	1.22	$5.4\pm0.8(-3)$	0.39	0.39	$8.4\pm5.6(18)$	$1.5\pm1.0(-7)$	TW.1.2
Per-emb 33A	0	N	320	16	1.4(2)	0.53	1.22	$5.6\pm0.8(-3)$	0.53	0.53	$1.0\pm0.9(17)$	$3.5\pm3.4(-9)$	TW.1.6
Per-emb 33BC	0	N	320	4.8	65	0.53	1.22	$2.6\pm0.4(-3)$	0.53	0.53	$<2.8(15)$	$<9.5(-11)$	TW.1.6
Per-emb 35A	I	Y	320	10	17	0.58	1.22	$5.9\pm0.9(-4)$	0.58	0.58	$3.3\pm3.1(17)$	$1.3\pm1.2(-8)$	TW.1.8,9
Per-emb 35B	I	N	320	7.4	12	0.58	1.22	$4.3\pm0.6(-4)$	0.58	0.58	$1.1\pm1.0(17)$	$4.5\pm4.4(-9)$	TW.1.8

Table 3.A.2: continued.

Source	Class	Disk	d pc	L_{bol} L_{\odot}	F_{cont} mJy/beam	$\theta_{\text{b,c}}$ ''	λ_{cont} mm	$M_{\text{dust},0}$ M_{\odot}	θ_{b} ''	θ_{s} ''	$N\text{CH}_3\text{OH}$ cm^{-2}	$M\text{CH}_3\text{OH}$ M_{\odot}	Ref.
Per-emb 36	I	N	320	10	1.0(2)	0.58	1.22	$3.6 \pm 0.5(-3)$	0.58	0.58	$< 2.3(15)$	$< 9.4(-11)$	TW.1.6
Per-emb 37	0	N	320	0.9	8.9	0.58	1.22	$3.1 \pm 0.5(-4)$	0.58	0.58	$< 1.8(15)$	$< 7.2(-11)$	TW.1.6
Per-emb 40	I	N	320	3.8	9.7	0.38	1.22	$8.5 \pm 1.3(-4)$	0.38	0.38	$< 4.2(15)$	$< 7.3(-11)$	TW.1.8
Per-emb 42	I	N	320	2.9	13	0.53	1.22	$3.8 \pm 0.6(-4)$	0.53	0.53	$1.9 \pm 1.8(17)$	$6.5 \pm 6.4(-9)$	TW.1.6
Per-emb 44	Burst	N	320	57	1.1(2)	0.58	1.22	$3.8 \pm 0.6(-3)$	0.58	0.58	$1.1 \pm 0.6(19)$	$4.5 \pm 2.3(-7)$	TW.1.8
Per-emb 50	I	Y	320	45	76	0.58	1.22	$2.6 \pm 0.4(-3)$	0.58	0.58	$< 1.7(15)$	$< 6.8(-11)$	TW.1.8,9
Per-emb 53	I	N	320	9.1	15	0.58	1.22	$9.6 \pm 1.4(-4)$	0.38	0.38	$< 4.2(15)$	$< 7.2(-11)$	TW.1.6
Per-emb 54	I	N	320	32	1.8	0.58	1.22	$1.1 \pm 0.9(-5)$	0.58	0.58	$< 1.6(15)$	$< 6.5(-11)$	TW.1.6
Per-emb 55	I	N	320	2.9	3.1	0.38	1.22	$2.0 \pm 0.3(-4)$	0.38	0.38	$< 4.2(15)$	$< 7.4(-11)$	TW.1.6
Per-emb 60	I	N	320	0.5	1.3	0.58	1.22	$4.4 \pm 0.7(-5)$	0.58	0.58	$< 1.4(15)$	$< 5.6(-11)$	TW.1.8
SVS 13A2	I	N	320	6.3	11	0.58	1.22	$3.9 \pm 0.6(-4)$	0.58	0.58	$1.7 \pm 1.6(17)$	$7.0 \pm 6.9(-9)$	TW.1.8
SVS 13B	0	Y	320	1.9	1.0(2)	0.58	1.22	$3.6 \pm 0.5(-3)$	0.58	0.58	$< 1.7(15)$	$< 6.8(-11)$	TW.1.8,9
81635A	HM	-	4.0(3)	2.4(3)	39	1.22	1.37	$1.4 \pm 0.2(-3)$	1.22	1.22	$< 2.1(15)$	$< 5.8(-8)$	TW.11.12
81635B	HM	-	4.0(3)	1.4(3)	24	1.22	1.37	$8.8 \pm 1.3(-4)$	1.22	1.22	$< 1.7(15)$	$< 4.6(-8)$	TW.11.12
81635C	HM	-	4.0(3)	1.3(3)	21	1.22	1.37	$7.7 \pm 1.1(-4)$	1.22	1.22	$< 1.9(15)$	$< 5.1(-8)$	TW.11.12
83968A	HM	-	3.4(3)	3.2(3)	24	1.23	1.37	$8.1 \pm 1.2(-4)$	1.23	1.23	$< 1.1(15)$	$< 2.3(-8)$	TW.11.12
83968B	HM	-	3.4(3)	2.0(3)	15	1.23	1.37	$5.1 \pm 0.8(-4)$	1.23	1.23	$< 1.3(15)$	$< 2.7(-8)$	TW.11.12
83968C	HM	-	3.4(3)	1.9(3)	14	1.23	1.37	$4.9 \pm 0.7(-4)$	1.23	1.23	$1.4 \pm 1.3(17)$	$3.0 \pm 2.9(-6)$	TW.11.12
83968D	HM	-	3.4(3)	1.8(3)	14	1.23	1.37	$4.7 \pm 0.7(-4)$	1.23	1.23	$< 3.3(15)$	$< 6.8(-8)$	TW.11.12
83968E	HM	-	3.4(3)	1.7(3)	14	1.23	1.37	$4.6 \pm 0.7(-4)$	1.23	1.23	$< 1.7(15)$	$< 3.6(-8)$	TW.11.12
86213A	HM	-	4.2(3)	2.0(4)	39	1.23	1.37	$1.5 \pm 0.2(-3)$	1.23	1.23	$< 1.5(15)$	$< 4.8(-8)$	TW.11.12
86213B	HM	-	4.2(3)	2.0(4)	38	1.23	1.37	$1.4 \pm 0.2(-3)$	1.23	1.23	$3.1 \pm 2.8(16)$	$9.9 \pm 9.0(-7)$	TW.11.12
86213C	HM	-	4.2(3)	1.1(4)	20	1.23	1.37	$7.5 \pm 1.1(-4)$	1.23	1.23	$8.0 \pm 7.6(16)$	$2.6 \pm 2.4(-6)$	TW.11.12
101899	HM	-	4.6(3)	9.2(4)	1.2(2)	1.25	1.37	$4.1 \pm 0.6(-3)$	1.25	1.25	$1.1 \pm 0.7(18)$	$4.1 \pm 2.9(-5)$	TW.11.12
103421	HM	-	4.6(3)	2.1(4)	71	1.24	1.37	$2.7 \pm 0.4(-3)$	1.24	1.24	$7.0 \pm 6.1(16)$	$2.6 \pm 2.3(-6)$	TW.11.12
106756A	HM	-	4.6(3)	1.3(5)	31	1.23	1.37	$1.2 \pm 0.2(-3)$	1.23	1.23	$8.4 \pm 7.7(16)$	$3.2 \pm 3.0(-6)$	TW.11.12
106756B	HM	-	4.6(3)	5.7(4)	18	1.23	1.37	$6.9 \pm 1.0(-4)$	1.23	1.23	$< 4.2(15)$	$< 1.6(-7)$	TW.11.12
106756C	HM	-	4.6(3)	5.5(4)	17	1.23	1.37	$6.5 \pm 1.0(-4)$	1.23	1.23	$< 5.0(15)$	$< 1.9(-7)$	TW.11.12
126120A	HM	-	4.6(3)	4.0(3)	18	1.17	1.37	$7.5 \pm 1.1(-4)$	1.17	1.17	$7.7 \pm 7.3(16)$	$2.6 \pm 2.5(-6)$	TW.11.12
126120B	HM	-	4.6(3)	3.3(3)	15	1.17	1.37	$6.4 \pm 1.0(-4)$	1.17	1.17	$4.3 \pm 4.1(16)$	$1.5 \pm 1.4(-6)$	TW.11.12
126120C	HM	-	4.6(3)	1.9(3)	8.8	1.17	1.37	$3.7 \pm 0.6(-4)$	1.17	1.17	$< 5.7(15)$	$< 2.0(-7)$	TW.11.12
126120D	HM	-	4.6(3)	1.5(3)	7	1.17	1.37	$2.9 \pm 0.4(-4)$	1.17	1.17	$< 1.0(15)$	$< 3.5(-8)$	TW.11.12
126348	HM	-	4.4(3)	6.8(3)	1.7(2)	1.16	1.37	$6.9 \pm 1.0(-3)$	1.16	1.16	$5.9 \pm 3.4(17)$	$1.8 \pm 1.1(-5)$	TW.11.13
565926A	HM	-	4.7(3)	6.0(3)	4.4	0.58	1.37	$5.4 \pm 0.8(-4)$	0.58	0.58	$< 5.0(15)$	$< 4.4(-8)$	TW.11.13
565926B	HM	-	4.7(3)	3.3(3)	2.4	0.58	1.37	$2.9 \pm 0.4(-4)$	0.58	0.58	$< 2.5(15)$	$< 2.9(-8)$	TW.11.13
565926C	HM	-	4.7(3)	3.0(3)	2.2	0.58	1.37	$2.7 \pm 0.4(-4)$	0.58	0.58	$< 2.8(15)$	$< 2.4(-8)$	TW.11.13
586092A	HM	-	1.8(3)	3.3(3)	57	0.92	1.37	$2.2 \pm 0.3(-3)$	0.92	0.92	$4.3 \pm 1.4(17)$	$1.4 \pm 0.5(-6)$	TW.11.13
586092B	HM	-	1.8(3)	1.5(3)	26	0.92	1.37	$9.8 \pm 1.5(-4)$	0.92	0.92	$1.5 \pm 1.4(17)$	$5.2 \pm 4.9(-7)$	TW.11.13
586092C	HM	-	1.8(3)	1.3(3)	22	0.92	1.37	$8.5 \pm 1.3(-4)$	0.92	0.92	$< 2.9(15)$	$< 9.7(-9)$	TW.11.13
615590	HM	-	2.7(3)	5.5(3)	1.2(2)	0.64	1.37	$9.1 \pm 1.4(-3)$	0.64	0.64	$4.2 \pm 1.1(18)$	$1.5 \pm 0.4(-5)$	TW.11.13
640076	HM	-	5.5(3)	2.2(5)	1.4(2)	0.87	1.37	$9.9 \pm 1.5(-3)$	0.87	0.87	$1.2 \pm 1.1(17)$	$3.2 \pm 3.1(-6)$	TW.11.13
644284A	HM	-	4.8(3)	-	1.9(2)	0.86	1.37	$1.3 \pm 0.2(-2)$	0.86	0.86	$1.0 \pm 0.5(18)$	$2.0 \pm 1.0(-5)$	TW.11
644284B	HM	-	4.8(3)	-	1.1(2)	0.86	1.37	$7.6 \pm 1.1(-3)$	0.86	0.86	$1.0 \pm 0.5(18)$	$2.0 \pm 1.0(-5)$	TW.11
693050	HM	-	4.3(3)	1.2(4)	1.9(3)	0.99	1.37	$1.0 \pm 0.2(-1)$	0.99	0.99	$8.9 \pm 4.4(17)$	$1.9 \pm 1.0(-5)$	TW.11.12

Table 3.A.2: continued.

Source	Class	Disk	d pc	L_{bol} L_{\odot}	F_{cont} mJy/beam	$\theta_{\text{b,c}}$ ''	λ_{cont} mm	$M_{\text{dust},0}$ M_{\odot}	θ_{b} ''	θ_{a} ''	$N\text{CH}_3\text{OH}$ cm^{-2}	$M\text{CH}_3\text{OH}$ M_{\odot}	Ref.
695243	HM	-	4.4(3)	8.5(2)	29	0.98	1.37	$1.5 \pm 0.2(-3)$	0.98	0.98	$<2.1(15)$	$<4.6(-8)$	TW.11.12
704792	HM	-	3.0(3)	5.2(4)	68	1.29	1.37	$2.0 \pm 0.3(-3)$	1.29	1.29	$<1.2(15)$	$<2.9(-8)$	TW.11.12
705768	HM	-	6.9(3)	9.2(4)	1.4(2)	0.87	1.37	$1.2 \pm 0.2(-2)$	0.87	0.87	$1.1 \pm 0.7(18)$	$4.7 \pm 2.8(-5)$	TW.11.12
706733A	HM	-	6.8(3)	1.5(4)	8.9	0.87	1.37	$7.0 \pm 1.1(-4)$	0.87	0.87	$<4.5(15)$	$<1.8(-7)$	TW.11.12
706733B	HM	-	6.8(3)	1.0(4)	5.9	0.87	1.37	$4.7 \pm 0.7(-4)$	0.87	0.87	$<1.7(15)$	$<6.7(-8)$	TW.11.12
706733C	HM	-	6.8(3)	7.6(3)	4.3	0.87	1.37	$3.4 \pm 0.5(-4)$	0.87	0.87	$<2.4(15)$	$<9.8(-8)$	TW.11.12
706785A	HM	-	6.4(3)	5.2(4)	15	0.88	1.37	$1.1 \pm 0.2(-3)$	0.88	0.88	$1.3 \pm 1.2(17)$	$4.8 \pm 4.7(-6)$	TW.11.12
706785B	HM	-	6.4(3)	4.7(4)	14	0.88	1.37	$1.0 \pm 0.2(-3)$	0.88	0.88	$9.5 \pm 9.4(16)$	$3.5 \pm 3.4(-6)$	TW.11.12
706785C	HM	-	6.4(3)	3.6(4)	10	0.88	1.37	$7.6 \pm 1.1(-4)$	0.88	0.88	$<1.5(15)$	$<5.5(-8)$	TW.11.12
706785D	HM	-	6.4(3)	2.8(4)	8	0.88	1.37	$6.1 \pm 0.9(-4)$	0.88	0.88	$<3.9(15)$	$<1.4(-7)$	TW.11.12
707948	HM	-	7.1(3)	2.0(5)	6.0(2)	0.88	1.37	$4.8 \pm 0.7(-2)$	0.88	0.88	$1.4 \pm 0.7(19)$	$4.9 \pm 3.4(-4)$	TW.11.12
717461A	HM	-	4.3(3)	3.3(3)	55	1.29	1.37	$1.9 \pm 0.3(-3)$	1.29	1.29	$7.1 \pm 5.1(17)$	$2.6 \pm 1.8(-5)$	TW.11.12
717461B	HM	-	4.3(3)	1.4(3)	28	1.29	1.37	$7.9 \pm 1.2(-4)$	1.29	1.29	$<3.4(15)$	$<1.2(-7)$	TW.11.12
721992	HM	-	5.4(3)	2.6(3)	47	0.85	1.37	$3.5 \pm 0.5(-3)$	0.85	0.85	$2.2 \pm 1.8(17)$	$5.5 \pm 4.3(-6)$	TW.11.12
724566	HM	-	4.9(3)	2.3(2)	89	0.83	1.37	$6.5 \pm 1.0(-3)$	0.83	0.83	$1.1 \pm 0.6(18)$	$2.2 \pm 1.1(-5)$	TW.11.12
732038	HM	-	5.6(3)	7.5(4)	72	0.82	1.37	$5.6 \pm 0.9(-3)$	0.82	0.82	$1.6 \pm 1.0(17)$	$4.0 \pm 2.4(-6)$	TW.11.12
744757A	HM	-	2.5(3)	1.2(4)	1.0(2)	1.30	1.37	$2.6 \pm 0.4(-3)$	1.30	1.30	$1.2 \pm 0.8(18)$	$1.6 \pm 1.0(-5)$	TW.11.12
744757B	HM	-	2.5(3)	8.6(3)	71	1.30	1.37	$1.9 \pm 0.3(-3)$	1.30	1.30	$7.5 \pm 6.3(16)$	$9.4 \pm 7.9(-7)$	TW.11.12
759150A	HM	-	3.8(3)	4.3(3)	16	1.29	1.37	$5.1 \pm 0.8(-4)$	1.29	1.29	$<2.0(15)$	$<5.6(-8)$	TW.11.12
759150B	HM	-	3.8(3)	2.3(3)	8.1	1.29	1.37	$2.7 \pm 0.4(-4)$	1.29	1.29	$<5.9(14)$	$<1.7(-8)$	TW.11.12
759150C	HM	-	3.8(3)	1.5(3)	5.3	1.29	1.37	$1.7 \pm 0.3(-4)$	1.29	1.29	$<6.2(14)$	$<1.7(-8)$	TW.11.12
759150D	HM	-	3.8(3)	1.4(3)	4.8	1.29	1.37	$1.6 \pm 0.2(-4)$	1.29	1.29	$<1.2(15)$	$<3.4(-8)$	TW.11.12
759150E	HM	-	3.8(3)	1.4(3)	4.8	1.29	1.37	$1.6 \pm 0.2(-4)$	1.29	1.29	$<1.7(15)$	$<4.7(-8)$	TW.11.12
767784	HM	-	4.0(3)	1.4(5)	7.9(2)	1.29	1.37	$2.7 \pm 0.4(-2)$	1.29	1.29	$2.1 \pm 0.7(18)$	$6.8 \pm 2.3(-5)$	TW.11.12
800287	HM	-	4.9(3)	1.0(5)	69	0.80	1.37	$5.2 \pm 0.8(-3)$	0.80	0.80	$7.8 \pm 2.2(17)$	$1.4 \pm 0.4(-5)$	TW.11.12
854214A	HM	-	4.5(3)	1.2(4)	54	1.26	1.37	$2.0 \pm 0.3(-3)$	1.26	1.26	$6.4 \pm 5.7(16)$	$2.4 \pm 2.2(-6)$	TW.11.12
854214B	HM	-	4.5(3)	5.5(3)	25	1.26	1.37	$9.4 \pm 1.4(-4)$	1.26	1.26	$6.2 \pm 6.1(16)$	$2.8 \pm 2.2(-6)$	TW.11.12
863312A	HM	-	4.7(3)	8.4(4)	36	0.83	1.37	$2.5 \pm 0.4(-3)$	0.83	0.83	$<3.8(15)$	$<6.9(-8)$	TW.11.12
863312B	HM	-	4.7(3)	4.9(4)	21	0.83	1.37	$1.5 \pm 0.2(-3)$	0.83	0.83	$<2.3(15)$	$<4.2(-8)$	TW.11.12
865468A	HM	-	3.0(3)	4.8(4)	8.2(2)	1.24	1.37	$2.6 \pm 0.4(-2)$	1.24	1.24	$1.2 \pm 0.2(19)$	$1.9 \pm 0.3(-4)$	TW.11.12
865468B	HM	-	3.0(3)	1.8(4)	3.1(2)	1.24	1.37	$9.7 \pm 1.5(-3)$	1.24	1.24	$4.6 \pm 2.2(17)$	$7.7 \pm 3.7(-6)$	TW.11.12
865468C	HM	-	3.0(3)	1.3(4)	2.2(2)	1.24	1.37	$6.8 \pm 1.0(-3)$	1.24	1.24	$4.6 \pm 2.2(17)$	$7.7 \pm 3.7(-6)$	TW.11.12
876288	HM	-	6.0(3)	5.8(4)	1.7(2)	0.81	1.37	$1.4 \pm 0.2(-2)$	0.81	0.81	$1.1 \pm 1.0(18)$	$3.0 \pm 2.8(-5)$	TW.11.12
881427A	HM	-	1.5(3)	9.8(2)	6.6(2)	1.23	1.37	$1.5 \pm 0.2(-2)$	1.23	1.23	$5.7 \pm 2.8(18)$	$2.8 \pm 1.1(-5)$	TW.11.13
881427B	HM	-	1.5(3)	6.5(2)	4.4(2)	1.23	1.37	$9.8 \pm 1.5(-3)$	1.23	1.23	$1.5 \pm 0.6(18)$	$5.9 \pm 2.5(-6)$	TW.11.13
881427C	HM	-	1.5(3)	4.6(2)	3.1(2)	1.23	1.37	$6.8 \pm 1.0(-3)$	1.23	1.23	$8.5 \pm 4.2(18)$	$3.4 \pm 1.7(-5)$	TW.11.13
G028.3891+00.1851	HM	-	1.1(4)	9.2(4)	55	1.24	1.37	$3.2 \pm 0.5(-3)$	1.24	1.24	$3.7 \pm 1.1(17)$	$7.9 \pm 2.3(-5)$	TW.11.12
G023.6566-00.1273	HM	-	3.2(3)	4.8(3)	85	1.24	1.37	$2.7 \pm 0.4(-3)$	1.24	1.24	$7.0 \pm 2.0(17)$	$1.8 \pm 0.4(-5)$	TW.11.12
G025.6498+01.0491	HM	-	1.2(4)	4.2(5)	1.5(2)	1.17	1.37	$1.1 \pm 0.2(-2)$	1.17	1.17	$2.0 \pm 0.8(18)$	$4.7 \pm 1.9(-4)$	TW.11.12
G030.1981-00.1691	HM	-	5.8(3)	2.2(4)	15	0.60	1.37	$1.9 \pm 0.3(-3)$	0.60	0.60	$3.0 \pm 1.5(17)$	$4.2 \pm 2.1(-6)$	TW.11.12
G233.8306-00.1803	HM	-	3.5(3)	1.1(4)	36	0.81	1.37	$2.3 \pm 0.3(-3)$	0.81	0.81	$<2.4(15)$	$<2.2(-8)$	TW.11.13
G305.2017+00.2072A1	HM	-	4.0(3)	2.0(4)	94	1.30	1.37	$3.1 \pm 0.5(-3)$	1.30	1.30	$8.5 \pm 4.3(17)$	$2.7 \pm 1.4(-5)$	TW.13
G305.2017+00.2072A2	HM	-	4.0(3)	1.0(4)	45	1.30	1.37	$1.5 \pm 0.2(-3)$	1.30	1.30	$2.4 \pm 2.3(17)$	$7.6 \pm 7.4(-6)$	TW.13
G310.0135+00.3892	HM	-	3.0(3)	3.5(4)	3.7(2)	1.30	1.37	$1.1 \pm 0.2(-2)$	1.30	1.30	$7.3 \pm 6.8(16)$	$1.3 \pm 1.2(-6)$	TW.11.12

Table 3.A.2: continued.

Source	Class	Disk	d pc	L_{bol} L_{\odot}	F_{cont} mJy/beam	$\theta_{\text{b,c}}$ ''	λ_{cont} mm	$M_{\text{dust},0}$ M_{\odot}	θ_{b} ''	θ_{s} ''	$N\text{CH}_3\text{OH}$ cm^{-2}	$M\text{CH}_3\text{OH}$ M_{\odot}	Ref.
G314.3197+00.1125	HM	—	8.2(3)	6.6(4)	1.0(2)	1.30	1.37	4.9±0.7(-3)	1.30	1.30	8.2±4.1(17)	1.1±0.6(-4)	TW.11.12
G316.6412+00.0867	HM	—	2.7(3)	8.1(3)	1.4(2)	1.29	1.37	3.9±0.6(-3)	1.29	1.29	2.0±0.8(18)	3.0±1.2(-5)	TW.11.12
G318.0489+00.0854B	HM	—	3.2(3)	3.6(4)	1.5(2)	1.30	1.37	4.4±0.7(-3)	1.30	1.30	7.9±3.9(17)	1.6±0.8(-5)	TW.11.12
G318.0480+00.1969A1	HM	—	1.0(4)	2.1(5)	2.2(2)	1.29	1.37	1.2±0.2(-2)	1.29	1.29	5.5±3.3(18)	1.2±0.7(-3)	TW.11.12
G318.0480+00.1969A2	HM	—	1.0(4)	6.6(4)	69	1.29	1.37	3.7±0.6(-3)	1.29	1.29	8.1±7.7(16)	1.7±1.6(-5)	TW.11.12
G323.7399+00.2617B1	HM	—	3.2(3)	1.7(3)	1.5(2)	1.28	1.37	4.5±0.7(-3)	1.28	1.28	5.7±3.8(17)	1.1±0.7(-5)	TW.13
G323.7399+00.2617B2	HM	—	3.2(3)	1.5(3)	1.3(2)	1.28	1.37	3.9±0.6(-3)	1.28	1.28	4.7±2.8(18)	9.3±5.6(-5)	TW.13
G323.7399+00.2617B3	HM	—	3.2(3)	1.2(3)	1.0(2)	1.28	1.37	3.1±0.5(-3)	1.28	1.28	7.4±6.0(16)	1.5±1.2(-6)	TW.13
G323.7399+00.2617B4	HM	—	3.2(3)	9.5(2)	78	1.28	1.37	2.4±0.4(-3)	1.28	1.28	7.7±6.5(16)	1.5±1.3(-6)	TW.13
G323.7399+00.2617B5	HM	—	3.2(3)	7.3(2)	60	1.28	1.37	1.8±0.3(-3)	1.28	1.28	7.0±6.9(16)	1.4±1.3(-6)	TW.13
G323.7399+00.2617B6	HM	—	3.2(3)	5.8(2)	52	1.28	1.37	1.6±0.2(-3)	1.28	1.28	8.9±8.8(16)	1.8±1.7(-6)	TW.13
G323.7399+00.2617B7	HM	—	3.2(3)	5.8(2)	54	1.28	1.37	1.6±0.2(-3)	1.28	1.28	4.1±4.0(16)	8.2±8.1(-7)	TW.13
G327.1192+00.5103	HM	—	4.7(3)	5.4(4)	70	1.25	1.37	5.2±0.8(-3)	0.81	0.81	1.9±0.6(18)	3.3±1.1(-5)	TW.11.12
G343.1261+00.0623	HM	—	2.0(3)	3.4(4)	3.7(2)	1.25	1.37	9.3±1.4(-3)	1.25	1.25	4.7±1.4(17)	3.4±1.1(-6)	TW.11.12
G345.5043+00.3480	HM	—	2.0(3)	2.9(4)	3.8(2)	1.25	1.37	9.5±1.4(-3)	1.25	1.25	5.0±3.0(18)	3.7±2.2(-5)	TW.11.12
G348.7342+01.0359B1	HM	—	2.8(3)	1.5(4)	62	1.23	1.37	1.9±0.3(-3)	1.23	1.23	9.6±8.8(16)	1.3±1.2(-6)	TW.13
G348.7342+01.0359B2	HM	—	2.8(3)	1.0(4)	43	1.23	1.37	1.3±0.2(-3)	1.23	1.23	1.5±1.4(17)	2.1±2.0(-6)	TW.13
G348.7342+01.0359B3	HM	—	2.8(3)	9.7(3)	41	1.23	1.37	1.2±0.2(-3)	1.23	1.23	<2.1(15)	<2.9(-8)	TW.13
HH 212	0	Y	400	9	1.1(2)	0.35	0.85	2.7±0.4(-3)	0.35	0.11	1.4±0.6(18)	3.2±1.4(-9)	14.15,16,17,18
IRAS 16293A	0	N	140	18	1.0(3)	0.50	0.88	1.2±0.2(-2)	0.50	0.50	1.3±0.4(19)	7.5±2.3(-8)	19,20,21
IRAS 16293B	0	N	140	3	2.0(3)	0.50	0.88	2.5±0.4(-2)	0.50	0.50	1.0±0.2(19)	5.9±1.3(-8)	19,20,22
L483	0	N	200	12	50	0.13	0.86	5.3±0.8(-3)	0.13	0.34	1.7±0.4(19)	9.5±2.1(-8)	23,24
IRAS 4A1	0	Y	320	9.1	3.9(2)	0.59	1.22	1.3±0.2(-2)	0.59	0.22	>1.0(19)	>5.8(-8)	TW.1.8,9,25
IRAS 4A2	0	N	320	4.5	1.9(2)	0.59	1.22	6.4±1.0(-3)	0.59	0.24	>1.0(18)	>6.9(-9)	TW.1.8,25
L1527	0	Y	140	2.3	1.3(2)	1.00	1.00	7.9±1.2(-4)	0.50	1.00	<2.0(15)	<4.6(-11)	26,27,28,29
BHR 71	0	N	200	11	5.9(2)	0.32	0.88	1.7±0.3(-2)	0.32	0.50	2.5±0.5(18)	2.9±0.6(-8)	2,30,31
Serpens SMM1-a	0	—	436	1.1(2)	8.0(2)	0.33	0.87	3.2±0.5(-2)	0.33	1.20	1.1±0.6(18)	3.5±1.9(-7)	4,27,32,33
BI-BS	0	N	320	0.6	1.5(2)	0.39	1.22	9.2±1.4(-3)	0.63	0.35	3.6±0.8(17)	5.3±1.2(-9)	TW.1.6,34
Ser-emb 1	0	—	436	4.1	1.2(2)	0.46	1.29	7.9±1.2(-3)	0.46	0.35	>2.2(-9)	>8.0(16)	1.5,35
Ser-emb 11W	1	—	436	4.9	70	0.53	1.29	3.7±0.6(-3)	0.53	0.14	3.8±0.4(18)	1.6±0.2(-8)	1.5,36
B335	0	N	100	0.8	4.8	0.05	1.30	4.3±0.6(-3)	0.05	0.15	>6.7(18)	>1.8(-9)	2,37,38
SVS 18A	Burst	N	320	57	1.1(2)	0.58	1.22	3.8±0.6(-3)	0.00	0.30	1.4±0.3(19)	1.5±0.3(-7)	TW.1.8,39
L1551 IRS5	1	Y	140	23	1.5(2)	0.19	1.30	2.1±0.3(-2)	0.19	0.15	>2.0(19)	>1.0(-8)	2,26,40,41
GSS30-IRS1	1	Y	139	11	30	0.37	0.88	5.8±0.9(-4)	0.37	0.15	<2.5(15)	<1.3(-12)	42,43,44
[GY92] 30	1	Y	139	0.1	80	0.37	0.88	1.6±0.2(-3)	0.37	0.17	<2.5(15)	<8.2(-13)	42,43,44
WL 12	1	Y	139	1.4	1.4(2)	0.37	0.88	2.8±0.4(-3)	0.37	0.12	<2.5(15)	<8.2(-13)	42,43,44
[GY92] 197	1	Y	139	0.2	71	0.37	0.88	1.4±0.2(-3)	0.37	0.24	<2.5(15)	<3.8(-12)	42,43,44
Eliax 29	1	Y	139	18	34	0.37	0.88	6.6±1.0(-4)	0.37	0.16	<2.5(15)	<1.6(-12)	42,43,44
IRS 43	1	Y	139	3.3	32	0.37	0.88	6.3±0.9(-4)	0.37	0.17	<2.5(15)	<1.6(-12)	42,43,44
IRS 44	1	Y	139	7.1	29	0.37	0.88	5.7±0.9(-4)	0.37	0.21	<2.5(15)	<2.5(-12)	42,43,44
IRS 16253	0	Y	139	0.2	32	0.37	0.88	6.2±0.9(-4)	0.37	0.17	<2.5(15)	<1.6(-12)	42,43,44
ISO-Oph 203	1	Y	139	0.1	11	0.37	0.88	2.1±0.3(-4)	0.37	0.08	<2.5(15)	<3.6(-13)	42,43,44
IRS 67	1	Y	139	2.8	1.3(2)	0.37	0.88	2.4±0.4(-3)	0.37	0.17	<2.5(15)	<1.6(-12)	42,43,44
V883 Ori	Burst	Y	400	2.2(2)	2.9(2)	0.20	0.88	2.4±0.4(-2)	0.20	0.60	4.3±0.7(17)	2.9±0.5(-8)	14,45,46,47

Table 3.A.2: continued.

Source	Class	Disk	d pc	L_{bol} L_{\odot}	F_{cont} mJy/beam	$\theta_{\text{b,c}}$ ''	λ_{cont} mm	$M_{\text{dust},0}$ M_{\odot}	θ_{b} ''	θ_{s} ''	$N\text{CH}_3\text{OH}$ cm^{-2}	$M\text{CH}_3\text{OH}$ M_{\odot}	Ref.
AFGL 4176	HM	Y	3.7(3)	9.7(4)	29	0.30	1.20	$5.3 \pm 0.8(-3)$	0.30	0.30	$5.5 \pm 0.4(18)$	$8.0 \pm 0.6(-6)$	48,49,50,51
Sgr B2(N2)	HM	—	8.3(3)	2.6(5)	1.4(2)	1.50	3.00	$8.2 \pm 1.2(-2)$	1.50	1.40	$4.1 \pm 0.9(19)$	$6.5 \pm 1.4(-3)$	52,53,54,55
Sgr B2(N3)	HM	—	8.3(3)	4.5(4)	—	—	—	—	1.50	0.40	$4.1 \pm 0.9(18)$	$5.3 \pm 1.2(-5)$	52,53,54,56
Sgr B2(N4)	HM	—	8.3(3)	3.9(5)	34	1.50	3.00	$2.0 \pm 0.3(-2)$	1.50	1.00	$2.6 \pm 0.6(17)$	$2.1 \pm 0.5(-5)$	52,53,54,56
Sgr B2(N5)	HM	—	8.3(3)	2.8(5)	62	1.50	3.00	$3.7 \pm 0.6(-2)$	1.50	1.00	$7.9 \pm 2.1(17)$	$7.9 \pm 1.7(-5)$	52,53,54,56
NGC6334I MM1 I	HM	—	1.3(3)	5.8(4)	2.4(3)	0.53	1.30	$1.4 \pm 0.2(-1)$	0.20	0.87	$1.2 \pm 0.3(20)$	$1.8 \pm 0.5(-4)$	52,57,58,59
NGC6334I MM1 II	HM	—	1.3(3)	1.1(4)	4.5(2)	0.54	1.30	$2.7 \pm 0.4(-2)$	0.20	0.87	$9.9 \pm 0.9(19)$	$1.5 \pm 0.1(-4)$	52,57,58,59
NGC6334I MM1 III	HM	—	1.3(3)	5.1(4)	2.1(3)	0.50	1.30	$1.4 \pm 0.2(-1)$	0.20	0.87	$7.8 \pm 1.7(19)$	$1.2 \pm 0.3(-4)$	52,57,58,59
NGC6334I MM1 IV	HM	—	1.3(3)	1.1(4)	4.5(2)	0.54	1.30	$2.7 \pm 0.4(-2)$	0.20	0.87	$6.9 \pm 1.5(19)$	$1.0 \pm 0.2(-4)$	52,57,58,59
NGC6334I MM1 V	HM	—	1.3(3)	1.1(4)	4.5(2)	0.55	1.30	$2.6 \pm 0.4(-2)$	0.20	0.87	$1.9 \pm 0.4(19)$	$2.9 \pm 0.6(-5)$	52,57,58,59
NGC6334I MM2 I	HM	—	1.3(3)	7.5(3)	3.2(2)	0.34	1.30	$3.8 \pm 0.6(-2)$	0.20	0.87	$5.2 \pm 1.6(19)$	$7.8 \pm 2.4(-5)$	52,57,58,59
NGC6334I MM2 II	HM	—	1.3(3)	1.5(3)	8	0.18	1.30	$2.5 \pm 0.4(-3)$	0.20	0.87	$1.5 \pm 0.3(19)$	$2.2 \pm 0.5(-5)$	52,57,58,59
NGC6334I MM3 I	HM	—	1.3(3)	—	—	—	—	—	0.20	0.87	$6.5 \pm 1.4(18)$	$9.7 \pm 2.1(-6)$	52,59
NGC6334I MM3 II	HM	—	1.3(3)	—	—	—	—	—	0.20	0.87	$6.0 \pm 1.3(18)$	$9.0 \pm 2.0(-6)$	52,59

Notes. $a(b)$ represents $a \times 10^b$. In the disk column we indicate whether a disk is confirmed (Y), whether no disk on > 50 au scales is confirmed (N), or whether no information about a disk is available (—). $\theta_{\text{b,c}}$ and θ_{b} represent the beam size of the continuum and line data, respectively, and θ_{s} is the assumed source size.

References. References for distances, bolometric luminosities (scaled to the reported distance), continuum fluxes, column densities, and, if applicable, a disk detection: TW: This work; 1: Ortiz-León et al. (2018); 2: Karska et al. (2018); 3: van Gelder et al. (2020); 4: Ortiz-León et al. (2017); 5: Enoch et al. (2011); 6: Murillo et al. (2016); 7: Enoch et al. (2009); 8: Tobin et al. (2016); 9: Segura-Cox et al. (2018); 10: Maury et al. (2019); 11: Mège et al. (2021); 12: Elia et al. (2017); 13: Lumsden et al. (2013); 14: Kounkel et al. (2017); 15: Zinnecker et al. (1992); 16: Lee et al. (2008); 17: Lee et al. (2019a); 18: Lee et al. (2017b); 19: Dzib et al. (2018b); 20: Jacobsen et al. (2018); 21: Manigand et al. (2020); 22: Jørgensen et al. (2018); 23: Jacobsen et al. (2019); 24: Tafalla et al. (2000); 25: De Simone et al. (2020); 26: Zucker et al. (2019); 27: Kristensen et al. (2012); 28: Belloche et al. (2020); 29: Tobin et al. (2012); 30: Seidensticker & Schmidt-Kaler (1989); 31: Yang et al. (2020); 32: Hull et al. (2017); 33: Ligterink et al. (2021); 34: Marcelino et al. (2018); 35: Martín-Doménech et al. (2019); 36: Martín-Doménech et al. (2021); 37: Olofsson & Olofsson (2009); 38: Bjerkeli et al. (2019); 39: Bianchi et al. (2017a); 40: Bianchi et al. (2020); 41: Cruz-Sáenz de Miera et al. (2019); 42: Mamajek (2008); 43: Dunham et al. (2015); 44: Artur de la Villarmois et al. (2019); 45: Furlan et al. (2016); 46: Lee et al. (2019b); 47: Cieza et al. (2016); 48: Bailer-Jones et al. (2018); 49: Beltrán et al. (2006); 50: Bøgelund et al. (2019); 51: Johnston et al. (2015); 52: Reid et al. (2014); 53: Bonfand et al. (2019); 54: Belloche et al. (2016); 55: Müller et al. (2016); 56: Bonfand et al. (2017); 57: Sandell (2000); 58: Brogan et al. (2016); 59: Bøgelund et al. (2018).

3.B Transitions of CH₃OH and isotopologues

Table 3.B.1: Transitions of CH₃OH and isotopologues covered in the various ALMA programs.

Species	Transition		Frequency	A_{ij}	E_{up}
	(J K L M - J K L M)		(GHz)	(s ⁻¹)	(K)
2017.1.01174.S ($\theta_{beam} \sim 0.45''$, $rms_{line} \sim 0.15$ K)					
CH ₃ OH	20 8 13 2 - 21 7 14 2		260.0643	2.1×10^{-5}	808.2
	20 3 18 0 - 20 2 19 0		260.3815	9.1×10^{-5}	536.9
	2 1 1 1 - 1 0 1 1		261.8057	5.6×10^{-5}	28.0
¹³ CH ₃ OH	2 1 1 0 - 1 0 1 0		259.9865	5.5×10^{-5}	27.9
	18 3 16 +0 - 18 2 17 -0		260.0888	9.2×10^{-5}	437.2
	20 3 18 +0 - 20 2 19 -0		262.7673	9.4×10^{-5}	525.4
	7 4 4 -0 - 8 3 5 -0		262.9130	1.7×10^{-5}	144.2
	7 4 3 +0 - 8 3 6 +0		262.9203	1.7×10^{-5}	144.2
	5 2 3 0 - 4 1 3 0		263.1133	7.4×10^{-5}	56.3
	11 2 10 -0 - 10 3 7 -0		263.3060	2.9×10^{-5}	187.3
	25 -7 18 0 - 26 -6 20 0		263.5779	2.8×10^{-5}	996.5
CH ₃ ¹⁸ OH	12 2 10 4 - 13 3 10 4		260.0355	7.1×10^{-5}	537.2
	16 3 13 0 - 16 2 14 0		260.3163	9.3×10^{-5}	352.6
	15 1 15 1 - 14 2 13 1		260.4403	2.8×10^{-5}	272.2
	12 3 9 0 - 12 2 10 0		261.8972	9.2×10^{-5}	223.6
	11 3 8 0 - 11 2 9 0		262.1524	9.2×10^{-5}	196.9
	7 3 4 0 - 7 2 5 0		262.7722	8.6×10^{-5}	112.4
	6 3 3 0 - 6 2 4 0		262.8532	8.3×10^{-5}	96.8
	5 3 2 0 - 5 2 3 0		262.9139	7.7×10^{-5}	83.5
	4 3 1 0 - 4 2 2 0		262.9583	6.8×10^{-5}	72.3
	5 3 3 0 - 5 2 4 0		262.9825	7.7×10^{-5}	83.5
	4 3 2 0 - 4 2 3 0		262.9878	6.8×10^{-5}	72.3
	3 3 0 0 - 3 2 1 0		262.9897	4.8×10^{-5}	63.4
	6 3 4 0 - 6 2 5 0		262.9900	8.3×10^{-5}	96.8
	3 3 1 0 - 3 2 2 0		262.9995	4.8×10^{-5}	63.4
	7 3 5 0 - 7 2 6 0		263.0177	8.6×10^{-5}	112.4
	8 3 6 0 - 8 2 7 0		263.0739	8.9×10^{-5}	130.2
	9 3 7 0 - 9 2 8 0		263.1684	9.0×10^{-5}	150.2
	10 3 8 0 - 10 2 9 0		263.3116	9.2×10^{-5}	172.5
	16 5 12 4 - 17 6 12 4		263.4603	5.8×10^{-5}	846.9
	11 3 9 0 - 11 2 10 0		263.5151	9.2×10^{-5}	196.9
2017.1.01350.S ($\theta_{beam} \sim 0.3''$, $rms_{line} \sim 0.5$ K)					
CH ₃ OH	20 1 19 1 - 20 0 20 1		217.8865	3.4×10^{-5}	508.4
	25 3 23 1 - 24 4 20 1		219.9837	2.0×10^{-5}	802.2
	23 5 18 1 - 22 6 17 1		219.9937	1.7×10^{-5}	775.9
	10 5 6 2 - 11 4 8 2		220.4013	1.1×10^{-5}	251.6
	10 2 9 0 - 9 3 6 0		231.2811	1.8×10^{-5}	165.3

Table 3.B.1: continued.

Species	Transition		Frequency	A_{ij}	E_{up}
	(J K L M - J K L M)		(GHz)	(s^{-1})	(K)
$^{13}\text{CH}_3\text{OH}$	11 6 5 4 - 11 7 4 4		233.1212	1.0×10^{-5}	745.0
	18 3 15 0 - 17 4 14 0		233.7957	2.2×10^{-5}	446.6
	13 3 11 6 - 14 4 11 6		233.9170	1.4×10^{-5}	868.5
	13 3 10 6 - 14 4 10 6		233.9170	1.4×10^{-5}	868.5
	4 2 3 0 - 5 1 4 0		234.6834	1.9×10^{-5}	60.9
	14 1 13 -0 - 13 2 12 -0		217.0446	2.4×10^{-5}	254.3
$^{13}\text{CH}_3\text{OH}$	21 -4 18 0 - 20 -5 15 0		231.3891	2.1×10^{-5}	611.1
	24 5 20 0 - 23 6 18 0		233.4879	2.2×10^{-5}	815.4
	5 1 5 +0 - 4 1 4 +0		234.0116	5.3×10^{-5}	48.3
	9 1 9 1 - 8 0 8 1		234.5609	3.6×10^{-5}	393.3
	26 3 23 0 - 25 4 21 0		234.8658	2.5×10^{-5}	843.0
$\text{CH}_3^{18}\text{OH}$	26 3 23 2 - 25 4 21 2		216.6903	1.9×10^{-5}	828.8
	14 1 14 1 - 13 2 12 1		217.1729	1.7×10^{-5}	238.9
	18 6 13 4 - 17 7 11 4		217.9223	1.5×10^{-5}	874.1
	5 1 5 6 - 4 1 4 6		230.4823	5.0×10^{-5}	712.0
	11 0 11 0 - 10 1 10 0		230.9519	6.4×10^{-5}	146.8
	5 2 3 8 - 4 2 2 8		230.9544	4.4×10^{-5}	617.8
	5 1 5 7 - 4 1 4 7		230.9582	5.1×10^{-5}	563.6
	5 1 5 3 - 4 1 4 3		230.9590	5.1×10^{-5}	358.0
	5 4 2 5 - 4 4 1 5		231.1535	1.9×10^{-5}	397.3
	5 3 3 5 - 4 3 2 5		231.1639	3.4×10^{-5}	450.3
	5 4 1 4 - 4 4 0 4		231.1689	1.9×10^{-5}	437.7
	5 3 2 4 - 4 3 1 4		231.1709	3.4×10^{-5}	356.1
	5 4 1 3 - 4 4 0 3		231.1757	1.9×10^{-5}	514.0
	5 4 2 3 - 4 4 0 3		231.1757	1.9×10^{-5}	514.0
	5 2 3 4 - 4 2 2 4		231.1787	4.4×10^{-5}	397.4
	5 2 3 3 - 4 2 2 3		231.1820	4.4×10^{-5}	331.8
	5 3 3 3 - 4 3 2 3		231.1836	3.4×10^{-5}	428.0
	5 3 2 3 - 4 3 1 3		231.1836	3.4×10^{-5}	428.0
	5 2 4 3 - 4 2 3 3		231.1852	4.4×10^{-5}	331.8
	5 1 5 5 - 4 1 4 5		231.1917	5.1×10^{-5}	324.4
	5 0 5 4 - 4 0 4 4		231.1942	5.3×10^{-5}	333.4
	5 2 4 5 - 4 2 3 5		231.1962	4.5×10^{-5}	431.4
	5 1 4 4 - 4 1 3 4		231.2260	5.1×10^{-5}	444.6
	5 0 5 3 - 4 0 4 3		231.2553	5.3×10^{-5}	454.7
	5 1 4 6 - 4 1 3 6		231.3405	5.1×10^{-5}	712.1
	17 2 16 3 - 16 1 15 3		233.6336	4.0×10^{-5}	637.9
	5 1 4 0 - 4 1 3 0		233.7279	5.3×10^{-5}	48.0
	2016.1.01501.S & 2017.1.01426.S ($\theta_{\text{beam}} \sim 0.4''$, $\text{rms}_{\text{line}} \sim 0.2$ K)				
CH_3OH	5 1 4 0 - 4 1 3 0		243.9158	6.0×10^{-5}	49.7
	20 3 17 0 - 20 2 18 0		246.0746	8.2×10^{-5}	537.0
	19 3 16 0 - 19 2 17 0		246.8733	8.3×10^{-5}	490.7

Table 3.B.1: continued.

Species	Transition (J K L M - J K L M)								Frequency (GHz)	A_{ij} (s^{-1})	E_{up} (K)
$^{13}\text{CH}_3\text{OH}$	2 1 1 1	-	1 0 1 1						261.8057	5.6×10^{-5}	28.0
	23 4 19 0	-	22 5 18 0						246.4261	2.6×10^{-5}	721.0
	23 3 20 -0	-	23 2 21 +0						247.0863	8.5×10^{-5}	674.9
	17 3 15 +0	-	17 2 16 -0						259.0365	9.1×10^{-5}	396.5
$\text{CH}_3^{18}\text{OH}$	11 2 10 0	-	10 3 7 0						246.2566	2.3×10^{-5}	184.3
	15 1 14 4	-	16 2 14 4						246.8637	1.3×10^{-5}	677.5
2019.1.00195.L ($\theta_{\text{beam}} \sim 1''$, $\text{rms}_{\text{line}} \sim 0.2$ K)											
CH_3OH	6 1 5 3	-	7 2 5 3						217.2992	4.3×10^{-5}	373.9
	15 6 9 3	-	16 5 11 3						217.6427	1.9×10^{-5}	745.6
	15 6 10 3	-	16 5 12 3						217.6427	1.9×10^{-5}	745.6
	20 1 19 1	-	20 0 20 1						217.8865	3.4×10^{-5}	508.4
	4 2 3 1	-	3 1 2 1						218.4401	4.7×10^{-5}	45.5
	25 3 23 1	-	24 4 20 1						219.9837	2.0×10^{-5}	802.2
	23 5 18 1	-	22 6 17 1						219.9937	1.7×10^{-5}	775.9
	8 0 8 1	-	7 1 6 1						220.0786	2.5×10^{-5}	96.6
	10 5 6 2	-	11 4 8 2						220.4013	1.1×10^{-5}	251.6
$^{13}\text{CH}_3\text{OH}$	14 1 13 -0	-	13 2 12 -0						217.0446	2.4×10^{-5}	254.3
	10 2 8 +0	-	9 3 7 +0						217.3995	1.5×10^{-5}	162.4
	17 7 11 +0	-	18 6 12 +0						220.3218	1.3×10^{-5}	592.3
	17 7 10 -0	-	18 6 13 -0						220.3218	1.3×10^{-5}	592.3
$\text{CH}_3^{18}\text{OH}$	14 1 14 1	-	13 2 12 1						217.1729	1.7×10^{-5}	238.9
	18 6 13 4	-	17 7 11 4						217.9223	1.5×10^{-5}	874.1
	17 5 13 4	-	18 6 13 4						218.5521	3.2×10^{-5}	884.6
	21 1 20 2	-	21 0 21 1						218.8351	3.4×10^{-5}	534.5
	23 4 19 2	-	22 5 18 2						219.0356	1.8×10^{-5}	709.6
	4 2 2 2	-	3 1 2 2						219.4078	4.6×10^{-5}	44.6
	8 7 1 5	-	7 6 1 5						219.8433	2.8×10^{-5}	663.2
	18 3 16 5	-	19 4 16 5						219.9572	5.1×10^{-5}	795.8
	8 1 8 1	-	7 0 7 1						220.1951	3.6×10^{-5}	85.7

Notes. The typical beam size and rms are listed for each data set.

3.C Toy model of a spherically symmetric infalling envelope

In this simple toy model of a spherically symmetric infalling envelope, the envelope is heated by the luminosity of the central protostar. The density structure at a

radius R can be written as

$$n_{\text{H}} = n_{\text{H},0} \left(\frac{R}{R_0} \right)^{-p}, \quad (3.6)$$

with $n_{\text{H},0}$ the density at a radius R_0 . The snow line radius of a molecule with sublimation temperature T_{sub} then scales as (for details, see Appendix B of Nazari et al. 2021)

$$R_{\text{sub}} = R_0 \left(\frac{T_{\text{sub}}}{T_0} \right)^{-1/\gamma}, \quad (3.7)$$

where γ is the slope of the temperature profile in the envelope and T_0 is the temperature at a radius R_0 . In this work, a sublimation temperature of 100 K is adopted based on experiments of pure CH_3OH and mixed $\text{H}_2\text{O}:\text{CH}_3\text{OH}$ ices (e.g., Collings et al. 2004). At a typical inner envelope density of 10^7 cm^{-3} , the adopted T_{sub} corresponds to a binding energy of $\sim 5000 \text{ K}$, which is slightly higher than that recommended by Penteado et al. (2017). Radiative transfer calculations show that, for protostellar envelopes, $\gamma = 2/5$ at $> 10 \text{ au}$ scales and that $T_0 \propto L_{\text{bol}}^{1/5}$ (Adams & Shu 1985). Equation (3.7) can then be written as

$$R_{\text{sub}} \propto L_{\text{bol}}^{1/2}, \quad (3.8)$$

which (except for a pre-factor) is similar to the relation that was derived by Bisschop et al. (2007) for the 100 K radius in high-mass protostars and more recently seen to be remarkably similar for low-mass protostars (van 't Hoff et al. 2022). Using Eqs. (3.6) and (3.7), the total warm methanol mass inside the snow line is proportional to (Nazari et al. 2021)

$$M_{\text{CH}_3\text{OH}} \propto n_{\text{H},0} L_{\text{bol}}^{(3-p)/(5\gamma)}. \quad (3.9)$$

Using $p = 3/2$ for an infalling envelope and $\gamma = 2/5$ and assuming that $n_{\text{H},0} \propto M_0$ (i.e., a more massive envelope is denser at a certain radius R_0) yields

$$M_{\text{CH}_3\text{OH}} \propto M_0 L_{\text{bol}}^{3/4}, \quad (3.10)$$

where M_0 is the total warm plus cold mass contained within a radius R_0 .

3.D Calculating the reference dust mass

The dust mass is estimated from the peak continuum flux, F_{cont} , within the central beam. Since the continuum fluxes in this work are derived from multiple data sets that cover different frequencies (but all in Band 6), the measured fluxes are scaled to a wavelength of 1.2 mm (i.e., $\sim 250 \text{ GHz}$) through

$$F_{1.2\text{mm}} = F_{\text{cont}} \left(\frac{\lambda_{\text{cont}}}{1.2 \text{ mm}} \right)^\alpha, \quad (3.11)$$

where λ_{cont} is the wavelength of the observations and α is the power-law index of the dust continuum. In this work, $\alpha = 2.5$ is assumed for the low-mass sources (Tychoniec et al. 2020) and $\alpha = 3.5$ for the high-mass sources (Palau et al. 2014). The dust mass within the beam, $M_{\text{dust,beam}}$, is calculated from the continuum flux using the equation from Hildebrand (1983),

$$M_{\text{dust,beam}} = \frac{F_{1.2\text{mm}} d^2}{\kappa_\nu B_\nu(T_{\text{dust}})}, \quad (3.12)$$

with B_ν the Planck function for a given dust temperature, T_{dust} , and κ_ν the dust opacity in the optically thin limit. Here, a dust temperature of 30 K is assumed for low-mass ($L_{\text{bol}} \lesssim 100 L_\odot$) sources, which is typical for the inner envelopes of embedded protostellar systems (Whitney et al. 2003). For high-mass sources ($L_{\text{bol}} \gtrsim 1000 L_\odot$), a dust temperature of 50 K is adopted. Although the dust temperature in the inner regions may be as high as a few hundred kelvin, the dust emitting at millimeter wavelengths in our $\sim 1''$ beam likely resides at larger distances (~ 1000 au) from the source, where the dust temperature is on the order of 50 K (e.g., van der Tak et al. 2013; Palau et al. 2014). The dust opacity, κ_ν , is set to $2.3 \text{ cm}^2 \text{ g}^{-1}$ for a wavelength of 1.2 mm (e.g., Ansdell et al. 2016).

The $M_{\text{dust,beam}}$ is an estimate of the dust mass within the beam with a physical radius R_{beam} (see Eq. (3.2)) (e.g., Saraceno et al. 1996). The observational data used in this work probe different physical scales depending on the beam size and the distance to the source. For example, the PEACHES beam of $\sim 0.4 - 0.5''$ probes the disk and inner envelope on $R_{\text{beam}} \sim 50$ au scales in Perseus, while the ALMAGAL beam of $\sim 1 - 2''$ probes a larger fraction of the envelope at $R_{\text{beam}} \sim 1000 - 5000$ au scales for sources at $\sim 1 - 5$ kpc. Therefore, the dust masses are scaled to a common arbitrary radius of $R_0 = 200$ au assuming the mass contained in the beam follows a typical free-falling envelope power-law scaling of $p = 3/2$ (see Eq. (3.6)),

$$M_{\text{dust},0} = M_{\text{dust,beam}} \left(\frac{R_0}{R_{\text{beam}}} \right)^{3-p}. \quad (3.13)$$

The derived values of $M_{\text{dust},0}$ are listed in Table 3.A.2 for all sources. The uncertainty in $M_{\text{dust},0}$ is estimated based on a 10 % uncertainty on the observed continuum flux, F_{cont} , and a 50 % uncertainty in the assumed T_{dust} for both the low-mass and high-mass sources. Spatial sampling in the PEACHES observations (i.e., resolving out large-scale continuum emission on $\gtrsim 500$ au scales) compared to the ALMAGAL observations does not affect our estimated dust masses here since only the peak continuum flux within the central beam is used for the dust mass estimate.

Chapter 4

Methanol deuteration in high-mass protostars

M. L. van Gelder, J. Jaspers, P. Nazari, A. Ahmadi, E. F. van Dishoeck, M. T. Beltrán, G. A. Fuller, Á. Sánchez-Monge, P. Schilke

Accepted for publication in A&A

Abstract

Context. The deuteration of molecules forming in the ices such as methanol (CH_3OH) is sensitive to the physical conditions during their formation in dense cold clouds and can be probed through observations of deuterated methanol in hot cores.

Aims. The aim is to determine the D/H ratio of methanol for a large sample of 99 high-mass protostars and to link this to the physical conditions during the formation of methanol in the prestellar phases.

Methods. Observations with the Atacama Large Millimeter/submillimeter Array (ALMA) containing transitions of CH_3OH , CH_2DOH , CHD_2OH , $^{13}\text{CH}_3\text{OH}$, and $\text{CH}_3^{18}\text{OH}$ are investigated. The column densities of CH_2DOH , CHD_2OH , and CH_3OH are determined for all sources, where the column density of CH_3OH is derived from optically thin ^{13}C and ^{18}O isotopologues. Consequently, the D/H ratio of methanol is derived taking statistical effects into account.

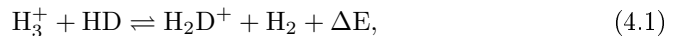
Results. Singly deuterated methanol (CH_2DOH) is detected at the 3σ level toward 25 of the 99 sources in our sample of the high-mass protostars. Including upper limits, the $(\text{D}/\text{H})_{\text{CH}_3\text{OH}}$ ratio inferred from $N_{\text{CH}_2\text{DOH}}/N_{\text{CH}_3\text{OH}}$ was derived for 38 of the 99 sources and varies between $\sim 10^{-3} - 10^{-2}$. Including other high-mass hot cores from the literature, the mean methanol D/H ratio is $1.1 \pm 0.7 \times 10^{-3}$. This is more than one order of magnitude lower than what is seen for low-mass protostellar systems ($2.2 \pm 1.2 \times 10^{-2}$). Doubly deuterated methanol (CHD_2OH) is detected at the 3σ level toward 11 of the 99 sources. Including upper limits for 15 sources, the $(\text{D}/\text{H})_{\text{CH}_2\text{DOH}}$ ratios derived from $N_{\text{CHD}_2\text{OH}}/N_{\text{CH}_2\text{DOH}}$ are more than two orders of magnitude higher than $(\text{D}/\text{H})_{\text{CH}_3\text{OH}}$ with an average of $2.0 \pm 0.8 \times 10^{-1}$ which is similar to what is found for low-mass sources. Comparison with literature GRAINOBLE models suggests that the high-mass prestellar phases are either warm (> 20 K) or live shorter than the free-fall timescale. In contrast, for low-mass protostars, both a low temperature of < 15 K and a prestellar phase timescale longer than the free-fall timescale are necessary.

Conclusions. The $(\text{D}/\text{H})_{\text{CH}_3\text{OH}}$ ratio drops by more than an order of magnitude between low-mass and high-mass protostars due to either a higher temperature during the prestellar phases or shorter prestellar phases. However, successive deuteration toward CHD_2OH seems equally effective between low-mass and high-mass systems.

4.1 Introduction

Isotopologues have proven to be vital in our understanding of the star and planet formation process. They allow for the most abundant species to be studied for which the emission originating from the main isotopologue is optically thick. Moreover, the sensitivity of isotopologue ratios to the physical conditions such as temperature and ultraviolet (UV) radiation has proven key in understanding the molecular journey during the entire star formation process (see e.g., reviews by Caselli & Ceccarelli 2012; Tielens 2013; Ceccarelli et al. 2014). One of the most studied types of isotopologues are those that contain deuterium (D). These deuterated molecules are suggested to form already in the cold prestellar phases (e.g., van Dishoeck et al. 1995; Caselli & Ceccarelli 2012; Ceccarelli et al. 2014). Especially for molecules such as methanol (CH_3OH) that form on the surfaces of dust grains in dense cores, D/H fractionation ratios up to 10% are found toward low-mass protostars (e.g., Bianchi et al. 2017a,b; Taquet et al. 2019; van Gelder et al. 2020), more than four orders of magnitude larger than the canonical D/H ratio derived for the local interstellar medium (ISM) of $\sim 2 \times 10^{-5}$ (Linsky et al. 2006; Prodanović et al. 2010). It is thus key to understand the deuterium fractionation process in the earliest phases of star formation.

The gaseous atomic D/H ratio can be increased in the prestellar phases through the exothermic reaction (Watson 1974; Aikawa & Herbst 1999; Ceccarelli et al. 2014),



where $\Delta E = 232$ K. Since in the cold ($\lesssim 20$ K) prestellar cores the backward reaction in Eq. (4.1) is less efficient, H_2D^+ is enhanced and the atomic D/H ratio in the gas phase can be effectively increased through dissociative recombination of H_2D^+ with free electrons. Moreover, gaseous CO is the main destructor of H_3^+ and H_2D^+ (Brown & Millar 1989; Roberts et al. 2003) and thus the heavy CO freeze-out in dense ($\gtrsim 10^4 \text{ cm}^{-3}$) prestellar cores additionally stimulates the increase of the gaseous atomic D/H ratio. In turn, the enhanced atomic D/H ratio in the gas can translate into a higher D/H ratio of molecules forming in the ices (Tielens 1983; Nagaoka et al. 2005). Measuring the deuteration of molecules that form in the ices is thus a powerful tool to determine the physical conditions such as density (e.g., CO freeze-out) and temperature during their formation.

Methanol forms on the surfaces of dust grains in dense prestellar phases through the hydrogenation of CO ice (e.g., Watanabe & Kouchi 2002; Fuchs et al. 2009) and reactions between its grains-surface products (e.g., H_2CO and CH_3O ; Simons et al. 2020; Santos et al. 2022) and is therefore expected to exhibit a high D/H ratio. This is in strong contrast to, for example, water for which the bulk of the ice is formed in the warmer translucent cloud phase leading to a rather low overall $\text{HDO}/\text{H}_2\text{O}$ ratio ($\lesssim 0.1\%$; Persson et al. 2014; Furuya et al. 2016; Jensen et al. 2019; van 't Hoff et al. 2022). The sensitivity of the methanol deuteration process to temperature was investigated by Bøgelund et al. (2018) using the GRAINOBLE gas-grain chemical model (Taquet et al. 2012, 2013, 2014), finding a strong correlation between the D/H ratio of methanol and the formation temperature. Moreover, Taquet et al.

(2019) showed that the timescale of the prestellar phase is highly relevant for methanol deuteration.

Methanol and its (deuterated) isotopologues are readily observed as they desorb from the dust grains. Mono deuterated methanol, CH_2DOH and CH_3OD , have been observed in the warm inner regions of both low-mass and high-mass protostellar systems (e.g., Fuente et al. 2014; Belloche et al. 2016; Bøgelund et al. 2018; van Gelder et al. 2020; van der Walt et al. 2021). Similarly, both doubly and triply deuterated methanol have been detected in hot cores (e.g., Parise et al. 2002, 2004; Bianchi et al. 2017a; Drozdovskaya et al. 2022; Ilyushin et al. 2022). Moreover, CH_2DOH has also been detected in both low-mass prestellar cores (e.g., Bizzocchi et al. 2014; Lattanzi et al. 2020; Ambrose et al. 2021) and high-mass starless cores (e.g., Fontani et al. 2015). Across this mass and evolutionary range, the D/H ratio of singly deuterated methanol varies orders of magnitude. The D/H ratio is on the order of 10% for low-mass prestellar cores, low-mass protostars, and comets (e.g., Bianchi et al. 2017a,b; Jørgensen et al. 2018; Taquet et al. 2019; Manigand et al. 2020; van Gelder et al. 2020; Lattanzi et al. 2020; Ambrose et al. 2021; Drozdovskaya et al. 2021). Interestingly, successive deuteration toward CHD_2OH and CD_3OH seems to be quite effective in low-mass protostars (about 15–25%; Drozdovskaya et al. 2022; Ilyushin et al. 2022). On the other hand, the D/H ratio derived from CH_2DOH is as low as 0.1 – 0.01% for high-mass starless cores and high-mass protostars (Fontani et al. 2015; Neill et al. 2013; Belloche et al. 2016; Bøgelund et al. 2018). However, the sample of high-mass protostars for which reliable and interferometrically derived methanol D/H ratios are available (e.g., Orion KL, Sgr B2(N2), NGC 6334I) remains small compared to the low-mass sources (~ 20 sources). Furthermore, no interferometric detections of CHD_2OH in high-mass sources have been presented thus far.

In this work, the methanol D/H ratios are derived for an additional 99 high-mass sources based on ALMA observations of CH_2DOH , CHD_2OH , CH_3OH , $^{13}\text{CH}_3\text{OH}$, $\text{CH}_3^{18}\text{OH}$. In Sect. 4.2, the observations and derivation of the column densities are explained. The resulting D/H ratios of CH_3OH and CH_2DOH are presented in Sect. 4.3. In Sect. 4.4, the methanol D/H ratios derived for our high-mass sources are compared to their low-mass counterparts and prestellar phases. Furthermore, through comparison with the GRAINOBLE models computed by Bøgelund et al. (2018) and Taquet et al. (2019), the effect of physical conditions on the methanol D/H ratio is discussed. Our main conclusions are listed in Sect. 4.5.

4.2 Methodology

4.2.1 Observations

The dataset analyzed in this work was taken from the ALMA Evolutionary study of High Mass Protocluster Formation in the Galaxy (ALMAGAL) survey (2019.1.00195.L; PI: S. Molinari) that targeted over 1000 dense clumps with $M > 500 M_\odot$ based on the *Herschel* Hi-Gal survey (Molinari et al. 2010; Elia et al. 2017, 2021). The ALMAGAL survey covers frequencies from ~ 217 GHz to ~ 221 GHz

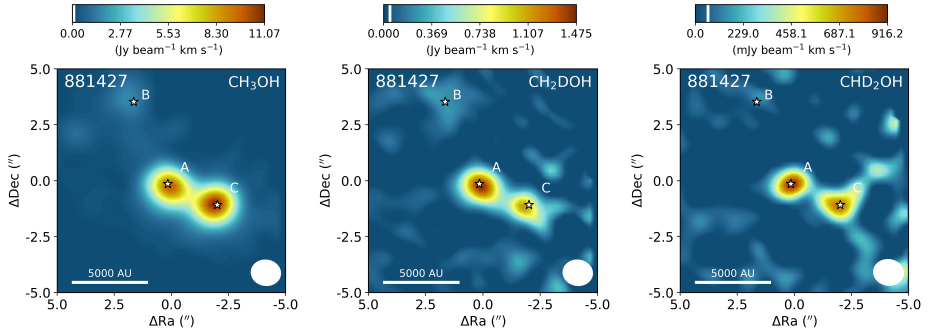


Figure 4.1: Integrated intensity maps of the CH_3OH $8_{0,8} - 7_{1,6}$ ($E_{\text{up}} = 97$ K, left), CH_2DOH $17_{1,16} e_0 - 17_{0,17} e_0$ ($E_{\text{up}} = 336$ K, middle), and CHD_2OH $7_{0,1} e_1 - 6_{1,1} e_1$ ($E_{\text{up}} = 74$ K, right) lines for 881427. The color scale is shown on top of each image. The image is integrated over $[-5, 5] \text{ km s}^{-1}$ with respect to the V_{lsr} of source A. The white vertical line in the colorbar indicates the 3σ threshold. The source positions based on the continuum emission are indicated with the white stars. The white ellipse in the lower right of each image depicts the beam size and in the lower left a physical scale bar is displayed.

with multiple configurations of ALMA down to $\sim 0.1''$ resolution at a spectral resolution of between $\sim 0.2 - 0.7 \text{ km s}^{-1}$. In this work a subsample of 40 high-mass cores is selected based on high bolometric luminosity ($L_{\text{bol}} > 1000 L_{\odot}$) and the sources being rich in lines from complex organic molecules (COMs) such as CH_3OH and CH_3CN . Only archival data with a beam smaller than $2''$ ($\sim 1000 - 5000 \text{ au}$) that were public before February 2021 are included. This selection introduces a bias in our sample to line-rich sources and means that not all high-mass cores in the ALMAGAL survey are covered. In the higher resolution ALMA data, the 40 Hi-Gal high-mass cores are resolved into in total 99 sources based on the continuum emission (labeled A, B, C, etc., see Appendix 4.B). These 99 sources are all studied in this work and are the same as those that were analyzed by van Gelder et al. (2022). The data were pipeline calibrated and imaged with the Common Astronomy Software Applications¹ (CASA; McMullin et al. 2007) version 5.6.1. The angular resolution of the data ranges from $0.5 - 1.25''$, corresponding to about $\sim 2500 - 10000 \text{ au}$ at the range of distances covered ($2 - 12 \text{ kpc}$; Mège et al. 2021), and the data have a sensitivity of $\sim 0.2 \text{ K}$. The ALMAGAL data cover several transitions of CH_3OH , four transitions of $^{13}\text{CH}_3\text{OH}$, nine transitions of $\text{CH}_3^{18}\text{OH}$, 21 transitions of CH_2DOH , and 22 transitions of CHD_2OH (see Appendix 4.A). Also nine transitions of CD_3OH are covered (Ilyushin et al. 2022), but these are not detected toward any of the sources. No transitions of CH_3OD are covered in the observed frequency range. Both CD_3OH and CH_3OD are therefore not analyzed further in this paper.

Integrated intensity maps of the CH_3OH $8_{0,8} - 7_{1,6}$, CH_2DOH $17_{1,16} e_0 - 17_{0,17} e_0$, and CHD_2OH $7_{0,1} e_1 - 6_{1,1} e_1$ lines for the source 881427 are presented

¹<https://casa.nrao.edu/>

in Fig. 4.1. The source 881427 hosts three nearby hot cores with varying line strengths and line widths and is a representative source of the rest of the sample. Whereas the emission of CH_3OH is often larger than the central beam, the emission of both CH_2DOH and CHD_2OH is generally confined within the central beam similar to the ^{13}C and ^{18}O isotopologues. The main exception for this is CH_2DOH $5_{1,5} e_0 - 4_{1,4} e_0$ ($E_{\text{up}} = 36$ K) which often shows more extended emission. This is likely because the low upper energy level of this line is also sensitive to cold ($T \lesssim 70$ K) material where methanol is nonthermally desorbed from the grains (e.g., Perotti et al. 2020, 2021). To exclude the contribution of extended emission, this transition is not included in the analysis described below.

The spectra were extracted from the peak pixel in the CH_3OH $8_{0,8} - 7_{1,6}$ ($E_{\text{up}} = 97$ K) integrated intensity maps for all sources that show this at the $> 3\sigma$ level. This line is strongest transition of CH_3OH in the sample with $E_{\text{up}} > 70$ K (lines with lower E_{up} can suffer from contamination by the outflow or extended emission). For sources that do not show emission from the CH_3OH $8_{0,8} - 7_{1,6}$ line, spectra were extracted from the peak continuum pixel and only upper limits on the column densities of CH_3OH (and isotopologues) are derived. In the G323.7399-00.2617B cluster, which contains seven nearby cores, all spectra were extracted from the same positions as van Gelder et al. (2022). In G023.3891+00.1851, the emission of CH_2DOH peaks offset by about half the beam ($\sim 0.6''$) and therefore the spectrum was extracted from the peak of CH_2DOH $17_{1,16} e_0 - 17_{0,17} e_0$ ($E_{\text{up}} = 336$ K). For all other sources, the the peak in CH_3OH coincides with the peaks of CH_2DOH and CHD_2OH . For sources also included by Nazari et al. (2022a), our spectral extraction locations are the same as theirs, which were extracted from the peak position of the CH_3CN $12_4 - 11_4$ integrated intensity maps, except for 721992 and G023.3891+00.1851 where the CH_3OH $8_{0,8} - 7_{1,6}$ and CH_2DOH $17_{1,16} e_0 - 17_{0,17} e_0$ emission peaks offset from the CH_3CN $12_4 - 11_4$ emission by about $1''$. It is important to note that these spectral extraction positions are different by up to $1''$ from van Gelder et al. (2022) who extracted their spectra from the peak continuum pixel for all sources. Therefore, the column densities derived in this work may deviate from theirs. The reason why our spectra are extracted from the peak pixel of CH_3OH is to have the highest signal-to-noise in methanol lines and its isotopologues the extracted spectra.

4.2.2 Deriving the column densities

The column densities of all methanol isotopologues were derived using the spectral analysis tool CASSIS² (Vastel et al. 2015) under the assumption of local thermodynamic equilibrium (LTE). The line lists of CH_3OH , $^{13}\text{CH}_3\text{OH}$, and $\text{CH}_3^{18}\text{OH}$ were taken from the CDMS catalog³ (Müller et al. 2001, 2005; Endres et al. 2016). These entries include the first three (CH_3OH) and two ($^{13}\text{CH}_3\text{OH}$ and $\text{CH}_3^{18}\text{OH}$) torsional states and are based on the works of Xu et al. (2008), Xu & Lovas (1997), and Fisher et al. (2007), respectively. The difference between the statistical weight factors g_{I} of $^{13}\text{CH}_3\text{OH}$ ($g_{\text{I}} = 1$) and $\text{CH}_3^{18}\text{OH}$ and CH_3OH ($g_{\text{I}} = 4$) is correctly

²<http://cassis.irap.omp.eu/>

³<https://cdms.astro.uni-koeln.de/>

taken into account in the CDMS database entries and therefore does not affect any column densities derived in this work. The line list of CH₂DOH was taken from the JPL catalog⁴ (Pickett et al. 1998), where the entry is based on the work of Pearson et al. (2012). The line list of CHD₂OH was taken from Drozdovskaya et al. (2022), which is mostly based on the the work of Coudert et al. (2021).

Only transitions with $E_{\text{up}} \geq 50$ K were used to derive the column densities since lines with lower E_{up} likely include also emission from non-thermally desorbed methanol and emission possibly related to outflows. For ¹³CH₃OH, the 14_{1,13} – 13_{2,12} ($E_{\text{up}} = 254$ K) transition gives the only constraint on the column density for many sources as the other transitions suffer from severe line blending. Similarly, for CH₃¹⁸OH only the 8_{1,8} – 7_{0,7} ($E_{\text{up}} = 86$ K) and 14_{1,14} – 13_{2,12} ($E_{\text{up}} = 239$ K) transitions provide constraints on the column density as well as some information on the excitation temperature. Furthermore, for CH₂DOH the 5_{2,4} e_1 – 4_{1,5} e_1 ($E_{\text{up}} = 59$ K) line, as well as several other lines, have rather low Einstein A_{ij} values ($< 10^{-5} \text{ s}^{-1}$) and are often blended with other COMs. Moreover, the spectroscopy of the CH₂DOH 18_{1,17} o_1 – 18_{2,17} e_0 line is unreliable and shows large discrepancies in A_{ij} between the JPL catalog entry ($A_{ij} = 1.8 \times 10^{-5} \text{ s}^{-1}$) and that derived by Coudert et al. (2014, $A_{ij} = 8.9 \times 10^{-7} \text{ s}^{-1}$) and is therefore also excluded from the analysis. Consequently, the 17_{1,16} e_0 – 17_{0,17} e_0 ($E_{\text{up}} = 336$ K) transition of CH₂DOH provided the best constraint on the column density of CH₂DOH. However, although the 5_{1,5} e_0 – 4_{1,4} e_0 ($E_{\text{up}} = 36$ K) transition is excluded from the fitting, it can provide information on the excitation temperature of CH₂DOH as the best-fit LTE model should not overproduce this line. Lastly, for CHD₂OH, the 7_{0,1} e_1 – 6_{1,1} e_1 ($E_{\text{up}} = 74$ K) transition is the only detected line in our sample and therefore is the only constraint on the column density of CHD₂OH.

As a consequence of only single or a few lines being available, the excitation temperature was fixed to 150 K, which is roughly the mean temperature as measured toward other high-mass hot cores (e.g., Neill et al. 2013; Belloche et al. 2016; Bøgelund et al. 2018, 2019). However, if clear anticorrelations between the best-fit LTE model and the data were present, the excitation temperature was varied by eye in steps of 25 K until the anticorrelations disappeared in a similar way as the by-eye fit method of Nazari et al. (2021, see their Appendix C).

The column densities N of ¹³CH₃OH, CH₃¹⁸OH, CH₂DOH, and CHD₂OH were derived following a similar method as van Gelder et al. (2020). A grid of N and the full width at half maximum (FWHM) of the line was set and a model spectrum was computed for each grid point assuming LTE conditions. The size of the emitting region was fixed to the size of the beam (see Appendix 4.B). Blended lines were excluded from the fitting procedure and similarly broad lines (FWHM $\geq 10 \text{ km s}^{-1}$) and lines with $E_{\text{up}} \leq 50$ K were excluded in the fit to exclude any emission possibly related to outflows. The best-fit column density and the 2σ uncertainty were computed from the grid for each isotopologue. The main contributors to the uncertainty of N are the uncertainty on the flux calibration of ALMA (assumed to be 10%) and the assumed excitation temperature. However, changing the excitation temperature in the 100-300 K range leads to at most a factor 3 variation in the derived column densities. For several sources (e.g., 705768), the lines are broad

⁴<https://spec.jpl.nasa.gov/>

($> 7 \text{ km s}^{-1}$) making automated line fitting complicated. For these sources the column density was estimated using the by eye fitting method of Nazari et al. (2021). In this case, a 50% uncertainty on the column density was assumed. Moreover, the sources 101899, 615590, 865468, and G345.5043+00.3480 showed line profiles consisting of multiple components. The column density of each component was derived and reported separately.

For all sources, the column density of CH_3OH was derived from $\text{CH}_3^{18}\text{OH}$ and, when no lines originating from $\text{CH}_3^{18}\text{OH}$ were detected, from $^{13}\text{CH}_3\text{OH}$. The adopted $^{12}\text{C}/^{13}\text{C}$ and $^{16}\text{O}/^{18}\text{O}$ ratios are dependent on the galactocentric distance and are determined using the relations of Milam et al. (2005) and Wilson & Rood (1994), respectively. In cases where only upper limits on the column densities of both $^{13}\text{CH}_3\text{OH}$ and $\text{CH}_3^{18}\text{OH}$ could be derived, the range in $N_{\text{CH}_3\text{OH}}$ was calculated by setting the 3σ upper limit based on scaling the 3σ upper limit of $^{13}\text{CH}_3\text{OH}$ and the lower limit based on the main isotopologue. Lastly, when CH_3OH was not detected, the 3σ upper limit was derived directly from CH_3OH lines.

4.3 Results

The derived column densities of all isotopologues are presented in Table 4.B.1 for the reported excitation temperature. In Fig. 4.2, the best-fit models to the $\text{CH}_2\text{DOH } 17_{1,16} e_0 - 17_{0,17} e_0$ and $\text{CHD}_2\text{OH } 7_{0,1} e_1 - 6_{1,1} e_1$ lines are presented for three hot cores in 881427 (see Fig. 4.1). Toward 25 sources, at least one clean unblended line of CH_2DOH is detected at the 3σ level, allowing for the determination of the column density. For the remaining 74 sources where no (unblended) transitions of CH_2DOH are detected, the 3σ upper limit is reported. For CHD_2OH , the column density could be determined for 11 sources. In Table 4.B.1, the column densities of $^{13}\text{CH}_3\text{OH}$, $\text{CH}_3^{18}\text{OH}$, and CH_3OH are also reported.

The column densities of CH_2DOH are generally between one and three orders of magnitude lower than those of CH_3OH , see also Fig. 4.3. Furthermore, the column densities of CHD_2OH are about a factor 3–10 lower than that of CH_2DOH , see Fig. 4.4. In order to translate the column density ratios to the D/H ratios, statistical weighting has to be taken into account since a deuterium atom has a three times higher probability to land in the CH_3 group compared to the OH group. Therefore, the D/H ratios of CH_3OH and CH_2DOH can be derived through,

$$N_{\text{CH}_2\text{DOH}}/N_{\text{CH}_3\text{OH}} = 3(\text{D}/\text{H})_{\text{CH}_3\text{OH}}, \quad (4.2)$$

$$N_{\text{CHD}_2\text{OH}}/N_{\text{CH}_2\text{DOH}} = (\text{D}/\text{H})_{\text{CH}_2\text{DOH}}. \quad (4.3)$$

The derived D/H ratios are also listed in Table 4.B.1.

The resulting $(\text{D}/\text{H})_{\text{CH}_3\text{OH}}$ and $(\text{D}/\text{H})_{\text{CH}_2\text{DOH}}$ ratios are presented in Figs. 4.3 and 4.4, respectively. Including upper limits, a (limit on the) $(\text{D}/\text{H})_{\text{CH}_3\text{OH}}$ and $(\text{D}/\text{H})_{\text{CH}_2\text{DOH}}$ ratios could be derived for 38 and 26 of the 99 studied sources, respectively. Besides the ALMAGAL sources, also other classical high-mass hot cores such as Sgr B2(N2) (Belloche et al. 2016), NGC 6334I (Bøgelund et al. 2018), Orion KL (Neill et al. 2013), and CygX-N30 (van der Walt et al. 2021) are included in Figs. 4.3 and 4.4. Only sources where $N_{\text{CH}_3\text{OH}}$ is derived from the ^{13}C or ^{18}O

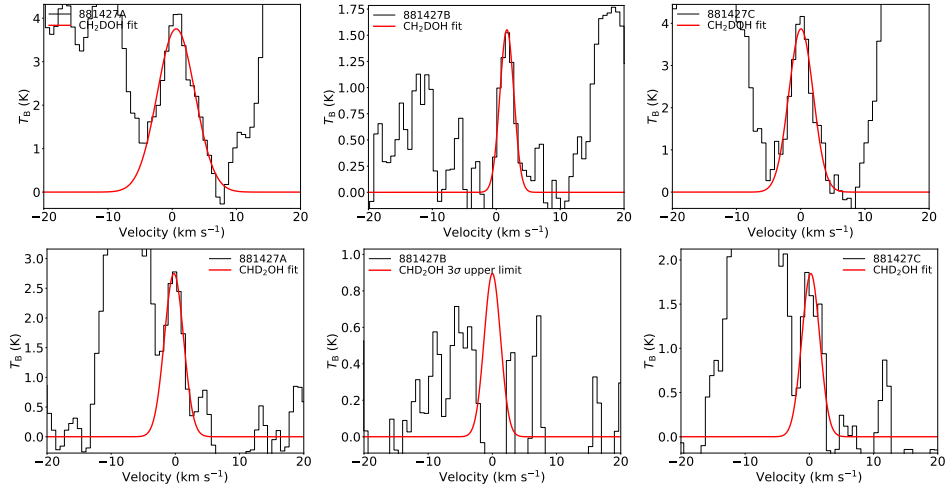


Figure 4.2: Spectral line fits of $\text{CH}_2\text{DOH } 17_{1,16} e_0 - 17_{0,17} e_0$ ($E_{\text{up}} = 336$ K, top row) and $\text{CHD}_2\text{OH } 7_{0,1} e_1 - 6_{1,1} e_1$ ($E_{\text{up}} = 74$ K, bottom row) for 881427A (left), 881427B (middle), and 881427C (right). The data corrected for the V_{lsr} are shown in black and the best fit for $T_{\text{ex}} = 150$ K is shown in red.

isotopologues are included in Fig. 4.3 to ensure that $N_{\text{CH}_3\text{OH}}$ is not underestimated. The $(\text{D}/\text{H})_{\text{CH}_3\text{OH}}$ ratios lie mostly in the $10^{-2} - 10^{-4}$ range. Interestingly, all the ALMAGAL sources and Orion KL show higher $(\text{D}/\text{H})_{\text{CH}_3\text{OH}}$ ratios ($10^{-2} - 10^{-3}$) than Sgr B2(N2) and NGC 6334I ($10^{-3} - 10^{-4}$). No clear correlation between the detection of CH_2OH or the derived $(\text{D}/\text{H})_{\text{CH}_3\text{OH}}$ and protostellar parameters such as L_{bol} and envelope mass is present among the high-mass sources. Excluding upper limits, the average $(\text{D}/\text{H})_{\text{CH}_3\text{OH}}$ ratio is $1.1 \pm 0.7 \times 10^{-3}$. This is almost two orders of magnitude higher than the D/H ratio in the local ISM of $\sim 2 \times 10^{-5}$ (Linsky et al. 2006; Prodanović et al. 2010), suggesting effective deuteration in the cold high-mass prestellar phases. However, both the range of observed $(\text{D}/\text{H})_{\text{CH}_3\text{OH}}$ values and the average is more than one order of magnitude lower than what is generally observed toward low-mass sources ($\sim \text{few} \times 10^{-2}$, e.g., Bianchi et al. 2017a,b, 2020; Jacobsen et al. 2019; van Gelder et al. 2020, see Sect. 4.4.1 for further discussion).

Interestingly, the $(\text{D}/\text{H})_{\text{CH}_2\text{DOH}}$ ratio (Eq. (4.3)) is significantly higher than the $(\text{D}/\text{H})_{\text{CH}_3\text{OH}}$ ratio, see Fig. 4.4. For the high-mass sources, only ALMAGAL datapoints are shown since no other interferometric studies of CHD_2OH in high-mass protostellar systems are available. The derived $(\text{D}/\text{H})_{\text{CH}_2\text{DOH}}$ ratios lie mostly in the $0.1 - 1$ range, with an average of $2.0 \pm 0.8 \times 10^{-1}$, which is more than two orders of magnitude higher than the $(\text{D}/\text{H})_{\text{CH}_3\text{OH}}$ ratio. Furthermore, this indicates that about 1/5 of the single deuterated methanol molecules gets successively deuterated further toward CH_2DOH in high-mass protostellar systems. This is in good agreement with low-mass protostellar systems where about 1/4 of the CH_2DOH is successively deuterated toward CHD_2OH (Drozdovskaya et al. 2022).

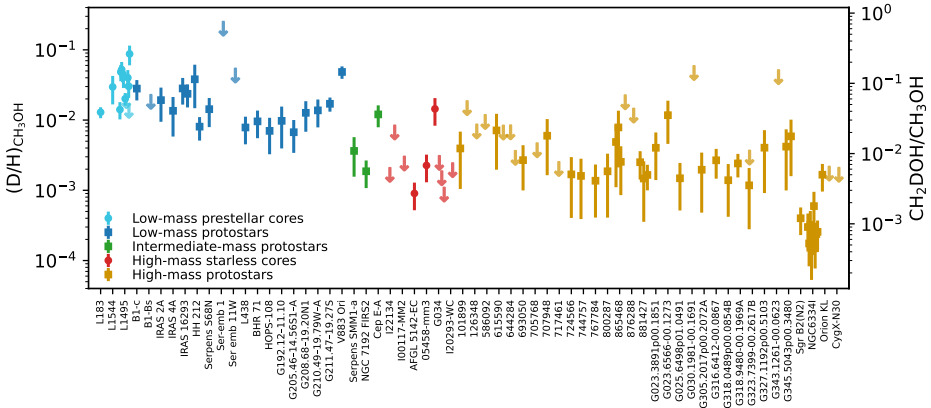


Figure 4.3: $(D/H)_{CH_3OH}$ ratio (squares) derived from the N_{CH_2DOH}/N_{CH_3OH} for low-mass, intermediate-mass, and high-mass protostellar systems including data from both this study and the literature (see Appendix 4.C for references). Only D/H ratios derived from interferometric observations are included to minimize effects of beam dilution and to exclude any contribution from larger scales. Also data for low-mass prestellar cores and high-mass starless cores (circles) from the literature (including observations with single dish telescopes) are included. Upper limits are presented as arrows.

4.4 Discussion

4.4.1 Methanol deuteration from low to high mass

In this work, a (limit on the) $(D/H)_{CH_3OH}$ ratio could be derived for 38 of the 99 studied high-mass sources. Since large samples of both low-mass and high-mass protostellar systems with methanol D/H values are now available, a more significant comparison over the mass regime can be made. In Fig. 4.3, also $(D/H)_{CH_3OH}$ ratios derived for both low-mass prestellar cores and high-mass starless cores are included. It is evident that the $(D/H)_{CH_3OH}$ ratio is lower in high-mass hot cores ($10^{-4} - 10^{-2}$) than in their low-mass counterpart ($10^{-2} - 10^{-1}$). Intermediate-mass protostars show values in between ($10^{-3} - 10^{-2}$), but this subsample only consists of three sources (NGC 7192 FIR2, Cep E-A, and Serpens SMM1-a, Fuente et al. 2014; Ospina-Zamudio et al. 2018; Ligterink et al. 2022, the D/H ratio of NGC 7192 FIR2 is taken from the beam averaged values). However, interestingly the $(D/H)_{CH_2DOH}$ ratio seems very similar between low-mass protostars and high-mass protostars ($0.1 - 1$, see Fig. 4.4). Among the low-mass sources, IRAS 2A and IRAS 4A show somewhat elevated $(D/H)_{CH_2DOH}$, but these were derived using older spectroscopic data of CHD_2OH (Taquet et al. 2019).

In Fig. 4.5, the mean $(D/H)_{CH_3OH}$ ratio is presented for low-mass, intermediate-mass, and high-mass protostellar systems. The average $(D/H)_{CH_3OH}$ ratio for high-mass hot cores ($1.1 \pm 0.7 \times 10^{-3}$) lies more than one order of magnitude lower than the average ratio for low-mass hot corinos ($2.2 \pm 1.2 \times 10^{-2}$), with the average $(D/H)_{CH_3OH}$ for intermediate-mass protostars in between ($8.9 \pm 7.4 \times 10^{-3}$). A

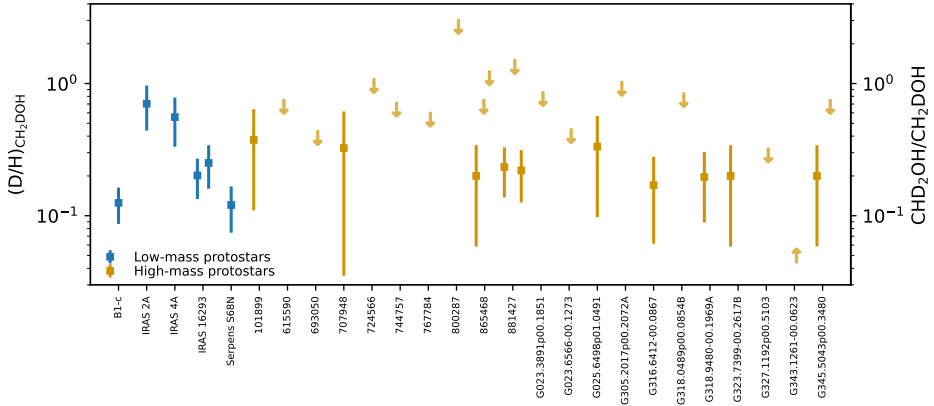


Figure 4.4: $(D/H)_{CH_2DOH}$ ratio derived from the N_{CHD_2OH}/N_{CH_2DOH} for low-mass and high-mass protostellar systems including data from both this study and the literature (see Appendix 4.C for references). Upper and lower limits are presented as arrows. Only D/H ratios derived from interferometric observations are included to minimize effects of beam dilution and to exclude any contribution from larger scales. The $(D/H)_{CH_2DOH}$ of IRAS 2A and IRAS 4A were derived using older spectroscopic data (Taquet et al. 2019).

similar trend is seen for the high-mass and low-mass prestellar phases where the average $(D/H)_{CH_3OH}$ ratios are $5.9 \pm 5.1 \times 10^{-3}$ and $3.4 \pm 1.9 \times 10^{-2}$, respectively. The lower $(D/H)_{CH_3OH}$ ratio in both high-mass hot cores and high-mass prestellar phases compared to their lower-mass counterparts suggests a lower deuteration efficiency already in the high-mass prestellar phases (see Sect. 4.4.3).

The methanol D/H ratios derived in low-mass prestellar cores agree well with those derived for low-mass protostars (see Fig. 4.3). Since CH_3OH is formed through the hydrogenation of CO ice (e.g., Watanabe & Kouchi 2002; Fuchs et al. 2009; Simons et al. 2020; Santos et al. 2022), this is a strong indication for inheritance of methanol and other COMs ices between low-mass prestellar phases and protostars. On the other hand, the average $(D/H)_{CH_3OH}$ ratio for high-mass starless cores ($5.9 \pm 5.1 \times 10^{-3}$) seems to be about a factor of five higher than that for high-mass protostars ($1.1 \pm 0.7 \times 10^{-3}$). However, the average $(D/H)_{CH_3OH}$ of the high-mass starless cores has a large errorbar since it is based on three detections of which one (G034-G2(MM2)) has a high $(D/H)_{CH_3OH}$ ratio of $\sim 10^{-2}$ (Fontani et al. 2015). The other two detections (AFGL 5142-EC and 0548-mm3; Fontani et al. 2015) and all the upper limits show $D/H \lesssim 2 \times 10^{-3}$ which agree well with most of the ALMAGAL sources as well as with Orion KL (Neill et al. 2013). Only Sgr B2(N2) and most of the cores in NGC 6334I show slightly lower D/H ratios at the 10^{-4} level. This therefore also suggests inheritance of methanol ice from the high-mass prestellar phase to the protostellar phase.

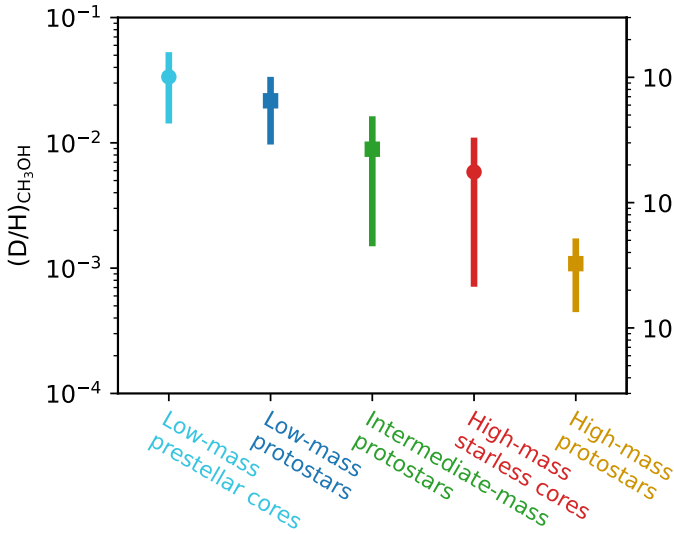


Figure 4.5: Average $(D/H)_{CH_3OH}$ ratio derived from N_{CH_2DOH}/N_{CH_3OH} for low-mass, intermediate-mass, and high-mass protostellar systems and low-mass prestellar cores and high-mass starless cores. The prestellar phases are indicated with circles and the protostellar phases with squares.

4.4.2 Singly vs doubly deuterated methanol

As evident from Figs. 4.3 and 4.4, the methanol D/H ratio derived for CH_2DOH is significantly higher than that derived for CH_3OH . The average $(D/H)_{CH_2DOH}$ ratio is about two orders of magnitude higher ($2.0 \pm 0.8 \times 10^{-1}$) than $(D/H)_{CH_3OH}$. In contrast to $(D/H)_{CH_3OH}$, this is in good agreement with the average of $3.0 \pm 2.0 \times 10^{-1}$ for low-mass protostars, suggesting that successive deuteration happens almost equally effective in both low-mass and high-mass systems.

Having higher D/H ratios for the doubly deuterated isotopologue compared with singly deuterated isotopologue is not unique to methanol. For water, the D_2O/HDO ratios are on the order of 10^{-2} (e.g., Coutens et al. 2014; Jensen et al. 2021), which is about an order of magnitude higher than typical HDO/H_2O ratios ($\lesssim 10^{-3}$; Persson et al. 2014; Jensen et al. 2019; van 't Hoff et al. 2022). This difference was attributed to be the result of layered ice chemistry (Dartois et al. 2003; Furuya et al. 2016), where the bulk of the water ice is formed in the warmer translucent cloud phase with a low D/H ratio whereas the surface layers formed in the cold prestellar phases show higher D/H ratios. However, methanol is thought to only start forming in the cold prestellar phases where CO is frozen out (e.g., Watanabe & Kouchi 2002; Fuchs et al. 2009) with little to no formation in the warmer translucent phases. Indeed, also for a direct precursor of CH_3OH on the surface of dust grains, H_2CO , the $D_2CO/HDCO$ ratio in IRAS 16293-2422 points toward a high D/H ratio of $\sim 25\%$ compared to a much lower D/H ratio derived

from HDCO/H₂CO ($\sim 3\%$; Persson et al. 2018). Small variations in temperature in the 10–20 K range can change the D/H ratio of ice mantle species such as methanol (see Sect. 4.4.3), but this should affect both CH₂DOH and CHD₂OH in a similar way and should therefore not lead to the observed difference.

One possible explanation could be the optical depth of CH₂DOH. In the low-mass source L1551 IRS5, the emission of CH₂DOH (as well as ¹³CH₃OH) was suggested to be optically thick (Bianchi et al. 2020). However, since the (D/H)_{CH₃OH} ratios derived from CH₂DOH clearly show lower values in high-mass protostellar systems compared to their lower-mass counterpart (see Sect. 4.4.1), this does not seem like a viable solution. Very recently, spectroscopic data for ¹³CH₂DOH has become available (Ohno et al. 2022), but these do not yet include a calculation of the partition function and line properties such as A_{ij} . When assuming that the source size is equal to the beam size, the line optical depth of the most constraining transition, ($17_{1,16} e_0 - 17_{0,17} e_0$, $E_{up} = 336$ K) is $\tau < 10^{-2}$. Only for source sizes smaller than $< 0.5''$ does CH₂DOH become marginally optically thick ($\tau > 0.1$) for the most line rich sources. Also, the (D/H)_{CH₃OH} ratios where N_{CH_3OH} was derived from the possibly optically thick ¹³C isotopologue are on average less than a factor ~ 3 higher than the (D/H)_{CH₃OH} ratios where N_{CH_3OH} could be derived using the optically thin ¹⁸O isotopologue (see Fig. 4.E.1).

A more realistic explanation is that successive deuteration of molecules is more effective than the first deuteration. This explanation is supported by several laboratory studies performed at low temperatures of 10–20 K (e.g., Nagaoka et al. 2005, 2007; Hidaka et al. 2009). Drozdovskaya et al. (2022) showed that their observed (D/H)_{CH₃OH} ratio as derived from CH₂DOH for the low-mass binary IRAS 16293-2422 could be well explained by these experiments whereas CHD₂OH and CD₃OH were overproduced by the experiments. The latter could be the result of the high atomic D/H flux of 0.1 used in the laboratory studies in contrast to the ISM value of $\sim 10^{-5}$, although the atomic D/H ratio is enhanced in cold dense prestellar cores. Assuming that the (D/H)_{CH₃OH} ratio is a direct representative of the gaseous atomic D/H ratio available in the prestellar phases (i.e., that H/D addition reactions are equally effective), a D/H flux of $\sim 10^{-3}$ may be more realistic for high-mass cold dense cores.

4.4.3 Linking the methanol D/H to the physical conditions during formation

Given the sensitivity of the methanol deuteration process to both temperature and density (i.e., CO freeze-out), the measured methanol D/H ratios are linked to these physical properties during the prestellar phases. To quantify this for the protostellar systems studied in this work, the observed D/H ratios are compared to the astrochemical gas-grain models presented by Bøgelund et al. (2018) and Taquet et al. (2019). These works used the GRAINOBLE model (Taquet et al. 2012, 2013, 2014) to test the effect of the dust and gas temperature T (assumed to be equal) and hydrogen density $n_H = n(H) + 2n(H_2)$ on the resulting (D/H)_{CH₃OH} ratio in the ices during the prestellar phases. In this work, we compare our results to their results and therefore only a brief description of the model is presented.

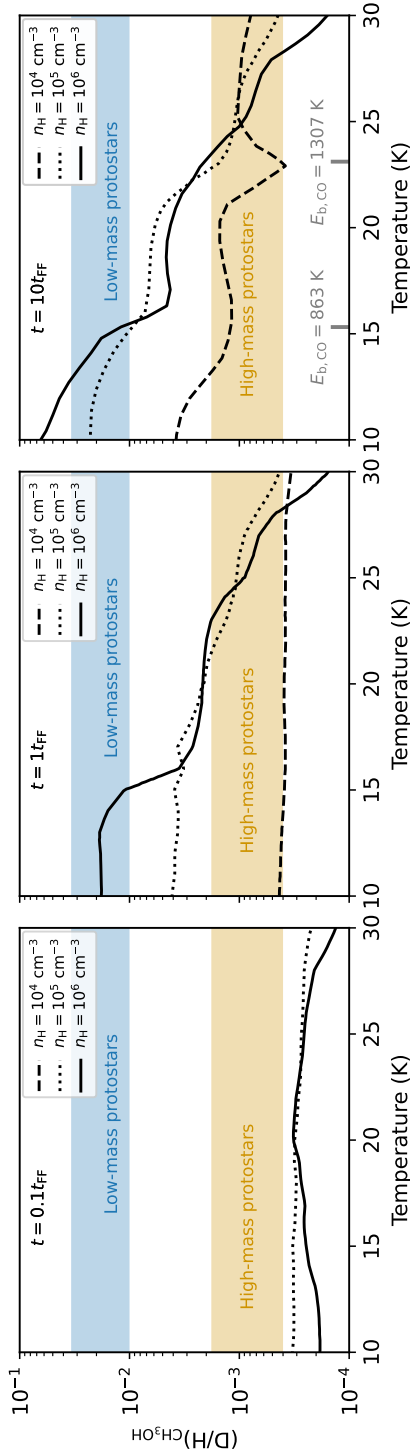


Figure 4.6: $(D/H)_{CH_3OH}$ ratio in the ices as function of the gas and dust temperature for $n_H = 10^4$ (dashed), 10^5 (dotted), and 10^6 cm^{-3} (solid) as modeled by Bøgelund et al. (2018) and Taquet et al. (2019) using the GRAINOBLE model (Taquet et al. 2012, 2013, 2014). The model results are shown for 0.1 (left), 1 (middle), and 10 (right) times free-fall timescales t_{FF} . The observed average $(D/H)_{CH_3OH}$ ratios are indicated in blue and orange for the low-mass and high-mass protostars, respectively. In the right panel, the range of possible desorption temperature of CO ice is indicated with the gray bars for binding energies between 863 K and 1307 K for CO ice deposited on non-porous amorphous solid water (Noble et al. 2012).

In GRAINOBLE, the gas-ice chemistry is computed in three phases: the bulk ice, the ice surface layers, and in the gas phase, following the approach initially presented by Hasegawa & Herbst (1993). The model includes both adsorption and desorption reactions and computes the rate equations in each phase. The chemical network used for the gas-phase chemistry is described in Taquet et al. (2014) and includes both ion-neutral chemistry and all molecules relevant for the chemistry of methanol (e.g., CO, HCO, H₂CO). Moreover, the model computes the deuteration of ice species based on laboratory experiments and includes both the hydrogenation (with both H and D atoms) reactions leading to methanol as well as hydrogen/deuterium abstraction reactions in low temperature ($\sim 10 - 15$ K) conditions (Hidaka et al. 2009).

The effect of T and n_{H} on the resulting methanol D/H ratio is presented in Fig. 4.6 as computed by Bøgelund et al. (2018) and Taquet et al. (2019). For a constant temperature and density, the chemistry was evolved over a timescale indicated on the top of each panel, where the free-fall timescale t_{FF} is 4.4×10^5 , 1.4×10^5 , and 4.4×10^4 years for $n_{\text{H}} = 10^4$, 10^5 , and 10^6 cm^{-3} , respectively. For the longest timescales ($t = 10t_{\text{FF}}$), it is evident that for all densities the methanol D/H ratio drops with increasing temperature. The strongest decrease is seen for 10^6 cm^{-3} , where the methanol D/H ratio decreases from $\sim 6 \times 10^{-2}$ for $T = 10$ K to as low as $\sim 10^{-4}$ when $T = 30$ K. A similar trend is visible for 10^5 cm^{-3} where the D/H ratio decreases from $\sim 2 \times 10^{-2}$ for $T = 10$ K to $\sim 4 \times 10^{-4}$ at $T \sim 30$ K. The decreasing D/H ratios for both these densities is the direct consequence of the decrease of atomic deuterium enhancement in Eq. (4.1) with increasing temperature. For $n_{\text{H}} = 10^4 \text{ cm}^{-3}$, the methanol D/H ratio also decreases with temperature, but only by a factor ~ 4 between $10 - 30$ K.

Another interesting trend is that for decreasing timescales (i.e., moving from right to left in Fig. 4.6), the D/H ratio at a given temperature also drops for all densities. The strongest drops are seen for the higher density cases at low temperatures (< 15 K) where the D/H ratio drops two orders of magnitude from $t = 10t_{\text{FF}}$ toward $t = 0.1t_{\text{FF}}$. This is the direct result of having less time where CO is frozen out and hence less time to deuterate ice species such as methanol. For higher temperatures ($T > 20$ K), this effect is less evident since significantly less CO freezes out, although a slightly higher binding energy of CO (up to ~ 1300 K; Noble et al. 2012) could result in CO frozen out till higher temperatures of ~ 25 K and hence a higher deuteration efficiency also above 20 K. However, even when CO does not freeze out, CO molecules can still land on the grain for a short period and react with H or D atoms toward HCO, H₂CO, and eventually (deuterated) methanol. This effect is most efficient for higher densities of $10^5 - 10^6 \text{ cm}^{-3}$ and reduces when timescales smaller than the free-fall timescale are considered. For the lowest density of 10^4 cm^{-3} , this effect is most evident since the CO freeze-out timescale is the highest and therefore the methanol deuteration is hampered the most.

Overplotted in Fig. 4.6 are the observed methanol (D/H)_{CH₃OH} ratios for both low-mass and high-mass protostars. It is evident that the observed (D/H)_{CH₃OH} ratios suggest a different temperature during methanol formation or different prestellar phase lifetimes for low-mass and high-mass protostars. For high-mass

protostars, a temperature of > 20 K is needed when the density is larger than 10^5 cm^{-3} and the timescale of the high-mass prestellar phase is $> t_{\text{FF}}$. A lower temperature of > 13 K at low densities of 10^4 cm^{-3} can also explain the observed methanol D/H ratio toward high-mass protostars, but such low densities in the dense high-mass starless phase are unlikely. Alternatively, the temperature in the high-mass prestellar phases can be in the $15 < T < 20$ K range with a lifetime of $\lesssim t_{\text{FF}}$. For prestellar lifetimes much smaller than the free-fall timescale, any temperature can explain the observed methanol deuteration toward high-mass protostars.

Contrary to the high-mass protostars, the observed $(\text{D}/\text{H})_{\text{CH}_3\text{OH}}$ ratio for low-mass protostars suggests both a temperature of < 15 K and a prestellar phase duration longer than $\geq t_{\text{FF}}$. Furthermore, the observed methanol D/H ratio for low-mass protostars can not be explained by a low density of 10^4 cm^{-3} at any modeled timescale.

It is important to note that the methanol D/H ratio is observed in the gas phase with ALMA whereas the GRAINOBLE models predict the ice abundances in the prestellar phases. Several processes can affect the D/H ratio as the ices warm up while infalling toward the protostar (e.g., Ratajczak et al. 2009; Faure et al. 2015). However, one of the likely dominant processes, CH_2DOH formation through H-D substitution in methanol ice (Nagaoka et al. 2005) is included in the model but this does not dominate over hydrogenation of CO.

These results thus suggest that the high-mass prestellar phases are generally either warm ($T \gtrsim 20$ K) or short ($t \lesssim t_{\text{FF}}$) while the low-mass prestellar phases are colder ($T < 15$ K) and long ($t \geq t_{\text{FF}}$). The observed methanol D/H ratios toward high-mass starless cores and low-mass prestellar cores also fit this picture, see Fig. 4.E.2. On the other hand, the spread in observed abundance ratios of nitrogen-bearing COMs suggests that the scatter in timescales of high-mass prestellar phases is rather small and similar to that of low-mass prestellar phases (Nazari et al. 2022a), implying that warmer high-mass pre-stellar phases are a more likely explanation. One possible explanation for the discrepancy between the low-mass and high-mass methanol D/H ratios could be that high-mass stars generally form in clusters with other nearby high-mass stars that heat the surrounding cloud which can affect the D/H ratios molecules forming in the ices (e.g., such as seen for water toward low-mass protostars; Jensen et al. 2019). The majority of the sources studied in this work are located in a clustered environments but these do not show significantly lower D/H ratios than high-mass sources that are single sources at our angular resolution. More modeling work similar to those performed by Bøgelund et al. (2018) and Taquet et al. (2019) including CHD_2OH is needed to further test these hypotheses.

4.5 Conclusion

In this work, (limits on) the D/H ratios of CH_3OH and CH_2DOH are determined for 38 and 26 sources, respectively, out of the 99 studied sources using ALMA observations of CH_2DOH , CHD_2OH , CH_3OH , $^{13}\text{CH}_3\text{OH}$, and $\text{CH}_3^{18}\text{OH}$. The de-

rived $(\text{D}/\text{H})_{\text{CH}_3\text{OH}}$ and $(\text{D}/\text{H})_{\text{CH}_2\text{DOH}}$ ratios are compared to each other as well as to other high-mass protostars, low-mass protostars, and both low-mass and high-mass prestellar phases. Furthermore, comparison with the gas-grain chemical code GRAINOBLE links the observed D/H ratios to the temperature during methanol formation and the lifetime of the prestellar phases. The main conclusions of this work are as follows:

- The $(\text{D}/\text{H})_{\text{CH}_3\text{OH}}$ ratios of the high-mass protostars studied in this work lie in the $10^{-3} - 10^{-2}$ range. Combining our sample with other high-mass protostars studied with ALMA, an average $(\text{D}/\text{H})_{\text{CH}_3\text{OH}}$ ratio of $1.1 \pm 0.7 \times 10^{-3}$ is derived. This is in good agreement with the $(\text{D}/\text{H})_{\text{CH}_3\text{OH}}$ ratio derived for high-mass starless cores ($5.9 \pm 5.1 \times 10^{-3}$), but is more than an order of magnitude lower than the average $(\text{D}/\text{H})_{\text{CH}_3\text{OH}}$ ratio for low-mass protostars ($2.2 \pm 1.2 \times 10^{-2}$) and low-mass prestellar cores ($3.4 \pm 1.9 \times 10^{-2}$).
- For $(\text{D}/\text{H})_{\text{CH}_2\text{DOH}}$, significantly higher values than $(\text{D}/\text{H})_{\text{CH}_3\text{OH}}$ are found ranging from 0.1–1 with an average of $2.0 \pm 0.8 \times 10^{-1}$. The latter is in good agreement with results on low-mass protostars and suggests that about 1/5 singly deuterated methanol molecules gets successively deuterated further independent of the mass of the system.
- Based on a comparison with GRAINOBLE models in the literature, the lower $(\text{D}/\text{H})_{\text{CH}_3\text{OH}}$ ratios toward high-mass protostars suggest either a temperature of $\gtrsim 20$ K in the high-mass prestellar phases or a short lifetime ($\lesssim t_{\text{FF}}$) of the high-mass prestellar phases. This is in strong contrast with the low-mass sources for which the higher $(\text{D}/\text{H})_{\text{CH}_3\text{OH}}$ ratio can only be achieved when the low-mass prestellar phases are both cold (< 15 K) and long lived ($\geq t_{\text{FF}}$).

This work demonstrates that the deuteration of the CH_3 -group of methanol as measured toward protostellar systems could be used to probe the physical conditions (e.g., temperature) of the prestellar phases. The discrepancy in $(\text{D}/\text{H})_{\text{CH}_3\text{OH}}$ between low-mass and high-mass sources indicates that the physical conditions are already different before the onset of star formation. Additional observations of multiple deuterated methanol isotopologues (e.g., CHD_2OH , CD_3OH) as well as CH_3OD will shed further light on the efficiency of methanol deuteration between low-mass and high-mass systems. In combination with additional modeling studies (such as those performed by Bøgelund et al. 2018; Taquet et al. 2019; Kulterer et al. 2022), this can provide further insight on the relevant deuterium chemistry and how the D/H ratio varies across the protostellar mass range.

Acknowledgments

The authors would like to thank the anonymous referee for their constructive comments on the manuscript and L. Coudert for discussions on the CH_2DOH spectroscopy. This paper makes use of the following ALMA data:

ADS/JAO.ALMA#2017.1.01174.S, ADS/JAO.ALMA#2019.1.00195.L. ALMA is a partnership of ESO (representing its member states), NSF (USA) and NINS

(Japan), together with NRC (Canada), MOST and ASIAA (Taiwan), and KASI (Republic of Korea), in cooperation with the Republic of Chile. The Joint ALMA Observatory is operated by ESO, AUI/NRAO and NAOJ. Astrochemistry in Leiden is supported by the Netherlands Research School for Astronomy (NOVA), by funding from the European Research Council (ERC) under the European Union's Horizon 2020 research and innovation programme (grant agreement No. 101019751 MOLDISK), and by the Dutch Research Council (NWO) grants TOP-1 614.001.751, 648.000.022, and 618.000.001. Support by the Danish National Research Foundation through the Center of Excellence "InterCat" (Grant agreement no.: DNRF150) is also acknowledged.

Appendix

4.A Transitions of CH₃OH and isotopologues

Table 4.A.1: Transitions of CH₃OH and isotopologues with $A_{ij} > 10^{-6}$ and $E_{\text{up}} < 1000$ K covered in the ALMAGAL (2019.1.00195.L) program.

Species	Transition		Frequency (GHz)	A_{ij} (s ⁻¹)	E_{up} (K)
	(J K L M)	- (J K L M)			
CH ₃ OH	6 1 5 3	- 7 2 5 3	217.2992	4.3×10^{-5}	373.9
	15 6 9 3	- 16 5 11 3	217.6427	1.9×10^{-5}	745.6
	15 6 10 3	- 16 5 12 3	217.6427	1.9×10^{-5}	745.6
	20 1 19 1	- 20 0 20 1	217.8865	3.4×10^{-5}	508.4
	4 2 3 1	- 3 1 2 1	218.4401	4.7×10^{-5}	45.5
	25 3 23 1	- 24 4 20 1	219.9837	2.0×10^{-5}	802.2
	23 5 18 1	- 22 6 17 1	219.9937	1.7×10^{-5}	775.9
	8 0 8 1	- 7 1 6 1	220.0786	2.5×10^{-5}	96.6
	10 5 6 2	- 11 4 8 2	220.4013	1.1×10^{-5}	251.6
¹³ CH ₃ OH	14 1 13 -0	- 13 2 12 -0	217.0446	2.4×10^{-5}	254.3
	10 2 8 +0	- 9 3 7 +0	217.3995	1.5×10^{-5}	162.4
	17 7 11 +0	- 18 6 12 +0	220.3218	1.3×10^{-5}	592.3
	17 7 10 -0	- 18 6 13 -0	220.3218	1.3×10^{-5}	592.3
CH ₃ ¹⁸ OH	14 1 14 1	- 13 2 12 1	217.1729	1.7×10^{-5}	238.9
	18 6 13 4	- 17 7 11 4	217.9223	1.5×10^{-5}	874.1
	17 5 13 4	- 18 6 13 4	218.5521	3.2×10^{-5}	884.6
	4 2 2 2	- 3 1 2 2	219.4078	4.6×10^{-5}	44.6
	8 7 1 5	- 7 6 1 5	219.8433	2.8×10^{-5}	663.2
	18 3 16 5	- 19 4 16 5	219.9572	5.1×10^{-5}	795.8
	8 1 8 1	- 7 0 7 1	220.1951	3.6×10^{-5}	85.7
CH ₂ DOH	26 4 22 0	- 26 3 24 2	217.2664	2.0×10^{-5}	817.1
	26 1 25 2	- 26 1 26 2	217.3300	1.1×10^{-5}	777.9
	17 4 13 2	- 16 5 11 1	217.3436	5.2×10^{-6}	409.7
	17 4 14 2	- 16 5 12 1	217.3593	5.3×10^{-6}	409.7
	23 6 18 1	- 22 7 15 0	217.3818	6.4×10^{-6}	742.6
	23 6 17 1	- 22 7 16 0	217.3825	6.4×10^{-6}	742.6
	18 1 17 2	- 18 2 17 0	217.4479	1.8×10^{-5}	391.5
	25 1 25 2	- 25 0 25 1	217.6429	4.7×10^{-5}	712.4
	12 7 6 0	- 13 6 7 1	217.6446	2.5×10^{-6}	357.2
	12 7 5 0	- 13 6 8 1	217.6446	2.5×10^{-6}	357.2
	18 0 18 0	- 17 1 16 2	218.1095	8.9×10^{-6}	363.2
	5 2 4 1	- 5 1 5 1	218.3164	9.1×10^{-6}	58.7
	24 3 21 1	- 24 2 23 2	218.5348	3.9×10^{-5}	687.7
	20 5 16 1	- 19 6 13 0	219.2043	1.5×10^{-5}	557.6
	20 5 15 1	- 19 6 14 0	219.2061	1.5×10^{-5}	557.6
	5 1 5 1	- 4 1 4 1	219.5515	7.0×10^{-6}	48.2

Table 4.A.1: continued.

Species	Transition					Frequency	A_{ij}	E_{up}
	(J K L M	-	J K L M)			(GHz)	(s^{-1})	(K)
	5 1 5 0	-	4 1 4 0			220.0718	3.3×10^{-5}	35.8
	29 4 26 0	-	29 3 26 2			220.3492	2.5×10^{-5}	997.1
	17 1 16 0	-	17 0 17 0			220.5526	3.8×10^{-5}	335.9
	21 1 20 1	-	21 1 21 1			220.6256	2.0×10^{-6}	515.1
	21 2 19 2	-	21 1 20 2			220.7358	3.9×10^{-5}	531.1
CHD ₂ OH	6 2 2 1	-	5 1 2 2			217.0702	1.8×10^{-6}	61.9
	13 2 1 2	-	12 3 1 2			217.1181	8.8×10^{-6}	213.0
	16 5 1 2	-	17 4 1 0			217.2651	2.4×10^{-6}	366.8
	7 0 1 2	-	6 1 1 2			217.4912	2.9×10^{-5}	74.3
	7 4 2 1	-	8 3 2 0			217.4946	4.4×10^{-6}	111.1
	7 4 1 1	-	8 3 1 0			217.5430	4.4×10^{-6}	111.1
	24 9 1 1	-	25 8 1 0			217.8034	9.0×10^{-6}	854.9
	24 9 2 1	-	25 8 2 0			217.8034	9.0×10^{-6}	854.9
	2 2 1 1	-	3 1 1 0			218.0092	5.5×10^{-6}	25.8
	7 2 1 0	-	7 1 2 0			218.1279	1.2×10^{-5}	68.8
	16 3 2 2	-	15 4 2 2			218.2323	6.9×10^{-6}	318.2
	20 2 2 2	-	20 2 1 1			218.4156	9.0×10^{-6}	449.9
	11 2 1 2	-	11 1 2 2			218.4824	2.3×10^{-5}	163.0
	12 2 1 2	-	12 1 2 2			219.2181	4.9×10^{-6}	187.0
	23 10 2 2	-	24 9 2 2			219.3323	5.1×10^{-6}	872.6
	23 10 1 2	-	24 9 1 2			219.3323	5.1×10^{-6}	872.6
	16 3 1 0	-	15 4 1 0			219.3377	6.5×10^{-6}	300.9
	22 5 2 0	-	22 4 1 2			219.6514	2.6×10^{-6}	583.5
	22 5 1 0	-	22 4 2 2			219.7983	2.5×10^{-6}	583.4
	13 2 1 0	-	12 3 1 0			220.2430	4.7×10^{-6}	195.3
	11 6 1 1	-	12 5 1 1			220.5567	1.1×10^{-6}	249.5
	11 6 2 1	-	12 5 2 1			220.5569	1.1×10^{-6}	249.5

Notes. The typical beam size is $\theta_{\text{beam}} \sim 1''$ and the typical rms is $\text{rms}_{\text{line}} \sim 0.2$ K.

4.B Observational details

Table 4.B.1: Column densities of $^{13}\text{CH}_3\text{OH}$, $\text{CH}_3^{18}\text{OH}$, CH_3OH , CH_2DOH , and CHD_2OH and derived methanol D/H ratios.

Source	RA (J2000)	Dec (J2000)	θ_b "	T_{ex} K	$N^{^{13}\text{CH}_3\text{OH}}$ cm^{-2}	$N^{\text{CH}_3\text{OH}}$ cm^{-2}	$N^{\text{CH}_2\text{DOH}}$ cm^{-2}	$N^{\text{CHD}_2\text{OH}}$ cm^{-2}	(D/H) $_{\text{CH}_3\text{OH}}(^{\circ})$	(D/H) $_{\text{CH}_2\text{DOH}}(^{\circ})$
86213A	18:26:48.92	-12:26:24.51	1.23	150	<3.3(15)	<1.0(15)	0.4-14.8(16)	<2.1(15)	-	-
86213B	18:26:47.96	-12:26:20.73	1.23	150	<4.0(15)	<1.6(15)	0.3-17.9(16)	<1.5(15)	-	-
86213C	18:26:48.73	-12:26:25.98	1.23	150	<1.9(15)	<1.1(15)	0.5-8.7(16)	<1.7(15)	-	-
81635A	18:25:00.82	-13:15:34.46	1.22	150	<3.8(15)	<2.8(15)	0.1-17.7(16)	<2.5(15)	-	-
81635B	18:25:01.01	-13:15:38.57	1.22	150	<2.7(15)	<1.5(15)	<4.0(15)	<3.6(15)	-	-
81635C	18:25:01.65	-13:15:28.99	1.22	150	<10.0(15)	<1.5(15)	<4.0(15)	<4.0(15)	-	-
83968A	18:25:10.59	-12:42:22.16	1.23	150	<2.2(15)	<1.4(15)	0.1-10.9(16)	<1.5(15)	-	-
83968B	18:25:10.69	-12:42:26.14	1.23	150	<3.0(15)	<1.2(15)	<1.5(15)	<1.7(15)	-	-
83968C	18:25:10.82	-12:42:24.68	1.23	150	<2.3(15)	<0.9(14)	<1.3(16)	<3.2(15)	-	-
83968D	18:25:10.62	-12:42:19.43	1.23	150	<2.3(15)	<1.2(15)	<1.3(15)	<5.0(15)	-	-
83968E	18:25:10.65	-12:42:24.74	1.23	150	<2.3(15)	<1.2(15)	<1.3(15)	<3.0(15)	-	-
101899 C1	18:34:40.29	-09:00:38.44	1.25	150	1.5 \pm 0.3(16)	<4.0(15)	6.8 \pm 3.6(17)	8.0 \pm 4.0(15)	3.9 \pm 2.9(-3)	3.8 \pm 2.7(-1)
101899 C2	18:34:40.29	-09:00:38.44	1.25	150	6.7 \pm 1.5(15)	<4.0(15)	2.9 \pm 1.6(17)	<6.0(15)	<1.5(-2)	-
103421	18:33:23.98	-08:33:31.92	1.24	150	<4.3(15)	<1.0(15)	0.1-1.9(17)	<3.3(15)	-	-
106756A	18:34:23.98	-07:54:48.26	1.23	150	<2.5(15)	<2.7(15)	0.2-11.2(16)	<3.5(15)	-	-
106756B	18:34:25.55	-07:54:46.39	1.23	150	<4.0(15)	<2.0(15)	<4.2(15)	<3.5(15)	-	-
106756C	18:34:25.59	-07:54:43.11	1.23	150	<1.1(16)	<2.6(15)	<4.3(15)	<3.5(15)	-	-
126120A	18:42:37.55	-04:02:05.17	1.17	150	<1.9(15)	<5.7(14)	0.5-9.1(16)	<1.7(15)	-	-
126120B	18:42:37.66	-04:02:07.27	1.17	150	<2.0(15)	<7.8(14)	0.2-9.5(16)	<1.8(15)	-	-
126120C	18:42:36.85	-04:02:17.66	1.17	150	<3.8(15)	<1.8(15)	<5.7(15)	<4.2(15)	-	-
126120D	18:42:37.14	-04:02:02.37	1.17	150	<3.4(15)	<0.8(14)	<1.0(15)	<2.0(15)	-	-
126348	18:42:51.98	-03:59:54.37	1.16	150	1.1 \pm 0.3(16)	3.0 \pm 2.0(15)	9.4 \pm 6.9(17)	<5.0(15)	<6.9(-3)	-
565926A	08:02:42.97	-34:31:48.77	0.58	150	<5.1(15)	<2.5(15)	<2.5(15)	<4.1(15)	-	-
565926B	08:02:42.94	-34:31:49.96	0.58	150	<5.0(15)	<2.4(15)	<4.5(15)	<6.2(15)	-	-
565926C	08:02:42.72	-34:31:49.61	0.58	150	<5.1(15)	<2.5(15)	<2.5(15)	<4.1(15)	-	-
586092A	08:32:08.70	-43:13:45.44	0.92	75	5.1 \pm 1.1(15)	1.5 \pm 0.3(15)	8.0 \pm 4.5(17)	<1.0(16)	<8.4(-3)	-
586092B	08:32:08.48	-43:13:49.28	0.92	150	<2.9(15)	<1.6(15)	0.1-2.1(17)	<5.6(15)	-	-
586092C	08:32:09.06	-43:13:43.28	0.92	150	<2.8(15)	<1.7(15)	<2.5(15)	<4.8(15)	-	-
615590 C1	09:24:41.96	-52:02:08.04	0.64	200	2.0 \pm 0.5(16)	<5.0(15)	1.4 \pm 0.7(18)	3.0 \pm 1.5(16)	<1.0(16)	<6.7(-1)
615590 C2	09:24:41.96	-52:02:08.04	0.64	150	1.5 \pm 0.3(16)	<5.0(15)	1.1 \pm 0.6(18)	<1.0(16)	<6.7(-3)	-
640076A	10:20:15.66	-58:03:56.32	0.87	150	<4.1(15)	<1.2(15)	0.1-2.9(17)	<4.3(15)	-	-
640076B	10:31:29.78	-58:03:53.47	0.87	150	<4.1(15)	<2.6(15)	0.1-2.9(17)	<3.0(15)	-	-
644284A	10:31:29.78	-58:02:19.27	0.86	150	6.2 \pm 1.4(15)	1.5 \pm 0.3(15)	4.2 \pm 2.2(17)	<4.0(15)	<6.7(-3)	-
644284B	10:31:29.63	-58:02:18.82	0.86	100	8.2 \pm 1.8(15)	1.5 \pm 0.3(15)	7.8 \pm 4.3(17)	<3.0(15)	<3.9(15)	-
693030	12:35:35.05	-68:02:31.19	0.99	200	1.4 \pm 0.3(16)	3.1 \pm 0.7(15)	1.3 \pm 0.8(18)	1.1 \pm 0.3(16)	2.7 \pm 1.7(-3)	<3.9(-1)
695243	12:43:31.51	-62:36:13.25	0.98	150	<4.0(15)	<1.2(15)	<1.8(15)	<5.9(15)	-	-
704792	13:11:14.14	-62:45:06.80	1.29	150	<4.5(15)	<8.2(14)	<1.2(15)	<4.5(15)	-	-
705768	13:12:36.17	-62:33:34.43	0.87	150	9.3 \pm 2.2(15)	3.0 \pm 1.3(15)	1.3 \pm 0.8(18)	<6.3(15)	<3.7(-3)	-
706733A	13:14:22.78	-62:45:59.48	0.87	150	<6.7(15)	<1.8(15)	0.2-16.4(16)	<4.8(15)	<2.9(15)	-
706733B	13:14:22.99	-62:45:54.35	0.87	150	<2.7(15)	<1.5(15)	<2.0(15)	<6.6(15)	-	-
706733C	13:14:23.07	-62:45:47.54	0.87	150	<5.6(15)	<1.8(15)	<2.5(15)	<4.9(15)	-	-
706785A	13:14:26.92	-62:44:29.72	0.88	150	<3.2(15)	<2.1(15)	0.1-1.9(17)	<6.2(15)	-	-
706785B	13:14:26.55	-62:44:31.80	0.88	150	<3.3(15)	<2.9(15)	0.0-2.0(17)	<6.0(15)	-	-
706785C	13:14:26.38	-62:44:30.24	0.88	150	<2.7(15)	<1.3(15)	<1.7(15)	<5.9(15)	-	-
706785D	13:14:25.64	-62:44:30.36	0.88	150	<4.4(15)	<3.2(15)	0.1-2.7(17)	<6.1(15)	-	-
707948	13:16:43.19	-62:58:32.83	0.88	150	1.8 \pm 0.4(17)	1.5 \pm 0.3(16)	1.1 \pm 0.6(19)	2.0 \pm 1.0(17)	6.0 \pm 4.3(-3)	3.2 \pm 2.9(-1)
717461A	13:43:01.68	-62:08:51.42	1.29	150	7.6 \pm 1.9(15)	2.6 \pm 0.8(15)	1.1 \pm 0.4(18)	<3.7(15)	<2.0(-3)	-

Table 4.B.1: continued.

Source	RA (J2000)	Dec (J2000)	θ_b "	T_{ex} K	$N^{\text{CH}_3\text{OH}}$ cm^{-2}	$N^{\text{CH}_3\text{OH}}$ cm^{-2}	$N^{\text{CH}_3\text{OH}}$ cm^{-2}	$N^{\text{CH}_3\text{OH}}$ cm^{-2}	$(D/H)_{\text{CH}_3\text{OH}}^{(D)}$	$(D/H)_{\text{CH}_3\text{OH}}^{(B)}$
717461B	13:43:01.74	-62:08:55.34	1.29	150	<2.2(15)	<1.9(15)	<2.8(15)	<3.6(15)	-	-
721992	13:51:58.27	-61:15:41.04	0.85	150	<4.4(15)	<1.9(15)	0.5-2.5(17)	<7.3(15)	-	-
724566	13:59:30.92	-61:48:38.27	0.83	150	2.9±0.6(16)	1.0±0.2(16)	4.0±2.3(18)	2.0±1.0(16)	1.7±1.3(-3)	<9.6(-1)
732038	14:13:15.05	-61:16:53.19	0.82	150	<7.6(15)	<4.8(15)	1.2-4.2(17)	<8.8(15)	<7.5(15)	-
744757A	14:45:26.35	-58:49:15.55	1.30	150	1.4±0.4(16)	4.1±0.9(15)	1.7±1.0(18)	8.0±4.0(15)	1.6±1.2(-3)	<6.3(-1)
744757B	14:45:26.16	-58:49:19.87	1.30	150	<1.9(15)	<1.1(15)	1.3±1.1(16)	<2.9(15)	<2.3(15)	-
759150A	15:10:43.13	-57:44:49.63	1.29	150	<1.9(15)	<1.2(15)	0.3-10.1(16)	<5.0(15)	<2.3(15)	-
759150B	15:10:43.52	-57:44:44.82	1.29	150	<2.4(15)	<9.6(14)	<1.5(15)	<5.0(15)	<2.8(15)	-
759150C	15:10:44.48	-57:44:47.33	1.29	150	<2.2(15)	<9.6(14)	<8.6(14)	<5.0(15)	<2.3(15)	-
759150D	15:10:42.71	-57:44:52.85	1.29	150	<5.0(15)	<9.7(14)	<1.2(15)	<4.9(15)	<2.3(15)	-
759150E	15:10:44.10	-57:44:52.03	1.29	150	<2.1(15)	<9.6(14)	<9.9(14)	<4.8(15)	<2.3(15)	-
767784	15:29:19.31	-56:31:22.02	1.29	100	3.9±0.5(16)	7.2±1.9(15)	2.5±1.4(18)	1.0±0.4(16)	1.4±1.0(-3)	<5.3(-1)
800287	16:11:26.57	-51:41:57.14	0.80	100	1.5±0.3(16)	6.2±1.4(15)	1.8±1.1(18)	1.0±0.5(16)	1.9±1.5(-3)	<2.7(0)
854214A	16:52:32.74	-43:23:49.60	1.26	150	<2.2(15)	<1.7(15)	0.7-9.5(16)	<3.8(15)	<5.0(15)	-
854214B	16:52:33.02	-43:23:50.26	1.26	150	<5.0(15)	<7.8(14)	0.1-2.1(17)	<3.8(15)	<2.7(15)	-
863312A	17:02:08.36	-41:46:56.89	0.83	150	<8.9(15)	<3.7(15)	<3.8(15)	<2.0(16)	<1.4(16)	-
863312B	17:02:09.14	-41:46:45.04	0.83	150	<3.7(15)	<1.9(15)	<2.0(15)	<6.0(15)	<4.2(15)	-
865468A C1	17:05:10.90	-41:29:06.99	1.23	100	1.3±0.3(17)	3.1±0.7(16)	1.0±0.6(19)	1.5±0.8(17)	4.0±2.0(16)	2.7±1.9(-1)
865468A C2	17:05:10.90	-41:29:06.99	1.23	150	5.1±1.1(16)	3.0±0.5(15)	2.5±1.4(18)	6.0±3.0(16)	2.0(16)	7.9±5.7(-3)
865468B	17:05:11.22	-41:29:07.65	1.24	150	1.3±0.2(16)	2.6±0.9(15)	8.6±5.0(17)	6.5±2.0(15)	<5.0(15)	2.5±1.7(-3)
865468C	17:05:11.12	-41:29:03.47	1.24	150	5.0±1.9(15)	1.0±0.2(15)	3.4±2.0(17)	7.5(15)	<5.8(15)	<1.8(-2)
876288	17:11:51.02	-39:09:29.18	0.81	150	8.9±2.9(15)	3.1±0.7(15)	5.7±3.9(17)	<3.0(15)	<5.0(15)	<1.2(-2)
881427A	17:20:06.31	-38:57:15.18	1.23	150	9.3±1.8(16)	2.6±0.7(16)	1.1±0.4(19)	8.3±1.6(16)	1.9±0.7(16)	2.3±1.0(-1)
881427B	17:20:06.46	-38:57:11.44	1.23	300	1.0±0.2(16)	8.2±1.8(15)	3.4±1.9(18)	1.5±0.8(16)	<1.0(16)	1.5±1.1(-3)
881427C	17:20:06.12	-38:57:15.84	1.23	150	7.4±1.6(16)	2.6±0.9(16)	1.1±0.4(19)	5.5±1.2(16)	1.2±0.5(16)	1.7±0.7(-3)
G023.3891+00.1851	18:33:14.32	-08:23:57.82	1.24	200	7.9±2.2(15)	2.5±1.2(15)	7.9±4.5(17)	9.5±3.0(15)	<5.0(15)	4.0±2.6(-3)
G023.6566-00.1273	18:34:51.57	-08:18:21.81	1.24	150	1.4±0.4(16)	<5.0(15)	7.1±2.5(17)	2.5±1.2(16)	<5.0(15)	1.2±0.7(-2)
G025.6498+01.0491	18:34:20.92	-05:59:42.08	1.17	150	3.0±0.6(16)	8.5±2.7(15)	3.4±1.4(18)	1.5±0.8(16)	5.0±2.5(15)	1.5±1.0(-3)
G030.1981-00.1691	18:47:03.05	-02:30:36.30	0.60	150	5.1±1.1(15)	<1.8(15)	2.2±1.2(17)	<1.5(16)	<1.6(16)	<4.7(-2)
G233.8306-00.1803	07:30:16.73	-18:35:49.06	0.81	150	<3.7(15)	<3.0(15)	<6.0(15)	<6.5(15)	<4.4(15)	-
G305.2017+00.2072A1	13:11:10.45	-62:34:38.60	1.30	150	1.2±0.3(16)	2.0±0.9(15)	8.5±4.8(17)	5.0±2.5(15)	<2.3(15)	2.0±1.5(-3)
G305.2017+00.2072A2	13:11:13.12	-62:34:42.74	1.30	150	<8.8(15)	<5.0(15)	0.1-5.3(17)	<8.0(15)	<1.2(16)	<9.1(-1)
G310.0139+00.3892	13:51:37.88	-61:39:07.74	1.30	150	<2.3(15)	<2.0(15)	0.3-13.5(16)	<7.9(15)	<2.9(15)	-
G314.3197+00.1125	14:26:26.25	-60:38:31.26	1.30	150	<2.4(15)	<2.2(15)	0.8-1.4(17)	<1.0(16)	<6.0(15)	-
G316.6412-00.0867	14:44:18.35	-59:55:11.28	1.29	100 ⁽³⁾	2.8±0.4(16)	8.6±2.7(15)	3.5±1.5(18)	2.8±0.5(16)	4.8±3.0(15)	2.7±1.2(-3)
G318.0489+00.0854B	14:53:42.64	-59:08:53.02	1.30	150	1.7±0.3(16)	4.9±1.9(15)	1.9±0.9(18)	8.0±4.0(15)	<3.0(15)	1.4±1.0(-3)
G318.9480-00.1969A1	15:00:55.28	-58:58:52.60	1.29	100 ⁽³⁾	8.5±1.2(16)	2.2±0.4(16)	9.6±3.2(18)	7.0±1.1(16)	1.4±0.7(16)	2.4±0.9(-3)
G318.9480-00.1969A2	15:00:55.23	-58:58:55.88	1.29	150	<2.6(15)	<7.8(14)	0.4-16.0(16)	<6.5(15)	<2.3(15)	2.0±1.1(-1)
G323.7399-00.2617B1	15:31:45.64	-56:30:50.16	1.28	150	8.7±2.0(15)	2.0±0.9(15)	7.5±4.3(17)	<3.0(15)	<2.9(-3)	-
G323.7399-00.2617B2	15:31:45.45	-56:30:49.84	1.28	125	8.2±1.8(16)	1.5±0.3(16)	5.7±3.3(18)	2.0±1.0(16)	4.0±2.0(15)	2.0±1.4(-1)
G323.7399-00.2617B3	15:31:45.73	-56:30:51.93	1.28	150	<2.6(15)	<6.0(14)	1.4-13.4(16)	<4.7(15)	<2.3(15)	-
G323.7399-00.2617B4	15:31:45.94	-56:30:51.34	1.28	150	<2.6(15)	<6.9(14)	1.2-14.2(16)	<2.7(15)	<2.8(15)	-
G323.7399-00.2617B5	15:31:45.62	-56:30:45.62	1.28	150	<2.6(15)	<5.8(14)	0.1-13.9(16)	<5.0(15)	<2.7(15)	-
G323.7399-00.2617B6	15:31:45.84	-56:30:47.68	1.28	150	<3.9(15)	<1.2(15)	0.1-2.1(17)	<2.6(15)	<3.7(15)	-
G323.7399-00.2617B7	15:31:45.91	-56:30:46.10	1.28	150	<1.7(15)	<2.1(15)	0.1-9.3(16)	<3.9(15)	<1.6(15)	-
G327.1192+00.5103	15:47:32.72	-53:52:38.60	0.81	100	4.0±0.9(16)	9.2±2.0(15)	2.9±1.7(18)	3.5±1.8(16)	4.0±3.1(-3)	<2.9(-1)
G343.1261-00.0623	16:58:17.22	-42:52:07.54	1.25	100	8.8±2.7(15)	<7.0(15)	5.0±1.8(17)	<4.0(16)	4.0±2.0(15)	<4.1(-2)
G345.5043+00.3480 C1	17:04:22.89	-40:44:23.06	1.25	125	5.1±1.1(16)	1.0±0.2(16)	4.0±2.3(18)	5.0±2.5(16)	1.0±0.5(16)	2.0±1.4(-1)

Table 4.B.1: continued.

Source	RA (J2000)	Dec (J2000)	θ_b "	T_{ex} K	$N^{\text{a}}_{\text{CH}_3\text{OH}}$ cm^{-2}	$N_{\text{CH}_3^{18}\text{OH}}$ cm^{-2}	$N_{\text{CH}_3\text{OH}}$ cm^{-2}	$N_{\text{CH}_3\text{DOH}}$ cm^{-2}	$N_{\text{CHD}_3\text{OH}}$ cm^{-2}	$(\text{D}/\text{H})_{\text{CH}_3\text{OH}}^{(1)}$	$(\text{D}/\text{H})_{\text{CH}_3\text{DOH}}^{(2)}$
G345.5043+00.3480 C2	17:04:22.89	-46:44:23.06	1.25	150	$3.1 \pm 0.7(16)$	$<1.0(16)$	$1.7 \pm 0.9(18)$	$3.0 \pm 1.5(16)$	$<1.0(16)$	$5.9 \pm 4.3(-3)$	$<6.7(-1)$
G348.7342-01.0359B1	17:20:07.08	-38:57:11.22	1.23	150	$<3.4(15)$	$<9.9(14)$	$1.3-17.7(16)$	$<1.2(16)$	$<3.9(15)$	—	—
G348.7342-01.0359B2	17:20:07.26	-38:57:09.82	1.23	150	$<2.3(15)$	$<1.7(15)$	$0.1-11.9(16)$	$<3.6(15)$	$<4.1(15)$	—	—
G348.7342-01.0359B3	17:20:07.38	-38:57:10.15	1.23	150	$<4.0(15)$	$<1.5(15)$	$<1.4(15)$	$<1.1(16)$	$<3.8(15)$	—	—

Notes. The coordinates mark the position from which the spectra were extracted. All column densities are derived for the reported T_{ex} and assuming the source size is equal to the size of the beam (i.e., beam dilution = 1). The column density of CH_3OH is derived from the $\text{CH}_3^{18}\text{OH}$ and $^{13}\text{CH}_3\text{OH}$ isotopologues when these are detected. If neither isotopologue is detected but CH_3OH is, a range in column densities is presented where the lower limit is the column density derived from CH_3OH and the upper limit is scaled from the upper limit on $^{13}\text{CH}_3\text{OH}$. If CH_3OH itself is also not detected, an upper limit is directly derived from its spectrum.

⁽¹⁾ Derived from $N_{\text{CH}_3\text{DOH}}$ using Eq. (4.2). ⁽²⁾ Derived from $N_{\text{CHD}_3\text{OH}}$ using Eq. (4.3). ⁽³⁾ T_{ex} is set to 150 K for deuterated isotopologues and to 100 K for the other isotopologues.

4.C Methanol D/H ratios of sources in the literature

Table 4.C.1: The $(D/H)_{CH_3OH}$ and $(D/H)_{CH_3DOH}$ ratios taken from the literature that are included in Figs. 4.3 and 4.4 .

Source	Type ⁽¹⁾	$(D/H)_{CH_3OH}$	$(D/H)_{CH_3DOH}$	Refs
B1-c	LMP	$2.8 \pm 0.9(-2)$	$1.3 \pm 0.2(-1)$	1,2
Serpens S68N	LMP	$1.4 \pm 0.6(-2)$	$1.2 \pm 0.5(-1)$	1,2
B1-bS	LMP	$<1.8(-2)$	–	1,2
HH212	LMP	$3.8 \pm 2.3(-2)$	–	3
		$8.1 \pm 3.0(-3)$	–	4
IRAS 16293A	LMP	$2.8 \pm 1.2(-2)$	$2.0 \pm 0.7(-1)$	5,6
IRAS 16293B	LMP	$2.4 \pm 0.9(-2)$	$2.5 \pm 0.9(-1)$	6,7
IRAS 2A	LMP	$1.9 \pm 1.0(-2)$	$7.0 \pm 2.6(-1)$	8
IRAS 4A	LMP	$1.4 \pm 0.8(-2)$	$5.6 \pm 2.2(-1)$	8
L483	LMP	$7.8 \pm 3.3(-3)$	–	9
BHR71	LMP	$9.6 \pm 4.1(-3)$	–	10
Ser-emb 1	LMP	$<2.0(-1)$	–	11
Ser-emb 11W	LMP	$<4.3(-2)$	–	12
HOPS-108	LMP	$7.0 \pm 3.8(-3)$	–	13
G192.12–11.10	LMP	$9.8 \pm 5.8(-3)$	–	14
G205.46–14.56S1–A	LMP	$6.7 \pm 3.3(-3)$	–	14
G208.68–19.20N1	LMP	$1.3 \pm 0.6(-2)$	–	14
G210.49–19.79W–A	LMP	$1.4 \pm 0.6(-2)$	–	14
G211.47–19.27S	LMP	$1.7 \pm 0.4(-2)$	–	14
V883 Ori	LMP	$4.8 \pm 1.0(-2)$	–	15
Serpens SMM1-a	IMP	$3.6 \pm 2.1(-3)$	–	16
NGC 7192 FIRS2	IMP	$1.9 \pm 0.8(-3)$	–	17
Cep E-A	IMP	$1.2 \pm 0.4(-2)$	–	18
Sgr B2(N2)	HMP	$4.0 \pm 1.7(-4)$	–	19,20
NGC6334I MM1 I	HMP	$3.0 \pm 1.7(-4)$	–	21
NGC6334I MM1 II	HMP	$1.8 \pm 0.9(-4)$	–	21
NGC6334I MM1 III	HMP	$3.2 \pm 1.8(-4)$	–	21
NGC6334I MM1 IV	HMP	$1.6 \pm 1.0(-4)$	–	21
NGC6334I MM1 V	HMP	$2.3 \pm 1.1(-4)$	–	21
NGC6334I MM2 I	HMP	$6.0 \pm 3.6(-4)$	–	21
NGC6334I MM2 II	HMP	$1.5 \pm 0.7(-4)$	–	21
NGC6334I MM3 I	HMP	$2.4 \pm 1.1(-4)$	–	21
NGC6334I MM3 II	HMP	$2.6 \pm 1.1(-4)$	–	21
Orion KL ridge	HMP	$1.7 \pm 0.7(-3)$	–	22
Orion KL HC	HMP	$<1.7(-3)$	–	22
CygX-N30	HMP	$<1.7(-3)$	–	23
L1495-B10 6	LMPC	$1.4 \pm 0.4(-2)$	–	24

Table 4.C.1: continued.

Source	Type ⁽¹⁾	(D/H) _{CH₃OH}	(D/H) _{CH₃DOH}	Refs
L1495-B10 7	LMPC	4.8±1.3(-2)	—	24
L1495-B10 8	LMPC	5.2±1.5(-2)	—	24
L1495-B10 9	LMPC	4.6±1.1(-2)	—	24
L1495-B10 10	LMPC	4.2±1.3(-2)	—	24
L1495-B10 11	LMPC	<1.9(-2)	—	24
L1495-B10 12	LMPC	2.0±0.4(-2)	—	24
L1495-B10 13	LMPC	<3.5(-2)	—	24
L1495-B10 14	LMPC	<1.4(-2)	—	24
L1495-B10 15	LMPC	4.0±1.1(-2)	—	24
L1495-B10 16	LMPC	3.0±1.0(-2)	—	24
L1495-B10 17	LMPC	8.8±2.7(-2)	—	24
L183	LMPC	1.3±0.2(-2)	—	25
L1544	LMPC	3.0±1.3(-2)	—	26
I00117-MM2	HMSC	<2.4(-3)	—	27
AFGL 5142-EC	HMSC	9.0±3.8(-4)	—	27
05458-mm3	HMSC	2.3±1.0(-3)	—	27
G034-G2(MM2)	HMSC	1.4±0.6(-2)	—	27
G034-F2(MM7)	HMSC	<2.5(-3)	—	27
G034-F1(MM8)	HMSC	<1.5(-3)	—	27
G034-C1(MM9)	HMSC	<8.7(-4)	—	27
I20293-WC	HMSC	<1.9(-3)	—	27
I22134-G	HMSC	<1.7(-3)	—	27
I22134-B	HMSC	<6.7(-3)	—	27

Notes. The (D/H)_{CH₃OH} and (D/H)_{CH₃DOH} ratios are either directly taken from the reported literature or computed using Eqs. (4.2) and (4.3) using the column densities from the reported literature. A 30% uncertainty was assumed in cases where no uncertainty was reported.

⁽¹⁾ LMP: low-mass protostar, IMS: intermediate-mass protostar, HMS: high-mass protostar, LMPC: low-mass prestellar core, HMSC: high-mass starless core.

References. 1: van Gelder et al. (2020); 2: Appendix 4.D; 3: Lee et al. (2019a); 4: Bianchi et al. (2017b); 5: Manigand et al. (2020); 6: Drozdovskaya et al. (2022); 7: Jørgensen et al. (2018); 8: Taquet et al. (2019); 9: Jacobsen et al. (2019); 10: Yang et al. (2020); 11: Martín-Doménech et al. (2019); 12: Martín-Doménech et al. (2021); 13: Chahine et al. (2022); 14: Hsu et al. (2022); 15: Lee et al. (2019b); 16: Ligterink et al. (2021); 17: Fuente et al. (2014); 18: Ospina-Zamudio et al. (2018); 19: Belloche et al. (2016); 20: Müller et al. (2016); 21: Bøgelund et al. (2018); 22: Neill et al. (2013); 23: van der Walt et al. (2021); 24: Ambrose et al. (2021); 25: Lattanzi et al. (2020); 26: Bizzocchi et al. (2014); 27: Fontani et al. (2015).

4.D Doubly deuterated methanol in B1-c, Serpens S68N, and B1-bS

Using the database entry of CHD₂OH provided by Drozdovskaya et al. (2022), transitions from CHD₂OH can also be searched for in a few COM-rich low-mass protostars. Here, this is done for B1-c, Serpens S68N (hereafter S68N), and B1-bS from the 2017.1.01174.S ALMA program. The content of oxygen-bearing COMs for these sources was presented by van Gelder et al. (2020), but no public database entry was yet available for CHD₂OH at that time.

Only one strong transition of CHD₂OH ($7_{1,2} o_1 - 7_{0,1} e_0$, $E_{\text{up}} = 68$ K) is available for these sources which lies on the very edge of the covered frequency range. For B1-c and S68N, this transition is detected at the 3σ level, but given that only half the line is observed this detection is still tentative. Using the same method for deriving the column densities as used by van Gelder et al. (2020) and assuming an excitation temperature of 150 K, we derive column densities of $2.0 \pm 0.6 \times 10^{16} \text{ cm}^{-2}$ for B1-c, $7.2 \pm 2.7 \times 10^{15} \text{ cm}^{-2}$ for S68N, and $< 1.7 \times 10^{15} \text{ cm}^{-2}$ for B1-bS. The FWHM was fixed to the average FWHM of those sources of 3.2 km s^{-1} , 5.5 km s^{-1} , and 1.0 km s^{-1} , respectively (van Gelder et al. 2020). The resulting fits are shown in Fig. 4.D.1. Using these derived column densities and those reported for CH₃OH by van Gelder et al. (2020), the $(\text{D}/\text{H})_{\text{CH}_2\text{DOH}}$ ratios for B1-c and S68N (for B1-bS, both CH₂DOH and CHD₂OH are not detected) are shown in Fig. 4.4 and agree very well with those derived for other low-mass sources as well as with the high-mass sources.

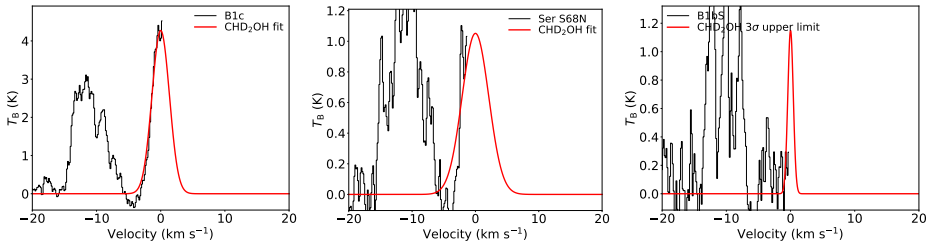


Figure 4.D.1: Spectral line fits of CHD₂OH $7_{1,2} o_1 - 7_{0,1} e_0$ ($E_{\text{up}} = 68$ K) line for B1-c (left), Serpens S68N (middle), and B1-bS (right). The data corrected for the V_{lsr} are shown in black and the best fit for $T_{\text{ex}} = 150$ K is shown in red.

4.E Additional figures

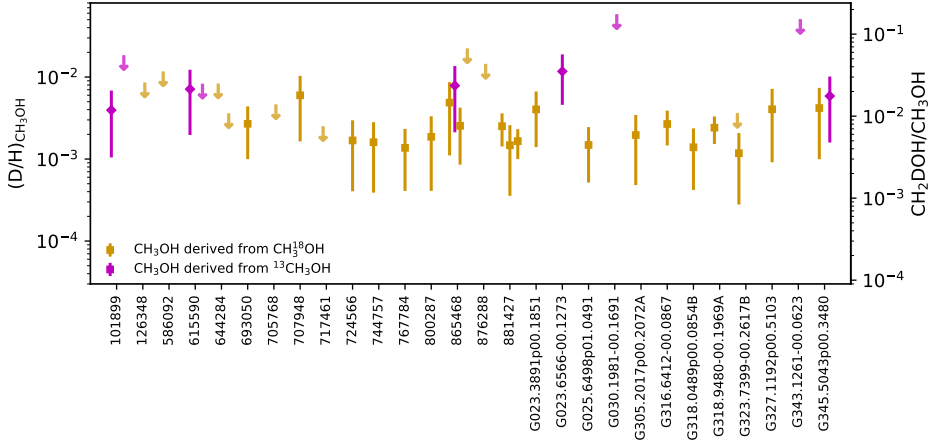


Figure 4.E.1: $(D/H)_{CH_3OH}$ ratios derived from the N_{CH_3DOH}/N_{CH_3OH} ratios for the ALMAGAL sources presented in this work, indicating whether N_{CH_3OH} was derived from the ¹³C isotopologue (magenta diamonds) or from the ¹⁸O isotopologue (orange squares). Upper limits are presented as arrows.

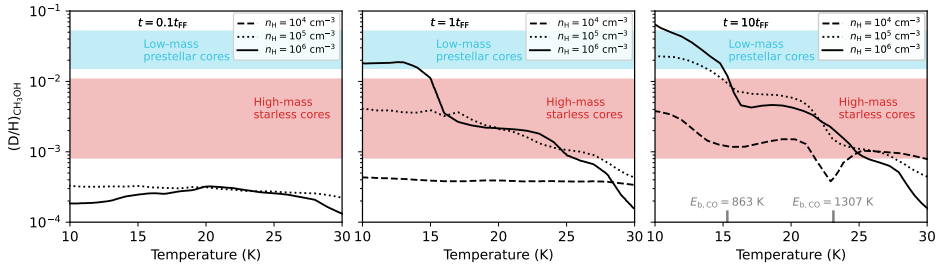


Figure 4.E.2: Same as Fig. 4.6 but now showing the average measured $(D/H)_{CH_3OH}$ for low-mass prestellar cores (light blue) and high-mass starless cores (red).

PART II

Inheritance versus reset:
accretion shocks

Chapter 5

Modeling accretion shocks at the disk-envelope interface

Sulfur chemistry

M. L. van Gelder, B. Tabone, E. F. van Dishoeck, B. Godard

A&A 653, A159 (2021)

Abstract

Context. As material from an infalling protostellar envelope hits the forming disk, an accretion shock may develop which could (partially) alter the envelope material entering the disk. Observations with the Atacama Large Millimeter/submillimeter Array (ALMA) indicate that emission originating from warm SO and SO₂ might be good tracers of such accretion shocks.

Aims. The goal of this work is to test under what shock conditions the abundances of gas-phase SO and SO₂ increase in an accretion shock at the disk-envelope interface.

Methods. Detailed shock models including gas dynamics were computed using the Paris-Durham shock code for nonmagnetized *J*-type accretion shocks in typical inner envelope conditions. The effect of the preshock density, shock velocity, and strength of the ultraviolet (UV) radiation field on the abundance of warm SO and SO₂ is explored. Compared with outflows, these shocks involve higher densities ($\sim 10^7 \text{ cm}^{-3}$), lower shock velocities ($\sim \text{few km s}^{-1}$), and large dust grains ($\sim 0.2 \mu\text{m}$) and thus probe a different parameter space.

Results. Warm gas-phase chemistry is efficient in forming SO under most *J*-type shock conditions considered. In lower-velocity ($\sim 3 \text{ km s}^{-1}$) shocks, the abundance of SO is increased through subsequent reactions starting from thermally desorbed CH₄ toward H₂CO and finally SO. In higher velocity ($\gtrsim 4 \text{ km s}^{-1}$) shocks, both SO and SO₂ are formed through reactions of OH and atomic S. The strength of the UV radiation field is crucial for SO and in particular SO₂ formation through the photodissociation of H₂O. Thermal desorption of SO and SO₂ ice is only relevant in high-velocity ($\gtrsim 5 \text{ km s}^{-1}$) shocks at high densities ($\gtrsim 10^7 \text{ cm}^{-3}$). Both the composition in the gas phase, in particular the abundances of atomic S and O, and in ices such as H₂S, CH₄, SO, and SO₂ play a key role in the abundances of SO and SO₂ that are reached in the shock.

Conclusions. Warm emission from SO and SO₂ is a possible tracer of accretion shocks at the disk-envelope interface as long as a local UV field is present. Observations with ALMA at high-angular resolution could provide further constraints given that other key species for the gas-phase formation of SO and SO₂, such as H₂S and H₂CO, are also covered. Moreover, the *James Webb* Space Telescope will give access to other possible slow, dense shock tracers such as H₂, H₂O, and [S I] 25 μm .

5.1 Introduction

It is currently still unknown how much reprocessing of material occurs during the collapse from a prestellar core to a protostar and disk. Two scenarios can be considered: the inheritance scenario where the chemical composition is conserved from a cloud to disk, or the (partial) reset scenario where the envelope material is modified during its trajectory from an envelope to disk. Some inheritance is suggested by the rough similarity between cometary and interstellar ices (Mumma & Charnley 2011; Drozdovskaya et al. 2018, 2019). On the other hand, some modification of envelope material is expected due to the increase in temperature and stellar ultraviolet (UV) radiation during infall (e.g., Aikawa et al. 1999; Visser et al. 2009). Moreover, as the infalling envelope hits the disk, an accretion shock may develop which can alter the composition of the material flowing into the disk, and therefore (partially) reset the chemistry. In the most extreme case, reset implies complete vaporization of all molecules back to atoms with subsequent reformation. Milder versions of reset include sputtering of ices, and gas and ice chemistry modifying abundances.

Already in the earliest Class 0 phase of the low-mass star-formation process, an accretion disk around the young protostar is formed (e.g., Tobin et al. 2012; Murillo et al. 2013). The impact of infalling envelope material onto the disk can cause a shock, raising temperatures of gas and dust at the disk-envelope interface to values much higher than from heating by stellar photons alone (Draine et al. 1983; Neufeld & Hollenbach 1994). These low-velocity (\sim few km s^{-1}) accretion shocks at high densities ($\sim 10^7 \text{ cm}^{-3}$) are widely found in models and simulations (e.g., Cassen & Moosman 1981; Li et al. 2013; Miura et al. 2017), and they are often invoked in Solar System formation to explain phenomena such as noble gas trapping (Owen et al. 1992). They are most powerful in the earliest stages when the disk is still small ($\lesssim 10 \text{ AU}$). However, that infalling material may eventually end up in the protostar and not in the disk. As the embedded disk reaches a size of (several) tens of AU, the envelope material entering the disk remains there and eventually forms the building blocks of planets (e.g., Harsono et al. 2018; Manara et al. 2018; Tychoniec et al. 2020).

These accretion shocks have not yet been undisputedly detected. Typical optical shock tracers such as [O I] 6300 Å and [S II] 6371 Å are more sensitive to high-velocity shocks ($\gtrsim 20 \text{ km s}^{-1}$, e.g., Podio et al. 2011; Banzatti et al. 2019) and difficult to detect in protostellar environments due to the high extinction by the surrounding envelope. Observations of mid-infrared (MIR) shock tracers such as H_2O , high-J CO, [S I] 25 μm , and [O I] 63 μm suffer from outflow contamination in low-spatial resolution space-based observations (e.g., Kristensen et al. 2012; Nisini et al. 2015; Rivière-Marichalar et al. 2016) and from the Earth's atmosphere for ground-based observations; here the launch of the *James Webb* Space Telescope (JWST) will provide a solution. At submillimeter wavelengths, classical diagnostics of shocks include sputtering or grain-destruction products such as CH_3OH and SiO (e.g., Caselli et al. 1997; Schilke et al. 1997; Gusdorf et al. 2008a,b; Guillet et al. 2009; Suutarinen et al. 2014). However, usually these species are only observed in relatively high-velocity outflows and jets through broad emission lines

(e.g., Tychoniec et al. 2019; Taquet et al. 2020; Codella et al. 2020).

Sulfur bearing species such as SO and SO₂ are suggested as possible accretion shock tracers. An enhancement of warm SO emission at the centrifugal barrier, the interface between envelope and disk, is observed in the L1527 Class 0/I system with the Atacama Large Millimeter/submillimeter Array (ALMA) at ~ 100 AU scales (Sakai et al. 2014, 2017). A similar rotating structure in SO is seen toward the Class I system Elias 29 (Oya et al. 2019). Equivalently, warm SO₂ emission possibly related to an accretion shock is observed toward the B335 Class 0 protostar (Bjerkeli et al. 2019) and a few Class I sources (Oya et al. 2019; Artur de la Villarmois et al. 2019). However, both SO and SO₂ are also seen related to outflow activity, both in large-scale outflows (e.g., Codella et al. 2014; Taquet et al. 2020) as in disk winds on smaller scales (e.g., Tabone et al. 2017; Lee et al. 2018). Moreover, high-angular resolution observations (~ 30 AU) of the Class I source TMC1A show narrow SO emission lines coming from a ring-shaped morphology which may be linked to the warm inner envelope (Harsono et al. 2021). Emission from warm SO and SO₂ is thus not an unambiguous tracer of accretion shocks; comparison to shock models is necessary to make robust conclusions.

In shocks, the gas temperature readily rises to > 100 K (Draine et al. 1983; Flower & Pineau des Forêts 2003; Godard et al. 2019), enough to ignite gas-phase formation of SO and SO₂ (e.g., Prasad & Huntress 1980; Hartquist et al. 1980). A key species for this is the OH radical, which is efficiently produced in shocks through the endothermic reaction between H₂ and atomic oxygen, but also through photodissociation of H₂O. The OH radical reacts with atomic sulfur to form SO and subsequently to form SO₂. Moreover, SO can also be formed from the SH radical reaction with atomic oxygen (Hartquist et al. 1980). Since the gas-phase chemistry of SO and SO₂ in shocks is dependent on radicals such as OH and SH, the abundance of these species is not solely determined through the temperature in the shock but also through the strength of the local UV field.

Alternatively, thermal desorption of SO and SO₂ ice in shocks can enhance the gas-phase abundances of SO and SO₂. In interstellar ices, OCS is the only securely identified sulfur-bearing species (Geballe et al. 1985; Palumbo et al. 1995), with a tentative detection for SO₂ (Boogert et al. 1997; Zasowski et al. 2009). It is suggested that H₂S is the main sulfur carrier in the ices (e.g., Vidal et al. 2017), but so far only upper limits could be derived (Jiménez-Escobar & Muñoz Caro 2011). To date, SO ice has not yet been detected. All aforementioned species are observed in cometary ices such as 67P/Churyumov–Gerasimenko (Calmonte et al. 2016; Rubin et al. 2019; Altwegg et al. 2019). Miura et al. (2017) modeled low-velocity (2 km s^{-1}) accretion shocks taking into account the dust dynamics but without any gas-phase chemistry included and could only explain the observations of Sakai et al. (2014) if SO was thermally desorbed while adopting dust grains that were smaller than $0.1 \mu\text{m}$. Sputtering seems to be irrelevant as this becomes only efficient at larger shock velocities ($> 10 \text{ km s}^{-1}$; e.g., Aota et al. 2015). However, to thermally desorb sulfur-bearing ices such as SO and SO₂ from the grains, the dust temperature has to reach values on the order of $40\text{--}70$ K.

In this paper, we present a grid of irradiated low-velocity ($< 10 \text{ km s}^{-1}$) *J*-type accretion shock models at typical inner envelope densities ($10^5\text{--}10^8 \text{ cm}^{-3}$). This is

a different parameter space than usually explored in, for example, higher-velocity ($> 10 \text{ km s}^{-1}$) outflows at lower densities ($\sim 10^4 \text{ cm}^{-3}$). The goal is to test under what shock conditions the abundance of warm SO and SO₂ is significantly increased. In Sect. 5.2, the model and input parameters are introduced. We present the results of our analysis in Sect. 5.3, after which we discuss these results in Sect. 5.4. Our conclusions are summarized in Sect. 5.5.

5.2 Accretion shock model

5.2.1 Shock model

The accretion shock at the disk-envelope interface is modeled using a slightly modified version of the Paris-Durham shock code (Flower & Pineau des Forêts 2003; Lesaffre et al. 2013; Godard et al. 2019). This publicly available numerical tool¹ computes the dynamical, thermal, and chemical structure of stationary plane parallel shock waves. The models therefore represent a continuous inflow of envelope material onto the disk and thus a continuous sequence of shocks. The location of the accretion shock is expected to move outward as the disk grows and evolves (Visser & Dullemond 2010).

In this paper, only stationary nonmagnetized *J*-type accretion shocks are presented. The presence of a magnetic field can result in *C* or *CJ*-type shocks (e.g., Draine 1980; Flower & Pineau des Forêts 2003), see Appendix 5.E for details. However, the length of *C*-type accretion shocks is strongly dependent on the initial conditions and the size of dust grains and may reach envelope scales of $\sim 1000 \text{ AU}$, which is not consistent with the emission of SO and SO₂ seen on $< 100 \text{ AU}$ scales (e.g., Sakai et al. 2014, 2017; Artur de la Villarmois et al. 2019; Oya et al. 2019). *CJ*-type shocks could be relevant in intermediate magnetized inner envelopes ($\sim 0.1 \text{ mG}$; Hull et al. 2017, Appendix 5.E), but to compute *CJ*-type shocks across our specific parameter space (low velocities, high densities), the Paris-Durham code needs to be tuned, which is beyond the scope of this work. Nevertheless, the results of *CJ* and *C*-type shocks are not expected to be different from *J*-type shocks in terms of chemistry.

In the following sections, the main physical and chemical quantities and properties that are included in the model are introduced. In particular, the most relevant physical and chemical processes and updates on the version of the code presented by Godard et al. (2019) are highlighted.

Geometry

The shock is calculated following a stationary plane parallel structure, see Fig. 5.1. A shock front propagates with a velocity V_s in the direction of negative distance z . The entire structure is irradiated with an isotropic radiation field equal to the isotropic standard interstellar radiation field (ISRF) scaled with a factor G_0 (Mathis et al. 1983), as was implemented by Godard et al. (2019). In protostellar

¹<https://ism.obspm.fr>

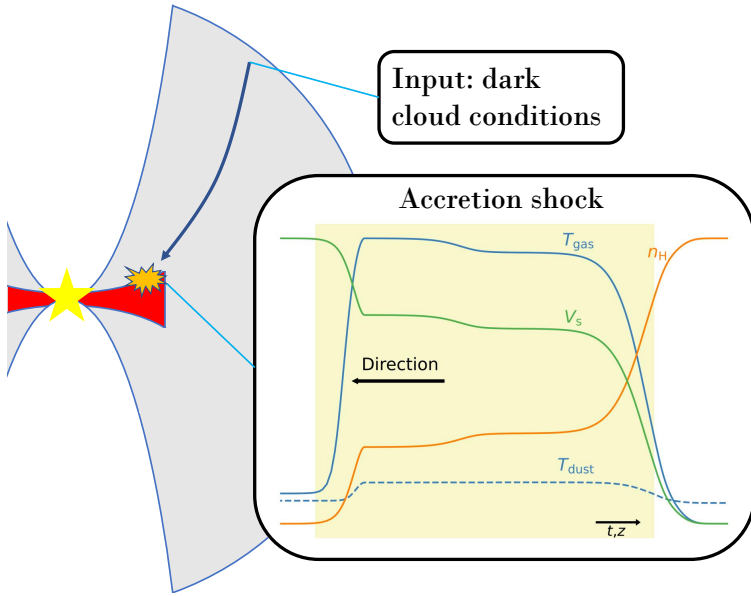


Figure 5.1: Physical structure of a protostellar envelope. Starting with dark cloud conditions, an accretion shock model is calculated. The shock profile in the bottom panel is shown on a logarithmic scale with the yellow region indicating the shocked region.

systems, the UV radiation can originate both from the accretion onto the protostar itself or from shocks in the bipolar jets (e.g., van Kempen et al. 2009a; Yıldız et al. 2012; Benz et al. 2016). Moreover, the extinction A_V between the source of UV irradiation and the shock at the disk-envelope interface can be as high as ~ 10 mag (e.g., Drozdovskaya et al. 2015) and is assumed to be taken into account with the choice of G_0 . Therefore, the exact source of UV radiation is irrelevant here as long as a reasonable range in G_0 is covered and since the radiation field is assumed to be isotropic. A diluted black body of 100 K representing far-infrared (FIR) dust emission from the accretion disk is added to the radiation field. Assuming an emitting region of 4.5 AU at a distance of 100 AU, the black body is diluted with a factor $W = 5 \times 10^{-4}$ (for details, see Appendix A of Tabone et al. 2020) and is constant for all models. Additionally, secondary UV photons created through the collisional excitation of H_2 by electrons produced by cosmic ray ionization are included.

Radiative transfer and photon processes

Photodissociation and photoionization processes of both the gas and dust are taken into account. The cross sections are taken from the Leiden database (Heays et al. 2017). To save computation time, the photoreaction cross sections were only used for the photodissociation of CH, CH_3 , CH_4 , NH, CN, O_2 , OH, H_2O , H_2CO , SH, H_2S , CS, OCS, SO, and SO_2 , and the photoionization of C, S, CH, CH_3 , CH_4 ,

O_2 , OH , H_2O , H_2CO , SH , H_2S , and SO . Photodissociation and photoionization of all other species are also included in the chemistry using the analytical expression of Heays et al. (2017). Due to the self-shielding properties of H_2 , CO , and N_2 , photodissociation of these species is assumed to be negligible. The destruction of atoms and molecules by far-ultraviolet photons between 911 Å and 2400 Å is calculated including both continuum and discrete processes.

Grains and PAHs

The grains are assumed to have grown in protostellar envelopes to larger sizes than the typical interstellar medium (ISM) distribution (e.g., Guillet et al. 2007; Miotello et al. 2014; Harsono et al. 2018; Galametz et al. 2019). Here, we assume that all grains have an initial core size of $0.2 \mu\text{m}$ (Guillet et al. 2020) and are either neutral, single negatively, or single positively charged. Moreover, the dust grains are assumed to be dynamically coupled to the gas. Grain-grain interactions are not included since vaporization and shattering of dust grains are only relevant for J -type shocks moving at high velocities ($> 20 \text{ km s}^{-1}$; Guillet et al. 2009). Dust coagulation can potentially be relevant in changing the grain size distribution (Guillet et al. 2011, 2020) but is not included here.

Other large species are polycyclic aromatic hydrocarbons (PAHs), which are modeled here as single particles with a size of 6.4 Å (Flower & Pineau des Forêts 2003). In most studies of interstellar shocks, the abundance of PAHs is set to the typical value of the ISM ($\sim 10^{-6}$ with respect to the proton density $n_{\text{H}} = 2n(\text{H}_2) + n(\text{H}) + n(\text{H}^+)$; Draine & Li 2007). However, given that PAHs freeze out in dense clouds, the abundance of PAHs in the gas is set to $\sim 10^{-8}$ with respect to n_{H} (Geers et al. 2009).

Chemical network

The chemical network adopted in this work consists of 143 species which can take place in about a thousand reactions, both in the gas phase and in the solid state. The network is largely similar to that used by Flower & Pineau des Forêts (2015) and Godard et al. (2019) with the addition of important sulfur bearing ices such as SO and SO_2 and their desorption and adsorption reactions. Moreover, the binding energies of all ice species were updated (e.g., 1800 K, 3010 K, and 2290 K for SO , SO_2 , and H_2S , respectively; Penteado et al. 2017). For a density of 10^8 cm^{-3} , this results in a sublimation temperature of 37 K, 62 K, and 47 K for SO , SO_2 , and H_2S , respectively. For simplicity, grain surface reactions have been disabled since the effect of these reactions on timescales of the shock is negligible. Sputtering of ices is not relevant here since in J -type shocks all material is coupled in one fluid.

Heating and cooling

The thermal balance is calculated consistently throughout the shock. The main sources of gas heating in nonmagnetized J -type shocks are through viscous stresses and compression of the medium at the shock front where T_{gas} increases adiabatically over a few mean free paths. A second form of heating occurs through ir-

radiation coming from the incident local UV radiation field and through gas-dust thermal coupling.

The gas is cooled through atomic lines of C, N, O, S, and Si, ionic lines of C^+ , N^+ , O^+ , S^+ , and Si^+ , and rotational and rovibrational lines of H_2 , OH, H_2O , NH_3 , ^{12}CO , and ^{13}CO (Flower & Pineau des Forêts 2003; Lesaffre et al. 2013; Godard et al. 2019). All cooling by atomic and ionic lines as well as rovibrational lines of H_2 are calculated in the optically thin limit. The cooling of OH is calculated using an analytical cooling function (Le Bourlot et al. 2002), which holds up to densities of 10^{10} cm^{-3} . However, for NH_3 , local thermodynamic equilibrium (LTE) effects become relevant already for densities $\gtrsim 10^8 \text{ cm}^{-3}$. The cooling through pure rotational lines of NH_3 has therefore been recalculated numerically using the RADEX software (van der Tak et al. 2007) in the optically thin limit, see Appendix 5.A. Cooling by rovibrational lines of H_2O , ^{12}CO , and ^{13}CO is computed using the tabulated values of Neufeld & Kaufman (1993) which take into account opacity effects. Additionally, the gas can be cooled through collisions with dust grains which subsequently radiate away the heat.

The temperature of the dust is calculated from the equilibrium between heating through absorption of photons, thermal collisions with the gas which can both heat and cool the dust, and cooling through infrared emission (Godard et al. 2019). The FIR radiation field of the 100 K black body is of particular importance for the heating for dust grains in the pre and postshock regimes as it sets a minimum dust temperature of $\sim 22 \text{ K}$. A dust temperature of $< 20 \text{ K}$ implies that even the most volatile species such as CO and N_2 are frozen out onto dust grains. However, observations of embedded protostellar systems suggest that CO and N_2 are not frozen out in the inner regions of such systems (e.g., van 't Hoff et al. 2018a). A higher dust temperature would result in more ice species being desorbed prior to the shock but the effect on the shock structure and chemistry is negligible.

5.2.2 Input parameters

The range of physical parameters explored in this paper is presented in Table 5.1. Important physical parameters are the initial proton density n_{H} , the cosmic ray ionization rate of H_2 ζ_{H} , the strength of the local incident radiation field, and the shock velocity V_{s} . Depending on the mass of the source and size of the disk, the density of infalling envelope material impacting the disk can be $\sim 10^5 - 10^8 \text{ cm}^{-3}$ (e.g., Harsono et al. 2015). Therefore, the investigated range of n_{H} covers $\sim 10^5 - 10^8 \text{ cm}^{-3}$, with the fiducial value at 10^7 cm^{-3} . The radiation field is parameterized as a combination of the ISRF multiplied with a factor G_0 (Mathis et al. 1983) and infrared emission from the disk (which is constant for all models). The strength of the local UV radiation field at the disk-envelope interface is highly uncertain and (among other things) dependent on the distance to the source of UV radiation (see Sect 5.2.1). Without extinction the local G_0 value could be as high as 10^4 at $\sim 100 \text{ AU}$ (Visser et al. 2012). However, taking into account the extinction the local strength will likely not be much higher than a G_0 of ~ 100 . Therefore, a large range in G_0 is considered: $10^{-3} - 10^2$, with a fiducial value of $G_0 = 1$. The fiducial V_{s} is set to 3 km s^{-1} , which is roughly equal to the velocity of the

Table 5.1: Fiducial model parameters and explored parameter range

	Units	Fiducial	Range
n_{H}	cm^{-3}	10^7	$10^5 - 10^8$
ζ_{H_2}	s^{-1}	10^{-17}	—
G_0	Mathis	1	$10^{-3} - 10^2$
V_{s}	km s^{-1}	3	1 – 10

infalling envelope at 100 AU for a $0.5 M_{\odot}$ star. Shock velocities of $1 - 10 \text{ km s}^{-1}$ are considered, which correspond to an infalling envelope at $10 - 1000 \text{ AU}$. The initial gas temperature is set to 25 K .

Input abundances of smaller molecules and atoms are set to match typical low-mass dark cloud conditions (van der Tak et al. 2003; Boogert et al. 2015; Navarro-Almaida et al. 2020; Tafalla et al. 2021; Goicoechea & Cuadrado 2021). The initial gas-phase abundance of atomic S and O is set to 10^{-6} with respect to n_{H} , with most of the oxygen and carbon reservoirs locked up in refractory grain cores or ices such as H_2O and CH_4 (10^{-4} and 10^{-6} , respectively; Boogert et al. 2015). The dominant sulfur carrier is assumed to be H_2S ice with an abundance of $\sim 2 \times 10^{-5}$ (e.g., Vidal et al. 2017; Navarro-Almaida et al. 2020). The abundance of both SO and SO_2 ice was set to 10^{-7} (e.g., Boogert et al. 2015; Rubin et al. 2019; Altwegg et al. 2019), with the initial gas-phase abundance at 10^{-9} (van der Tak et al. 2003). The full list of input abundances is presented in Appendix 5.B.

5.3 Results

5.3.1 Temperature and density

The gas and dust temperature, T_{gas} and T_{dust} , respectively, and density structure of the fiducial shock model are shown in the left of Fig. 5.2. At the start of the shock, T_{gas} increases to $\sim 500 \text{ K}$, which is in agreement with the analytic expression for a weakly magnetized and fully molecular shock derived by Lesaffre et al. (2013) from the Rankine-Hugoniot relations,

$$T_{\text{gas,max}} \approx 53V_{\text{s}}^2, \quad (5.1)$$

where V_{s} is the initial shock velocity in units of km s^{-1} . Following the jump in temperature, the gas is cooled down through radiation of rotational and rovibrational molecular lines and atomic lines. The most dominant coolant right after the shock front is H_2 , while cooling by (optically thick) pure rotational and rovibrational lines of CO and H_2O takes over as the temperature drops below $\lesssim 400 \text{ K}$. Cooling of the gas through gas-dust thermal coupling is negligible. Cooling through NH_3 in the optically thin limit is significant for shocks with $V_{\text{s}} \gtrsim 6 \text{ km s}^{-1}$ since in those shocks the abundance of NH_3 is significantly increased through high-temperature gas-phase chemistry. The end of the shock is defined as the distance where T_{gas} drops below 50 K , which corresponds to $\sim 3 \text{ AU}$ for the fiducial model. In the postshock, the thermal balance between gas and dust is determined by heating

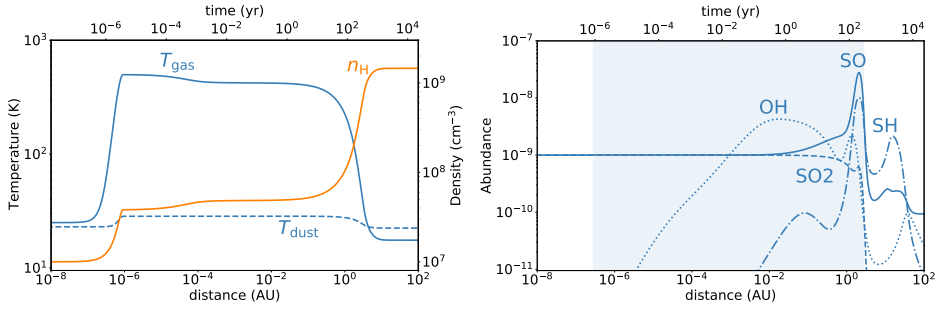
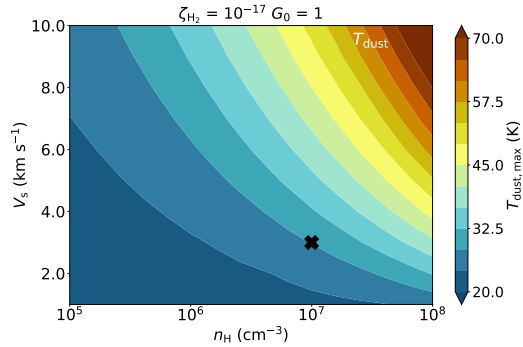


Figure 5.2: *Left:* Temperature and density structure in the fiducial J -type shock. The shock starts at 0 AU and ends at about 5 AU. The dust temperature does not increase enough for thermal sublimation of SO and SO₂. *Right:* Abundance profiles of SO (solid) and SO₂ (dashed) and the key species for gas-phase formation of these species: SH (dot-dashed) and OH (dotted). The region where $T_{\text{gas}} > 50$ K is indicated with the shaded blue region.

Figure 5.3: Maximum dust temperature reached (in color) in shock models as function of initial n_{H} and V_{s} . All other physical parameters are kept constant to the fiducial values and listed on top of the figure. The black cross indicates the position of the fiducial model.



of the dust through the FIR radiation field, gas-grain collisions that transfer the heat from dust to gas, and cooling of the gas through predominantly CO rotational transitions.

The dust temperature is very relevant for these shocks since it increases to values where thermal desorption of ices occurs. In the shock, the material compresses, increasing the density by up to two orders of magnitude (i.e., to about 10^9 cm^{-3} in Fig. 5.2). Due to the thermal coupling between the gas and dust, T_{dust} increases to ~ 30 K for the fiducial model, enough for thermal sublimation of volatile species such as CH₄ but not for more strongly bound ices such as H₂S, H₂O, and CH₃OH. However, as shown in Fig. 5.3, T_{dust} can become as large as > 70 K in the highest-velocity ($\sim 10 \text{ km s}^{-1}$) shocks in the densest (10^8 cm^{-3}) media, resulting in thermal sublimation of several ices including H₂S, SO, and SO₂. Dust heating through UV radiation is only significant for strongest irradiated environments with $G_0 \gtrsim 50$ and only up to $T_{\text{dust}} \lesssim 25$ K. Since photodesorption of ices is negligible on timescales of the shock (see Eq. (5.9)), thermal desorption is the dominant mechanism in releasing ices to the gas phase.

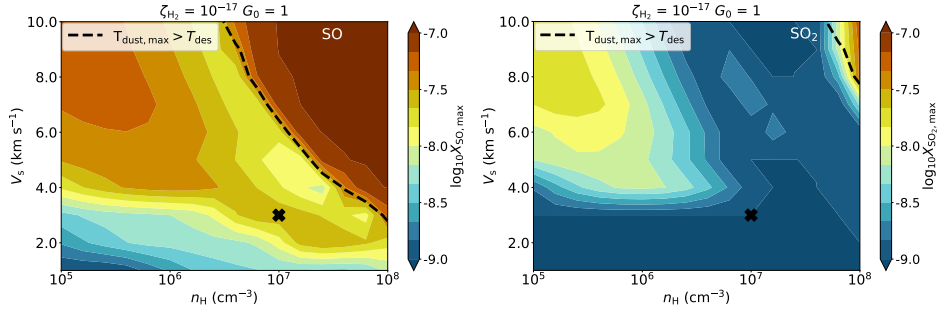


Figure 5.4: Maximum abundance reached (in color) of SO (left) and SO₂ (right) in shock models as function of initial n_{H} and V_{s} . All other physical parameters are kept constant to the fiducial values and listed on top of the figure. The black cross indicates the position of the fiducial model. The dashed black line shows the ice line, i.e., where 50% of the ice is thermally desorbed into the gas in the shock.

5.3.2 Chemistry of SO and SO₂

The abundance profiles of SO and SO₂ in the fiducial model are presented in the right part of Fig. 5.2. Toward the end of the shock, as the gas and dust are cooling down, a significant increase in the abundances of SO is visible up to the $\sim 5 \times 10^{-8}$ level. The abundance of SO₂ does not increase above the dark cloud abundance of 10^{-9} (van der Tak et al. 2003). The maximum abundance reached in the shock for SO and SO₂ as function of different initial n_{H} and V_{s} is presented in Fig. 5.4. In the following subsections different parts of the parameter space are highlighted using the relevant chemical formation pathways in Fig. 5.5.

Low-velocity shocks: $\sim 3 \text{ km s}^{-1}$

In low-velocity ($\sim 3 \text{ km s}^{-1}$) shocks, thermal desorption of SO and SO₂ ice does not occur since T_{dust} only rises to $\lesssim 35 \text{ K}$. Any increase in abundance thus originates from gas-phase chemistry. Here, the relevant chemical reaction leading to the formation of SO is,



The main formation pathway here of SH is via the green route of Fig. 5.5, that is, through the reaction of H₂CO with S⁺. Since H₂CO only desorbs directly from the ice when $T_{\text{dust}} \gtrsim 65 \text{ K}$, H₂CO is formed through the gas-phase reaction of the CH₃ radical with atomic O. To get a significant amount of CH₃ in the gas, CH₄ ice needs to desorb (at $T_{\text{dust}} \gtrsim 25 \text{ K}$; Penteado et al. 2017) and subsequently photodissociate into CH₃ and atomic H. The S⁺ ion originates from the photoionization of atomic S. The strongest increase in abundance through this route is at intermediate densities ($n_{\text{H}} \sim 10^7 \text{ cm}^{-3}$). It is important to note that H₂CO is a representative here of any hydrocarbon reacting with S⁺ to form SH.

Some SO₂ is also formed in low-velocity shocks through a reaction of SO with OH (see Reaction (5.4)). However, the abundance of SO₂ does not increase above

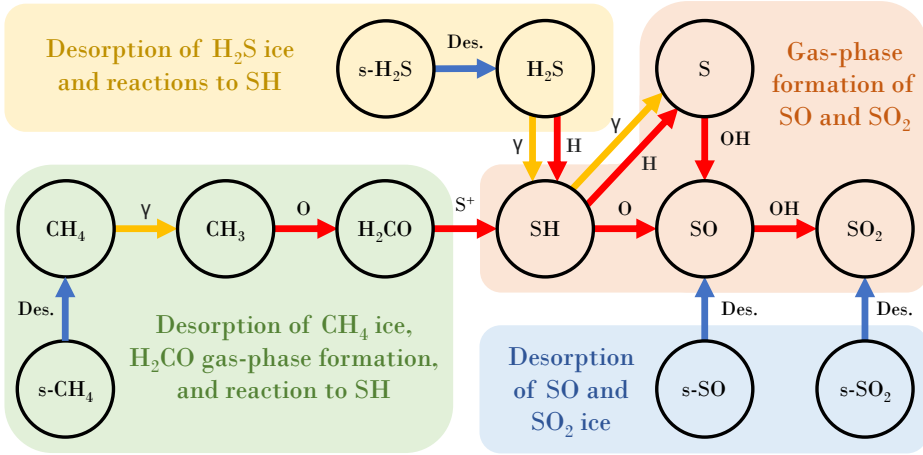
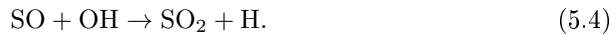


Figure 5.5: Chemical reactions leading to the formation of gas-phase SO and SO₂. Species denoted as s-X are located in the ice mantles of dust grains. Reverse reactions are not shown for clarity. Red arrows denote chemical reactions with the annotated species, yellow arrows photodissociation reactions, and blue arrows ice desorption via either thermal or nonthermal mechanisms. Relevant chemical pathways are highlighted with a colored background.

the initial dark cloud abundance of 10^{-9} because no significant amount of OH is available at these shock velocities.

High-velocity shocks: $> 4 \text{ km s}^{-1}$

For shocks propagating at higher velocities ($\gtrsim 4 \text{ km s}^{-1}$), both SO and SO₂ are efficiently formed through gas-phase chemistry, see Fig. 5.4. After the start of the shock, H₂O is readily formed through reactions of OH with H₂ (Flower & Pineau des Forêts 2010, see also Fig. 5.D.1). As the shock cools down to below $\lesssim 300 \text{ K}$, the production of H₂O stops, but OH is still being formed through photodissociation of H₂O. This increases the OH abundance in the gas which stimulates the formation of SO and SO₂ through the red route of Fig. 5.5,



The highest abundances are achieved in less dense environments ($\lesssim 10^6 \text{ cm}^{-3}$), with the maximum abundance of both SO and SO₂ dropping when moving toward intermediate densities ($\sim 10^6 - 10^7 \text{ cm}^{-3}$). In the latter conditions, NH₃ becomes a dominant coolant in the tail of the shock. Therefore, the shock cools down more quickly and hence the region of favorable conditions for SO and SO₂ formation ($100 \lesssim T_{\text{gas}} \lesssim 300 \text{ K}$) is reduced and their maximum abundances are lower.

At the highest densities ($n_{\text{H}} > 10^7 \text{ cm}^{-3}$), thermal desorption of sulfur-bearing ices becomes relevant for the chemistry (i.e., the blue route in Fig. 5.5). Thermal

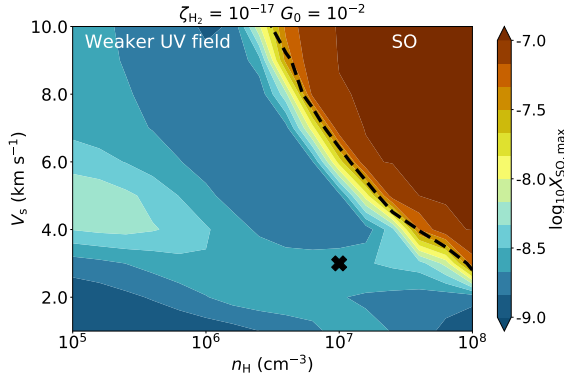


Figure 5.6: Similar figure as Fig. 5.4, but now for SO in shocks with a weaker UV field ($G_0 = 10^{-2}$).

sublimation of SO ice occurs as the dust temperature reaches ~ 37 K, leading to a strong increase in its gas-phase abundance (see Fig. 5.4). Thermal desorption of SO_2 only happens in the highest velocity shocks in the densest media. However, desorption of H_2S ice (at $T_{\text{dust}} \sim 47$ K) is also relevant for the gas-phase chemistry as subsequent photodissociation and reactions with atomic H lead to an increased abundance of SH and atomic S (i.e., the yellow route of Fig. 5.5).

Dependence on UV radiation field

As shown in Reactions (5.2)-(5.4) and Fig. 5.5, gas-phase formation of SO and SO_2 is dependent on radicals such as OH and SH. These radicals can be created in various ways, including high-temperature chemical reactions (Prasad & Huntress 1980; Hartquist et al. 1980). However, a more dominant physical process for enhancing the abundance of OH and SH is the photodissociation of H_2O , H_2S , and interestingly also CH_4 . This process is dependent on the strength of the local UV radiation field, which is parametrized here with G_0 .

In Fig. 5.6, the maximum abundance of SO as function of V_s and n_{H} is presented for $G_0 = 10^{-2}$. Similar figures of both SO and SO_2 for various G_0 are presented in Appendix 5.D.2. Decreasing the strength of the UV field decreases the amount of SO and SO_2 produced in high-velocity ($\gtrsim 4$ km s $^{-1}$) shocks due to less OH being produced through H_2O photodissociation. On the other end, increasing G_0 shifts the spot for efficient SO and SO_2 formation in the shock to higher densities to create the favorable conditions for their chemistry. Moreover, for $G_0 \gtrsim 10$, photodissociation of thermally desorbed H_2S (i.e., when $n_{\text{H}} \gtrsim 10^7$ cm $^{-3}$ and $V_s \gtrsim 4$ km s $^{-1}$) significantly increases the abundance of atomic S (i.e., yellow route of Fig. 5.5) which leads to an increase in abundances of SO and in particular SO_2 (see Fig. 5.D.3).

At lower shock velocities ($V_s \lesssim 4$ km s $^{-1}$), water is not formed in the shock and hence photodissociation of H_2O does not increase the abundance of SO and SO_2 . The increase in the SO abundance is here due to the green route of Fig. 5.5, which is initialized by thermal desorption and subsequent photodissociation of CH_4 . This formation route is most relevant for $G_0 = 1$; for lower G_0 , the UV radiation field is not strong enough to photodissociate significant amounts of CH_4 . For higher G_0 ,

Table 5.2: Input abundances of key Sulfur-bearing species

Case	S	SO	SO ₂	s-SO	s-SO ₂	s-H ₂ S
Fiducial	1(-6)	1(-9)	1(-9)	1(-7)	1(-7)	2(-5)
Low-S	1(-8)	1(-9)	1(-9)	1(-7)	1(-7)	2(-5)
High-S	2(-5)	1(-9)	1(-9)	1(-7)	1(-7)	1(-7)

Notes. a(b) represents $a \times 10^b$. Species denoted as s-X are located in the ice mantles of dust grains. All other abundances are the same as those presented in Appendix 5.B.

higher densities are required for the efficient production of SO through the green route.

Dependence on initial conditions

The abundances of all species reached in the shock, including SO and SO₂, are dependent on the initial abundances. The interstellar ice abundances of SO and SO₂ are not well known, with only a tentative detection for SO₂ (Boogert et al. 1997; Zasowski et al. 2009). Here, the ice abundances of SO and SO₂ are estimated at the 10^{-7} level based on what is found in cometary ices (Calmonte et al. 2016; Rubin et al. 2019; Altwegg et al. 2019). However, they are only relevant in the shocks where thermal desorption of these ices occurs (i.e., the blue route of Fig. 5.5 and to the right of the dashed line in Fig. 5.7). For those shocks, increasing or decreasing the ice abundances with an order of magnitude will also result in an increase or decrease in the gas-phase abundances with an order of magnitude, given that the ice abundance is dominant over what is achieved through gas-phase chemistry alone.

For shocks where the abundance of SO and SO₂ is mainly increased through gas-phase chemistry (i.e., to the left of the dashed line in Fig. 5.7), the maximum abundance reached is mostly directly dependent on the initial abundance of atomic sulfur. To test the effect of initial atomic S abundance on the maximum abundances of SO and SO₂, shock models are calculated for a lower gas-phase atomic sulfur abundance (Low-S: $X_S = 10^{-8}$) and assuming that almost all sulfur is atomic and in the gas phase (High-S: $X_S = 2 \times 10^{-5}$). The initial abundances for these cases are presented in Table 5.2. The resulting maximum SO and SO₂ abundances for these models are shown in Fig. 5.7.

In the Low-S case, the maximum abundance of SO drops for both low and high velocity shocks (excluding higher densities where the abundance is increased through thermal ice sublimation). This is straightforward to interpret since both S and S⁺ are main formation precursors of SO in both the red and green formation routes of Fig. 5.5, respectively. At lower densities ($\lesssim 10^6 \text{ cm}^{-3}$), the maximum SO₂ abundance drops in a similar way since less SO is formed. However, at intermediate densities ($\sim 10^7 \text{ cm}^{-3}$), slightly more SO₂ is formed in high velocity shocks compared to Fig. 5.4. This is because atomic S and SO are "competing" to react with OH to form respectively SO and SO₂. Dropping the initial atomic S abundance results in more SO₂ being formed, also because the majority of the

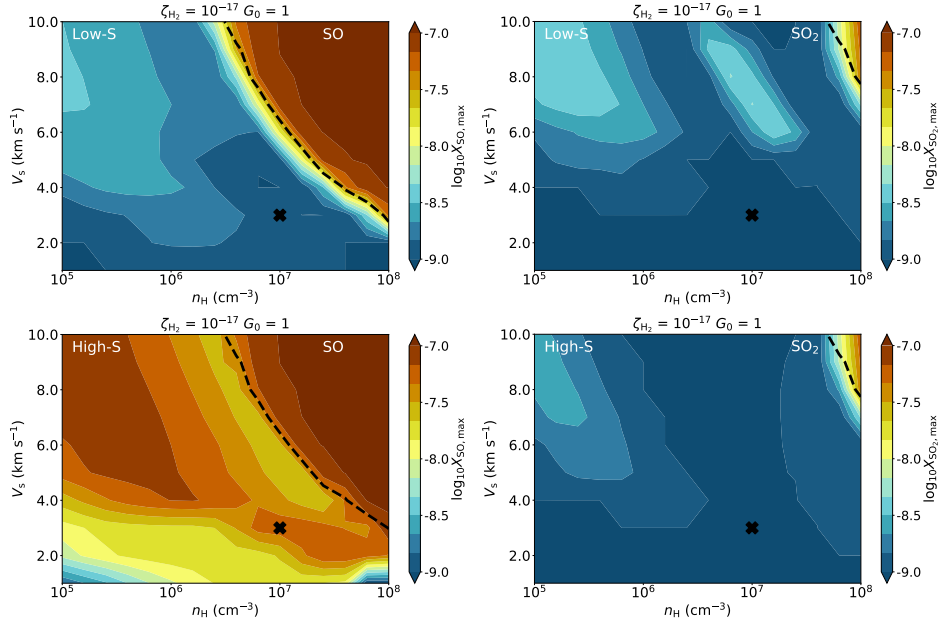


Figure 5.7: Maximum abundance reached (in color) of SO (left) and SO₂ (right) in shock models as function of initial n_{H} and V_{s} for an initial gas-phase atomic S abundance of 10^{-8} (top row) and 10^{-5} (bottom row). All other physical parameters are kept constant to the fiducial values and listed on top of the figure. The black cross indicates the position of the fiducial model. The dashed black line shows the ice line, i.e., where 50% of the ice is thermally desorbed into the gas in the shock.

gas-phase SO here originates from thermal ice sublimation.

In the High-S case, not only the chemistry but also the thermal structure of the shock is slightly altered since cooling through atomic S becomes significant. Furthermore, more SO is formed through both the red and green routes of Fig. 5.5. Interestingly, the maximum abundance of SO₂ attained decreases compared to Fig. 5.4 since with more atomic S in the gas phase to react with OH, less OH is available to react with SO toward SO₂.

The initial abundances of other species are also important for the chemistry of SO and SO₂. Increasing or decreasing the amount of atomic oxygen results in respectively more or less OH and H₂O formed in the shock and thus directly affects the abundances of SO and SO₂. Moreover, reactions with atomic carbon are a main destruction pathway for SO (forming CS; Hartquist et al. 1980). Hence an increased initial atomic carbon abundance results in lower abundances of both SO and SO₂ in the shock.

In reality, the initial dark cloud abundances may also be altered during the infall from the envelope toward the disk since both the temperature and the strength of the UV radiation field increase (e.g., Aikawa et al. 1999; Visser et al. 2009; Drozdovskaya et al. 2015). To take this into account, a preshock model should be

calculated. In Appendix 5.C, the effect of calculating such a preshock model on the abundance of SO attained in the shock is presented. Any alterations on the preshock conditions are only important for the chemistry of SO and SO₂ if the timescale over which the preshock is calculated is longer than about 10% of the photodesorption timescale. For typical infalling envelopes, this is not expected to be relevant.

5.3.3 Effect of grain size and PAHs

The size of the dust grains has an effect on both the physical structure of the shock and on the chemistry (e.g., Guillet et al. 2007; Miura et al. 2017). In Fig. 5.8, the abundance profiles of SO and SO₂ are shown for the fiducial model and for the same model while adopting a typical ISM grain size distribution (computed using a single size of $\sim 0.03 \mu\text{m}$; Mathis et al. 1977; Godard et al. 2019). The decrease in grain size leads to stronger coupling between gas and dust and thus to a slightly higher dust temperature ($\sim 35 \text{ K}$ against $\sim 30 \text{ K}$ for $0.2 \mu\text{m}$ grains). Moreover, the increased gas-grain coupling results in the dust being a dominant coolant in the tail of the shock, reducing the length of the shock ($\sim 1 \text{ AU}$ against $\sim 3 \text{ AU}$ for the fiducial model). Nevertheless, the abundance of SO is increased in the shock but the maximum abundance reached is about a factor of 2–3 lower compared to the fiducial model. No significant increase is seen for SO₂. Miura et al. (2017) found that the dust temperature easily reaches $\sim 50 \text{ K}$ in low-velocity shocks taking into account dust aerodynamics for ISM-size dust grains. The full treatment of dust physics, including aerodynamic heating and grain-grain interactions (Guillet et al. 2007, 2009, 2011, 2020; Miura et al. 2017), will likely move the ice line of Fig. 5.4 toward lower n_{H} and V_{s} . However, this is beyond the scope of this work.

Contrary to dust grains, the effect of PAHs on the physical structure of *J*-type shocks is negligible since PAHs do not contribute to the cooling and only little to the heating if a strong UV field is present. However, PAHs do play a key role in the ionization balance and are therefore highly relevant for the chemistry (Flower & Pineau des Forêts 2003). In Fig. 5.8, the abundances of SO and SO₂ are also shown for the fiducial model with a PAH abundance of 10^{-6} (equal to the value derived in the local diffuse ISM; Draine & Li 2007). The maximum abundance of SO is a factor 3–4 lower when the abundance of PAHs is at the ISM level because the PAHs are dominating the ionization balance. Consequently, the abundance of other ions, include S⁺, drops by more than an order of magnitude. Given that the green route of Fig. 5.5 is the dominant SO formation route here and dependent on S⁺, less SO and subsequently SO₂ are formed. For high-velocity shocks, this effect is not apparent since Reactions (5.3) and (5.4) dominate the formation of SO and SO₂ and are independent of ions.

5.3.4 Other molecular shock tracers: SiO, H₂O, H₂S, CH₃OH, and H₂

Other classical molecular shock tracers include SiO, H₂O, H₂S, CH₃OH, and H₂. Abundance maps similar to Fig. 5.4 of SiO, H₂O, H₂S, and CH₃OH are presented

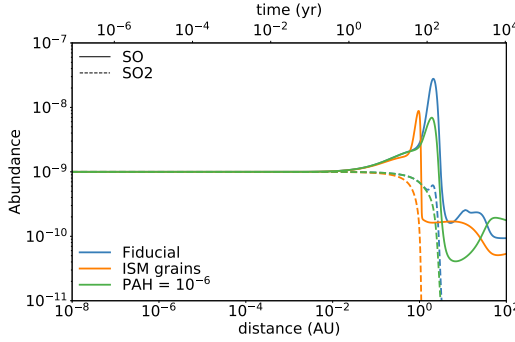


Figure 5.8: Abundance profile of SO (solid) and SO₂ (dashed) for the fiducial model (blue) with a PAH abundance of 10^{-8} using a grain size of $0.2 \mu\text{m}$. Overplotted are the same model using a typical ISM grain size of $0.03 \mu\text{m}$ (orange) and a model with a PAH abundance of 10^{-6} (green). All other parameters are kept at their fiducial value (see Table 5.1).

in Appendix 5.D.1. SiO is a tracer of shocks with significant grain destruction since then the silicon which is normally locked in dust grains can react with the OH radical to form SiO (e.g., Caselli et al. 1997; Schilke et al. 1997; Gusdorf et al. 2008a,b; Guillet et al. 2009). It is often observed in the high velocity bullets of jets originating from young Class 0 protostars (e.g., Guilloteau et al. 1992; Tychoniec et al. 2019; Taquet et al. 2020). However, the abundance of SiO is not significantly increased in our shock models because most of the Si remains locked up in silicates in the dust grains.

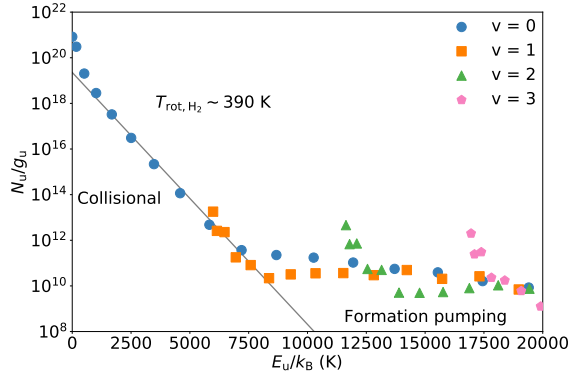
Water is the most abundant ice in protostellar envelopes (Boogert et al. 2015; van Dishoeck et al. 2021), but also frequently observed in outflow shocks (e.g., Flower & Pineau des Forêts 2010; Herczeg et al. 2012; Kristensen et al. 2012; Nisini et al. 2013; Karska et al. 2018). Here, H₂O is efficiently produced in shocks with $V_s \gtrsim 4 \text{ km s}^{-1}$ (see Fig. 5.D.1) and very important for the gas-phase chemistry of SO and SO₂. Thermal desorption of H₂O is negligible.

The main sulfur carrier in ices is suggested to be H₂S (e.g., Vidal et al. 2017), despite it being undetected thus far (Jiménez-Escobar & Muñoz Caro 2011). In the gas phase, it is generally observed close to Class 0 protostars where the emission may originate from thermal desorption (Tychoniec et al. 2021), or in outflow shocks (e.g., Holdship et al. 2016). In our shock models, gas-phase formation of H₂S becomes efficient at slightly higher velocities than for water ($V_s \gtrsim 5 \text{ km s}^{-1}$, see Fig. 5.D.1). Moreover, for high-velocity shocks in dense media, H₂S ice is thermally sublimated.

Methanol is a tracer of lower-velocity ($< 10 \text{ km s}^{-1}$) outflow shocks where ices are sputtered off the dust grains (e.g., Suutarinen et al. 2014). However, since sputtering is not relevant in our single-fluid *J*-type accretion shock models, no significant increase in the CH₃OH abundance is evident except at the highest densities ($\gtrsim 10^8 \text{ cm}^{-3}$) and velocities ($\gtrsim 10 \text{ km s}^{-1}$) where CH₃OH ice thermally sublimates.

Emission from warm H₂ is generally observed toward shocks in protostellar jets (e.g., McCaughrean et al. 1994). Contrary to the molecules discussed above, the abundance of H₂ remains constant along the shock and only thermal excitation occurs. Hence, H₂ can be a powerful diagnostic of accretion shocks in inferring the temperature from a rotational diagram. The population of the lowest 50 rotational and rovibrational levels of H₂ are computed during the shock (Flower & Pineau

Figure 5.9: Rotational diagram of H_2 created from the fiducial shock model. The levels of different vibrational states are indicated with different symbols and colors. Only the pure rotational levels with $E_u/k_B \lesssim 6000$ K are collisionally populated. The fit to the pure rotational levels is shown in gray line with the derived rotational temperature annotated.



des Forêts 2003). The rotational diagram of H_2 for the fiducial model is presented in Fig. 5.9. Since the temperature in this shock reaches about ~ 500 K, levels up to ~ 6000 K are collisionally populated. The population of all higher- E_{up} levels is set during the formation of H_2 on the dust grains following a Boltzmann distribution at 17248 K (1/3 of the dissociation energy of H_2 ; Black & van Dishoeck 1987). Using the rotational diagram of Fig. 5.9, a rotational temperature ~ 390 K is derived for this shock.

5.4 Discussion

5.4.1 Comparison to SO and SO_2 with ALMA

Emission of warm ($T_{\text{ex}} > 50$ K) SO and SO_2 around the disk-envelope interface has been suggested as a possible tracer of accretion shocks (Sakai et al. 2014, 2017; Bjerkeli et al. 2019; Oya et al. 2019; Artur de la Villarmois et al. 2019). Here, we have shown that the abundance of both SO and SO_2 can increase in shocks in typical inner envelope conditions. The abundance of SO is estimated to be $\sim 10^{-8}$ in the suggested accretion shock around the L1527 Class 0/I protostar (Sakai et al. 2014), but this is uncertain since the density of H_2 was guessed. Furthermore, by itself this does not provide strong constraints on the physical conditions of the shock (see Fig. 5.4), other than that a weak UV field should be present if SO ice is not thermally sublimated ($G_0 > 10^{-2}$; Fig. 5.D.2). However, it remains difficult to derive abundances with respect to n_{H} from observations.

Recent ALMA observations show that the amount of warm SO_2 seems to increase with the bolometric luminosity (i.e., stronger UV field; Artur de la Villarmois et al. 2019). This is in line with our results since the abundance of SO_2 only increases when a significant UV field is present (i.e., $G_0 \gtrsim 1$, see Fig. 5.D.3). Especially for higher velocity shocks (> 4 km s^{-1}) at higher densities ($> 10^7$ cm $^{-3}$) the maximum abundance of SO_2 increases with 2 orders of magnitude between $G_0 = 1$ and $G_0 = 100$. However, besides a significant UV field, a shock velocity of $V_s \gtrsim 4$ km s^{-1} is necessary to increase the abundance of SO_2 and the maximum abundance reached in the shock is also dependent on the initial density n_{H} .

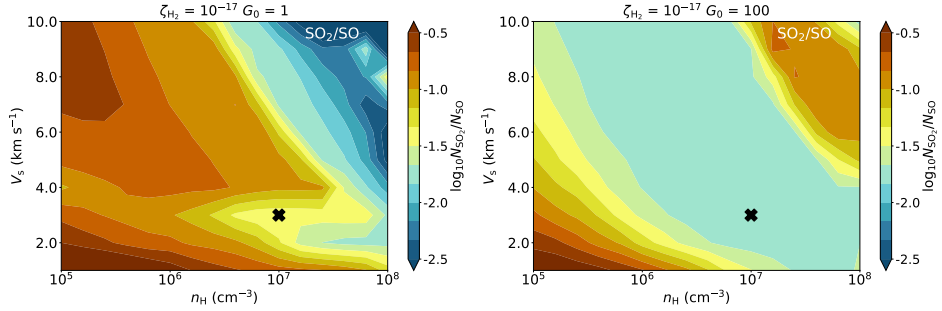


Figure 5.10: Ratio of column densities of SO₂ and SO as function of n_{H} and V_s for $G_0 = 1$ (left) and $G_0 = 100$ (right). All other physical parameters are kept constant to the fiducial values and listed on top of the figure. The black cross indicates the position of the fiducial model.

Comparing the ratio of observed column densities to those derived from our shock models can more accurately constrain the physical conditions in a shock. In Fig. 5.10, the column density ratio of SO₂/SO in the shock is presented as function of V_s and n_{H} for $G_0 = 1$ and $G_0 = 100$. The only protostellar source where both SO and SO₂ have been detected related to a possible accretion shock is Elias 29 (Oya et al. 2019), where a column density ratio of $0.5^{+0.4}_{-0.2}$ is derived. When $G_0 = 1$, this would imply a low-density shock ($< 10^6$ cm $^{-3}$) propagating at either low (< 2 km s $^{-1}$) or high (> 7 km s $^{-1}$) velocities, see upper panel in Fig. 5.10. For $G_0 = 100$, shocks propagating at higher velocities (> 4 km s $^{-1}$) at high densities ($> 10^7$ cm $^{-3}$) produce SO₂/SO column density ratios similar to that of Elias 29 (Oya et al. 2019, see lower panel in Fig. 5.10).

Since both SO and SO₂ emission is also linked to outflow activity and passive heating in the inner envelope (Codella et al. 2014; Tabone et al. 2017; Lee et al. 2018; Taquet et al. 2020; Harsono et al. 2021), high spatial resolution observations with ALMA are necessary to both spatially and spectrally disentangle the different protostellar components and determine their emitting area. Moreover, to robustly test if the SO and SO₂ emission traces the accretion shock, key species for their gas-phase formation such as H₂S and H₂CO should be observed on similar scales. This also allows for more accurately constraining the physical conditions of a shock.

5.4.2 Predicting H₂, H₂O, and [S I] with JWST

With the launch of JWST, near-infrared (NIR) and MIR shock tracers such as H₂, H₂O, and [S I] can be used to search for accretion shocks. Although the abundance of H₂ does not increase in accretion shocks, it is still thermally excited and therefore a good shock tracer at NIR and MIR wavelengths (e.g., McCaughrean et al. 1994). Observing the rotational sequence of H₂ in the NIR and MIR could thus put constraints on the physical properties of the shock. For low-velocity shocks ($\lesssim 5$ km s $^{-1}$), most of the strong H₂ transitions (i.e., 0-0 S(3) and 0-0 S(5)) are located in the JWST/MIRI range (5 – 28 μ m). For higher velocity shocks ($\gtrsim 5$ km s $^{-1}$),

also vibrational levels of H_2 get populated and the strongest H_2 transitions shift toward the NIRSpec range of JWST ($1 - 5 \mu\text{m}$).

Warm water is also a well-known and important tracer of shocks (e.g., Herczeg et al. 2012; Kristensen et al. 2012; Nisini et al. 2013; van Dishoeck et al. 2021). Observing H_2O toward an accretion shock is a clear indication of a high-velocity shock ($\gtrsim 4 \text{ km s}^{-1}$, see Fig. 5.D.1). Warm water should be easily detectable with JWST as both the vibrational band around $6 \mu\text{m}$ and several pure rotational transitions at $> 10 \mu\text{m}$ fall within the MIRI range ($5 - 28 \mu\text{m}$). Moreover, the detection of MIR lines of the OH radical can be an indication of H_2O photodissociation (Tabone et al. 2021) and therefore be spatially colocated with emission of warm SO and SO_2 in ALMA observations.

An alternative shock tracer in the JWST/MIRI band is the [S I] $25 \mu\text{m}$ transition. It is often observed in protostellar outflows (e.g., Neufeld et al. 2009; Lahuis et al. 2010; Goicoechea et al. 2012), where the intensity of the line can range from a few % of the H_2 0-0 S(3) and 0-0 S(5) lines to a factor of a few higher. It is therefore uncertain whether [S I] $25 \mu\text{m}$ will be detectable toward accretion shocks, also given that the sensitivity of MIRI drops at the highest wavelengths. Moreover, at $25 \mu\text{m}$, the angular resolution of JWST is $\sim 1''$ (i.e., 300 AU at a distance of 300 pc) which complicates the spatial disentanglement of an accretion shock with outflow emission.

5.5 Summary

We have modeled low-velocity ($\leq 10 \text{ km s}^{-1}$) nonmagnetized J -type shocks at typical inner envelope densities ($10^5 - 10^8 \text{ cm}^{-3}$) using the Paris-Durham shock code to test SO and SO_2 as possible molecular tracers of accretion shocks. The main conclusions of this work are as follows:

- In low-velocity ($\sim 3 \text{ km s}^{-1}$) shocks, SO can be efficiently formed at intermediate densities ($\sim 10^7 \text{ cm}^{-3}$) through the SH radical reacting with atomic O. Here, SH is formed through S^+ reacting primarily with H_2CO ; though the latter species is a representative of any hydrocarbon.
- Both SO and SO_2 can be efficiently formed through reactions of atomic S with OH in high-velocity ($\gtrsim 4 \text{ km s}^{-1}$) shocks in low-intermediate dense environments ($\lesssim 10^7 \text{ cm}^{-3}$). The formation of SO and SO_2 occurs in the end of the shock, where the abundance of OH is enhanced through photodissociation of earlier formed H_2O .
- Thermal desorption of SO ice can occur in high-velocity ($\gtrsim 4 \text{ km s}^{-1}$) shocks at high densities ($\gtrsim 10^7 \text{ cm}^{-3}$), while thermal desorption of SO_2 ice is only relevant at the highest shock velocities ($\gtrsim 10 \text{ km s}^{-1}$) and highest densities ($\gtrsim 10^8 \text{ cm}^{-3}$).
- The chemistry of both SO and SO_2 through all formation routes is strongly linked to the strength of the local UV radiation field since the formation of both the OH and SH radicals is dependent on photon processes such as

photodissociation and photoionization. In particular, SO_2 is only formed in the shock through gas-phase chemistry if the strength of the local UV radiation field is greater or equal to the ISRF.

- The composition of infalling material, in both gas-phase species such as atomic O and S and in the ices such as H_2S , CH_4 , SO, and SO_2 , is highly relevant for the chemistry of SO and SO_2 in accretion shocks.
- Observations of warm SO and SO_2 should be complemented with key species for their formation such as H_2S and H_2CO . Moreover, the launch of JWST will add additional NIR and MIR accretion shock tracers such as H_2 , H_2O , and [S I] $25\ \mu\text{m}$.

Our results highlight the key interplay between both physics and chemistry in accretion shocks. The abundances of gas-phase molecules such as SO and SO_2 is not solely determined through high-temperature gas-phase chemistry, but also thermal sublimation of ices and photodissociation through UV radiation play an important role. Additional high-angular resolution observations with ALMA are necessary to spatially disentangle the disk from the envelope in embedded systems in order to assess the physical properties of accretion shocks at the disk-envelope interface. Moreover, future facilities such as JWST will provide additional NIR and MIR shock tracers such as H_2 , OH, and H_2O . It is crucial to attain the physical structure of accretion shocks since it determines the chemical composition of material that enters the disk and is eventually incorporated in planets.

Acknowledgments

The authors would like to thank the anonymous referee for their constructive comments on the manuscript. The authors would also like to thank G. Pineau des Forêts for valuable discussions about the project. Astrochemistry in Leiden is supported by the Netherlands Research School for Astronomy (NOVA). MvG and BT acknowledge support from the Dutch Research Council (NWO) with project number NWO TOP-1 614.001.751.

Appendix

5.A Updated cooling of NH₃

Typically, cooling by NH₃ in the optically thin limit is calculated using the empirical relation derived by Le Bourlot et al. (2002). However, this relation does not take into account that the populations get thermalized if the density gets above the critical density. Therefore, the cooling by NH₃ is recalculated using the RADEX software (van der Tak et al. 2007). Assuming all emission is optically thin (i.e., low column densities) and emitted through rotational lines, a grid of gas temperatures and H₂ densities is set. The full range explored is 5–5000 K and 10²–10¹² cm⁻³, respectively. The linewidth is set to 2 km s⁻¹. The cooling (in erg s⁻¹) for each grid point is calculated by summing over the emission of each spectral line and dividing that by the assumed column density.

Using the cooling grid computed with RADEX, a cooling function, Λ , with T_{gas} and n_{H_2} as free parameters can be derived. Minimum χ^2 fitting of the grid computed with RADEX was used to calculate Λ , which resulted in,

$$\Lambda_{\text{NH}_3} = \Lambda_{\infty} \left(1 - \exp \left[\frac{-n_{\text{H}_2}}{n_0} \right] \right), \quad (5.5)$$

with Λ_{∞} and n_0 numerically derived as,

$$\Lambda_{\infty} = 2.85 \times 10^{-15} \left(1 - \exp \left[\frac{-T_{\text{gas}}}{81.7} \right] \right)^4, \quad (5.6)$$

$$n_0 = 8.33 \times 10^8 \left(1 - \exp \left[\frac{-T_{\text{gas}}}{125} \right] \right). \quad (5.7)$$

Here, Λ_{∞} is the cooling of NH₃ in the LTE limit, whereas n_0 is a measure of a critical density above which LTE effects become relevant. Both parameters are dependent on T_{gas} .

The function in Eq. (5.5) is presented in Fig. 5.A.1 for a few values of T_{gas} . Overplotted are the RADEX calculations and the empirical relation of Le Bourlot et al. (2002). Indeed, at high densities ($\gtrsim 10^9$ cm⁻³) the latter relation starts overproducing the cooling computed with RADEX by orders of magnitude. However, the updated cooling function represent the cooling by RADEX within a factor of three over the entire temperature and density range. Since densities of $\gtrsim 10^9$ cm⁻³ are frequently reached in our shock models, the updated cooling function was adopted in the updated version of the shock code.

In high-temperature shocks, significant amounts of NH₃ might be produced through gas-phase chemistry, enhancing the density and thus the optical depth of the spectral lines. Moreover, the density of NH₃ can be increased through ice sublimation in high-density shocks. If the lines of NH₃ become optically thick, Eq. 5.5 is no longer valid and cooling tables similar to those of Neufeld & Kaufman (1993) should be calculated for NH₃ taking into account opacity effects. This is beyond the scope of this work.

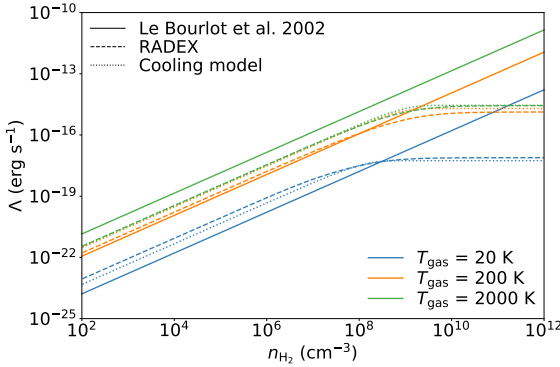


Figure 5.A.1: Cooling by NH_3 as function of n_{H_2} for various T_{gas} (colors). The empirical relation by Le Bourlot et al. (2002) is shown as the solid lines, the RADEX computations in the dashed line, and the derived cooling function of Eq. (5.A) in the dotted line.

5.B Input abundances

The input abundances used in the shock models are presented in Table 5.B.1. The total elemental abundances match those of Flower & Pineau des Forêts (2003). Most of the oxygen, carbon, and sulfur budget is locked up in dust grains and in the ice mantles. The initial abundances of oxygen and nitrogen-bearing ices are equivalent to those presented by Boogert et al. (2015), while the sulfur-bearing ice abundances are matched to those found in both protostellar envelopes and comets (Calmonte et al. 2016; Rubin et al. 2019; Altwegg et al. 2019; Navarro-Almaida et al. 2020). The gas-phase abundances of the key sulfur-bearing molecules, SO , SO_2 , CS , OCS , and H_2S , are taken from van der Tak et al. (2003). All other molecular gas-phase abundances are set equal to those derived on cloud scales by Tafalla et al. (2021). The gas-phase abundance of atomic S in protostellar envelopes is highly uncertain. It is set here at a 10^{-6} level, which is consistent with the models of Goicoechea & Cuadrado (2021). The effect of initial atomic S abundance on the maximum abundances of SO and SO_2 attained in the shock is presented in Sect. 5.3.2.

5.C Changing the preshock conditions

To test the effect of alteration of infalling dark cloud material in the inner envelope on an accretion shock, various preshock models were calculated. Since the increase in the temperature and protostellar radiation field are negligible in the outer parts of the envelope (e.g., Drozdovskaya et al. 2015), changes in temperature, composition, and ionization balance are most efficient in the inner ~ 1000 AU of the envelope when the material is already approaching the disk and protostar. Given that the infall velocity goes as $v(r) = \sqrt{2GM/r}$, it takes about ~ 100 years to move from 1000 AU to disk scales (~ 100 AU) for a $0.5 M_{\odot}$ star. However, depending on the mass of the protostar and the size of the disk, this preshock timescale t_{preshock} might range from, for example, $\sim 10 - 10^4$ years. Therefore, the effect of infall time (i.e., t_{preshock}) on the accretion shock is explored here. The thermal balance is included in the preshock model, but for simplicity the density

Table 5.B.1: Dark cloud input abundances

H	5.0×10^{-5}	Grains	4.6×10^{-11}
H ₂	5.0×10^{-1}	s-H ₂ O	1.0×10^{-4}
He	1.0×10^{-1}	s-O ₂	1.0×10^{-8}
C	1.0×10^{-8}	s-CO	8.3×10^{-6}
O	1.0×10^{-6}	s-CO ₂	1.3×10^{-5}
CO	8.5×10^{-5}	s-CH ₄	1.5×10^{-6}
C ₂ H	2.0×10^{-9}	s-N ₂	3.9×10^{-6}
C ₃ H ₂	2.0×10^{-10}	s-NH ₃	1.0×10^{-6}
CH ₃ OH	1.5×10^{-9}	s-CH ₃ OH	1.9×10^{-5}
N	1.0×10^{-6}	s-H ₂ CO	6.2×10^{-6}
CN	1.5×10^{-9}	s-HCO ₂ H	7.2×10^{-6}
HCN	3.0×10^{-9}	s-OCS	2.1×10^{-7}
HNC	1.0×10^{-9}	s-H ₂ S	1.8×10^{-5}
N ₂	3.5×10^{-5}	s-SO	1.0×10^{-7}
S	1.0×10^{-6}	s-SO ₂	1.0×10^{-7}
H ₂ S	1.0×10^{-9}	c-O	1.4×10^{-4}
CS	3.0×10^{-9}	c-Si	3.4×10^{-5}
SO	1.0×10^{-9}	c-Mg	3.7×10^{-5}
SO ₂	1.0×10^{-9}	c-Fe	3.2×10^{-5}
OCS	2.0×10^{-9}	c-C	1.6×10^{-4}
Si	1.0×10^{-10}	HCO ⁺	1.5×10^{-9}
Fe	1.5×10^{-8}	N ₂ H ⁺	1.5×10^{-10}
PAH	1.0×10^{-8}		

Notes. Abundances are with respect to n_{H} . Species in ice mantles on dust grains are indicated as s-X. Species in composing the cores of dust grains are denoted as c-X.

is assumed to remain constant.

Given that the infalling material is ionized and photodissociated on a timescale of (Heays et al. 2017),

$$\tau_{\text{ionize/disso}} \sim \frac{10 - 100}{G_0} \text{ yrs}, \quad (5.8)$$

the ionization balance is fully altered for all $t_{\text{presock}} \gtrsim 10$ years if the strength of the local UV field is $G_0 \gtrsim 1$. For models with weaker UV fields ($G_0 = 10^{-3} - 10^{-1}$), the ionization balance is dependent on t_{presock} . Moreover, the ice composition may be altered on the photodesorption and adsorption timescales for $0.2 \mu\text{m}$ grains of (Hollenbach et al. 2009; Godard et al. 2019),

$$\tau_{\text{photodes}} \approx \frac{2 \times 10^5}{G_0} \text{ yrs}, \quad (5.9)$$

$$\tau_{\text{adsorb}} \approx \frac{10^9 - 10^{10}}{n_{\text{H}}} \text{ yrs}. \quad (5.10)$$

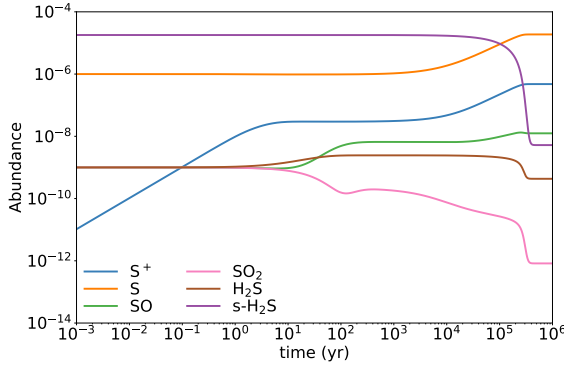


Figure 5.C.1: Abundances of S^+ , S, SO, SO_2 , H_2S , and s- H_2S during a preshock calculation. All physical parameters are kept constant to the fiducial values.

If $\tau_{\text{ionize/disso}} < \tau_{\text{adsorb}}$, any photodesorbed species are dissociated before they can adsorb back on the grain. This increases the abundance of atomic and ionic species.

The abundances of S^+ , S, SO, SO_2 , H_2S , and s- H_2S during a preshock calculation are presented in Fig. 5.C.1 for the fiducial model conditions (see Table 5.1). Following Eq. (5.8), the ionization balance of S^+/S is set after ~ 10 years. However, at longer timescales of $\sim 10^4 - 10^5$ years, the abundances of both S^+ and S increase above the initial abundance of atomic S. On these timescales, H_2S ice is photodesorbed (see Eq. (5.9)) and subsequently photodissociated, therefore enhancing the abundance of both atomic S and S^+ . Since the abundance of H_2S is much higher than that of atomic S in the gas phase, already on timescales of $0.1\tau_{\text{photodes}}$ the abundance of atomic S is increased with a factor of a few. Meanwhile, the abundance of SO is increased through gas-phase chemistry via Reaction (5.3), and SO_2 is photodissociated into SO and atomic O.

The effect of the length of the preshock model on the maximum abundances of SO in the subsequent accretion shock is presented in Fig. 5.C.2. Up to $t_{\text{preshock}} \lesssim 1000$ years, the maximum abundance reached in the shock is independent of the time over which the preshock model is calculated. In the $t_{\text{preshock}} = 10000$ years case, photodesorption and subsequent photodissociation of H_2S increases the initial atomic S abundance and hence the maximum abundance of SO reached in the shock. For different strengths of the UV radiation field (i.e., different G_0), the timescale for photodesorption changes (i.e., Eq. (5.9)). The effect of t_{preshock} on the final abundances of SO (and SO_2) in the shock is thus negligible if t_{preshock} is less than roughly $\sim 10\%$ of the photodesorption timescale τ_{photodes} , given that $\tau_{\text{adsorb}} > \tau_{\text{ionize/disso}}$.

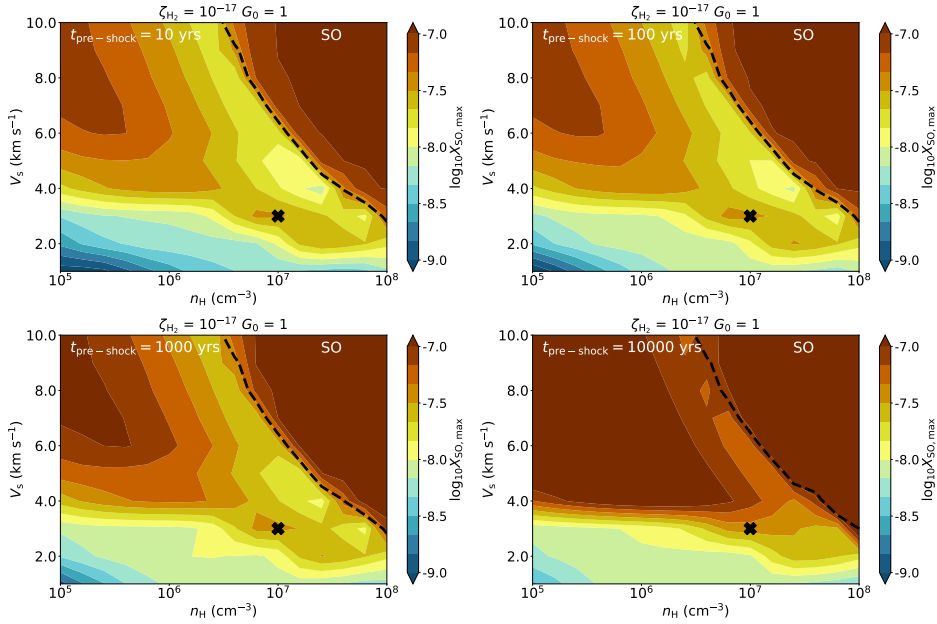


Figure 5.C.2: Maximum abundance reached (in color) of SO in shock models as function of initial n_{H} and V_s after calculating a preshock model for 10 (top left), 100 (top right), 1000 (bottom left), and 10000 (bottom right) years. All other physical parameters are kept constant to the fiducial values and listed on top of the figure. The black cross indicates the position of the fiducial model. The dashed black line shows the ice line, i.e., where 50% of the ice is thermally desorbed into the gas in the shock.

5.D Abundance grids

5.D.1 H_2S , H_2O , SiO , and CH_3OH for $G_0 = 1$

In Fig. 5.D.1, the maximum abundance for H_2S , H_2O , SiO , and CH_3OH are presented as function of initial n_{H} and V_s . All other parameters are set to their fiducial value (e.g., $G_0 = 1$).

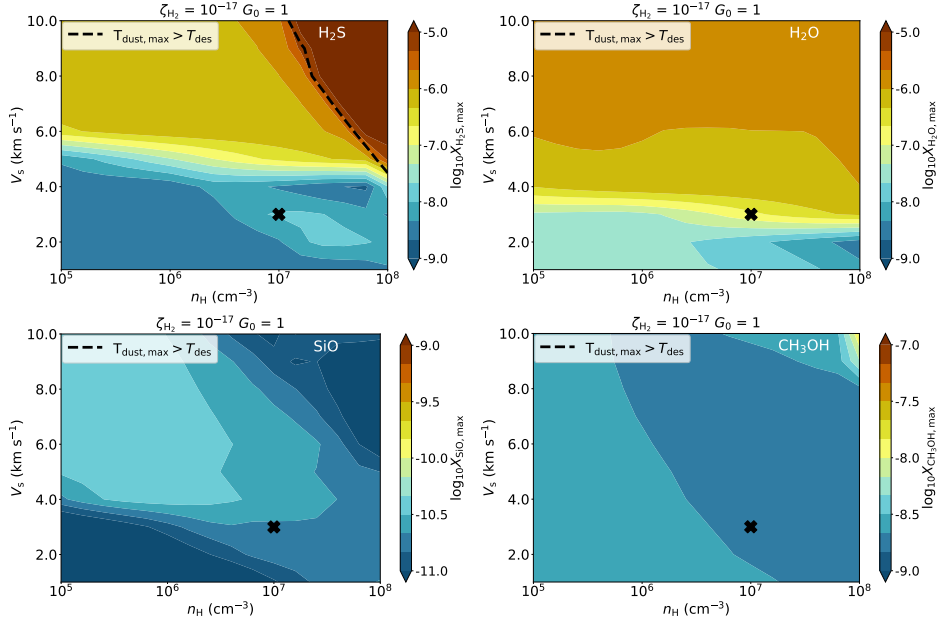


Figure 5.D.1: Similar figure as Fig. 5.4, but now for H_2S (top left), H_2O (top right), SiO (bottom left), and CH_3OH (bottom right). All other physical parameters are kept constant to the fiducial values and listed on top of the figure. The black cross indicates the position of the fiducial model. The dashed black line shows the ice line, i.e., where 50% of the ice is thermally desorbed into the gas in the shock.

5.D.2 SO and SO₂ for various G_0

In Figs. 5.D.2 and 5.D.3, the maximum abundance for respectively SO and SO₂ are presented as function of initial n_H and V_s for various strengths of the UV radiation field (i.e., $G_0 = 10^{-3} - 10^2$).

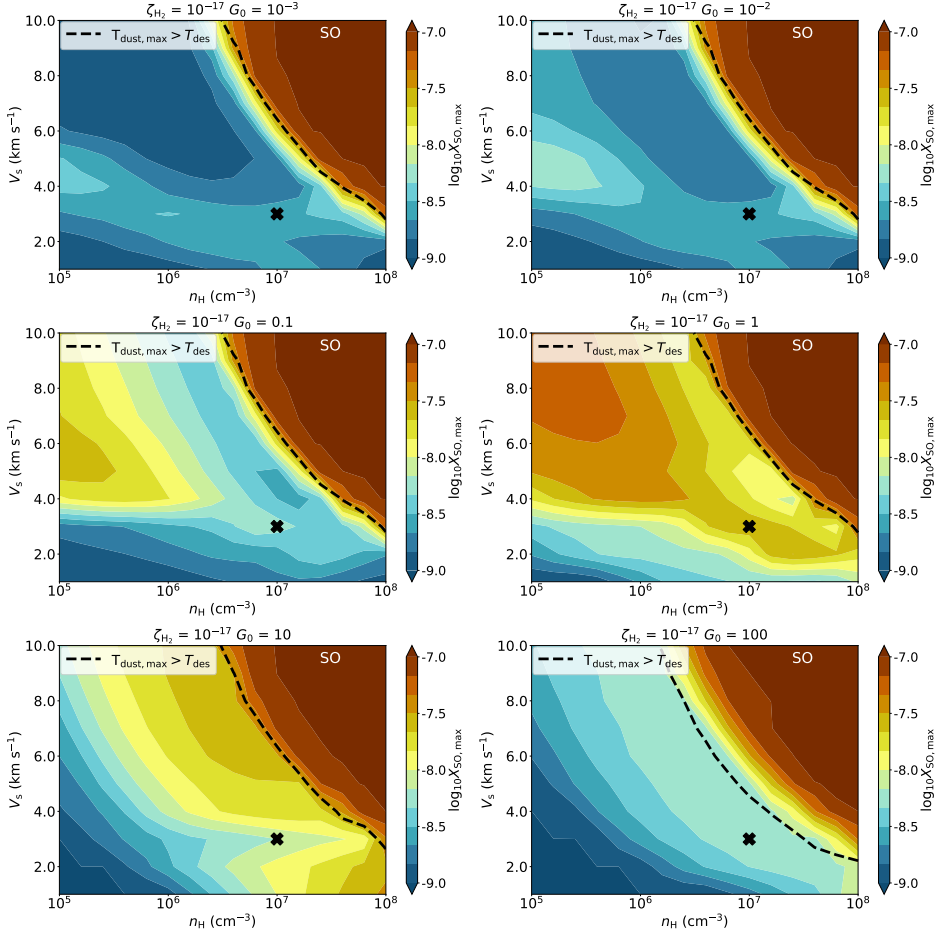


Figure 5.D.2: Maximum abundance reached (in color) of SO in shock models as function of initial n_H and V_s for $G_0 = 10^{-3}$ (top left), $G_0 = 10^{-2}$ (top right), $G_0 = 0.1$ (middle left), $G_0 = 1$ (middle right), $G_0 = 10$ (bottom left), and $G_0 = 100$ (bottom right). The black cross indicates the position of the fiducial model. The dashed black line shows the ice line, i.e., where 50% of the ice is thermally desorbed into the gas in the shock.

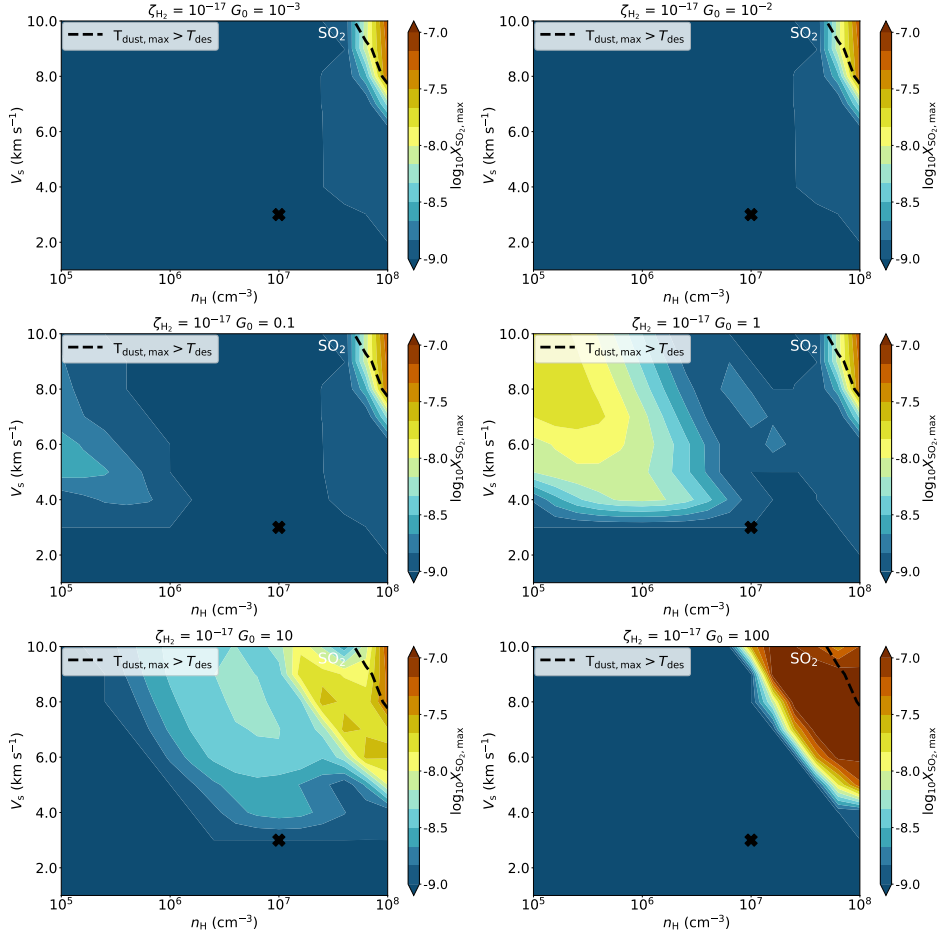


Figure 5.D.3: Maximum abundance reached (in color) of SO_2 in shock models as function of initial n_{H} and V_s for $G_0 = 10^{-3}$ (top left), $G_0 = 10^{-2}$ (top right), $G_0 = 0.1$ (middle left), $G_0 = 1$ (middle right), $G_0 = 10$ (bottom left), and $G_0 = 100$ (bottom right). The black cross indicates the position of the fiducial model. The dashed black line shows the ice line, i.e., where 50% of the ice is thermally desorbed into the gas in the shock.

5.E Higher magnetized environments

The focus of this paper is on nonmagnetized J -type shocks. However, in reality magnetic fields are present in protostellar envelopes where observations hint at intermediate or strong magnetic field strengths (i.e., $\sim 0.1 - 1$ mG; Hull et al. 2017). The structure of shocks depends strongly on the strength of the magnetic field. In weakly magnetized regions, the emerging shock will remain a magnetized J -type shock with a similar structure to nonmagnetized J -type shocks. However, in higher magnetized environments, the ions and electrons can decouple from the neutral species through the Lorentz force. While slowing down through the Lorentz force, the ions exert a drag force on the neutral fluid. Both fluids slow down and compress, resulting in an increase in the temperature and the emergence of a C -type (strong magnetic field strength) and CJ -type (intermediate magnetic field strength) shocks (Draine 1980; Flower & Pineau des Forêts 2003; Godard et al. 2019). Below, the results of C and CJ -type accretion shocks are shortly discussed, where in both cases a preshock model was calculated over a timescale $t_{\text{preshock}} = 100$ years (see Appendix 5.C for details).

5.E.1 C -type shocks

In interstellar C -shocks, the mass of the ionized fluid is dominated by small dust grains (which couple well to ions) and ionized PAHs (e.g., Godard et al. 2019). However, since dust grows to larger grains (here assumed at $0.2 \mu\text{m}$) in protostellar envelopes, it will likely be better coupled to the neutral fluid (Guillet et al. 2007, 2020). Moreover, PAHs are lacking in the gas, likely frozen out onto dust grains (Geers et al. 2009). Hence, the mass of the ion fluid exerting a drag force on the neutrals is determined solely by small ions such as S^+ , C^+ , HCO^+ , and N_2H^+ . Having more small ions (e.g., due to a stronger UV radiation field) therefore strongly affects the structure of the C -type shock.

Since the decoupling between ions and neutrals is very slow, the length of C -type shocks is on envelope scales (i.e., $\gtrsim 1000$ AU) for most of the parameter space considered (see Table 5.1). Only for high velocity ($> 8 \text{ km s}^{-1}$) C -shocks at high densities ($> 10^7 \text{ cm}^{-3}$), the total length of the shock is on disk scales of < 100 AU. For such shocks, the abundance of SO is slightly increased through gas-phase chemistry following the green route of Fig. 5.5, while the abundance of SO_2 is not increased in these C -type shocks.

Contrary to J -type shocks, an increased PAHs abundance also affects the physical structure of a C -type shock as ionized PAHs carry most of the mass of the ion fluid if dust grains are assumed to be coupled to the neutrals (Flower & Pineau des Forêts 2003). A higher abundance of PAHs results in a stronger decoupling between ions and neutrals and consequently a decrease in the shock length. Hence, in a larger part of the parameter space, C -type shocks on disk scales (< 100 AU) are produced. However, given the lack of PAH emission from Class 0 and I sources (Geers et al. 2009), a high PAH abundance is not realistic.

In reality, any small grains that are present in protostellar envelopes could be coupled to the ions (Guillet et al. 2007; Godard et al. 2019). In turn, this

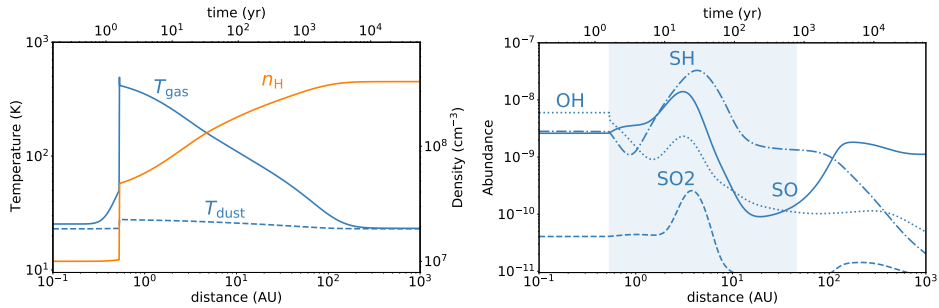


Figure 5.E.1: Same as Fig. 5.2, but for a CJ -type shock with $B \sim 160$ μG . All other parameters are kept at their fiducial value (see Table 5.1). In the right panel, the region where $T_{\text{gas}} > 50$ K is indicated with the shaded blue region.

also results in a larger fraction of the parameter space having a shock length of < 100 AU. However, the full treatment of grain dynamics in C -type shocks would have to include a separate fluid for each grain size (Ciolek & Roberge 2002; Guillet et al. 2007) with grain-grain interactions such as vaporization, shattering, and coagulation (Guillet et al. 2009, 2011). This is beyond the scope of this work.

5.E.2 CJ -type shocks

With decreasing magnetic field strength, the decoupling between ions and neutrals becomes weaker. The motion of the neutral velocity is no longer completely dominated by the ion-neutral drag, but also by the viscous stresses and thermal pressure gradient (Godard et al. 2019). The resulting CJ -shock structure is presented in left part of Fig. 5.E.1 for $B \sim 160$ μG . All other parameters are kept at their fiducial value (see Table 5.1). Initially, the drag of the ions slows down the neutrals, increasing the gas temperature to ~ 50 K. However, here the viscous stresses and thermal pressure take over, resulting in a jump in temperature and density as the neutral fluid jumps across the sonic point (Godard et al. 2019). Afterwards, the ions keep exerting a small drag force on the neutrals until the fluids recouple at about ~ 80 AU. Since the heating induced by this drag is lower than the cooling of the gas, the shock gradually cools down. The abundances of SO and SO₂ do show an increase in the CJ -shock, see right panel of Fig. 5.E.1. Here, SO is predominantly formed through Reaction (5.2) with SH coming from the green route of Fig. 5.5.

Given that the strength of the magnetic field on inner envelope scales might be high enough to create CJ -type shocks (Hull et al. 2017), these type of shocks are very relevant. However, in order to compute CJ -type shocks over the entire parameter space considered in this paper, the Paris-Durham shock code has to be tweaked to our specific parameter space. This is beyond the scope of this work. Nevertheless, as shown in Fig. 5.E.1, the chemical formation routes of Fig. 5.5 are still valid for CJ -type shocks since similar physical conditions are attained.

Chapter 6

Observing accretion shocks with ALMA.

Searching for SO and SO₂ in Class I disks

M. L. van Gelder, A. F. Pérez-Sánchez, B. Tabone, E. F. van
Dishoeck

in preparation

Abstract

Context. It remains unknown whether the chemical composition of embedded disks is inherited from their natal envelopes or whether it is reset in a strong accretion shock at the disk-envelope boundary. Both SO and SO₂ have been suggested as good tracers of such accretion shocks.

Aims. We search for accretion shocks with SO and SO₂ in three embedded Class I protostars: TMC1A in Taurus and Ced 110 IRS 4 and IRS 6 in Chameleon.

Methods. Resolved observations with an angular resolution of $\sim 0.15''$ (~ 10 au radius) taken with the Atacama Large Millimeter/submillimeter Array (ALMA) in Band 6 (1.3 mm) of SO, SO₂, and their isotopologues are investigated. Multiple transitions of SO₂ with a range of E_{up} between 55–119 K are covered to determine the excitation conditions through LTE modeling of spectra extracted from the peak SO₂ emission.

Results. Both SO and SO₂ are only detected toward TMC1A. The emission is spatially resolved and located around the dust continuum. None of the isotopologues are detected. The SO and SO₂ lines are narrow with a FWHM of 1.0 ± 0.1 km s⁻¹. An excitation temperature of 50 ± 20 K is derived for SO₂ and the column density ratio of SO₂/SO is found to be 0.6 ± 0.1 . Other molecules such as c-C₃H₂ and CH₃OH are not detected toward all sources.

Conclusions. An accretion shock origin can be excluded as the origin of the SO and SO₂ emission in TMC1A based on narrow line widths, low excitation temperature, and a comparison of the line ratio to shock models in the literature. Similarly, the lack of SO and SO₂ emission toward IRS 4 and IRS 6 suggests the absence of a strong ($T_{\text{gas,max}} > 100$ K) accretion shock. These results imply that the chemical composition of the embedded disks in these sources could be directly inherited from their natal envelopes. Furthermore, the presence of hot SO₂ emission from transitions with $E_{\text{up}} > 100$ K seems to be correlated with the bolometric luminosity, suggesting that energetic processes such as ultraviolet irradiation could be important for the formation of SO₂ in the gas phase.

6.1 Introduction

It remains unknown whether the chemical composition of embedded protostellar systems is conserved from envelope to disk (inheritance scenario) or whether it is modified en route (reset scenario). In case of reset, this can be either complete vaporization of all molecules back to atoms with subsequent reformation or a milder form of reset where ices may be sputtered off dust grains and the gas-phase molecular composition may be altered by energetic processes. Some modification to the composition is expected due to the changing temperatures and UV radiation along the infall paths (e.g., Aikawa et al. 1999; Visser et al. 2009; Drozdovskaya et al. 2014). On the other hand, some inheritance is suggested based on the similarities between interstellar and cometary ices (e.g., Mumma & Charnley 2011; Drozdovskaya et al. 2019). A major uncertainty remains whether a strong accretion shock at the disk-envelope boundary may (partially) reset the chemistry. Since planet formation is suggested to start in embedded protostellar disks (e.g., Harsono et al. 2018; Tychoniec et al. 2020), it is important to study such accretion shocks in these young systems to determine their strength and their effect on the chemical composition.

Accretion shocks are commonly seen in models and simulations of infalling envelopes (e.g., Cassen & Moosman 1981; Visser et al. 2009; Li et al. 2013). They are most powerful and result in complete vaporization at early times (Class 0 phase) when accretion occurs close to the star (< 1 au). However, that infalling material ends up in the star and thus does not contribute to the chemical composition of the disk at longer timescales. At later times (Class I phase), accretion occurs further out in the disk (tens of au), with typical shock speeds of a few km s^{-1} impacting gas with densities of $> 10^7 \text{ cm}^{-3}$. For these conditions, molecules largely survive (i.e., no complete reset) but gas temperatures just behind the shock can reach up to $\gtrsim 1000$ K which drives most of the gaseous oxygen into OH and H_2O . In turn, this leads to enhanced abundances of molecules like SO and SO_2 , especially if some ultraviolet (UV) radiation is present (Neufeld & Hollenbach 1994; van Gelder et al. 2021). The dust temperature is also raised, but only to about 50 K, enough to release weakly bound molecules (e.g., CH_4 , NH_3) but not strongly bound species like H_2O (Visser et al. 2009; Miura et al. 2017). Some sputtering of ice mantles can also occur.

It is important to observationally constrain the strength of accretion shocks to determine its effect on the disk composition. Common optical shock tracers such as [O I] 6300 Å and [S II] 6371 Å are more sensitive to more energetic shocks in the jet (e.g., Podio et al. 2011; Banzatti et al. 2019; Xie et al. 2021) and are largely extinguished in embedded systems by the envelope. For mid-infrared shock tracers such as H_2 , H_2O , [S I] 25 μm , and [O I] 63 μm , previous space observatories such as *Spitzer* and *Herschel* lacked the spatial resolution ($5 - 10''$, i.e., suffering from contamination by the outflow; Kristensen et al. 2012; Nisini et al. 2015; Rivière-Marichalar et al. 2016) whereas ground-based observatories suffer from the Earth's atmosphere at infrared wavelengths. The recently launched *James Webb* Space Telescope (JWST) does have both the spatial resolution and sensitivity to disentangle possible accretion shocks from the outflow and jet, but it does not

have the spectral resolution to study the kinematics.

At millimeter wavelengths, both SO and SO₂ have been suggested as good tracers of accretion shocks. With the Atacama Large Millimeter/submillimeter Array (ALMA), it is now possible to spatially and kinematically resolve disks and inner envelopes of embedded sources on scales of tens of au, delineating the Keplerian disk (e.g., Tobin et al. 2012; Murillo et al. 2013; Yen et al. 2014; Aso et al. 2017), the entrained outflow and jet (e.g., Arce et al. 2013; Tychoniec et al. 2019; Taquet et al. 2020), and even disk winds down to the launching point in the disk (e.g., Bjerkeli et al. 2016; Tabone et al. 2017). The suitability of SO and SO₂ to trace energetic processes at the disk-envelope interface was demonstrated by the detection of strong SO emission near the centrifugal barrier of the embedded disk around the L1527 Class 0/I protostar (Sakai et al. 2014, 2017). Later, also other detections of SO in possible accretion shocks were found (e.g., the Class I source Elias 29; Oya et al. 2019). Furthermore, strong SO₂ emission was observed related to accretion shocks for a few Class 0 and Class I sources (e.g., Bjerkeli et al. 2019; Artur de la Villarmois et al. 2019). Both SO and SO₂ are also seen at the interface between infalling streamers and disks in more evolved Class II sources (Garuffi et al. 2022). However, these two molecules do not exclusively trace accretion shocks but are also seen in outflows (e.g., Codella et al. 2014, 2021; Taquet et al. 2020), disk winds (e.g., Tabone et al. 2017; Lee et al. 2018), or in the warm inner envelopes that are passively heated by the central accreting protostar (e.g., Harsono et al. 2021). Moreover, a strong link between warm SO₂ emission arising from transitions with an upper energy level E_{up} of ~ 200 K with bolometric luminosity was observed (Artur de la Villarmois et al. 2019). The emission therefore has to be carefully compared to sophisticated models of accretion shocks (e.g., Miura et al. 2017; van Gelder et al. 2021) to make robust conclusions about its origin. Moreover, it is important to cover multiple lines of SO and SO₂ with high E_{up} (> 50 K) to exclude emission related to an extended outflow (Tychoniec et al. 2021) and to determine their excitation conditions in order to further characterize the presence of an accretion shock and its strength.

In this work, the presence of accretion shocks is investigated toward three Class I sources: TMC1A in Taurus and Ced 110 IRS 4 and Ced 110 IRS 6 (hereafter IRS 4 and IRS 6) in Chameleon. The main physical properties of these sources are presented in Table 6.1. All three protostars are firmly classified as Class I sources based on their spectral energy distribution (e.g., Evans et al. 2003), compact and warm CO and HCO⁺ emission (van Kempen et al. 2009b; Yıldız et al. 2013), outflowing molecular gas (e.g., van Kempen et al. 2009b; Yıldız et al. 2013; Bjerkeli et al. 2016), and the presence of a disk (Pontoppidan & Dullemond 2005; Harsono et al. 2014, 2021).

So far, few Class I sources have been observed with both SO and SO₂. Here, resolved ALMA observations with an angular resolution of $\sim 0.15''$ (~ 10 au radius) of TMC1A, IRS 4, and IRS 6 are presented covering two transitions of SO and five transitions of SO₂ with a range of E_{up} between 55 – 119 K which allow for determining their excitation conditions. Additionally, several transitions of the optically thin S¹⁸O, ³⁴SO₂, ³³SO₂, and SO¹⁸O isotopologues are also covered. In Sect. 6.2, the ALMA observations are detailed. The results are presented in

Table 6.1: Main physical properties of the three Class I sources discussed in this paper.

Source	RA (J2000) (hh:mm:ss.ss)	Dec (J2000) (dd:mm:ss.s)	d (pc)	L_{bol} (L_{\odot})	T_{bol} (K)	M_{env} (M_{\odot})
TMC1A	04:39:35.21	25:41:44.1	140 ⁽¹⁾	2.7 ⁽²⁾	118 ⁽²⁾	0.2 ⁽²⁾
Ced 110 IRS 4	11:06:46.37	-77:22:32.9	190 ⁽³⁾	1.0 ⁽⁴⁾	72 ⁽⁴⁾	0.07 ⁽⁵⁾
Ced 110 IRS 6	11:07:09.58	-77:23:05.0	190 ⁽³⁾	0.8 ⁽⁴⁾	260 ⁽⁴⁾	0.04 ⁽⁵⁾

Notes. The coordinates are those of the peak 1.3 mm continuum emission.

⁽¹⁾ Torres et al. (2007). ⁽²⁾ Kristensen et al. (2012). ⁽³⁾ Dzib et al. (2018a). ⁽⁴⁾ Lehtinen et al. (2001). ⁽⁵⁾ van Kempen et al. (2009b).

Sect. 6.3 and discussed in Sect. 6.4. Lastly, our conclusions are presented in Sect. 6.5.

6.2 Observations

The data of this work are taken with the 12m array of ALMA in Band 6 under the program 2021.1.01322.S (PI: M.L. van Gelder) with the aim of detecting multiple transitions of SO and SO₂ and their isotopologues (e.g., S¹⁸O, ³⁴SO₂), see Table 6.C.2 for a full list of the targeted transitions. The main technical properties of these data are listed in Table 6.C.1. TMC1A was observed in June 2022 in ALMA configuration C-6 with a angular resolution of 0.20×0.15'' (~ 10 au radius). The two Cederblad sources were observed in November 2021 in ALMA configuration C-7 with a synthesized beam of 0.16×0.10'' (~ 10 au radius). The spectral resolution of all spectral windows are 0.15 km s⁻¹ except for a continuum window which has a spectral resolution of 1.3 km s⁻¹. The line sensitivity over 0.15 km s⁻¹ is 2.3 K and 4.5 K for TMC1A and the two Chameleon sources, respectively.

The TMC1A data are pipeline calibrated and imaged with the Common Astronomy Software Applications¹ (CASA; McMullin et al. 2007) version 6.2.1.7. For the two Chameleon sources, the data are manually calibrated and imaged with CASA version 5.1.1. Continuum images are made from line-free channels. Following continuum subtraction in the uv -plane using the UVCONTSUB task of CASA, line images are made using a mask size that incorporates all the line emission with the TCLEAN task using a Briggs weighting of 0.5. The resulting continuum images are presented in Fig. 6.1 and integrated intensity maps of the SO 6₅ – 5₄ ($E_{\text{up}} = 50.7$ K) and SO₂ 13_{1,13} – 12_{0,12} ($E_{\text{up}} = 82.2$ K) lines are presented in Fig. 6.2. Spectra presented in this work are extracted from the peak of the integrated SO₂ 13_{1,13} – 12_{0,12} emission in Fig. 6.2 for TMC1A and from the peak of the continuum emission for IRS 4 and IRS 6 since no 3σ detections in SO₂ are present.

¹<https://casa.nrao.edu/>

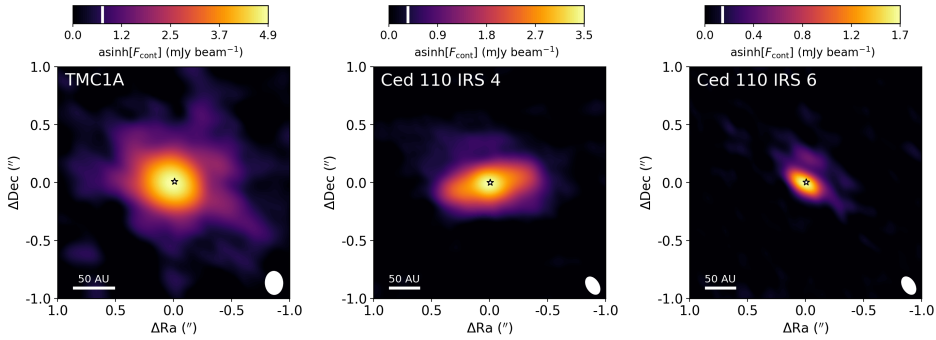


Figure 6.1: The 1.3 mm continuum emission of TMC1A (left), IRS 4 (middle), and IRS 6 (right). All images are shown with an asinh stretch to enhance fainter features without over-saturating bright emission (e.g., Andrews et al. 2018). For each map, a colorbar is displayed on top where the $3\sigma_{\text{cont}}$ level is indicated with the white bar (see Table 6.C.1 for σ_{cont} values). The peak of the continuum emission is highlighted with the star. The size of the synthesized beam is displayed in the bottom right of each image and on the bottom left a 50 au scale bar is shown.

6.3 Results

6.3.1 Dust continuum

The 1.3 mm continuum emission maps of the three sources studied in this work are presented in Fig. 6.1. In all three sources, a disk-like structure in the continuum is evident. For TMC1A, the disk was already kinematically confirmed from CO isotopologues (~ 100 au in radius; Harsono et al. 2014). Later, that dust disk was also spatially resolved in high-angular resolution ALMA observations of both the dust continuum and molecular emission (~ 30 au in radius; Harsono et al. 2021). For both IRS 4 and IRS 6, these are the first data where the continuum is spatially resolved. The dust disks of IRS 4 and IRS 6 are large with radii of about ~ 75 au and ~ 50 au, respectively. Interestingly, IRS 6 also shows some continuum emission toward the north, pointing toward a possible binary companion. If this emission indeed originates from a companion, the separation would be about ~ 40 au and the companion would have a dust disk of $\lesssim 25$ au in radius.

The total dust mass in these disks, $M_{\text{disk,dust}}$, can be estimated using the equation of Hildebrand (1983),

$$M_{\text{disk,dust}} = \frac{F_{\text{cont}} d^2}{\kappa_{\nu} B_{\nu}(T_{\text{dust}})}, \quad (6.1)$$

with F_{cont} the disk integrated continuum flux, B_{ν} the Planck function for a given dust temperature, T_{dust} , and κ_{ν} the dust opacity in the optically thin limit. The disk integrated continuum flux is computed through Gaussian fitting with the CASA task IMFIT. A dust temperature of 30 K is assumed, which is typical for the inner envelopes of embedded protostellar systems (Whitney et al. 2003). The

Table 6.2: Disk integrated continuum fluxes and disk masses computed for our three Class I sources.

Source	$F_{1.3\text{mm}}$ (mJy)	M_{disk} (M_{\odot})	$M_{\text{disk}}/M_{\text{env}}$
TMC1A	170 ± 34	$1.4 \pm 0.3(-2)$	$7.1 \pm 1.4(-2)$
Ced 110 IRS 4	64 ± 13	$9.8 \pm 2.0(-3)$	$1.4 \pm 0.3(-1)$
Ced 110 IRS 6	4.4 ± 0.9	$6.7 \pm 1.3(-4)$	$1.7 \pm 0.3(-2)$

Notes. $a(b)$ represents $a \times 10^b$. The total disk mass M_{disk} is computed the dust disk mass $M_{\text{disk,dust}}$ using Eq. (6.1) and multiplying this by a gas-to-dust mass ratio of 100.

dust opacity, κ_{ν} , is set to $2.3 \text{ cm}^2 \text{ g}^{-1}$ for a wavelength of 1.3 mm (e.g., Ansdell et al. 2016). Following this, the total disk mass M_{disk} is calculated by multiplying $M_{\text{disk,dust}}$ with a gas-to-dust mass ratio of 100. An error of 20% is assumed on F_{cont} which is propagated to M_{disk} . The calculated values for F_{cont} , M_{disk} , and $M_{\text{disk}}/M_{\text{env}}$ are reported in Table 6.2.

In all three sources, the envelope masses are higher than those of their disks, further proving the embedded nature of these sources. The disk mass of TMC1A is the largest within our sample and agrees within a factor 3 with that derived by Harsono et al. (2014) due a difference in the assumed κ_{ν} . IRS 4 hosts a disk with a similar mass, but its $M_{\text{disk}}/M_{\text{env}}$ ratio is higher than that of TMC1A. The disk in IRS 6 has the lowest mass of our sample as well as the lowest $M_{\text{disk}}/M_{\text{env}}$.

6.3.2 SO and SO₂

In Fig. 6.2, the integrated intensity maps of SO $6_5 - 5_4$ ($E_{\text{up}} = 50.7 \text{ K}$) and SO₂ $13_{1,13} - 12_{0,12}$ ($E_{\text{up}} = 82.2 \text{ K}$) are presented. Both SO and SO₂ are only detected toward TMC1A; IRS 4 and IRS 6 do not show emission from any molecule targeted within our observations. Only the $6_5 - 5_4$ transition of SO is detected toward TMC1A, the $2_1 - 1_2$ transition ($E_{\text{up}} = 15.8 \text{ K}$) is not detected although this may largely be due to a low intrinsic line strength ($A_{ij} = 1.4 \times 10^{-6} \text{ s}^{-1}$ versus $1.9 \times 10^{-4} \text{ s}^{-1}$ for the $6_5 - 5_4$ transition). The SO $6_5 - 5_4$ transition is the same line as was targeted by Harsono et al. (2021) and therefore shows the same emission morphology but with a factor three higher. Interestingly, the SO₂ emission seems to peak at a similar location as SO in TMC1A, to the south west of the continuum emission. However, the emission of SO₂ is more compact than that of SO, although this may possibly be limited by the sensitivity. Two other transitions of SO₂ with E_{up} of 55 and 94 K are also detected at a similar position as the SO₂ $13_{1,13} - 12_{0,12}$ line in Fig. 6.2. The two SO₂ transitions with $E_{\text{up}} > 100 \text{ K}$ are not detected. Other molecules targeted within the program, such as c-C₃H₂ and CH₃OH, are not detected toward any of the sources, see Appendix 6.A.

To determine the amount of SO and SO₂ in TMC1A, a spectrum is extracted from the peak pixel of the SO₂ emission in Fig. 6.2. Using the spectral analysis

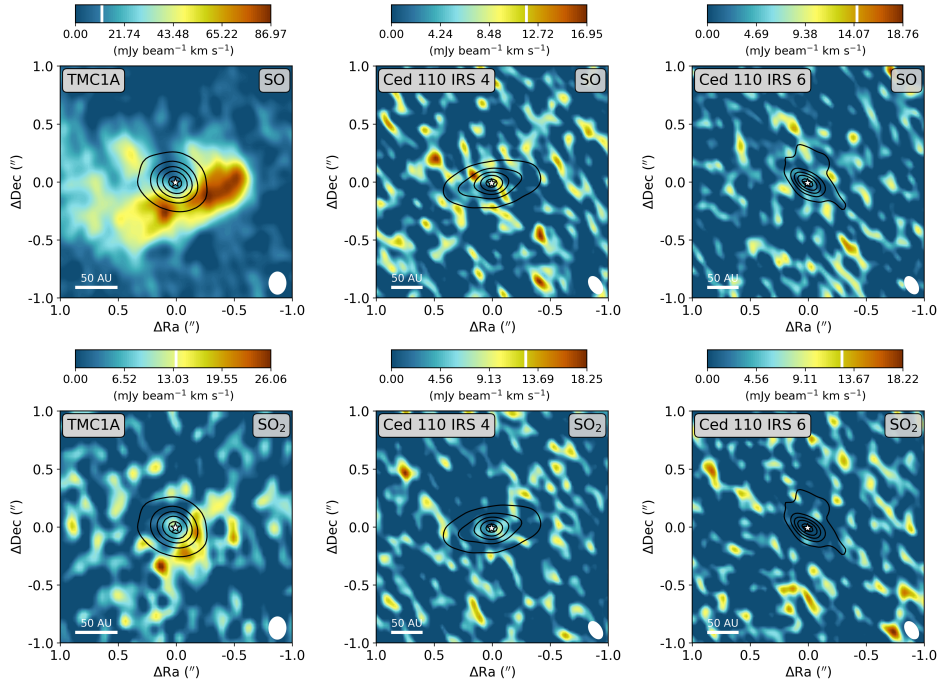


Figure 6.2: Integrated intensity maps of SO $6_5 - 5_4$ ($E_{\text{up}} = 50.7$ K, top row) and SO₂ $13_{1,13} - 12_{0,12}$ ($E_{\text{up}} = 82.2$ K, bottom row) of TMC1A (left), IRS 4 (middle), and IRS 6 (right). The images are integrated over $[-5, 5]$ km s⁻¹ with respect to the V_{lsr} . The color scale is shown on the top of each image, where the white bar indicates the $3\sigma_{\text{line}}$ level. The continuum flux is overplotted with the black contours at $[0.1, 0.3, 0.5, 0.7, 0.9]$ times the peak continuum flux of 67.5, 17.3, and 2.5 mJy beam⁻¹ for TMC1A, IRS 4, and IRS 6, respectively. The peak of the continuum emission is highlighted with the star. The size of the synthesized beam is displayed in the bottom right of each image and on the bottom left a scale bar is shown.

tool CASSIS² (Vastel et al. 2015) and assuming local thermodynamic equilibrium (LTE), a column density and excitation temperature are determined for SO₂ by using the grid fitting method of van Gelder et al. (2020). For SO, only one transition is detected and therefore the excitation temperature is fixed to that derived for SO₂. The line lists of SO and SO₂ are taken from the CDMS catalog³ (Müller et al. 2001, 2005; Endres et al. 2016). Since the emission is resolved, the source size is set equal to the beam size (i.e., beam dilution = 1). The critical densities of the SO and SO₂ lines lie around $\sim 10^6$ cm⁻³, indicating that non-LTE effects will contribute only if the inner envelopes have low density.

The best-fit model to the SO₂ lines of TMC1A is presented in Fig. 6.3. For SO₂, the best-fit column density and excitation temperature are $7.1 \pm 0.8 \times 10^{14}$ cm⁻²

²<http://cassis.irap.omp.eu/>

³<https://cdms.astro.uni-koeln.de/>

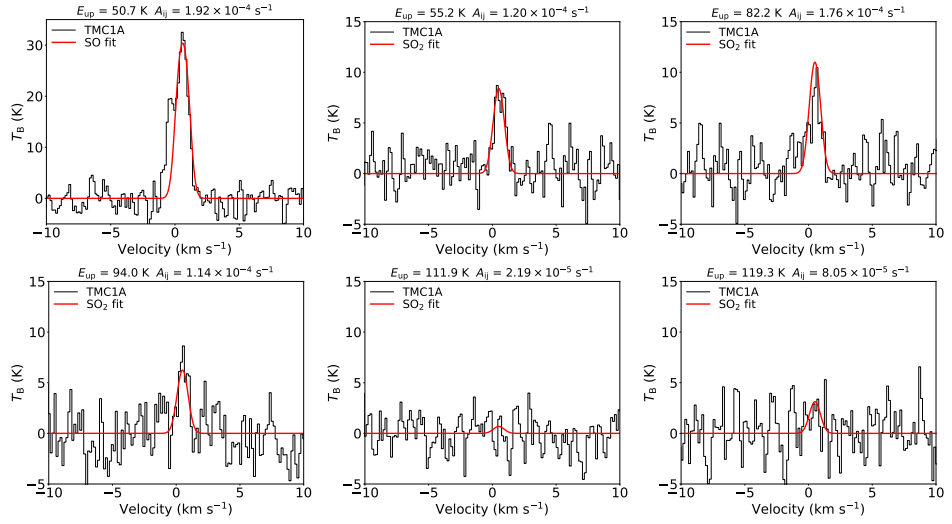


Figure 6.3: Spectrum of TMC1A (in black) centered around the SO $6_5 - 5_4$ (top left) and five SO₂ transitions (other five panels). The E_{up} and A_{ij} of the corresponding transitions are reported on the top of each panel. The best-fit LTE model is overlayed on top in red. For SO₂, the two lines with $E_{\text{up}} > 100 \text{ K}$ (bottom middle and right panels) are considered non-detections.

and $50 \pm 20 \text{ K}$, respectively. For SO, a column density of $1.1 \pm 0.2 \times 10^{15} \text{ cm}^{-2}$ is derived for an excitation temperature of 50 K. This is about a factor 2-3 higher than that of Harsono et al. (2021) which was computed over the full disk and assuming that $T_{\text{ex}} = 30 \text{ K}$. The observed column densities give a ratio of SO₂/SO of 0.6 ± 0.1 . The SO $6_5 - 5_4$ line is optically thick with $\tau_{\text{line}} > 1$. For most of the SO₂ lines, $\tau_{\text{line}} \sim 0.2$, indicating that the emission of SO₂ is marginally optically thick. Unfortunately, none of the isotopologues (in particular S¹⁸O and ³⁴SO₂) are detected to test the optical depth and the limits that can be placed from their non-detections do not provide stringent constraints. The derived excitation temperature of SO₂ of $50 \pm 20 \text{ K}$ is the same as the rotational temperature T_{rot} found using the traditional rotational diagram analysis (Goldsmith & Langer 1999).

Both SO and SO₂ show narrow lines toward TMC1A with a FWHM of $1.0 \pm 0.1 \text{ km s}^{-1}$ at a V_{lsr} of $7.1 \pm 0.1 \text{ km s}^{-1}$. It is important to note that the spectrum is extracted from a single position within the disk; the disk integrated spectrum shows broader lines at different velocities due to the rotation of the disk and envelope. However, the main interest here is to derive a ratio between SO and SO₂ at a single (possibly shocked) position rather than an integrated column over the full disk.

For IRS 4 and IRS 6, only upper limits can be derived for both SO and SO₂. Assuming an excitation temperature of 50 K and a FWHM of 1 km s^{-1} , the 3σ upper limits on the column densities are $3 \times 10^{14} \text{ cm}^{-2}$ and $7 \times 10^{14} \text{ cm}^{-2}$ for SO and SO₂, respectively. The spectra of IRS 4 and IRS 6 are presented in Appendix 6.B.

6.4 Discussion

6.4.1 Inheritance vs reset: constraining the shock strength

Both SO and SO₂ are commonly observed toward shocked regions, either in outflows or jets (e.g., Codella et al. 2014; Taquet et al. 2020) but also in disk winds (e.g., Tabone et al. 2017; Lee et al. 2018). In shocks, these molecules typically show broad lines ($> 5 \text{ km s}^{-1}$) originating from high- E_{up} transitions ($> 100 \text{ K}$). However, emission from either of these two molecules does not directly imply a shocked origin. In earlier observations of TMC1A, the emission of SO was attributed to the inner envelope that is passively heated by the central protostar (Harsono et al. 2021). To determine whether the SO and SO₂ emission is indeed related to an accretion shock, it is important to compare their excitation conditions and column density ratio to sophisticated shock models of low-velocity ($< 10 \text{ km s}^{-1}$) in high-density ($> 10^6 \text{ cm}^{-3}$) environments (e.g., Miura et al. 2017; van Gelder et al. 2021).

For TMC1A, our derived column density ratio of SO₂/SO of 0.6 ± 0.1 is high compared to what is presented in the shock models of van Gelder et al. (2021), see Fig. 6.4. In the presence of a strong UV field (> 100 times higher than that in the ISM; Mathis et al. 1983), it could imply either a high-velocity ($> 6 \text{ km s}^{-1}$) shock in a high-density ($> 10^7 \text{ cm}^{-3}$) environment or a low-velocity shock ($< 4 \text{ km s}^{-1}$) at lower densities ($< 10^6 \text{ cm}^{-3}$). If the UV field similar to that of the ISM, it would imply either a low-velocity ($< 2 \text{ km s}^{-1}$) or high-velocity ($> 6 \text{ km s}^{-1}$) shock in a low-density ($< 10^6 \text{ cm}^{-3}$) environment. In the absence of a UV field, the abundances of SO and in particular SO₂ barely increase in accretion shocks (van Gelder et al. 2021). Similarly, when a sufficiently high magnetic field is present so that the accretion shock is of *C*-type, no increase in SO and SO₂ abundance is present and the length of the shock approaches envelope scales ($> 1000 \text{ au}$). In such cases, the SO₂/SO ratio represents that of the abundance ratio in the gas of the infalling envelope.

A high-velocity ($> 5 \text{ km s}^{-1}$) shock can be excluded as the origin of the SO and SO₂ emission in TMC1A given that the lines of both SO and SO₂ are narrow ($1.0 \pm 0.1 \text{ km s}^{-1}$) and that a low excitation temperature of $50 \pm 20 \text{ K}$ is derived for SO₂. If the emission does arise from an accretion shock, the density is low ($< 10^6 \text{ cm}^{-3}$) and the shock propagates at low velocities ($< 2 \text{ km s}^{-1}$). A hot core origin is also not likely given that the SO₂/SO ratio observed toward the hot core IRAS 16293-2422 is higher ($\gtrsim 3$; Drozdovskaya et al. 2018) and also because CH₃OH is not detected (see Appendix 6.A). A more likely explanation for the origin of SO and SO₂ in TMC1A is the warm inner envelope that is passively heated by the central protostar (Harsono et al. 2021).

For the two Chameleon sources, the lack of SO and SO₂ emission is a strong indication of a weak (less than that in the ISM) UV field. If a UV field is still present, the velocity of the shock can be constrained to be $< 2 \text{ km s}^{-1}$ in case of a weakly magnetized environment (*J*-type) and $< 7 \text{ km s}^{-1}$ in case of a stronger magnetic fields (*C*-type).

The absence of clear shocked SO and SO₂ emission at the disk-envelope bound-

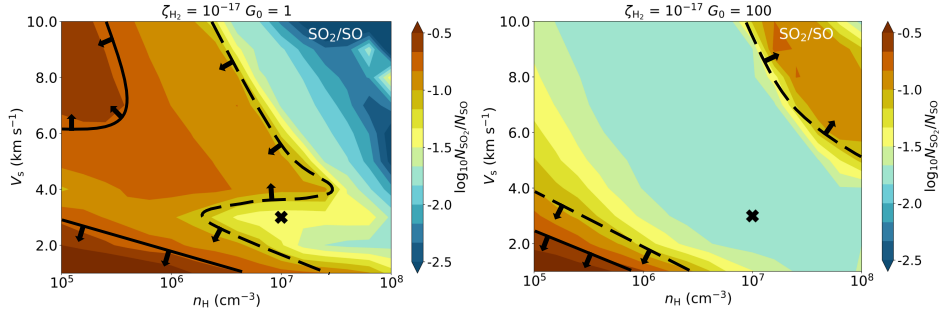


Figure 6.4: Column density ratios of SO_2/SO in the shock models of van Gelder et al. (2021, their Figure 10) as function of pre-shock density n_{H} and shock velocity V_{s} for a UV-radiation field equal to the ISM (left) and 100 times stronger than the ISM (right). A colorbar is displayed on the right of each panel and the black cross indicates their fiducial model. The black solid contours in each panel highlight the region in the parameter space where the observed column density ratio of TMC1A ($\log_{10} N_{\text{SO}_2}/N_{\text{SO}} = -0.3$) agrees with the models. The dashed black contours mark a region where the observed ratio agrees with the models within a factor of 3.

aries of these three sources indicates that either no accretion shocks are present or that the shocks are weak with temperatures of < 100 K (i.e., too low to trigger gas-phase formation or thermal desorption of SO and SO_2 Miura et al. 2017; van Gelder et al. 2021). This implies that the chemical composition of the envelope material that accretes onto these disks remains intact. In turn, this suggests that any planets forming in these three disks may directly inherit the chemical composition from their natal envelopes. A caveat in this conclusion is that most of the mass in the disk which remains there (i.e., does not directly fall onto the central star) is likely accreted in the late Class 0 and early Class I phases (e.g., Visser et al. 2009; Cridland et al. 2022). All three sources are Class I sources with still significant accretion occurring onto their disks (Pontoppidan & Dullemond 2005; van Kempen et al. 2009b; Aso et al. 2015). Accretion shocks could have existed in earlier stages which did (partially) affect the chemical composition entering the disk.

6.4.2 Relation between warm SO_2 and source properties

Despite the fact that the SO and SO_2 emission is not related to accretion shocks in the three sources studied here, a link between their presence and source properties such as L_{bol} and T_{bol} may still be present (e.g., Artur de la Villarmois et al. 2019). In Fig. 6.5, our sources are plotted as a function of L_{bol} and T_{bol} , indicating whether or not SO and SO_2 emission is present. A distinction is made between sources where hot SO_2 (transitions with $E_{\text{up}} > 100$ K) is detected or if only cold SO_2 ($E_{\text{up}} < 100$ K) is present. Besides our sources, also sources from the literature where SO and SO_2 are probed on disk scales (i.e., not in an outflow or jet) are presented in Fig. 6.5.

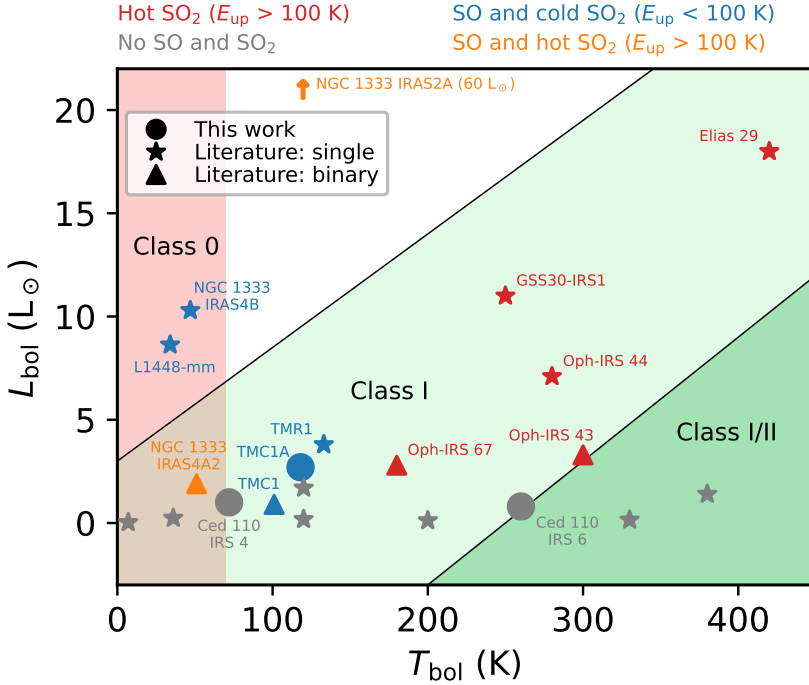


Figure 6.5: The presence of SO and SO₂ emission as function of the source properties L_{bol} and T_{bol} (updated version of Fig. 13 in Artur de la Villarmois et al. 2019). Besides the sources in this work (circles), also single sources (stars) and binary sources (triangle) from the literature are included (Artur de la Villarmois et al. 2019; Yang et al. 2021). With colors, a distinction is made between the detection of SO and hot SO₂ (transitions with $E_{\text{up}} > 100$ K) in orange, SO and cold SO₂ (only transitions with $E_{\text{up}} < 100$ K) in blue, hot SO₂ and no information in the literature on SO (red), and absence of both SO and SO₂ (gray). The shaded colors in the background indicate the empirical characterization of Class 0 (pink), Class I (light green), and more evolved Class I and Class II sources (dark green) based on the line emission of SO₂ and C¹⁷O (Artur de la Villarmois et al. 2019).

First, it is evident that all sources with $L_{\text{bol}} > 2 L_{\odot}$ show emission from either SO or SO₂. Interestingly, all sources showing emission from hot SO₂ lines ($E_{\text{up}} > 100$ K) are either single or binary sources with high $L_{\text{bol}} > 5 L_{\odot}$ (GSS30-IRS1, Oph-IRS 44, Elias 29, NGC 1333 IRAS 2A) or binaries with moderate $L_{\text{bol}} \sim 3 L_{\odot}$ (Oph-IRS 43, Oph-IRS 67, and NGC 1333 IRAS 4A2 Artur de la Villarmois et al. 2019; Yang et al. 2021). This trend was attributed to SO₂ tracing high-energetic processes possibly linked to high accretion rates (Artur de la Villarmois et al. 2019). For all the sources with hot SO₂, an accretion shock origin has not been excluded. Second, sources which only show cold SO₂ (and SO) are either younger Class 0 sources with higher $L_{\text{bol}} > 7 L_{\odot}$ or Class I sources

with lower $L_{\text{bol}} < 5 L_{\odot}$. Among these sources is TMC1A, for which an accretion shock origin of the SO_2 emission is excluded. The other two Class I sources in this category are TMR1 (Harsono et al. 2014) and the binary TMC1 (Harsono et al. 2014; Tychoniec et al. 2021). The reason that the Class 0 sources show only cold SO_2 could be related to their higher envelope mass than Class I sources. The energetic radiation from a Class 0 protostar is absorbed close to the protostar (and re-emitted at longer wavelengths) leading to a cold envelope and low T_{bol} whereas more evolved Class I sources with the same L_{bol} have less massive envelopes leading to more energetic radiation at larger scales leading to higher T_{bol} and thus warmer SO_2 . Lastly, sources that do not show any emission of both SO and SO_2 all have low $L_{\text{bol}} < 2 L_{\odot}$. Both the Chameleon sources studied in this work fall in this category. These sources are likely cold with little energetic processes to form or excite any SO and SO_2 in the gas phase.

This summary shows that high L_{bol} is necessary for SO and especially SO_2 to be formed in (or desorbed into) the gas phase. For the latter, a higher luminosity also leads to detections of more excited transitions. Low-mass protostars are known to undergo accretion outbursts in their embedded stages roughly every 5000-10 000 years where their luminosities can increase significantly (e.g., Jørgensen et al. 2015; Hsieh et al. 2019; van 't Hoff et al. 2022). Given the sensitivity of the chemistry of SO and SO_2 to the strength of the UV field (e.g., van Gelder et al. 2021), accretion shocks may therefore possibly be best traced by these molecules in outbursting and sufficiently luminous sources.

6.5 Conclusions

In this work, resolved ALMA observations with an angular resolution of $\sim 0.15''$ (~ 10 au radius) of SO and SO_2 are presented of three embedded Class I protostellar systems: TMC1A, Ced 110 IRS 4, and Ced 110 IRS 6. Both SO and SO_2 are only detected toward TMC1A and spectra are extracted from the peak pixel of SO_2 $13_{1,13} - 12_{0,12}$ ($E_{\text{up}} = 82.2$ K) emission. From the multiple SO_2 lines with a range of E_{up} between 55 – 119 K, the excitation temperature of SO_2 is derived to be $\sim 50 \pm 20$ K. All lines from both SO and SO_2 are narrow with a FWHM of 1.0 ± 0.1 km s $^{-1}$. An SO_2/SO column density ratio of 0.6 ± 0.1 is found.

Based on the low excitation temperature, narrow lines, and a comparison to sophisticated shock models, an accretion shock origin of the SO and SO_2 emission in TMC1A is excluded. Similarly, the absence of SO and SO_2 emission toward IRS 4 and IRS 6 indicates that no strong accretion shock is present at the disk-envelope boundary of these sources. These results imply that the chemical composition of their disks could be inherited from the natal envelopes with little reprocessing due to accretion shocks.

Emission of hot SO_2 (transitions with $E_{\text{up}} > 100$ K) is only present in single sources with high luminosities ($L_{\text{bol}} > 5 L_{\odot}$) or binary sources with moderate luminosities ($L_{\text{bol}} \sim 3 L_{\odot}$). Furthermore, all sources that do not have SO and SO_2 emission have low luminosities ($L_{\text{bol}} < 2 L_{\odot}$). Given that a higher L_{bol} is related to more energetic radiation (i.e., stronger UV field), this suggests that

energetic processes are important for the formation of SO_2 in the gas phase.

These results advocate that strong accretion shocks are not universal in embedded protostellar systems, at least not at the Class I stage, and that for these three sources the chemical composition in their disks could be directly inherited from their natal envelopes. Future observational studies of more embedded systems such as the ALMA programs 2022.1.00209.S (PI: E. Artur de la Villarmois) and 2022.1.01411.S (PI: M.L. van Gelder) will provide a larger statistical sample of Class I sources with or without strong accretion shocks to determine their relevance. Moreover, several JWST programs (i.e., 1290 and 1960: PI: E.F. van Dishoeck) with both the NIRSpec and MIRI instruments will provide data of near and mid-infrared shock tracers such as H_2 , H_2O , OH, [SI] $25\ \mu\text{m}$. These will clearly reveal the current hot spots in protostellar systems and can be combined with SO and SO_2 of ALMA to further constrain the presence and strength of accretion shocks.

Acknowledgments

The authors acknowledge assistance from Allegro, the European ALMA Regional Center node in the Netherlands. This paper makes use of the following ALMA data: ADS/JAO.ALMA#2021.1.01322.S. ALMA is a partnership of ESO (representing its member states), NSF (USA) and NINS (Japan), together with NRC (Canada), MOST and ASIAA (Taiwan), and KASI (Republic of Korea), in cooperation with the Republic of Chile. The Joint ALMA Observatory is operated by ESO, AUI/NRAO and NAOJ. Astrochemistry in Leiden is supported by the Netherlands Research School for Astronomy (NOVA), by funding from the European Research Council (ERC) under the European Union’s Horizon 2020 research and innovation programme (grant agreement No. 101019751 MOLDISK), and by the Dutch Research Council (NWO) grant TOP-1 614.001.751. Support by the Danish National Research Foundation through the Center of Excellence “InterCat” (Grant agreement no.: DNRF150) is also acknowledged.

Appendix

6.A Maps of c-C₃H₂ and CH₃OH

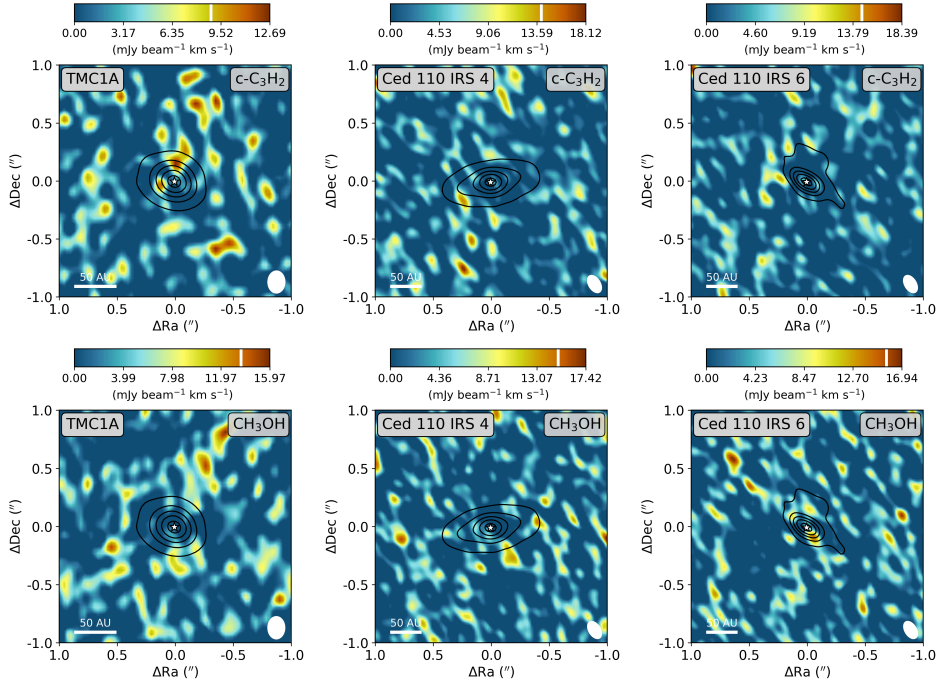


Figure 6.A.1: Integrated intensity maps of c-C₃H₂ $5_{2,3} - 4_{3,2}$ ($E_{\text{up}} = 41.0$ K, top row) and CH₃OH $11_{0,11} - 10_{1,10}$ ($E_{\text{up}} = 153$ K, bottom row) of TMC1A (left), IRS 4 (middle), and IRS 6 (right). The images are integrated over $[-5, 5]$ km s⁻¹ with respect to the V_{LSR} . The color scale is shown on the top of each image, where the white bar indicates the $3\sigma_{\text{line}}$ level. The continuum flux is overplotted with the black contours at $[0.1, 0.3, 0.5, 0.7, 0.9]$ times the peak continuum flux of 67.5, 17.3, and 2.5 mJy beam⁻¹ for TMC1A, IRS 4, and IRS 6, respectively. The peak of the continuum emission is highlighted with the star. The size of the synthesized beam is displayed in the bottom right of each image and on the bottom left a scale bar is shown.

6.B Spectra of SO and SO₂ for IRS 4 and IRS 6

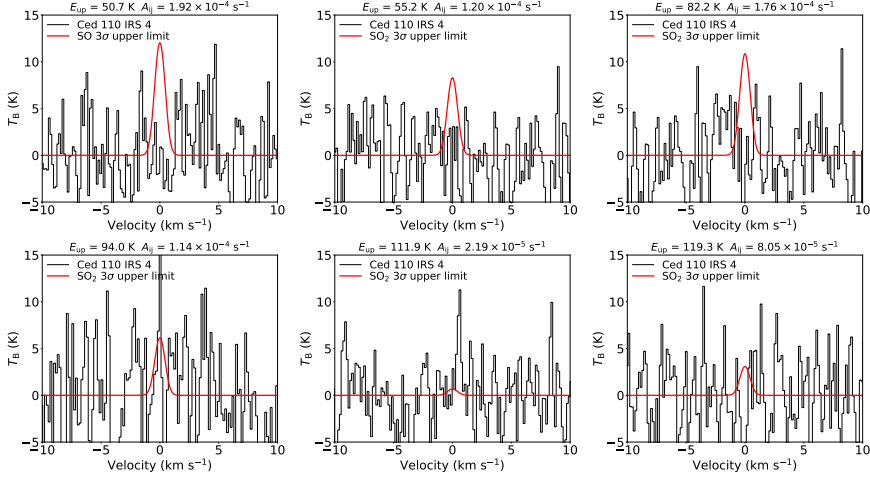


Figure 6.B.1: Spectrum of IRS 4 (in black) centered around the SO 6₅ – 5₄ (top left) and five SO₂ transitions (other five panels). The E_{up} and A_{ij} of the corresponding transitions are reported on the top of each panel. None of the transitions are detected. The LTE model of the 3 σ upper limit is overlayed on top in red.

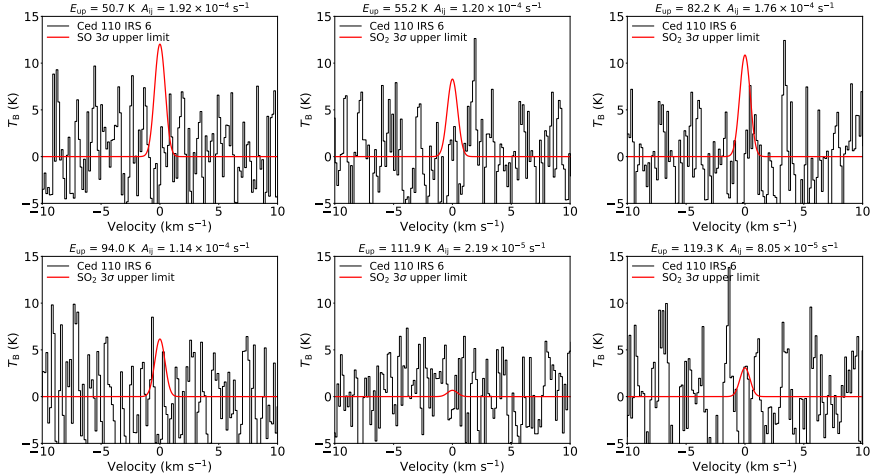


Figure 6.B.2: Spectrum of IRS 6 (in black) centered around the SO 6₅ – 5₄ (top left) and five SO₂ transitions (other five panels). The E_{up} and A_{ij} of the corresponding transitions are reported on the top of each panel. None of the transitions are detected. The LTE model of the 3 σ upper limit is overlayed on top in red.

6.C Additional tables

Table 6.C.1: Main observational properties of ALMA program 2021.1.01322.S.

Source	TMC1A	Ced 110 IRS 4	Ced 110 IRS 6
Configuration	C-6	C-7	C-7
Beam (")	0.20×0.15	0.16×0.10	0.16×0.10
LAS (")	2.0	1.5	1.5
ΔV (km s ⁻¹)	0.15	0.15	0.15
σ_{cont} (mJy/beam)	0.32	0.21	0.13
σ_{line} (K)	2.3	4.5	4.5

Table 6.C.2: Transitions of SO and SO₂ and isotopologues covered in the ALMA program 2021.1.01322.S. Only lines with $A_{ij} > 10^{-6}$ and $E_{\text{up}} < 1000$ K are included.

Species	Transition		Frequency	A_{ij}	E_{up}
	(J K L M - J K L M)		(GHz)	(s ⁻¹)	(K)
SO	2 1 - 1 2		236.4523	1.4×10^{-6}	15.8
	6 5 - 5 4		251.8258	1.9×10^{-4}	50.7
S ¹⁸ O	6 5 - 5 4		232.2658	1.5×10^{-4}	47.8
SO ₂	12 3 9 - 12 2 10		237.0688	1.1×10^{-4}	94.0
	15 2 14 - 15 1 15		248.0574	8.1×10^{-5}	119.3
	10 5 5 - 11 4 8		248.8308	2.2×10^{-5}	111.9
	13 1 13 - 12 0 12		251.1997	1.8×10^{-4}	82.2
	8 3 5 - 8 2 6		251.2106	1.2×10^{-4}	55.2
³³ SO ₂	31 9 23 29.5 - 32 8 24 30.5		232.0729	2.6×10^{-5}	650.5
	31 9 23 32.5 - 32 8 24 33.5		232.0729	2.6×10^{-5}	650.5
	31 9 23 30.5 - 32 8 24 31.5		232.0731	2.6×10^{-5}	650.5
	31 9 23 31.5 - 32 8 24 32.5		232.0732	2.6×10^{-5}	650.5
	4 2 2 4.5 - 3 1 3 3.5		232.4153	6.8×10^{-5}	18.8
	4 2 2 3.5 - 3 1 3 3.5		232.4156	1.0×10^{-5}	18.8
	4 2 2 3.5 - 3 1 3 2.5		232.4184	6.4×10^{-5}	18.8
	4 2 2 2.5 - 3 1 3 2.5		232.4193	1.0×10^{-5}	18.8
	4 2 2 4.5 - 3 1 3 4.5		232.4211	6.2×10^{-6}	18.8
	4 2 2 5.5 - 3 1 3 4.5		232.4222	7.4×10^{-5}	18.8
	4 2 2 2.5 - 3 1 3 1.5		232.4252	6.3×10^{-5}	18.8
	36 3 33 36.5 - 37 2 36 37.5		233.0263	1.8×10^{-6}	647.7
	36 3 33 35.5 - 37 2 36 36.5		233.0267	1.8×10^{-6}	647.7
	36 3 33 37.5 - 37 2 36 38.5		233.0363	1.8×10^{-6}	647.7
	36 3 33 34.5 - 37 2 36 35.5		233.0366	1.8×10^{-6}	647.7
	17 3 15 17.5 - 18 0 18 18.5		233.8339	1.4×10^{-6}	162.4
	17 3 15 16.5 - 18 0 18 17.5		233.8346	1.4×10^{-6}	162.4
	17 3 15 18.5 - 18 0 18 19.5		233.8428	1.4×10^{-6}	162.4
	17 3 15 15.5 - 18 0 18 16.5		233.8435	1.4×10^{-6}	162.4

Table 6.C.2: continued.

Species	Transition						Frequency	A_{ij}	E_{up}
	(J K L M	-	J K L M)				(GHz)	(s^{-1})	(K)
$^{34}\text{SO}_2$	10 5 5	-	11 4 8				233.2964	1.8×10^{-5}	109.7
	5 2 4	-	4 1 3				235.9275	7.9×10^{-5}	23.2
	10 3 7	-	10 2 8				235.9519	1.1×10^{-4}	71.9
	20 2 18	-	19 3 17				236.2251	4.8×10^{-5}	207.2
	19 3 17	-	20 0 20				236.4288	1.4×10^{-6}	195.9
	13 1 13	-	12 0 12				248.6986	1.7×10^{-4}	81.8
	21 3 19	-	22 0 22				248.8557	1.5×10^{-6}	233.5
	9 3 7	-	9 2 8				250.3585	1.2×10^{-4}	62.6
	11 3 9	-	12 0 12				251.1766	1.0×10^{-6}	81.9
SO^{18}O	38 10 29	-	39 9 30				232.4605	2.8×10^{-5}	882.8
	38 10 28	-	39 9 31				232.4621	2.8×10^{-5}	882.8
	17 3 15	-	18 0 18				233.2785	1.4×10^{-6}	154.6
	5 2 4	-	4 1 3				233.4976	7.6×10^{-5}	22.6
	12 3 9	-	12 2 10				233.5884	1.1×10^{-4}	89.5
	6 2 5	-	5 1 4				248.0745	8.7×10^{-5}	27.8
	10 5 6	-	11 4 7				250.3455	2.2×10^{-5}	107.7
	10 5 5	-	11 4 8				250.3718	2.2×10^{-5}	107.7
	5 3 3	-	5 2 4				250.4810	1.0×10^{-4}	34.6
	37 10 28	-	38 9 29				251.1877	3.4×10^{-5}	849.8
	37 10 27	-	38 9 30				251.1887	3.4×10^{-5}	849.8
	7 3 5	-	7 2 6				251.2187	1.1×10^{-4}	45.9

Notes. All transitions and their characteristics are taken from the CDMS catalog (Müller et al. 2001, 2005; Endres et al. 2016).

Bibliography

- Adams, F. C. & Shu, F. H. 1985, *ApJ*, 296, 655
- Aikawa, Y., Furuya, K., Yamamoto, S., & Sakai, N. 2020, *ApJ*, 897, 110
- Aikawa, Y. & Herbst, E. 1999, *ApJ*, 526, 314
- Aikawa, Y., Umebayashi, T., Nakano, T., & Miyama, S. M. 1999, *ApJ*, 519, 705
- ALMA Partnership, Brogan, C. L., Pérez, L. M., et al. 2015, *ApJ*, 808, L3
- Altwegg, K., Balsiger, H., & Fuselier, S. A. 2019, *ARA&A*, 57, 113
- Alves, F. O., Cleeves, L. I., Girart, J. M., et al. 2020, *ApJ*, 904, L6
- Ambrose, H. E., Shirley, Y. L., & Scibelli, S. 2021, *MNRAS*, 501, 347
- André, P., Men'shchikov, A., Bontemps, S., et al. 2010, *A&A*, 518, L102
- André, P., Ward-Thompson, D., & Barsony, M. 1993, *ApJ*, 406, 122
- Andrews, S. M., Huang, J., Pérez, L. M., et al. 2018, *ApJ*, 869, L41
- Ansdell, M., Williams, J. P., van der Marel, N., et al. 2016, *ApJ*, 828, 46
- Aota, T., Inoue, T., & Aikawa, Y. 2015, *ApJ*, 799, 141
- Arce, H. G., Mardones, D., Corder, S. A., et al. 2013, *ApJ*, 774, 39
- Arce, H. G., Santiago-García, J., Jørgensen, J. K., Tafalla, M., & Bachiller, R. 2008, *ApJ*, 681, L21
- Arce, H. G. & Sargent, A. I. 2006, *ApJ*, 646, 1070
- Artur de la Villarmois, E., Jørgensen, J. K., Kristensen, L. E., et al. 2019, *A&A*, 626, A71
- Aso, Y., Ohashi, N., Aikawa, Y., et al. 2017, *ApJ*, 849, 56
- Aso, Y., Ohashi, N., Saigo, K., et al. 2015, *ApJ*, 812, 27

- Bacmann, A., Taquet, V., Faure, A., Kahane, C., & Ceccarelli, C. 2012, *A&A*, 541, L12
- Bailer-Jones, C. A. L., Rybizki, J., Fouesneau, M., Mantelet, G., & Andrae, R. 2018, *AJ*, 156, 58
- Bally, J. 2016, *ARA&A*, 54, 491
- Balucani, N., Ceccarelli, C., & Taquet, V. 2015, *MNRAS*, 449, L16
- Banzatti, A., Pascucci, I., Edwards, S., et al. 2019, *ApJ*, 870, 76
- Barnard, E. E. 1919, *ApJ*, 49, 1
- Bellet, J., Samson, C., Steenbeckliers, G., & Wertheimer, R. 1971, *Journal of Molecular Structure*, 9, 49
- Belloche, A., Garrod, R. T., Müller, H. S. P., & Menten, K. M. 2014, *Science*, 345, 1584
- Belloche, A., Maury, A. J., Maret, S., et al. 2020, *A&A*, 635, A198
- Belloche, A., Müller, H. S. P., Garrod, R. T., & Menten, K. M. 2016, *A&A*, 587, A91
- Belloche, A., Müller, H. S. P., Menten, K. M., Schilke, P., & Comito, C. 2013, *A&A*, 559, A47
- Beltrán, M. T., Brand, J., Cesaroni, R., et al. 2006, *A&A*, 447, 221
- Beltrán, M. T. & de Wit, W. J. 2016, *A&A Rev.*, 24, 6
- Benz, A. O., Bruderer, S., van Dishoeck, E. F., et al. 2016, *A&A*, 590, A105
- Bergin, E. A. & Tafalla, M. 2007, *ARA&A*, 45, 339
- Bergner, J. B., Martín-Doménech, R., Öberg, K. I., et al. 2019, *ACS Earth and Space Chemistry*, 3, 1564
- Bergner, J. B., Öberg, K. I., Garrod, R. T., & Graninger, D. M. 2017, *ApJ*, 841, 120
- Bertin, M., Romanzin, C., Doronin, M., et al. 2016, *ApJ*, 817, L12
- Beuther, H., Churchwell, E. B., McKee, C. F., & Tan, J. C. 2007, in *Protostars and Planets V*, ed. B. Reipurth, D. Jewitt, & K. Keil, 165
- Bianchi, E., Chandler, C. J., Ceccarelli, C., et al. 2020, *MNRAS*, 498, L87
- Bianchi, E., Codella, C., Ceccarelli, C., et al. 2017a, *MNRAS*, 467, 3011
- Bianchi, E., Codella, C., Ceccarelli, C., et al. 2017b, *A&A*, 606, L7

- Bisschop, S. E., Jørgensen, J. K., Bourke, T. L., Bottinelli, S., & van Dishoeck, E. F. 2008, *A&A*, 488, 959
- Bisschop, S. E., Jørgensen, J. K., van Dishoeck, E. F., & de Wachter, E. B. M. 2007, *A&A*, 465, 913
- Bizzocchi, L., Caselli, P., Spezzano, S., & Leonardo, E. 2014, *A&A*, 569, A27
- Bjerkeli, P., Ramsey, J. P., Harsono, D., et al. 2019, *A&A*, 631, A64
- Bjerkeli, P., van der Wiel, M. H. D., Harsono, D., Ramsey, J. P., & Jørgensen, J. K. 2016, *Nature*, 540, 406
- Black, J. H. & van Dishoeck, E. F. 1987, *ApJ*, 322, 412
- Blake, G. A., Sutton, E. C., Masson, C. R., & Phillips, T. G. 1987, *ApJ*, 315, 621
- Boehler, Y., Weaver, E., Isella, A., et al. 2017, *ApJ*, 840, 60
- Bøgelund, E. G., Barr, A. G., Taquet, V., et al. 2019, *A&A*, 628, A2
- Bøgelund, E. G., McGuire, B. A., Ligterink, N. F. W., et al. 2018, *A&A*, 615, A88
- Bok, B. J. & Reilly, E. F. 1947, *ApJ*, 105, 255
- Bonfand, M., Belloche, A., Garrod, R. T., et al. 2019, *A&A*, 628, A27
- Bonfand, M., Belloche, A., Menten, K. M., Garrod, R. T., & Müller, H. S. P. 2017, *A&A*, 604, A60
- Bonnell, I. A. & Bate, M. R. 2006, *MNRAS*, 370, 488
- Bonnell, I. A., Bate, M. R., Clarke, C. J., & Pringle, J. E. 2001, *MNRAS*, 323, 785
- Bonnell, I. A., Bate, M. R., & Zinnecker, H. 1998, *MNRAS*, 298, 93
- Boogert, A. C. A., Gerakines, P. A., & Whittet, D. C. B. 2015, *ARA&A*, 53, 541
- Boogert, A. C. A., Pontoppidan, K. M., Knez, C., et al. 2008, *ApJ*, 678, 985
- Boogert, A. C. A., Schutte, W. A., Helmich, F. P., Tielens, A. G. G. M., & Wooden, D. H. 1997, *A&A*, 317, 929
- Booth, A. S., Walsh, C., Terwisscha van Scheltinga, J., et al. 2021, *Nature Astronomy*, 5, 684
- Bottinelli, S., Boogert, A. C. A., Bouwman, J., et al. 2010, *ApJ*, 718, 1100
- Bottinelli, S., Ceccarelli, C., Lefloch, B., et al. 2004, *ApJ*, 615, 354
- Bouvier, M., Ceccarelli, C., López-Sepulcre, A., et al. 2022, *ApJ*, 929, 10
- Brogan, C. L., Hunter, T. R., Cyganowski, C. J., et al. 2016, *ApJ*, 832, 187

- Brown, P. D. & Millar, T. J. 1989, *MNRAS*, 237, 661
- Brown, R. D., Crofts, J. G., Gardner, F. F., et al. 1975, *ApJ*, 197, L29
- Brown, R. D., Godfrey, P. D., McNaughton, D., Pierlot, A. P., & Taylor, W. H. 1990, *Journal of Molecular Spectroscopy*, 140, 340
- Bulak, M., Paardekooper, D. M., Fedoseev, G., & Linnartz, H. 2021, *A&A*, 647, A82
- Butler, R. A. H., De Lucia, F. C., Petkie, D. T., et al. 2001, *ApJS*, 134, 319
- Calcutt, H., Jørgensen, J. K., Müller, H. S. P., et al. 2018, *A&A*, 616, A90
- Calmonte, U., Altwegg, K., Balsiger, H., et al. 2016, *MNRAS*, 462, S253
- Caselli, P. & Ceccarelli, C. 2012, *A&A Rev.*, 20, 56
- Caselli, P., Hartquist, T. W., & Havnes, O. 1997, *A&A*, 322, 296
- Caselli, P., van der Tak, F. F. S., Ceccarelli, C., & Bacmann, A. 2003, *A&A*, 403, L37
- Caselli, P., Vastel, C., Ceccarelli, C., et al. 2008, *A&A*, 492, 703
- Cassen, P. & Moosman, A. 1981, *ICARUS*, 48, 353
- Cazaux, S., Tielens, A. G. G. M., Ceccarelli, C., et al. 2003, *ApJ*, 593, L51
- Ceccarelli, C., Caselli, P., Bockelée-Morvan, D., et al. 2014, in *Protostars and Planets VI*, ed. H. Beuther, R. S. Klessen, C. P. Dullemond, & T. Henning, 859
- Cernicharo, J., Agúndez, M., Cabezas, C., et al. 2022, *A&A*, 657, L16
- Cernicharo, J., Agúndez, M., Kaiser, R. I., et al. 2021, *A&A*, 652, L9
- Chahine, L., López-Sepulcre, A., Neri, R., et al. 2022, *A&A*, 657, A78
- Charnley, S. B., Tielens, A. G. G. M., & Millar, T. J. 1992, *ApJ*, 399, L71
- Chen, H., Myers, P. C., Ladd, E. F., & Wood, D. O. S. 1995, *ApJ*, 445, 377
- Christen, D., Coudert, L. H., Larsson, J. A., & Cremer, D. 2001, *Journal of Molecular Spectroscopy*, 205, 185
- Christen, D., Coudert, L. H., Suenram, R. D., & Lovas, F. J. 1995, *Journal of Molecular Spectroscopy*, 172, 57
- Christen, D. & Müller, H. S. P. 2003, *Physical Chemistry Chemical Physics (Incorporating Faraday Transactions)*, 5, 3600
- Chu, L. E. U., Hodapp, K., & Boogert, A. 2020, *ApJ*, 904, 86
- Chuang, K. J., Fedoseev, G., Ioppolo, S., van Dishoeck, E. F., & Linnartz, H. 2016, *MNRAS*, 455, 1702

- Chuang, K. J., Fedoseev, G., Qasim, D., et al. 2020, *A&A*, 635, A199
- Chuang, K. J., Fedoseev, G., Qasim, D., et al. 2017, *MNRAS*, 467, 2552
- Chuang, K. J., Fedoseev, G., Qasim, D., et al. 2018, *ApJ*, 853, 102
- Chuang, K. J., Fedoseev, G., Scirè, C., et al. 2021, *A&A*, 650, A85
- Churchwell, E. 2002, *ARA&A*, 40, 27
- Cieza, L. A., Casassus, S., Tobin, J., et al. 2016, *Nature*, 535, 258
- Ciolek, G. E. & Roberge, W. G. 2002, *ApJ*, 567, 947
- Codella, C., Bianchi, E., Podio, L., et al. 2021, *A&A*, 654, A52
- Codella, C., Ceccarelli, C., Bianchi, E., et al. 2020, *A&A*, 635, A17
- Codella, C., Ceccarelli, C., Caselli, P., et al. 2017, *A&A*, 605, L3
- Codella, C., Maury, A. J., Gueth, F., et al. 2014, *A&A*, 563, L3
- Coletta, A., Fontani, F., Rivilla, V. M., et al. 2020, *A&A*, 641, A54
- Collings, M. P., Anderson, M. A., Chen, R., et al. 2004, *MNRAS*, 354, 1133
- Copernicus, N. 1543, *De revolutionibus orbium coelestium*
- Coudert, L. H., Motiyenko, R. A., Margulès, L., & Tchana Kwabia, F. 2021, *Journal of Molecular Spectroscopy*, 381, 111515
- Coudert, L. H., Zemouli, M., Motiyenko, R. A., Margulès, L., & Klee, S. 2014, *J. Chem. Phys.*, 140, 064307
- Coutens, A., Jørgensen, J. K., Persson, M. V., et al. 2014, *ApJ*, 792, L5
- Coutens, A., Jørgensen, J. K., van der Wiel, M. H. D., et al. 2016, *A&A*, 590, L6
- Coutens, A., Ligterink, N. F. W., Loison, J. C., et al. 2019, *A&A*, 623, L13
- Crapsi, A., Caselli, P., Walmsley, C. M., et al. 2005, *ApJ*, 619, 379
- Crapsi, A., van Dishoeck, E. F., Hogerheijde, M. R., Pontoppidan, K. M., & Dullemond, C. P. 2008, *A&A*, 486, 245
- Cridland, A. J., Rosotti, G. P., Tabone, B., et al. 2022, *A&A*, 662, A90
- Crockett, N. R., Bergin, E. A., Neill, J. L., et al. 2015, *ApJ*, 806, 239
- Crockett, N. R., Bergin, E. A., Neill, J. L., et al. 2014, *ApJ*, 787, 112
- Cruz-Sáenz de Miera, F., Kóspál, Á., Ábrahám, P., Liu, H. B., & Takami, M. 2019, *ApJ*, 882, L4
- Csengeri, T., Belloche, A., Bontemps, S., et al. 2019, *A&A*, 632, A57

- Cuppen, H. M., Walsh, C., Lamberts, T., et al. 2017, *Space Sci. Rev.*, 212, 1
- Dartois, E., Schutte, W., Geballe, T. R., et al. 1999, *A&A*, 342, L32
- Dartois, E., Thi, W. F., Geballe, T. R., et al. 2003, *A&A*, 399, 1009
- De Simone, M., Ceccarelli, C., Codella, C., et al. 2020, *ApJ*, 896, L3
- Draine, B. T. 1980, *ApJ*, 241, 1021
- Draine, B. T. & Lee, H. M. 1984, *ApJ*, 285, 89
- Draine, B. T. & Li, A. 2007, *ApJ*, 657, 810
- Draine, B. T. & McKee, C. F. 1993, *ARA&A*, 31, 373
- Draine, B. T., Roberge, W. G., & Dalgarno, A. 1983, *ApJ*, 264, 485
- Drozdovskaya, M. N., Coudert, L. H., Margulès, L., et al. 2022, *A&A*, 659, A69
- Drozdovskaya, M. N., Schroeder I, I. R. H. G., Rubin, M., et al. 2021, *MNRAS*, 500, 4901
- Drozdovskaya, M. N., van Dishoeck, E. F., Jørgensen, J. K., et al. 2018, *MNRAS*, 476, 4949
- Drozdovskaya, M. N., van Dishoeck, E. F., Rubin, M., Jørgensen, J. K., & Altwegg, K. 2019, *MNRAS*, 490, 50
- Drozdovskaya, M. N., Walsh, C., van Dishoeck, E. F., et al. 2016, *MNRAS*, 462, 977
- Drozdovskaya, M. N., Walsh, C., Visser, R., Harsono, D., & van Dishoeck, E. F. 2014, *MNRAS*, 445, 913
- Drozdovskaya, M. N., Walsh, C., Visser, R., Harsono, D., & van Dishoeck, E. F. 2015, *MNRAS*, 451, 3836
- Dunham, M. M., Allen, L. E., Evans, Neal J., I., et al. 2015, *ApJS*, 220, 11
- Dzib, S. A., Loinard, L., Ortiz-León, G. N., Rodríguez, L. F., & Galli, P. A. B. 2018a, *ApJ*, 867, 151
- Dzib, S. A., Ortiz-León, G. N., Hernández-Gómez, A., et al. 2018b, *A&A*, 614, A20
- El-Abd, S. J., Brogan, C. L., Hunter, T. R., et al. 2019, *ApJ*, 883, 129
- Elia, D., Merello, M., Molinari, S., et al. 2021, *MNRAS*, 504, 2742
- Elia, D., Molinari, S., Schisano, E., et al. 2017, *MNRAS*, 471, 100
- Endres, C. P., Drouin, B. J., Pearson, J. C., et al. 2009, *A&A*, 504, 635

- Endres, C. P., Schlemmer, S., Schilke, P., Stutzki, J., & Müller, H. S. P. 2016, *Journal of Molecular Spectroscopy*, 327, 95
- Enoch, M. L., Corder, S., Duchêne, G., et al. 2011, *ApJS*, 195, 21
- Enoch, M. L., Evans, Neal J. I., Sargent, A. I., & Glenn, J. 2009, *ApJ*, 692, 973
- Evans, Neal J. I., Allen, L. E., Blake, G. A., et al. 2003, *PASP*, 115, 965
- Fabre, B., Krieger, D., & Muentert, J. S. 1977, *J. Chem. Phys.*, 67, 1576
- Faure, A., Faure, M., Theulé, P., Quirico, E., & Schmitt, B. 2015, *A&A*, 584, A98
- Fayolle, E. C., Bertin, M., Romanzin, C., et al. 2011, *ApJ*, 739, L36
- Fayolle, E. C., Bertin, M., Romanzin, C., et al. 2013, *A&A*, 556, A122
- Fayolle, E. C., Öberg, K. I., Garrod, R. T., van Dishoeck, E. F., & Bisschop, S. E. 2015, *A&A*, 576, A45
- Fayolle, E. C., Öberg, K. I., Jørgensen, J. K., et al. 2017, *Nature Astronomy*, 1, 703
- Fedoseev, G., Chuang, K. J., Ioppolo, S., et al. 2017, *ApJ*, 842, 52
- Fedoseev, G., Cuppen, H. M., Ioppolo, S., Lamberts, T., & Linnartz, H. 2015, *MNRAS*, 448, 1288
- Fedoseev, G., Qasim, D., Chuang, K.-J., et al. 2022, *ApJ*, 924, 110
- Ferrero, S., Zamirri, L., Ceccarelli, C., et al. 2020, *ApJ*, 904, 11
- Fisher, J., Paciga, G., Xu, L.-H., et al. 2007, *Journal of Molecular Spectroscopy*, 245, 7
- Flower, D. R. & Pineau des Forêts, G. 2003, *MNRAS*, 343, 390
- Flower, D. R. & Pineau des Forêts, G. 2010, *MNRAS*, 406, 1745
- Flower, D. R. & Pineau des Forêts, G. 2015, *A&A*, 578, A63
- Flower, D. R., Pineau des Forêts, G., & Hartquist, T. W. 1985, *MNRAS*, 216, 775
- Fontani, F., Busquet, G., Palau, A., et al. 2015, *A&A*, 575, A87
- Frank, A., Ray, T. P., Cabrit, S., et al. 2014, in *Protostars and Planets VI*, ed. H. Beuther, R. S. Klessen, C. P. Dullemond, & T. Henning, 451
- Frerking, M. A., Langer, W. D., & Wilson, R. W. 1982, *ApJ*, 262, 590
- Fuchs, G. W., Cuppen, H. M., Ioppolo, S., et al. 2009, *A&A*, 505, 629
- Fuente, A., Cernicharo, J., Caselli, P., et al. 2014, *A&A*, 568, A65
- Furlan, E., Fischer, W. J., Ali, B., et al. 2016, *ApJS*, 224, 5

- Furuya, K., van Dishoeck, E. F., & Aikawa, Y. 2016, *A&A*, 586, A127
- Galametz, M., Maury, A. J., Valdivia, V., et al. 2019, *A&A*, 632, A5
- Galilei, G. 1610, *Sidereus nuncius*
- Garrod, R., Park, I. H., Caselli, P., & Herbst, E. 2006, *Faraday Discussions*, 133, 51
- Garrod, R. T. 2013, *ApJ*, 765, 60
- Garrod, R. T. & Herbst, E. 2006, *A&A*, 457, 927
- Garrod, R. T., Jin, M., Matis, K. A., et al. 2022, *ApJS*, 259, 1
- Garrod, R. T., Widicus Weaver, S. L., & Herbst, E. 2008, *ApJ*, 682, 283
- Garufi, A., Podio, L., Codella, C., et al. 2022, *A&A*, 658, A104
- Geballe, T. R., Baas, F., Greenberg, J. M., & Schutte, W. 1985, *A&A*, 146, L6
- Geers, V. C., van Dishoeck, E. F., Pontoppidan, K. M., et al. 2009, *A&A*, 495, 837
- Geppert, W. D., Hamberg, M., Thomas, R. D., et al. 2006, *Faraday Discussions*, 133, 177
- Gerakines, P. A., Schutte, W. A., & Ehrenfreund, P. 1996, *A&A*, 312, 289
- Gerakines, P. A., Whittet, D. C. B., Ehrenfreund, P., et al. 1999, *ApJ*, 522, 357
- Gerin, M., Pety, J., Commerçon, B., et al. 2017, *A&A*, 606, A35
- Gibb, E. L., Whittet, D. C. B., Schutte, W. A., et al. 2000, *ApJ*, 536, 347
- Godard, B., Pineau des Forêts, G., Lesaffre, P., et al. 2019, *A&A*, 622, A100
- Goicoechea, J. R., Cernicharo, J., Karska, A., et al. 2012, *A&A*, 548, A77
- Goicoechea, J. R. & Cuadrado, S. 2021, *A&A*, 647, L7
- Goldsmith, P. F. & Langer, W. D. 1999, *ApJ*, 517, 209
- Goto, M., Vasyunin, A. I., Giuliano, B. M., et al. 2021, *A&A*, 651, A53
- Greene, T. P., Wilking, B. A., André, P., Young, E. T., & Lada, C. J. 1994, *ApJ*, 434, 614
- Grim, R. J. A. & Greenberg, J. M. 1987, *ApJ*, 321, L91
- Groner, P., Albert, S., Herbst, E., et al. 2002, *ApJS*, 142, 145
- Guillet, V., Hennebelle, P., Pineau des Forêts, G., et al. 2020, *A&A*, 643, A17
- Guillet, V., Jones, A. P., & Pineau Des Forêts, G. 2009, *A&A*, 497, 145

- Guillet, V., Pineau Des Forêts, G., & Jones, A. P. 2007, *A&A*, 476, 263
- Guillet, V., Pineau des Forêts, G., & Jones, A. P. 2011, *A&A*, 527, A123
- Guilloteau, S., Bachiller, R., Fuente, A., & Lucas, R. 1992, *A&A*, 265, L49
- Gusdorf, A., Cabrit, S., Flower, D. R., & Pineau des Forêts, G. 2008a, *A&A*, 482, 809
- Gusdorf, A., Pineau des Forêts, G., Cabrit, S., & Flower, D. R. 2008b, *A&A*, 490, 695
- Hacar, A. & Tafalla, M. 2011, *A&A*, 533, A34
- Hacar, A., Tafalla, M., & Alves, J. 2017, *A&A*, 606, A123
- Hacar, A., Tafalla, M., Kauffmann, J., & Kovács, A. 2013, *A&A*, 554, A55
- Harsono, D., Bjerkeli, P., van der Wiel, M. H. D., et al. 2018, *Nature Astronomy*, 2, 646
- Harsono, D., Jørgensen, J. K., van Dishoeck, E. F., et al. 2014, *A&A*, 562, A77
- Harsono, D., van der Wiel, M. H. D., Bjerkeli, P., et al. 2021, *A&A*, 646, A72
- Harsono, D., van Dishoeck, E. F., Bruderer, S., Li, Z. Y., & Jørgensen, J. K. 2015, *A&A*, 577, A22
- Hartmann, L., Herczeg, G., & Calvet, N. 2016, *ARA&A*, 54, 135
- Hartquist, T. W., Dalgarno, A., & Oppenheimer, M. 1980, *ApJ*, 236, 182
- Hasegawa, T. I. & Herbst, E. 1993, *MNRAS*, 263, 589
- Hatchell, J., Fuller, G. A., & Richer, J. S. 2007, *A&A*, 472, 187
- Heays, A. N., Bosman, A. D., & van Dishoeck, E. F. 2017, *A&A*, 602, A105
- Hennebelle, P., Commerçon, B., Chabrier, G., & Marchand, P. 2016, *ApJ*, 830, L8
- Henning, T. & Salama, F. 1998, *Science*, 282, 2204
- Herbst, E. & van Dishoeck, E. F. 2009, *ARA&A*, 47, 427
- Herczeg, G. J., Karska, A., Bruderer, S., et al. 2012, *A&A*, 540, A84
- Hidaka, H., Watanabe, M., Kouchi, A., & Watanabe, N. 2009, *ApJ*, 702, 291
- Hildebrand, R. H. 1983, *QJRAS*, 24, 267
- Hirano, N. & Liu, F.-c. 2014, *ApJ*, 789, 50
- Holdship, J., Viti, S., Jimenez-Serra, I., et al. 2016, *MNRAS*, 463, 802

- Hollenbach, D., Kaufman, M. J., Bergin, E. A., & Melnick, G. J. 2009, *ApJ*, 690, 1497
- Hollis, J. M., Lovas, F. J., & Jewell, P. R. 2000, *ApJ*, 540, L107
- Hsieh, T.-H., Murillo, N. M., Belloche, A., et al. 2019, *ApJ*, 884, 149
- Hsu, S.-Y., Liu, S.-Y., Liu, T., et al. 2022, *ApJ*, 927, 218
- Hudson, R. L., Gerakines, P. A., & Ferrante, R. F. 2018, *Spectrochimica Acta Part A: Molecular Spectroscopy*, 193, 33
- Hull, C. L. H., Girart, J. M., Tychoniec, Ł., et al. 2017, *ApJ*, 847, 92
- Ilee, J. D., Cyganowski, C. J., Nazari, P., et al. 2016, *MNRAS*, 462, 4386
- Ilyushin, V., Kryvda, A., & Alekseev, E. 2009, *Journal of Molecular Spectroscopy*, 255, 32
- Ilyushin, V. V., Müller, H. S. P., Jørgensen, J. K., et al. 2022, *A&A*, 658, A127
- Ioppolo, S., Fedoseev, G., Chuang, K. J., et al. 2021, *Nature Astronomy*, 5, 197
- Isokoski, K., Bottinelli, S., & van Dishoeck, E. F. 2013, *A&A*, 554, A100
- Jacobsen, S. K., Jørgensen, J. K., Di Francesco, J., et al. 2019, *A&A*, 629, A29
- Jacobsen, S. K., Jørgensen, J. K., van der Wiel, M. H. D., et al. 2018, *A&A*, 612, A72
- Jeans, J. H. 1928, *Astronomy and cosmogony*
- Jensen, S. S., Jørgensen, J. K., Kristensen, L. E., et al. 2021, *A&A*, 650, A172
- Jensen, S. S., Jørgensen, J. K., Kristensen, L. E., et al. 2019, *A&A*, 631, A25
- Jiménez-Escobar, A. & Muñoz Caro, G. M. 2011, *A&A*, 536, A91
- Jiménez-Serra, I., Vasyunin, A. I., Spezzano, S., et al. 2021, *ApJ*, 917, 44
- Johnson, H. R. & Strandberg, M. W. P. 1952, *J. Chem. Phys.*, 20, 687
- Johnston, K. G., Robitaille, T. P., Beuther, H., et al. 2015, *ApJ*, 813, L19
- Jørgensen, J. K., Belloche, A., & Garrod, R. T. 2020, *ARA&A*, 58, 727
- Jørgensen, J. K., Bourke, T. L., Myers, P. C., et al. 2005, *ApJ*, 632, 973
- Jørgensen, J. K., Harvey, P. M., Evans, Neal J., I., et al. 2006, *ApJ*, 645, 1246
- Jørgensen, J. K., Müller, H. S. P., Calcutt, H., et al. 2018, *A&A*, 620, A170
- Jørgensen, J. K., Schöier, F. L., & van Dishoeck, E. F. 2002, *A&A*, 389, 908

- Jørgensen, J. K., van der Wiel, M. H. D., Coutens, A., et al. 2016, *A&A*, 595, A117
- Jørgensen, J. K., van Dishoeck, E. F., Visser, R., et al. 2009, *A&A*, 507, 861
- Jørgensen, J. K., Visser, R., Williams, J. P., & Bergin, E. A. 2015, *A&A*, 579, A23
- Kaifu, N., Morimoto, M., Nagane, K., et al. 1974, *ApJ*, 191, L135
- Karska, A., Kaufman, M. J., Kristensen, L. E., et al. 2018, *ApJS*, 235, 30
- Kessler, M. F., Steinz, J. A., Anderegg, M. E., et al. 1996, *A&A*, 315, L27
- Keto, E. 2003, *ApJ*, 599, 1196
- Keto, E. 2007, *ApJ*, 666, 976
- Kleiner, I., Lovas, F. J., & Godefroid, M. 1996, *Journal of Physical and Chemical Reference Data*, 25, 1113
- Knacke, R. F., McCorkle, S., Puetter, R. C., Erickson, E. F., & Kraetschmer, W. 1982, *ApJ*, 260, 141
- Kounkel, M., Hartmann, L., Loinard, L., et al. 2017, *ApJ*, 834, 142
- Kristensen, L. E. & Dunham, M. M. 2018, *A&A*, 618, A158
- Kristensen, L. E., van Dishoeck, E. F., Bergin, E. A., et al. 2012, *A&A*, 542, A8
- Kristensen, L. E., van Dishoeck, E. F., van Kempen, T. A., et al. 2010, *A&A*, 516, A57
- Krumholz, M. R., Bate, M. R., Arce, H. G., et al. 2014, in *Protostars and Planets VI*, ed. H. Beuther, R. S. Klessen, C. P. Dullemond, & T. Henning, 243
- Kuiper, R. & Hosokawa, T. 2018, *A&A*, 616, A101
- Kulterer, B. M., Drozdovskaya, M. N., Antonellini, S., Walsh, C., & Millar, T. J. 2022, *ACS Earth and Space Chemistry*, 6, 1171
- Lacy, J. H., Faraji, H., Sandford, S. A., & Allamandola, L. J. 1998, *ApJ*, 501, L105
- Lacy, J. H., Knacke, R., Geballe, T. R., & Tokunaga, A. T. 1994, *ApJ*, 428, L69
- Lacy, J. H., Sneden, C., Kim, H., & Jaffe, D. T. 2017, *ApJ*, 838, 66
- Lada, C. J. 1987, in *Star Forming Regions*, ed. M. Peimbert & J. Jugaku, Vol. 115, 1
- Lada, C. J. & Lada, E. A. 2003, *ARA&A*, 41, 57
- Lahuis, F., van Dishoeck, E. F., Jørgensen, J. K., Blake, G. A., & Evans, N. J. 2010, *A&A*, 519, A3

- Langer, W. D., Velusamy, T., Kuiper, T. B. H., et al. 1997, *ApJ*, 480, L63
- Larson, R. B. 1969, *MNRAS*, 145, 271
- Lattanzi, V., Bizzocchi, L., Vasyunin, A. I., et al. 2020, *A&A*, 633, A118
- Lauvergnat, D., Coudert, L. H., Klee, S., & Smirnov, M. 2009, *Journal of Molecular Spectroscopy*, 256, 204
- Law, C. J., Zhang, Q., Öberg, K. I., et al. 2021, *ApJ*, 909, 214
- Le Bourlot, J., Pineau des Forêts, G., Flower, D. R., & Cabrit, S. 2002, *MNRAS*, 332, 985
- Lee, C.-F., Codella, C., Li, Z.-Y., & Liu, S.-Y. 2019a, *ApJ*, 876, 63
- Lee, C.-F., Ho, P. T. P., Bourke, T. L., et al. 2008, *ApJ*, 685, 1026
- Lee, C.-F., Ho, P. T. P., Li, Z.-Y., et al. 2017a, *Nature Astronomy*, 1, 0152
- Lee, C.-F., Li, Z.-Y., Hirano, N., et al. 2018, *ApJ*, 863, 94
- Lee, C.-F., Li, Z.-Y., Ho, P. T. P., et al. 2017b, *Science Advances*, 3, e1602935
- Lee, C.-F., Li, Z.-Y., Ho, P. T. P., et al. 2017c, *ApJ*, 843, 27
- Lee, J.-E., Lee, S., Baek, G., et al. 2019b, *Nature Astronomy*, 3, 314
- Lehmann, A., Godard, B., Pineau des Forêts, G., & Falgarone, E. 2020, *A&A*, 643, A101
- Lehtinen, K., Haikala, L. K., Mattila, K., & Lemke, D. 2001, *A&A*, 367, 311
- Lesaffre, P., Pineau des Forêts, G., Godard, B., et al. 2013, *A&A*, 550, A106
- Li, Z.-Y., Krasnopolsky, R., & Shang, H. 2013, *ApJ*, 774, 82
- Li, Z.-Y., Krasnopolsky, R., Shang, H., & Zhao, B. 2014, *ApJ*, 793, 130
- Ligterink, N. F. W., Ahmadi, A., Coutens, A., et al. 2021, *A&A*, 647, A87
- Ligterink, N. F. W., Ahmadi, A., Luitel, B., et al. 2022, *ACS Earth and Space Chemistry*, 6, 455
- Ligterink, N. F. W., Calcutt, H., Coutens, A., et al. 2018a, *A&A*, 619, A28
- Ligterink, N. F. W., Terwisscha van Scheltinga, J., Taquet, V., et al. 2018b, *MNRAS*, 480, 3628
- Ligterink, N. F. W., Walsh, C., Bhuin, R. G., et al. 2018c, *A&A*, 612, A88
- Linnartz, H., Ioppolo, S., & Fedoseev, G. 2015, *International Reviews in Physical Chemistry*, 34, 205
- Linsky, J. L., Draine, B. T., Moos, H. W., et al. 2006, *ApJ*, 647, 1106

- López-Sepulcre, A., Sakai, N., Neri, R., et al. 2017, *A&A*, 606, A121
- Lumsden, S. L., Hoare, M. G., Urquhart, J. S., et al. 2013, *ApJS*, 208, 11
- Lykke, J. M., Coutens, A., Jørgensen, J. K., et al. 2017, *A&A*, 597, A53
- Mamajek, E. E. 2008, *Astronomische Nachrichten*, 329, 10
- Manara, C. F., Morbidelli, A., & Guillot, T. 2018, *A&A*, 618, L3
- Mangum, J. G. & Shirley, Y. L. 2015, *PASP*, 127, 266
- Manigand, S., Calcutt, H., Jørgensen, J. K., et al. 2019, *A&A*, 623, A69
- Manigand, S., Jørgensen, J. K., Calcutt, H., et al. 2020, *A&A*, 635, A48
- Marcelino, N., Gerin, M., Cernicharo, J., et al. 2018, *A&A*, 620, A80
- Martín-Doménech, R., Bergner, J. B., Öberg, K. I., et al. 2021, *ApJ*, 923, 155
- Martín-Doménech, R., Bergner, J. B., Öberg, K. I., & Jørgensen, J. K. 2019, *ApJ*, 880, 130
- Mathis, J. S., Mezger, P. G., & Panagia, N. 1983, *A&A*, 500, 259
- Mathis, J. S., Rumpl, W., & Nordsieck, K. H. 1977, *ApJ*, 217, 425
- Maud, L. T., Cesaroni, R., Kumar, M. S. N., et al. 2019, *A&A*, 627, L6
- Maury, A. J., André, P., Testi, L., et al. 2019, *A&A*, 621, A76
- Maury, A. J., Belloche, A., André, P., et al. 2014, *A&A*, 563, L2
- McCaughrean, M. J., Rayner, J. T., & Zinnecker, H. 1994, *ApJ*, 436, L189
- McGuire, B. A. 2018, *ApJS*, 239, 17
- McGuire, B. A. 2022, *ApJS*, 259, 30
- McKee, C. F. & Tan, J. C. 2002, *Nature*, 416, 59
- McMullin, J. P., Waters, B., Schiebel, D., Young, W., & Golap, K. 2007, in *Astronomical Society of the Pacific Conference Series*, Vol. 376, *Astronomical Data Analysis Software and Systems XVI*, ed. R. A. Shaw, F. Hill, & D. J. Bell, 127
- Mège, P., Russeil, D., Zavagno, A., et al. 2021, *A&A*, 646, A74
- Mehring, D. M., Snyder, L. E., Miao, Y., & Lovas, F. J. 1997, *ApJ*, 480, L71
- Mellon, R. R. & Li, Z.-Y. 2008, *ApJ*, 681, 1356
- Milam, S. N., Savage, C., Brewster, M. A., Ziurys, L. M., & Wyckoff, S. 2005, *ApJ*, 634, 1126

- Minissale, M., Aikawa, Y., Bergin, E., et al. 2022, *ACS Earth and Space Chemistry*, 6, 597
- Minissale, M., Dulieu, F., Cazaux, S., & Hocuk, S. 2016, *A&A*, 585, A24
- Miotello, A., Testi, L., Lodato, G., et al. 2014, *A&A*, 567, A32
- Miura, H., Yamamoto, T., Nomura, H., et al. 2017, *ApJ*, 839, 47
- Molinari, S., Swinyard, B., Bally, J., et al. 2010, *A&A*, 518, L100
- Moscadelli, L., Beuther, H., Ahmadi, A., et al. 2021, *A&A*, 647, A114
- Motte, F., Bontemps, S., & Louvet, F. 2018, *ARA&A*, 56, 41
- Muñoz Caro, G. M., Chen, Y. J., Aparicio, S., et al. 2016, *A&A*, 589, A19
- Müller, H. S. P., Belloche, A., Xu, L.-H., et al. 2016, *A&A*, 587, A92
- Müller, H. S. P. & Christen, D. 2004, *Journal of Molecular Spectroscopy*, 228, 298
- Müller, H. S. P., Schlöder, F., Stutzki, J., & Winnewisser, G. 2005, *Journal of Molecular Structure*, 742, 215
- Müller, H. S. P., Thorwirth, S., Roth, D. A., & Winnewisser, G. 2001, *A&A*, 370, L49
- Mumma, M. J. & Charnley, S. B. 2011, *ARA&A*, 49, 471
- Murillo, N. M., Bruderer, S., van Dishoeck, E. F., et al. 2015, *A&A*, 579, A114
- Murillo, N. M., Hsieh, T. H., & Walsh, C. 2022, *A&A*, 665, A68
- Murillo, N. M., Lai, S.-P., Bruderer, S., Harsono, D., & van Dishoeck, E. F. 2013, *A&A*, 560, A103
- Murillo, N. M., van Dishoeck, E. F., Tobin, J. J., & Fedele, D. 2016, *A&A*, 592, A56
- Murillo, N. M., van Dishoeck, E. F., van der Wiel, M. H. D., et al. 2018, *A&A*, 617, A120
- Nagaoka, A., Watanabe, N., & Kouchi, A. 2005, *ApJ*, 624, L29
- Nagaoka, A., Watanabe, N., & Kouchi, A. 2007, *Journal of Physical Chemistry A*, 111, 3016
- Navarro-Almaida, D., Le Gal, R., Fuente, A., et al. 2020, *A&A*, 637, A39
- Nazari, P., Meijerhof, J. D., van Gelder, M. L., et al. 2022a, *A&A*, in press.
- Nazari, P., Tabone, B., Rosotti, G. P., et al. 2022b, *A&A*, 663, A58
- Nazari, P., van Gelder, M. L., van Dishoeck, E. F., et al. 2021, *A&A*, 650, A150

- Neill, J. L., Bergin, E. A., Lis, D. C., et al. 2014, *ApJ*, 789, 8
- Neill, J. L., Crockett, N. R., Bergin, E. A., Pearson, J. C., & Xu, L.-H. 2013, *ApJ*, 777, 85
- Neufeld, D. A. & Hollenbach, D. J. 1994, *ApJ*, 428, 170
- Neufeld, D. A. & Kaufman, M. J. 1993, *ApJ*, 418, 263
- Neufeld, D. A., Nisini, B., Giannini, T., et al. 2009, *ApJ*, 706, 170
- Nisini, B., Benedettini, M., Codella, C., et al. 2010, *A&A*, 518, L120
- Nisini, B., Santangelo, G., Antonucci, S., et al. 2013, *A&A*, 549, A16
- Nisini, B., Santangelo, G., Giannini, T., et al. 2015, *ApJ*, 801, 121
- Noble, J. A., Congiu, E., Dulieu, F., & Fraser, H. J. 2012, *MNRAS*, 421, 768
- Öberg, K. I. 2016, *Chemical Reviews*, 116, 9631
- Öberg, K. I. & Bergin, E. A. 2021, *Phys. Rep.*, 893, 1
- Öberg, K. I., Boogert, A. C. A., Pontoppidan, K. M., et al. 2008, *ApJ*, 678, 1032
- Öberg, K. I., Boogert, A. C. A., Pontoppidan, K. M., et al. 2011, *ApJ*, 740, 109
- Öberg, K. I., Bottinelli, S., Jørgensen, J. K., & van Dishoeck, E. F. 2010, *ApJ*, 716, 825
- Öberg, K. I., Garrod, R. T., van Dishoeck, E. F., & Linnartz, H. 2009, *A&A*, 504, 891
- Öberg, K. I., Guzmán, V. V., Furuya, K., et al. 2015, *Nature*, 520, 198
- Ohno, Y., Oyama, T., Tamanai, A., et al. 2022, *ApJ*, 932, 101
- Olofsson, S. & Olofsson, G. 2009, *A&A*, 498, 455
- Ordu, M. H., Zingsheim, O., Belloche, A., et al. 2019, *A&A*, 629, A72
- Ortiz-León, G. N., Dzib, S. A., Kounkel, M. A., et al. 2017, *ApJ*, 834, 143
- Ortiz-León, G. N., Loinard, L., Dzib, S. A., et al. 2018, *ApJ*, 865, 73
- Ospina-Zamudio, J., Lefloch, B., Ceccarelli, C., et al. 2018, *A&A*, 618, A145
- Owen, T., Bar-Nun, A., & Kleinfeld, I. 1992, *Nature*, 358, 43
- Oya, Y., López-Sepulcre, A., Sakai, N., et al. 2019, *ApJ*, 881, 112
- Pagani, L., Favre, C., Goldsmith, P. F., et al. 2017, *A&A*, 604, A32
- Palau, A., Estalella, R., Girart, J. M., et al. 2014, *ApJ*, 785, 42

- Palumbo, M. E., Geballe, T. R., & Tielens, A. G. G. M. 1997, *ApJ*, 479, 839
- Palumbo, M. E., Tielens, A. G. G. M., & Tokunaga, A. T. 1995, *ApJ*, 449, 674
- Parise, B., Castets, A., Herbst, E., et al. 2004, *A&A*, 416, 159
- Parise, B., Ceccarelli, C., Tielens, A. G. G. M., et al. 2002, *A&A*, 393, L49
- Pearson, J. C., Brauer, C. S., & Drouin, B. J. 2008, *Journal of Molecular Spectroscopy*, 251, 394
- Pearson, J. C., Yu, S., & Drouin, B. J. 2012, *Journal of Molecular Spectroscopy*, 280, 119
- Penteado, E. M., Walsh, C., & Cuppen, H. M. 2017, *ApJ*, 844, 71
- Perotti, G., Jørgensen, J. K., Fraser, H. J., et al. 2021, *A&A*, 650, A168
- Perotti, G., Rocha, W. R. M., Jørgensen, J. K., et al. 2020, *A&A*, 643, A48
- Persson, M. V., Harsono, D., Tobin, J. J., et al. 2016, *A&A*, 590, A33
- Persson, M. V., Jørgensen, J. K., Müller, H. S. P., et al. 2018, *A&A*, 610, A54
- Persson, M. V., Jørgensen, J. K., van Dishoeck, E. F., & Harsono, D. 2014, *A&A*, 563, A74
- Pezzuto, S., Elia, D., Schisano, E., et al. 2012, *A&A*, 547, A54
- Pickett, H. M., Poynter, R. L., Cohen, E. A., et al. 1998, *J. Quant. Spectr. Rad. Transf.*, 60, 883
- Podio, L., Eisloffel, J., Melnikov, S., Hodapp, K. W., & Bacciotti, F. 2011, *A&A*, 527, A13
- Pontoppidan, K. M., Dartois, E., van Dishoeck, E. F., Thi, W. F., & d'Hendecourt, L. 2003a, *A&A*, 404, L17
- Pontoppidan, K. M. & Dullemond, C. P. 2005, *A&A*, 435, 595
- Pontoppidan, K. M., Fraser, H. J., Dartois, E., et al. 2003b, *A&A*, 408, 981
- Pontoppidan, K. M., van Dishoeck, E. F., & Dartois, E. 2004, *A&A*, 426, 925
- Prasad, S. S. & Huntress, W. T., J. 1980, *ApJS*, 43, 1
- Prodanović, T., Steigman, G., & Fields, B. D. 2010, *MNRAS*, 406, 1108
- Qasim, D., Fedoseev, G., Chuang, K. J., et al. 2019a, *A&A*, 627, A1
- Qasim, D., Fedoseev, G., Lamberts, T., et al. 2019b, *ACS Earth and Space Chemistry*, 3, 986
- Rachid, M. G., Brunken, N., de Boe, D., et al. 2021, *A&A*, 653, A116

- Rachid, M. G., Terwisscha van Scheltinga, J., Koletzki, D., & Linnartz, H. 2020, *A&A*, 639, A4
- Ratajczak, A., Quirico, E., Faure, A., Schmitt, B., & Ceccarelli, C. 2009, *A&A*, 496, L21
- Reid, M. J., Menten, K. M., Brunthaler, A., et al. 2014, *ApJ*, 783, 130
- Rivière-Marichalar, P., Merín, B., Kamp, I., Eiroa, C., & Montesinos, B. 2016, *A&A*, 594, A59
- Rivilla, V. M., Beltrán, M. T., Cesaroni, R., et al. 2017, *A&A*, 598, A59
- Roberts, H., Fuller, G. A., Millar, T. J., Hatchell, J., & Buckle, J. V. 2002, *A&A*, 381, 1026
- Roberts, H., Herbst, E., & Millar, T. J. 2003, *ApJ*, 591, L41
- Roberts, H. & Millar, T. J. 2000, *A&A*, 361, 388
- Robitaille, T. P., Whitney, B. A., Indebetouw, R., Wood, K., & Denzmore, P. 2006, *ApJS*, 167, 256
- Rosotti, G. P., Ilee, J. D., Facchini, S., et al. 2021, *MNRAS*, 501, 3427
- Rubin, M., Altwegg, K., Balsiger, H., et al. 2019, *MNRAS*, 489, 594
- Sahu, D., Liu, S.-Y., Su, Y.-N., et al. 2019, *ApJ*, 872, 196
- Sakai, N., Hanawa, T., Zhang, Y., et al. 2019, *Nature*, 565, 206
- Sakai, N., Oya, Y., Higuchi, A. E., et al. 2017, *MNRAS*, 467, L76
- Sakai, N., Sakai, T., Hirota, T., et al. 2014, *Nature*, 507, 78
- Salpeter, E. E. 1955, *ApJ*, 121, 161
- Sana, H., de Mink, S. E., de Koter, A., et al. 2012, *Science*, 337, 444
- Sánchez-Monge, Á., Cesaroni, R., Beltrán, M. T., et al. 2013, *A&A*, 552, L10
- Sandell, G. 2000, *A&A*, 358, 242
- Santos, J. C., Chuang, K.-J., Lamberts, T., et al. 2022, *ApJ*, 931, L33
- Saraceno, P., André, P., Ceccarelli, C., Griffin, M., & Molinari, S. 1996, *A&A*, 309, 827
- Schilke, P., Walmsley, C. M., Pineau des Forêts, G., & Flower, D. R. 1997, *A&A*, 321, 293
- Schutte, W. A., Boogert, A. C. A., Tielens, A. G. G. M., et al. 1999, *A&A*, 343, 966

- Schutte, W. A. & Greenberg, J. M. 1997, *A&A*, 317, L43
- Schutte, W. A. & Khanna, R. K. 2003, *A&A*, 398, 1049
- Scibelli, S., Shirley, Y., Vasyunin, A., & Launhardt, R. 2021, *MNRAS*, 504, 5754
- Segura-Cox, D. M., Looney, L. W., Tobin, J. J., et al. 2018, *ApJ*, 866, 161
- Segura-Cox, D. M., Schmiedeke, A., Pineda, J. E., et al. 2020, *Nature*, 586, 228
- Seidensticker, K. J. & Schmidt-Kaler, T. 1989, *A&A*, 225, 192
- Shu, F. H., Adams, F. C., & Lizano, S. 1987, *ARA&A*, 25, 23
- Simons, M. A. J., Lamberts, T., & Cuppen, H. M. 2020, *A&A*, 634, A52
- Skouteris, D., Balucani, N., Ceccarelli, C., et al. 2018, *ApJ*, 854, 135
- Skouteris, D., Vazart, F., Ceccarelli, C., et al. 2017, *MNRAS*, 468, L1
- Smette, A., Sana, H., Noll, S., et al. 2015, *A&A*, 576, A77
- Smith, R. G., Sellgren, K., & Tokunaga, A. T. 1989, *ApJ*, 344, 413
- Stark, R., van der Tak, F. F. S., & van Dishoeck, E. F. 1999, *ApJ*, 521, L67
- Suutarinen, A. N., Kristensen, L. E., Mottram, J. C., Fraser, H. J., & van Dishoeck, E. F. 2014, *MNRAS*, 440, 1844
- Tabone, B., Cabrit, S., Bianchi, E., et al. 2017, *A&A*, 607, L6
- Tabone, B., Cabrit, S., Pineau des Forêts, G., et al. 2020, *A&A*, 640, A82
- Tabone, B., van Hemert, M. C., van Dishoeck, E. F., & Black, J. H. 2021, *A&A*, 650, A192
- Tafalla, M., Myers, P. C., Mardones, D., & Bachiller, R. 2000, *A&A*, 359, 967
- Tafalla, M., Usero, A., & Hacar, A. 2021, *A&A*, 646, A97
- Tan, J. C., Beltrán, M. T., Caselli, P., et al. 2014, in *Protostars and Planets VI*, ed. H. Beuther, R. S. Klessen, C. P. Dullemond, & T. Henning, 149
- Taquet, V., Bianchi, E., Codella, C., et al. 2019, *A&A*, 632, A19
- Taquet, V., Ceccarelli, C., & Kahane, C. 2012, *A&A*, 538, A42
- Taquet, V., Charnley, S. B., & Sipilä, O. 2014, *ApJ*, 791, 1
- Taquet, V., Codella, C., De Simone, M., et al. 2020, *A&A*, 637, A63
- Taquet, V., López-Sepulcre, A., Ceccarelli, C., et al. 2015, *ApJ*, 804, 81
- Taquet, V., Peters, P. S., Kahane, C., et al. 2013, *A&A*, 550, A127

- Terada, H. & Tokunaga, A. T. 2012, *ApJ*, 753, 19
- Tercero, B., Cuadrado, S., López, A., et al. 2018, *A&A*, 620, L6
- Terwisscha van Scheltinga, J., Ligterink, N. F. W., Boogert, A. C. A., van Dishoeck, E. F., & Linnartz, H. 2018, *A&A*, 611, A35
- Terwisscha van Scheltinga, J., Marcandalli, G., McClure, M. K., Hogerheijde, M. R., & Linnartz, H. 2021, *A&A*, 651, A95
- Theulé, P., Duvernay, F., Danger, G., et al. 2013, *Advances in Space Research*, 52, 1567
- Tielens, A. G. G. M. 1983, *A&A*, 119, 177
- Tielens, A. G. G. M. 2013, *Reviews of Modern Physics*, 85, 1021
- Tielens, A. G. G. M., McKee, C. F., Seab, C. G., & Hollenbach, D. J. 1994, *ApJ*, 431, 321
- Tielens, A. G. G. M., Tokunaga, A. T., Geballe, T. R., & Baas, F. 1991, *ApJ*, 381, 181
- Tobin, J. J., Hartmann, L., Chiang, H.-F., et al. 2012, *Nature*, 492, 83
- Tobin, J. J., Looney, L. W., Li, Z.-Y., et al. 2016, *ApJ*, 818, 73
- Torres, R. M., Loinard, L., Mioduszewski, A. J., & Rodríguez, L. F. 2007, *ApJ*, 671, 1813
- Tychoniec, Ł., Hull, C. L. H., Kristensen, L. E., et al. 2019, *A&A*, 632, A101
- Tychoniec, Ł., Hull, C. L. H., Tobin, J. J., & van Dishoeck, E. F. 2018a, in *IAU Symposium*, Vol. 332, *IAU Symposium*, ed. M. Cunningham, T. Millar, & Y. Aikawa, 249–253
- Tychoniec, Ł., Manara, C. F., Rosotti, G. P., et al. 2020, *A&A*, 640, A19
- Tychoniec, Ł., Tobin, J. J., Karska, A., et al. 2018b, *ApJS*, 238, 19
- Tychoniec, Ł., van Dishoeck, E. F., van 't Hoff, M. L. R., et al. 2021, *A&A*, 655, A65
- van Broekhuizen, F. A., Pontoppidan, K. M., Fraser, H. J., & van Dishoeck, E. F. 2005, *A&A*, 441, 249
- van der Marel, N., Booth, A. S., Leemker, M., van Dishoeck, E. F., & Ohashi, S. 2021, *A&A*, 651, L5
- van der Tak, F. F. S., Black, J. H., Schöier, F. L., Jansen, D. J., & van Dishoeck, E. F. 2007, *A&A*, 468, 627
- van der Tak, F. F. S., Boonman, A. M. S., Braakman, R., & van Dishoeck, E. F. 2003, *A&A*, 412, 133

- van der Tak, F. F. S., Chavarría, L., Herpin, F., et al. 2013, *A&A*, 554, A83
- van der Walt, S. J., Kristensen, L. E., Jørgensen, J. K., et al. 2021, *A&A*, 655, A86
- van Dishoeck, E. F., Blake, G. A., Jansen, D. J., & Groesbeck, T. D. 1995, *ApJ*, 447, 760
- van Dishoeck, E. F., Herbst, E., & Neufeld, D. A. 2013, *Chemical Reviews*, 113, 9043
- van Dishoeck, E. F., Kristensen, L. E., Mottram, J. C., et al. 2021, *A&A*, 648, A24
- van Gelder, M. L., Nazari, P., Tabone, B., et al. 2022, *A&A*, 662, A67
- van Gelder, M. L., Tabone, B., Tychoniec, Ł., et al. 2020, *A&A*, 639, A87
- van Gelder, M. L., Tabone, B., van Dishoeck, E. F., & Godard, B. 2021, *A&A*, 653, A159
- van Kempen, T. A., van Dishoeck, E. F., Güsten, R., et al. 2009a, *A&A*, 501, 633
- van Kempen, T. A., van Dishoeck, E. F., Hogerheijde, M. R., & Güsten, R. 2009b, *A&A*, 508, 259
- van 't Hoff, M. L. R., Bergin, E. A., Jørgensen, J. K., & Blake, G. A. 2020a, *ApJ*, 897, L38
- van 't Hoff, M. L. R., Harsono, D., Tobin, J. J., et al. 2020b, *ApJ*, 901, 166
- van 't Hoff, M. L. R., Harsono, D., van Gelder, M. L., et al. 2022, *ApJ*, 924, 5
- van 't Hoff, M. L. R., Tobin, J. J., Harsono, D., & van Dishoeck, E. F. 2018a, *A&A*, 615, A83
- van 't Hoff, M. L. R., Tobin, J. J., Trapman, L., et al. 2018b, *ApJ*, 864, L23
- van 't Hoff, M. L. R., van Dishoeck, E. F., Jørgensen, J. K., & Calcutt, H. 2020c, *A&A*, 633, A7
- Vastel, C., Bottinelli, S., Caux, E., Glorian, J. M., & Boiziot, M. 2015, in *SF2A-2015: Proceedings of the Annual meeting of the French Society of Astronomy and Astrophysics*, 313–316
- Vidal, T. H. G., Loison, J.-C., Jaziri, A. Y., et al. 2017, *MNRAS*, 469, 435
- Visser, R., Doty, S. D., & van Dishoeck, E. F. 2011, *A&A*, 534, A132
- Visser, R. & Dullemond, C. P. 2010, *A&A*, 519, A28
- Visser, R., Kristensen, L. E., Bruderer, S., et al. 2012, *A&A*, 537, A55

- Visser, R., van Dishoeck, E. F., Doty, S. D., & Dullemond, C. P. 2009, *A&A*, 495, 881
- Walsh, C., Millar, T. J., Nomura, H., et al. 2014, *A&A*, 563, A33
- Ward-Thompson, D., André, P., Crutcher, R., et al. 2007, in *Protostars and Planets V*, ed. B. Reipurth, D. Jewitt, & K. Keil, 33
- Watanabe, N. & Kouchi, A. 2002, *ApJ*, 571, L173
- Watson, W. D. 1974, *ApJ*, 188, 35
- Werner, M. W., Roellig, T. L., Low, F. J., et al. 2004, *ApJS*, 154, 1
- Whitney, B. A., Wood, K., Bjorkman, J. E., & Cohen, M. 2003, *ApJ*, 598, 1079
- Whittet, D. C. B. 2010, *ApJ*, 710, 1009
- Wilson, T. L. & Rood, R. 1994, *ARA&A*, 32, 191
- Xie, C., Haffert, S. Y., de Boer, J., et al. 2021, *A&A*, 650, L6
- Xu, L.-H., Fisher, J., Lees, R. M., et al. 2008, *Journal of Molecular Spectroscopy*, 251, 305
- Xu, L.-H. & Lovas, F. J. 1997, *Journal of Physical and Chemical Reference Data*, 26, 17
- Yang, Y.-L., Evans, Neal J., I., Smith, A., et al. 2020, *ApJ*, 891, 61
- Yang, Y.-L., Sakai, N., Zhang, Y., et al. 2021, *ApJ*, 910, 20
- Yen, H.-W., Koch, P. M., Takakuwa, S., et al. 2017, *ApJ*, 834, 178
- Yen, H.-W., Takakuwa, S., Ohashi, N., et al. 2014, *ApJ*, 793, 1
- Yildız, U. A., Kristensen, L. E., van Dishoeck, E. F., et al. 2012, *A&A*, 542, A86
- Yildız, U. A., Kristensen, L. E., van Dishoeck, E. F., et al. 2013, *A&A*, 556, A89
- Yorke, H. W., Bodenheimer, P., & Laughlin, G. 1993, *ApJ*, 411, 274
- Young, C. H. & Evans, Neal J., I. 2005, *ApJ*, 627, 293
- Zasowski, G., Kemper, F., Watson, D. M., et al. 2009, *ApJ*, 694, 459
- Zhang, Y., Tan, J. C., Sakai, N., et al. 2019, *ApJ*, 873, 73
- Zinnecker, H., Bastien, P., Arcoragi, J.-P., & Yorke, H. W. 1992, *A&A*, 265, 726
- Zinnecker, H. & Yorke, H. W. 2007, *ARA&A*, 45, 481
- Zucker, C., Speagle, J. S., Schlafly, E. F., et al. 2019, *ApJ*, 879, 125

Nederlandse samenvatting

Al sinds het ontstaan van de mensheid kijken we regelmatig omhoog naar de sterrenhemel en vragen we ons af wat die verre lichtpuntjes zijn. Al snel zagen we hier patronen in, de sterrenbeelden, en leerden we de sterren gebruiken als navigatie. Zelfs de planeten in ons eigen zonnestelsel konden al herkend worden aangezien deze lichtpuntjes zich anders aan de hemel bewegen dan de rest. Door de jaren heen werd het steeds duidelijker dat deze lichtpuntjes sterren zijn die heel ver van onze Aarde af liggen. Onze eigen Zon is ook een ster en alleen speciaal omdat deze zo dichtbij staat en ons van licht en warmte voorziet. Ondertussen weten we ook al dat er planeten rond andere sterren hangen. Inmiddels zijn er al meer dan 5000 planeten ontdekt rond andere sterren dan de Zon, wat statistisch gezien suggereert dat er gemiddeld één planeet rond elke ster draait. Planeten zijn dus heel gewoon in het universum, maar de diversiteit in planeten is groot. Rond sommige sterren draait bijvoorbeeld een Jupiter-achtige planeet ver binnen de baan van Mercurius, terwijl in andere planetenstelsels helemaal geen Jupiter-achtige planeet voorkomt. Ook de atmosferen van deze planeten verschillen enorm. Sommige zijn zoals hier op Aarde maar andere worden juist gedomineerd door methaan of zwavel.

Dit roept gelijk ook een aantal vragen op: hoe vormen sterren zoals de Zon? Hoe zijn de planeten in ons eigen zonnestelsel en rond andere sterren gevormd? Wat bepaalt de chemische samenstelling van deze planeten en is er ook leven op deze planeten? Inmiddels weten we dat planeten tegelijkertijd vormen met hun ster. Om dus te onderzoeken hoe de samenstelling van planeten tot stand komt kan men naar jonge sterren in vorming kijken. Dit proefschrift kijkt specifiek naar dit soort jonge sterren in vorming en onderzoekt of de samenstelling van het materiaal waaruit sterren en planeten vormen is geërfd van de moleculaire wolk waar ze uit worden geboren of dat de samenstelling onderweg verandert.

Jonge protosterren

Sterren vormen uit gigantische wolken die bestaan uit moleculair gas en kleine stofkorrels. Een voorbeeld van zo'n stervormingsgebied is afgebeeld in Fig. 1. Een wolk is heel dynamisch met een onregelmatige vorm en uit één wolk vormen zich

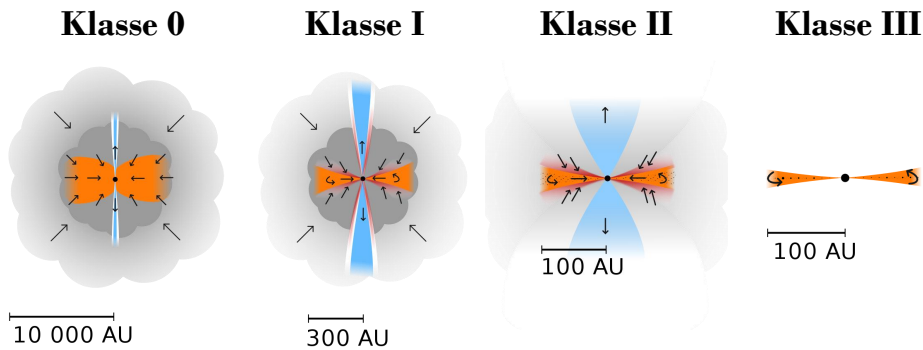


Figuur 1: De Carinanevel zoals gezien door de James Webb Ruimtetelescoop. In deze wolken worden nieuwe sterren en planeten geboren. De blauwe en gele sterren liggen op de voorgrond, terwijl de meest rode sterren zich diep in de moleculaire wolk bevinden. Afbeelding van: NASA, ESA, CSA, en STScI.

vaak ook meerdere sterren. Door een lokale instabiliteit kan een deel van de wolk ineen storten onder zijn eigen zwaartekracht. In de volgende fasen van stervorming is het belangrijk om een onderscheid te maken tussen hoe lage massa sterren (zoals de Zon) vormen en hoe hoge massa sterren, sterren die veel zwaarder zijn dan de Zon, vormen.

In het geval van lage massa sterren begint er in de kern van de ineenstortende wolk een protoster te vormen, zie Fig. 2. Door het behoud van draaimoment in de wolk vormt zich rond deze jonge protoster een schijf van materiaal. Gedurende de volgende 500 000 jaar groeit de massa van de ster doordat materiaal van de schijf op de ster valt. De schijf zelf groeit ook doordat de omliggende wolk op de schijf blijft vallen (Klassen 0 en I). Geleidelijk verdwijnt de omliggende wolk doordat deze op de schijf valt, maar ook omdat er sterke straalstromen worden gelanceerd vanuit de protoster die de wolk meeslepen. Er blijft een voor-hoofdreeksster over die is omringd door een protoplanetaire schijf (Klasse II). In deze protoplanetaire schijven bevinden zich hoogstwaarschijnlijk al embryo's van planeten. Gedurende de volgende tien miljoen jaar verdwijnt de protoplanetaire schijf doordat deze op planeten of de centrale ster valt en doordat deze wordt weggeblazen door de straling van de ster. Er blijft een zogeheten puinschijf over (Klasse III). Uiteindelijk wordt de ster geboren als er waterstoffusie begint in diens kern.

In het geval van een hoge massa ster (> 8 keer zo zwaar als de Zon) verschilt de evolutie van die van een lagere massa ster. Allereerst vormt een hoge massa ster vele malen sneller, binnen ongeveer 100 000 jaar. Al vroeg in diens evolutie worden de centrale regionen van het protostellair systeem warm genoeg om een



Figuur 2: Schematische weergave van de verschillende stadia van stervorming. In dit proefschrift ligt de focus op de jongste stadia, de Klasse 0 en Klasse I protosterren. Een AU is gelijk aan de (gemiddelde) afstand tussen de Aarde en de Zon (~ 150 miljoen kilometer). Afbeelding van: Magnus Persson.

rijke en complexe moleculaire chemie mogelijk te maken. Tevens begint er al ver voordat de omliggende wolk verdwenen is waterstoffusie in de kern van de zware ster, waardoor deze grote hoeveelheden ultraviolet (UV) licht gaat produceren. Dit leidt tot de totstandkoming van een klein gebied van geïoniseerd waterstof, een zogeheten HII gebied. Vergelijkbaar met lage massa sterren vormt zich een schijf van materiaal rondom de zware ster waardoor de ster zelf nog in massa kan toenemen. Uiteindelijk zorgt de grote stralingsdruk van de hoge massa ster ervoor dat de schijf en de omliggende wolk compleet worden weggeblazen.

Complexe organische moleculen

Gedurende alle stadia van het stervormingsproces kunnen waarnemingen van moleculen gebruikt worden om de eigenschappen van het protostellair systeem te beschrijven. Moleculair waterstof (H_2) is het meest voorkomende molecuul, gevolgd door koolstofmonoxide (CO). Andere veelvoorkomende moleculen zijn water (H_2O), ammonia (NH_3) en methaan (CH_4). De chemie in de interstellaire ruimte kan echter nog veel complexere moleculen produceren. Het meest voorkomende *complexe organische molecuul*, een molecuul met 6 of meer atomen waarvan één koolstof is, is methanol (CH_3OH). Deze organische moleculen kunnen echter nog meer complex worden zoals ethanol ($\text{C}_2\text{H}_5\text{OH}$), methylformiaat (CH_3OCHO) en glycolaldehyde (CH_2OHCHO). Ook prebiotische moleculen zoals formamide (NH_2CHO) en ureum ($(\text{NH}_2)_2\text{CO}$) zijn gedetecteerd rond jonge protosterren.

Deze complexe organische moleculen worden geproduceerd op de oppervlakte van stofkorrels in moleculaire wolken. De temperaturen in deze wolken zijn te laag (< 15 K) voor actieve chemie in de gasfase. Ook al bevatten de stofkorrels, die bestaan uit silicaten en koolstofachtig materiaal, maar ongeveer 1% van de totale massa, ze zijn ideale katalysatoren onder deze condities. Onder lage temperaturen blijven simpele moleculen, zoals CO , namelijk plakken aan deze stofkorrels en deze

vormen zo een *ijslaag* op het oppervlak. In dit ijs landen ook waterstofatomen die zich gemakkelijk door het ijs kunnen bewegen en kunnen reageren met moleculen in het ijs. Door opeenvolgende reacties van CO met waterstof worden HCO, formaldehyde (H_2CO) en uiteindelijk CH_3OH gevormd. Reacties tussen radicalen (zeer reactieve moleculen) leiden ook tot de vorming van nog complexere moleculen in het ijs zoals CH_3OCHO en CH_2OHCHO . Deze complexe moleculen blijven ook plakken in het ijs zolang de temperatuur beneden de ~ 100 K blijft.

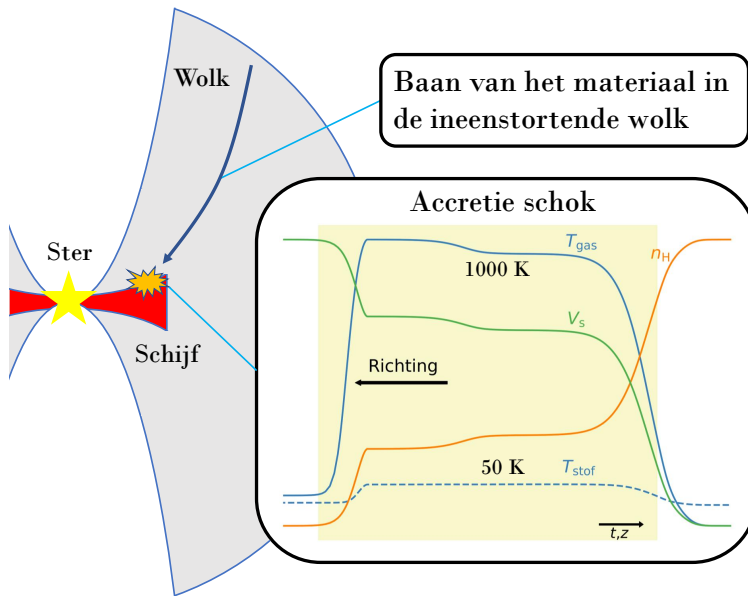
De temperatuur stijgt echter als het materiaal in de ineenstortende wolk dicht bij de centrale protoster komt. Wanneer de temperatuur boven de 100 K komt, sublimeren alle complexe moleculen tezamen met water van de stofkorrels. Dit gebeurt in de zogenaamde *hete kernen* van protostellaire systemen. Voornamelijk in de jongste protostellaire systemen (Klasse 0) zijn deze hete kernen groot in omvang waardoor deze complexe moleculen daar makkelijker zijn waar te nemen. In oudere systemen (Klasse I, II) is de temperatuur lager door de aanwezigheid van een (grote) protoplanetaire schijf. In de gasfase zijn complexe moleculen gemakkelijk waar te nemen met telescopen zoals de Atacama Large Millimeter/submillimeter Array (ALMA). Deze telescoop bevindt zich in Chili en kijkt op millimeter golflengten die mensen met het blote oog niet kunnen zien.

Gedurende de afgelopen jaren zijn deze complexe moleculen gronding bestudeerd in meerdere protostellaire systemen. Interessant genoeg lijken sommige verhoudingen tussen de abundanties van deze moleculen heel constant te zijn tussen de verschillende bronnen. Een goed voorbeeld is de verhouding tussen CH_3OCHO en CH_3OCH_3 , die ongeveer één is in zowel lage massa protosterren, hoge massa sterren en kometen. Dit geeft aan dat deze moleculen in vergelijkbare fysische condities vormen, in de moleculaire wolken op de oppervlakte van stofkorrels. De verhoudingen tussen andere complexe moleculen, zoals NH_2CHO en CH_3OH , laten echter grotere variaties zien, wat erop kan duiden dat lokale fysische condities in de hete kernen de verhoudingen kunnen veranderen. Het is dus interessant om de complexe moleculen te bestuderen en zo meer te weten komen over de chemische samenstelling en ook over de fysische condities in deze jonge protostellaire systemen.

Accretie schokken

De complexe organische moleculen worden dus vooral gevormd in de koude moleculaire wolken, maar met de ALMA telescoop nemen we ze vooral waar in de centrale en warme regionen rond protosterren. Tussen de koude wolk en de hete kern veranderen de fysische condities drastisch, zowel de temperatuur en dichtheid als de sterkte van de UV straling. Dit kan op zijn beurt effect hebben op de chemie. Het is daarom nog steeds onduidelijk of de chemische samenstelling in de schijf en hete kern worden geërfd van de koude wolk of dat deze (deels) wordt gereset, waar de moleculaire samenstelling (deels) wordt verandert. Een mogelijke manier die tot zo'n reset kan leiden, is een *accretie schok* op de grens tussen de ineenstortende wolk en de schijf, zie Fig. 3.

Een schok ontstaat als twee materialen met elkaar botsen en resulteert in een



Figuur 3: Schematische weergave van een protostellair systeem. De centrale protoster is weergegeven als de gele ster en de schijf in het rood. De ineenstortende wolk is afgebeeld in het grijs met daarin een voorbeeld van een baan die het materiaal richting de schijf volgt. Als het materiaal de schijf raakt, ontstaat er een accretie schok.

significante verhoging van de temperatuur en een onomkeerbare verhoging van de dichtheid. De sterkte van de schok hangt af van verschillende fysische factoren, voornamelijk de dichtheid, snelheid en de sterkte van het magnetisch veld. In het geval van accretie schokken is de snelheid relatief laag ($< 10 \text{ km s}^{-1}$) waardoor de temperatuur niet ver boven een paar duizend graden uit komt. Onder deze temperaturen dissociëert H_2 niet, maar het zorgt ervoor dat chemische reacties die niet gebeuren in de koude wolk nu wel plaats kunnen vinden. De temperatuur van het stof gaat ook omhoog, maar wordt niet veel hoger dan 50 K (-223°C). Hierdoor sublimeren simpele ijzen zoals CO en CH_4 , maar blijven water en complexe organische moleculen bevroren op de stofkorrels. Een deel van deze ijzen kan wel van de stofkorrels worden gesputterd door botsingen tussen stofkorrels en gas.

Voor de gasfase chemie van interstellaire schokken is het OH radicaal cruciaal. Deze wordt gevormd onder hoge temperaturen ($> 100 \text{ K}$) door een chemische reactie tussen H_2 en atomair zuurstof. Het OH radicaal is heel reactief en reageert daardoor snel met andere moleculen zoals H_2 wat leidt tot de vorming van water. Dit is vooral relevant als de temperatuur boven de 300 K ligt. Voor lagere temperaturen wordt geen water gevormd, maar reageert het OH radicaal vooral met zavel (S) waardoor er zwavelmonoxide (SO) en zwaveldioxide ontstaan (SO_2).

Het zijn ook deze twee moleculen (SO en SO_2) die vaak worden geassocieerd met accretie schokken. Waarnemingen met ALMA hebben laten zien dat warme straling van deze twee moleculen zich kan bevinden bij de grens van wolk en

schijf. Echter, straling van deze twee moleculen kan ook uit andere plekken van het protostellaire systeem komen, zoals uit de straalstromen. Het is daardoor nog onzeker of accretie schokken echt bestaan. Om robuuste conclusies te trekken over de oorsprong van de SO en SO₂ straling moet deze daarom goed vergeleken worden met schokmodellen. Dit is ook belangrijk om de sterkte van een accretie schok te bepalen en daarmee hoeveel de schok de chemie uit de wolk reset als het materiaal de schijf invloet.

Dit proefschrift

Dit proefschrift onderzoekt de mate waarin de moleculaire samenstelling in protostellaire schijven geërfd wordt van de moleculaire wolk. Twee onderwerpen staan centraal:

1. Complexe organische moleculen en wat deze kunnen vertellen over de fysische condities in zowel het protostellaire systeem zelf als de moleculaire wolk waaruit de ster wordt gevormd (Hoofdstukken 2, 3 en 4).
2. Het waarnemen en modelleren van accretie schokken en wat voor invloed deze kunnen hebben op de moleculaire samenstelling van het materiaal dat de schijf invloet (Hoofdstukken 5 en 6).

In de volgende paragrafen wordt per hoofdstuk een korte samenvatting gegeven van de belangrijkste resultaten.

Hoofdstuk 2 presenteert ALMA waarnemingen van drie lage massa Klasse 0 protosterren. Aan de hand van spectra worden de kolomdichtheden en excitatie temperaturen bepaald voor verschillende complexe organische moleculen die zuurstof bevatten. De abundanties van verscheidene moleculen zoals CH₃OCHO en di-methyl ether (CH₃OCH₃) ten opzichte van methanol zijn opmerkelijk constant in de drie bestudeerde protosterren, alsmede in andere protosterren die met ALMA zijn bestudeerd in de literatuur. Dit suggereert dat deze moleculen gevormd zijn onder vergelijkbare fysische condities, waarschijnlijk in de ijzen op het oppervlak van stofkorrels in de koude moleculaire wolken. Voor sommige bestudeerde moleculen zoals acetaldehyde (CH₃CHO) en C₂H₅OH zijn de abundanties ten opzichte van CH₃OH echter veel variabelere tussen de verschillende protosterren. Dit duidt erop dat voor deze moleculen de lokale fysische condities (o.a., temperatuur, UV straling) in de protostellaire systemen belangrijk zijn. In één van de protosterren is ook een koudere component van straling van de complexe moleculen aanwezig.

In *Hoofdstuk 3* kijken we alleen naar de straling van CH₃OH in zowel lage massa als hoge massa protosterren met als doel een link te leggen tussen de aanwezigheid van CH₃OH in de gasfase en fysische eigenschappen van het protostellaire systeem. Met het laatste wordt hier voornamelijk de aanwezigheid van een schijf bedoeld die de temperatuur in het systeem gemiddeld verlaagt of de aanwezigheid van optisch dikke stofkorrels die de straling van de hete kern van het protostellaire systeem blokkeren. Hiervoor worden ALMA waarnemingen gebruikt van Hoofdstuk 2 en uit het ALMA archief, van de Perseus ALMA Chemistry Survey (PEACHES) en

de ALMA Evolutionary study of High Mass Protocluster Formation in the Galaxy (ALMAGAL) programma's. Met data van de literatuur erbij worden er in totaal 184 verschillende protosterren bestudeerd. Er is duidelijk een correlatie tussen de totale methanol massa en de bolometrische lichtkracht, maar er is ook een spreiding van meer dan vier orden van grootte aanwezig voor zowel lage massa als hoge massa protosterren. Een simpel model van een sferische ineenstortende wolk beschrijft de bronnen met een hoge methanol massa heel goed, maar om de spreiding te kunnen verklaren zijn (grote) schijven en optisch dikke stofkorrels nodig.

In *Hoofdstuk 4* wordt er ook gekeken naar methanol, maar meer specifiek naar de verhouding van deuteriumatomen (D) tot waterstofatomen (H). De D/H verhouding van methanol is heel gevoelig voor de temperatuur in de koude moleculaire wolk en door deze te bestuderen in protostellare systemen kunnen we dus achterhalen wat de temperatuur in eerdere stadia was. Hiervoor gebruiken we de ALMAGAL data uit Hoofdstuk 3 en kijken we naar de versies van methanol die deuterium bevatten: CH₂DOH en CHD₂OH. De CH₂DOH/CH₃OH verhouding in hoge massa protosterren is meer dan een orde van grootte lager dan in lage massa protosterren. Door dit te vergelijken met modellen in de literatuur kan geconcludeerd worden dat de wolken waar hoge massa sterren uit vormen waarschijnlijk warmer zijn ($\sim 20 - 25$ K) dan die van lage massa sterren (< 15 K). Een alternatief is dat de levensduur van hoge massa moleculaire wolken korter is. De verhouding tussen CHD₂OH en CH₂DOH laat echter weinig verschil zien tussen hoge en lage massa protosterren, wat suggereert dat herhaaldelijke deuteratie even efficiënt is.

Hoofdstuk 5 presenteert modellen van accretie schokken met als doel te bekijken onder welke condities de abundantie van SO en SO₂ significant hoger wordt. De gedetailleerde schokmodellen zijn berekend met de Paris-Durham schokcode voor gebieden met een zwak magnetisch veld. In lage snelheid accretie schokken (~ 3 km s⁻¹) stijgt alleen de SO abundantie. In hogere snelheid schokken (> 4 km s⁻¹) stijgt de abundantie van zowel SO als SO₂. Hierin is de sterkte van de UV straling cruciaal sinds deze H₂O dissocieert tot OH, wat op zijn beurt kan reageren met atomair zwavel. Als de dichtheid hoog genoeg is ($> 10^7$ cm⁻³) kunnen ook SO en SO₂ ijzen sublimeren wat diens abundanties in de gasfase verhogen.

In *Hoofdstuk 6* worden ALMA waarnemingen van drie Klasse I protosterren bekeken om te zoeken naar SO en SO₂ straling dat geassocieerd kan worden met accretie schokken. De schijven van alle drie de protostellare systemen zijn ruimtelijk opgelost, maar SO en SO₂ zijn maar in één van de drie bronnen gedetecteerd. Door de fysische condities waar deze moleculen zich in bevinden te vergelijken met schokmodellen zoals beschreven in Hoofdstuk 5, kan geconcludeerd worden dat de SO en SO₂ zich niet in een accretie schok bevinden of dat deze schok heel zwak is. Dit suggereert dus dat de moleculaire samenstelling momenteel onveranderd de schijf in vloeit. In dit hoofdstuk wordt tevens een link gelegd tussen de aanwezigheid van straling van warm SO₂ en een hoge bolometrische lichtkracht, wat kan duiden op het belang van energetische processen zoals UV straling voor de chemie van SO₂.

Toekomstperspectief

De toekomst van het onderzoek naar complexe organische moleculen en accretie schokken is rooskleurig. Allereerst volgen er steeds meer waarnemingen van ALMA waarmee de vraagstukken van dit proefschrift verder bestudeerd kunnen worden. Er worden niet meer slechts enkele protostellaire systemen waargenomen, maar er wordt er ook naar meerdere bronnen tegelijkertijd gekeken. Dit zorgt ervoor dat de verbanden tussen verschillende protostellaire systemen steeds meer duidelijk worden. Tevens zullen meer ruimtelijk opgeloste waarnemingen van accretie schokken met ALMA duidelijkheid geven over hun aanwezigheid en effect op de chemische samenstelling van het materiaal dat de schijf in vloeit.

De lancering van de James Webb Ruimtetelescoop (JWST) maakt het ook weer mogelijk om met infraroodogen naar het heelal te kijken. Het ruimtelijk oplossend vermogen en de gevoeligheid van JWST zijn ongeëvenaard. Eén van de eerste resultaten die van JWST worden verwacht, zijn de ontdekkingen van complexe organische moleculen zoals acetaldehyde en ethanol in de ijzen. Dit zal antwoord geven op een groot vraagstuk waar nog veel over wordt gedebatteerd: vormen complexe organische moleculen in de ijzen op het oppervlak van stofkorrels of vormen ze vooral in de gasfase? Tevens kan JWST de locaties van accretie schokken nog helderder zien dan ALMA. Hierdoor kan de aanwezigheid en sterkte van accretie schokken verder in kaart worden gebracht en daarmee ook de vraag beantwoorden of de chemische samenstelling in protostellaire schijven is geërfd van de moleculaire wolken of niet.

Publications

1. *N-bearing complex organics toward high-mass protostars. Constant ratios pointing to formation in similar pre-stellar conditions across a large mass range*
Nazari, P., Meijerhof, J. D., **van Gelder, M. L.**, Ahmadi, A., van Dishoeck, E. F., Tabone, B., Langeroodi, D., Ligterink, N. F. W., Jaspers, J., Beltrán, M. T., Fuller, G. A., Sánchez-Monge, Á., Schilke, P., 2022, accepted for publication in *Astronomy & Astrophysics*.
2. *Methanol deuteration in high-mass protostars*
van Gelder, M. L., Jaspers, J., Nazari, P., Ahmadi, A., van Dishoeck, E. F., Beltrán, M. T., Fuller, G. A., Sánchez-Monge, Á., Schilke, P., 2022, accepted for publication in *Astronomy & Astrophysics*, *Chapter 4*.
3. *Importance of source structure on complex organics emission II. Can disks explain lack of methanol emission from some low-mass protostars?*
Nazari, P., Tabone, B., Rosotti, G. P., **van Gelder, M. L.**, Meshaka, R., van Dishoeck, E. F., 2022, *Astronomy & Astrophysics*, 663, A58.
4. *Importance of source structure on complex organics emission. I. Observations of CH₃OH from low-mass to high-mass protostars*
van Gelder, M. L., Nazari, P., Tabone, B., Ahmadi, A., van Dishoeck, E. F., Beltrán, M. T., Fuller, G. A., Sakai, N., Sánchez-Monge, Á., Schilke, P., Yang, Y.-L., Zhang, Y., 2022, *Astronomy & Astrophysics*, 662, A67, *Chapter 3*.
5. *Imaging the water snowline around protostars with water and HCO⁺ isotopologues*
van 't Hoff, M. L. R., Harsono, D., **van Gelder, M. L.**, Hsieh, T.-H., Tobin, J. J., Jensen, S. S., Hirano, N., Jørgensen, J. K., Bergin, E. A., van Dishoeck, E. F., 2022, *The Astrophysical Journal*, 924, 5.
6. *Which molecule traces what: Chemical diagnostics of protostellar sources*
Tychoniec, Ł., van Dishoeck, E. F., van 't Hoff, M. L. R., **van Gelder, M. L.**, Tabone, B., Chen, Y., Harsono, D., Hull, C. L. H., Hogerheijde, M. R., Murillo, N. M., Tobin, J. J., 2021, *Astronomy & Astrophysics*, 655, A65.

7. *Modeling accretion shocks at the disk-envelope interface. Sulfur chemistry*
van Gelder, M. L., Tabone, B., van Dishoeck, E. F., Godard, B., 2021, *Astronomy & Astrophysics*, 653, A159, *Chapter 5*.
8. *Complex organic molecules in low-mass protostars on Solar System scales. II. Nitrogen-bearing species*
Nazari, P., **van Gelder, M. L.**, van Dishoeck, E. F., Tabone, B., van 't Hoff, M. L. R., Ligterink, N. F. W., Beuther, H., Boogert, A. C. A., Caratti o Garatti, A., Klaassen, P. D., Linnartz, H., Taquet, V., Tychoniec, Ł., 2021, *Astronomy & Astrophysics*, 650, A150.
9. *Chemically tracing the water snowline in protoplanetary disks with HCO^+*
Leemker, M., van 't Hoff, M. L. R., Trapman, L., **van Gelder, M. L.**, Hogerheijde, M. R., Ruíz-Rodríguez, D., van Dishoeck, E. F., 2021, *Astronomy & Astrophysics*, 646, A3.
10. *Complex organic molecules in low-mass protostars on Solar System scales. I. Oxygen-bearing species*
van Gelder, M. L., Tabone, B., Tychoniec, Ł., van Dishoeck, E. F., Beuther, H., Boogert, A. C. A., Caratti o Garatti, A., Klaassen, P. D., Linnartz, H., Müller, H. S. P., Taquet, V., 2020, *Astronomy & Astrophysics*, 639, A87, *Chapter 2*.
11. *VLT/X-shooter spectroscopy of massive young stellar objects in the 30 Doradus region of the Large Magellanic Cloud*
van Gelder, M. L., Kaper, L., Japelj, J., Ramírez-Tannus, M. C., Ellerbroek, L. E., Barbá, R. H., Bestenlehner, J. M., Bik, A., Gräfenr, G., de Koter, A., de Mink, S. E., Sabbi, E., Sana, H., Sewilo, M., Vink, J. S., Walborn, N. R., 2020, *Astronomy & Astrophysics*, 636, A54.

Curriculum Vitae

It was in the afternoon of February 8th 1994 that I was born to Erik van Gelder and Ellen Niggebrugge in the “hofstad” of the Netherlands, The Hague. I am the youngest of three children, with my brother Jeroen and sister Pauline both being four years older (yes, they are twins). Already from a very young age, they would be great examples of what to do and also what things one should not do. It was a great pleasure to grow up in the Vogelwijk of The Hague with many green areas to play around as well as the dunes, beach, and sea very close.

With a dad who had studied experimental physics and a mom who had studied chemistry, it was not unexpected that math and physics were very interesting to me already at a very young age. Numbers were just more interesting to work with than, for example, languages. It was thus also no surprise that on my elementary school, the Nutsschool Laan van Poot, I passed the math classes with little effort but that I hated parsing Dutch sentences.

For my high school I chose the Christelijk gymnasium Sorghvliet, a rather small school at about a 15 minute bike ride. Also at high school, my main interest in the natural sciences (physics, chemistry, biology, math) grew. Since physics was the most interesting course and also the one for which I had the highest grades, I decided to start studying Physics and Astronomy at Utrecht University in 2012.

At Utrecht university, however, the first thing I was told was: “if you are here to study astronomy, that’s bad luck because the > 400 year old astronomy department has been removed from the university due to budget cuts”. Most of my bachelor’s studies were therefore focused on many aspects of physics with only two astronomy courses available in Utrecht. Nevertheless, my interest in astronomy resulted in me doing my Bachelor’s research project at SRON (then still in Utrecht) under supervision of dr. Elisa Costantini and dr. Tom Prokopec. The topic was on X-ray absorption spectroscopy of the hot interstellar medium near the Galactic center. It was during this research project that my interest in astronomy manifested itself and I decided to pursue my master in Astronomy and Astrophysics at the Anton Pannekoek Institute of the University of Amsterdam. Of course, first a 4 month backpack trip through Australia was necessary to explore the world.

The journey of my master started in 2016 with many courses covering topics from black holes and general relativity to stellar structure and evolution. However,

it was the star and planet formation course that attracted me most. I was grateful that I could participate in the La Palma observing project, where we were allowed to take our own observations with the Mercator telescope. For my MSc project, I started with a project under the supervision of prof. dr. Lex Kaper on X-shooter observations of massive young stellar objects in the 30 Doradus region of the Large Magellanic Cloud. I graduated cum laude from the University of Amsterdam in the summer of 2018. Both the observational project and the master project convinced me that I really liked working with observational data and that I wanted to keep doing so in the future. Therefore I decided that I was going to apply for PhD positions in astronomy.

I was fortunate enough to receive an offer for a PhD position from prof. dr. Ewine van Dishoeck from Leiden Observatory. The topic of astrochemistry during star and planet formation caught my eye, as well as the fact that I could start working with the newest data from the newest telescope, the James Webb Space Telescope (JWST). Unfortunately, the launch of JWST was delayed by more than three years, but that did not mean that no observational data were available. Plenty of data from the Atacama Millimeter/submillimeter Array were taken to pursue my main research topics: complex organic molecules and accretion shocks in young protostellar systems. Finishing this PhD thesis would not have been possible without my daily supervisor across from me in the office, dr. Benoît Tabone. Throughout the four years of my PhD I presented at various conferences, both in person and online, and learned how to setup and do a research project. Toward the end, also the world of outreach has opened itself up to me, with a talk at Astronomy on Tap and many demonstrations with the beautiful 1:10 scale model of JWST.

The next stop in my career will actually not be far away. I will stay at Leiden Observatory for an additional two years as a postdoctoral researcher. Now, I finally get to work with the newest data from the newest telescope as part of the JOYS, JWST Observations of Young protoStars, team.

Acknowledgements

This PhD thesis would not have been possible without the support and friendship of many people around me. Especially during the years of the pandemic when we were locked up in our houses, all social interactions were a great support.

First of all, I would like to thank you Ewine for giving me the opportunity and the framework to pursue a PhD in (mostly) observational astronomy. Your guidance, knowledge, and support have made it possible to pursue the projects covered during my PhD. I am also grateful that you offered me a postdoc position in Leiden to (finally) work with the JWST data for which I was originally hired as a PhD student. Michiel, you were always very kind to help with various issues that I had, especially related to ALMA data. Last but definitely not least: Benoît, thank you for always answering all my questions in a very clear way. I will really miss our discussions on both science and non-science topics, as well as the occasional French swear words. I am grateful for the PEACHES and ALMAGAL teams that I could use their ALMA data for the various projects of this thesis. Also a great thank you to the Allegro team for helping me with the ALMA datasets presented in this work.

It was a great pleasure to be part of the large astrochemistry research group. Łukasz, thanks for the joint adventure in supervising our first master students and for getting me up to speed in the group. Also thanks for letting me use your apartment as an office in the beginning of pandemic, I hope this evens the times I opened the door for you when you lost the keys. Pooneh, thank you for all the endless discussions on COMs and for always being so happy and energetic. Margot, thanks for always seeing humor in everything and jointly complaining about various aspects of science and life. I have never used DALI, but now know its pros and even more of its cons. Alice, your little dances always cheer me up. You will never have to change arm poses in my pictures. Lisa, you always found time for a talk and discuss the various aspects of life, thank you for helping me with the German trains. Ardjan, your down to earth mentality is very useful for the times when I was stressed. Lucas, you have taken over the L-G meetings in a great manner. Logan, next time you can smuggle your own beer mug past an angry German airport security lady. Arthur and Alex, the corridors on the fifth floor are so quiet without your laughter. Merel, you were a great office mate, thank you for answering all my basic questions. Nadia, Daniel, our discussions as embedded

task force will not be forgotten. Sierk, thank you for showing me how to run the L-G meeting. Leon, keep making the nice cocktails. Giovanni, I always liked our talks about both science and life. Sierra, Giulio, Teresa, Andrés, you were great hosts during our recent group retreat in Garching, it's always nice to see you in 3D again. To 'my' master students Yuan, Micha, Jeroen, Jurrian, Gabriëlla, and Nelleke, it was an honor to supervise you during your master projects. Yuan, I am proud that you joined our group again as a PhD student. Jerry, although we do not have a 'private' office anymore, I will still find time to talk. Milou, Marissa, Logan, thank you for releasing me from my private office with Jerry. Thank you also to everyone that helped with the demo's with our big JWST model.

The fortunate part of our group was to also share the floor with the lab. Jeroen, you were always easy to find, thank you all the rather interesting conversations during borrels. Pranjali, our borrel talks were always of significant quality. Marina, your beers always taste amazing. Katie, your logo for JOYS is beautiful. Will, you are a great guru for ice observations. Dana, Gleb, Ko-Ju, Michal, Julia, many thanks for the many discussions on COMs.

Ofcourse, also the interaction with various other people at the observatory have made the PhD life much more pleasant. Anna, Mantas, it was a great honor to serve the great Big Dipper together. Fraser, thank you enjoyable discussions and for cleaning up after borrel. Marta, although I agree the Dutch weather is not great, it can be sunny occasionally. Anniek, great to see a fellow UvA student coming to Leiden. Kirsty, thanks for the many weird conversations. Hiddo, you were always very happy and Frisian. Also to the many other people at the Observatory, Andrés, Andrew, Aida, Bas, Danny, Dario, Dilovan, Folkert, Frits, Gabriëlla, Josh, Lýdia, Martijn, Matthieu, Nicco, Roland, and many people I am very likely forgetting, thank you for the coffee breaks, borrels, and everything else.

Also outside of the observatory, I was fortunately surrounded by many friends. Jeroen, great that you have arranged it with the PhD, thanks for keeping me caffeinated with our many 'plonko' breaks. Jesse, I promise I will be online more often, thanks for the many adventures over the past decade. Marijn, we'll visit you more often in Deventer. Mirjam, Wouter, Anne-Bibi, Baptiste, Rianne, Justin, I loved our regular online pub quizzes during the pandemic as well as the new year's parties. Ariane, Chris, David, Hessel, Jan, Jay, Jasper, Joost, Sjoerd, thank you for the many enjoyable moments during our studies in Utrecht, and also afterwards. Frank, I can never eat broccoli, corn, leek, radish, and tomato again without thinking back at our Europe interrail trip. Wieger, Floris, Koen, Max, I will never forget our many adventures in The Hague.

Tenslotte, pap, mam, Jeroen, Pauline, Eric, dank jullie wel voor de onvoorwaardelijke support gedurende mijn hele leven. Ik zal Nederland goed bewaken gedurende jullie avonturen in het buitenland. Isaac, voor als je over enkele jaren hebt leren lezen: je bent een geweldig leuke toevoeging aan de familie. Trudy, Hans, Ivar, Arvid, Diana, BA, ik voel me altijd direct thuis bij jullie in 's Gravenzande. Birgit, ik kan je niet genoeg bedanken voor alle support en liefde die je me geeft. Zonder jou was dit allemaal niet mogelijk geweest.